UNIVERSITY OF SOUTHAMPTON

FACULTY OF ENGINEERING AND THE ENVIRONMENT

Aerodynamics and Flight Mechanics Group

Modelling of Multiphase Multicomponent Chemically Reacting Flows through Packed Beds

by

Robert-Jan Koopmans

Thesis for the degree of Doctor of Philosophy

May 2013

UNIVERSITY OF SOUTHAMPTON

ABSTRACT

FACULTY OF ENGINEERING AND THE ENVIRONMENT

Aerodynamics and Flight Mechanics Group

Doctor of Philosophy

MODELLING OF MULTIPHASE MULTICOMPONENT CHEMICALLY REACTING FLOWS THROUGH PACKED BEDS

by Robert-Jan Koopmans

Currently used rocket propellants such as hydrazine, monomethylhydrazine, unsymmetrical dimethylhydrazine and nitrogen tetroxide are carcinogenic and toxic to the environment and therefore special protective measures are required when producing, transporting, storing and handling them. Employing alternatives could possibly save costs and this has revived the research interest in so called green propellants. Hydrogen peroxide is such a possible alternative. It requires a catalyst bed to decompose the liquid peroxide into steam and oxygen.

The purpose of this work is to design numerical tools that describe the processes in the catalyst bed and subsequently employ these tools to predict the performance of the catalyst bed and investigate the influence of design choices on the performance. In contrast to the models described in the literature, the tools developed in this thesis are two-fluid models. In order to test the reliability of the tools results are compared with experimental data.

A single control volume two-fluid model has been developed to investigate the pressure drop over the catalyst bed and the influence of the shape and size of catalyst pellets on the pressure drop. Parametric studies with this model revealed that the Tallmadge equation gives a better prediction of the pressure gradient than the more traditionally employed Ergun equation. It was also found that for a given bed length cylindrical pellets with a diameter to length ratio of 2 or more give a lower pressure drop than cylindrical pellets, while achieving the same level of decomposition.

A one-dimensional two-fluid model has been developed to obtain longitudinal variations of fluid properties. This model revealed that the catalyst bed can be divided into 3 sections: a pre-boiling region, rapid conversion region and a dry-out region. It was shown that most of the mass transfer takes place due to evaporation. A sensitivity analysis showed that the gas-liquid interfacial area hardly influences the results.

Table of Contents

List of Figures

List of Tables

Declaration of Authorship

I, Robert-Jan Koopmans, declare that the thesis entitled *Modelling of Multiphase Multicomponent Chemically Reacting Flows through Packed Beds* and the work presented in the thesis are both my own, and have been generated by me as the result of my own original research. I confirm that:

- this work was done wholly or mainly while in candidature for a research degree at this University;
- where any part of this thesis has previously been submitted for a degree or any other qualification at this University or any other institution, this has been clearly stated;
- where I have consulted the published work of others, this is always clearly attributed;
- where I have quoted from the work of others, the source is always given. With the exception of such quotations, this thesis is entirely my own work;
- I have acknowledged all main sources of help;
- where the thesis is based on work done by myself jointly with others, I have made clear exactly what was done by others and what I have contributed myself;
- parts of this work have been published as given in the list of publications.

Signed: .....

Date: .....

List of Publications

Journal Articles

R. Koopmans, J.S. Shrimpton, G.T. Roberts, and A.J. Musker. A one-dimensional multicomponent two-fluid model of a reacting packed bed including mass, momentum and energy interphase transfer. *International Journal of Multiphase Flow*, 2013, Accepted for publication.

R. Koopmans, J.S. Shrimpton, G.T. Roberts, and A.J. Musker. Influence of Shape and Size of Catalyst Pellets on the Pressure Drop in a Hydrogen Peroxide Thruster. *Journal of Propulsion and Power*, 2013, Under review.

Conference Papers

R. Koopmans, J.S. Shrimpton, G.T. Roberts, and A.J. Musker. A Zero-Dimensional Model of a Hydrogen Peroxide Propulsion System. In *Proceedings of Space Propulsion 2010 Conference, San Sebastian, Spain*, 2010.

R. Koopmans, J.S. Shrimpton, and G.T. Roberts. Parametric Studies for a Hydrogen Peroxide Rocket Engine. In *4th European Conference for Aerospace Sciences 2011, Saint Petersburg, Russia*, 2011.

R. Koopmans, J.S. Shrimpton, and G.T. Roberts. Validation and Design Optimization for a Hydrogen Peroxide Thruster. In *47th AIAA/ASME/SAE/ASEE Joint Propulsion Conference and Exhibit, San Diego, California*, number AIAA 2011-5696, 2011.

R. Koopmans, J.S. Shrimpton, and G.T. Roberts. Simulations with a one-dimensional two-fluid model of a hydrogen peroxide catalyst bed. In *5th European Conference for Aerospace Sciences 2013, Munich, Germany*, 2013.

Acknowledgement

There are many people who have contributed to this thesis, either directly or indirectly, who deserve a thank you.

First of all I would like to thank my supervisors Dr. Graham Roberts and Dr. John Shrimpton for guiding me into the research world. Their advice and encouragement have been invaluable. A photo of Graham reading my thesis during his holiday on Gran Canaria won't be forgotten. Many thanks also to Professor Tony Musker. His role as adviser has proven to be indispensable for obtaining experimental data and for providing advice during difficult times. Very much appreciated are the comments from Professor Kai Luo during my transfer viva. Also a special thanks to Matt Palmer with whom I have been closely working together over the past few years. He was the first Brit I got to know a little bit better and he showed me several aspects of being student in the UK. I wish him all the best in bringing his research to a satisfactory conclusion.

I would like to thank Agi Kourmatzis, Matt Palmer, Andy Ju, Sina Heari, Kangping Zhang, Man Zhang and Yu Zhao, whom I have shared the office with, for the fruitful discussions and the occasional banter and so have made all these years bearable. Also thanks to all my friends back home as well as the friends I have made here for their support and helping me to relax. As there are so many I won't try to name them all; afraid that I will forget to include a couple.

Last but not least I would like to thank my parents and sister for their never ceasing support and encouragement during my studies. Although it did not come as a surprise that I would go abroad, it took some time before they got used to the idea. Particular important was the support from my sister Suzanne, who, being a PhD student herself, understood very well the difficulties I came across. I wish her all the best with finalising and the defence of her thesis. And finally a massive thank you to my girlfriend, Beckie, for her love and support and for generally putting up with me during my research. I wish her all the best on her journey to obtain a PhD degree.

Nomenclature

Roman symbols

ΔH_{fg}	latent heat	$[J\,kg^{-1}]$
$\dot{h}$	heat transfer rate	$[J\,kg^{-1}\,s^{-1}]$
$\dot{r}$	reaction rate	$[kg\,m^{-3}\,s^{-1}]$
$\mathbf{M}$	momentum source	$[N\,m^{-3}]$
$\mathbf{u}$	velocity vector	$[m\,s^{-1}]$
$\mathcal{D}$	binary diffusion coefficient	$[m^2\,s^{-1}]$
$\mathcal{D}_{eff}$	effective diffusivity	$[m^2\,s^{-1}]$
$\overline{n}$	control volume density	$[m^{-3}]$
A	surface area	$[m^2]$
A_0	pre-exponential factor	$[s^{-1}]$
a_α	coefficient of discretised equations of phase α	
a_{sp}	specific surface area	$[m^{-1}]$
B	general source term	$[kg\,m^{-3}\,s^{-1}\,[\phi]]$
b	all remaining terms in the discretised equation	$[-]$
C	Chisholm constant	$[-]$
c_d	discharge coefficient	$[-]$
c_p	specific heat at constant pressure	$[J\,kg^{-1}\,K^{-1}]$

D	diameter	$[m]$
E_A	activation energy	$[J\,mol^{-1}]$
h	specific enthalpy	$[J\,kg^{-1}]$
h_T	heat transfer coefficient	$[W\,m^{-2}\,K^{-1}]$
H_{21}	curvature	$[m^{-1}]$
J	molar flux	$[mole\,m^{-2}\,s^{-1}]$
j	mass flux	$[kg\,m^{-2}\,s^{-1}]$
K	permeability	$[m^{-2}]$
k	thermal conductivity	$[W\,m^{-1}\,K^{-1}]$
k'''	volumetric reaction rate constant	$[s^{-1}]$
k''	surface reaction rate constant	$[m\,s^{-1}]$
k_1, k_2, k_3	reaction rate constants	$[s^{-1}]$
k_4, k_5, k_6	reaction rate constants	$[cm^3\,mol^{-1}\,s^{-1}]$
k_7, k_8	reaction rate constants	$[cm^3\,mol^{-1}\,s^{-1}]$
k_M	mass transfer coefficient	$[m\,s^{-1}]$
K_r	equilibrium constant k_{ad}/k_{de}	$[m^2\,mol^{-1}]$
k_{ad}	adsorption rate constant	$[m^2\,mol^{-1}\,s^{-1}]$
k_{de}	desorption rate constant	$[s^{-1}]$
k_{reac}	decomposition rate constant	$[s^{-1}]$
L	length	$[m]$
L_p	length of cylindrical catalyst pellets	$[m]$
M	molar mass	$[kg\,mol^{-1}]$
m	mass	$[kg]$
N	number of active sites	$[]$
p	pressure, sometimes given in bar ($= 1 \cdot 10^5\,Pa$)	$[Pa]$

p_i°	vapour pressure of pure component i	$[Pa]$
Q	energy source	$[J\,m^{-3}\,s^{-1}]$
R	gas constant	$[J\,kg^{-1}\,K^{-1}]$
r	radius	$[m]$
r'	non-dimensional radial coordinate	$[-]$
r_{min}	radius reference value	$[m]$
S	species mass source term	$[kg\,m^{-3}\,s^{-1}]$
T	temperature	$[K]$
t	time	$[s]$
T_b	normal boiling point	$[K]$
T_c	critical temperature	$[K]$
T_r	reduced temperature	$[-]$
t_r	radial thickness	$[m]$
u_0	superficial velocity	$[m\,s^{-1}]$
u_r	radial velocity	$[m\,s^{-1}]$
V	volume	$[m^3]$
x_i	mol fraction of component i in the liquid phase	$[-]$
Y	mass fraction	$[-]$
y_i	mol fraction of component i in the gas phase	$[-]$

Greek symbols

β	evaporation coefficient	$[-]$
τ	viscous stress	$[Pa]$
χ	Lockhart-Martinelli parameter	$[-]$
δ	boundary layer thickness	$[m]$
$\Delta_r H$	reaction enthalpy	$[J\,kg^{-1}]$

ε	volume fraction	$[-]$
ε_f	void fraction	$[-]$
η	passability	$[m^{-1}]$
η_{eff}	effectiveness factor	$[-]$
Γ	mass source term	$[kg\,m^{-3}\,s^{-1}]$
γ	ratio of specific heats	$[-]$
γ_i	activity coefficient of component i	$[-]$
κ	non-dimensional constant for hydrogen peroxide mixture boiling point	$[-]$
μ	dynamic viscosity	$[Pa\,s]$
ν	stoichiometric reaction coefficient	$[-]$
ω	underrelaxation factor	$[-]$
Φ	generalised Thiele modulus	$[-]$
Ψ	two-phase multiplier	$[-]$
ψ	Thiele modulus	$[-]$
ρ	density	$[kg\,m^{-3}]$
σ	surface tension	$[N\,m^{-1}]$
θ	fractional coverage	$[-]$
ζ	temperature constant for hydrogen peroxide mixture boiling point	$[K]$

Subscripts

α	refers to phase α
A	refers to component A
atm	refers to atmospheric conditions
b	refers to the catalyst bed
bed	refers to the catalyst bed
i	refers to the interface

inj	refers to the injector
lg	refers to the liquid-gas interface
loc	refers to local conditions
m	refers to the mixture
$mean$	refers to the mean
nb	refers to all neighbouring nodes
p	refers to the pellet
ps	refers to the a radius of a sphere with equivalent volume of a non-spherical particle
rod	refers to a group of catalyst pellets if they are put next to each
s	refers to the solid phase or the droplet surface
sat	refers to saturation conditions
sg	refers to the solid-gas interface
sl	refers to the solid-liquid interface
$tank$	refers to the tank
wet	refers to the wetted part of a catalyst pellet
d	refers to a droplet
g	refers to the gas phase
l	refers to the liquid phase
v	refers to the vapour component(s)

Superscripts

ϕ'	most recent value of ϕ from the last inner loop iteration
dec	refers to decomposition
$evap$	refers to evaporation
n	refers to the value at the end of the time step
$n-1$	refers to the value from the previous iteration

new	refers to the intermediate value in the time step
S	refers to the catalyst surface

Dimensionless numbers

$\mathsf{B_T}$	Spalding heat transfer number
$\mathsf{Da_I}$	first Damköhler number
$\mathsf{Da_{III}}$	third Damköhler number
$\mathsf{Da_{II}}$	second Damköhler number
$\mathsf{Da_{IV}}$	fourth Damköhler number
Ec	Eckert number
Eu	Euler number
Fr	Froude number
Le	Lewis number
Ma	Mach number
Nu	Nusselt number
Pe	Péclet number
Pr	Prandtl number
Re	Reynolds number
Sc	Schmidt number
Sh	Sherwood number
B_M	Spalding mass transfer number

Constants

g	gravitational acceleration	$9.80665\,m\,s^{-2}$
R_c	universal gas constant	$8.314472\,J\,mol^{-1}\,K^{-1}$

Acronyms

ATO	Assisted Take-Off
CEA	Chemical Equilibrium with Applications
CFD	Computational Fluid Dynamics
ChemSec	Internal Chemical Secretariat
CMR	Carcinogenic, Mutagenic and toxic for Reproduction
DNAPL	Dense Non-Aqueous Phase Liquid
ECHA	European Chemicals Agency
ESA	European Space Agency
EU	European Union
GRASP	GReen Advanced Space Propulsion
HTP	High Test Peroxide
MEMS	MicroElectroMechanical Systems
MMH	MonoMethylHydrazine, CH_6N_2
MON	Mixed Oxides of Nitrogen
NGO	Non-Governmental Organisation
NTO	Nitrogen TetrOxide, N_2O_4
REACH	Regulation, Evaluation, Authorization and Restriction of Chemicals
SIMPLE	Semi Implicit Method for Pressure-Linked Equations
SIN	Substitute It Now
SVHC	Substances of Very High Concern
TRL	Technology Readiness Level
UDMH	Unsymmetrical DiMethylHydrazine, $C_2H_8N_2$

Notation

ϕ^*	non-dimensional value of ϕ

ϕ^+	positively charged component ϕ
ϕ^-	negatively charged component ϕ
$\phi^\bullet$	radical of component ϕ
ϕ_0	reference value of ϕ
$[\phi]$	molar concentration of ϕ

Miscellaneous

$LC50$	lethal concentration for 50% of the population	$[mg \cdot m^{-3}]$
$LD50$	lethal dose for 50% of the population	$[mg \cdot kg^{-1}]$

Preface

When I finished secondary school I thought I knew a little bit. Two weeks after I started university I discovered I knew nothing. When I finished my MSc degree I thought again I knew something. A couple of weeks into my PhD degree I discovered once again that I knew nothing. Now I am at the end of my PhD degree and all I know is that I know hardly anything, but I can learn anything.
Although the above seems to be a cliche, it reflects that obtaining a PhD degree has not just been about doing research and making a contribution to the field but a journey during which many personal characteristics have been revealed and challenged. Having a number of people in my environment who are pursuing or have just finished a PhD degree as well, it seems to me that this is inherent to the degree. This thesis is just reporting on that part of the journey that was the reason to start it in the first place: making an original contribution to the field of study.

Robert-Jan Koopmans
Southampton, April 2013

Chapter 1

Introduction

The main topic of this thesis is the study of the behaviour of highly concentrated hydrogen peroxide in pellet based catalyst beds with numerical tools. This chapter provides the justification of this research by giving a short overview of the history of hydrogen peroxide from its discovery until the renewed interest in recent years. The discussion on hydrogen peroxide in this chapter and in the remainder of this thesis is limited to highly concentrated peroxide: typically concentrations of 70% and above, also known as high test peroxide (HTP). At these concentrations, hydrogen peroxide is used as propellant in rockets, torpedoes and other high performance engines. The disadvantages of currently used rocket propellants and the opportunity for alternatives are discussed by having a closer look at the toxicity of different propellants. Advantages of hydrogen peroxide are mentioned as well. The reservations the space community has towards hydrogen peroxide is discussed next by means of discussing the counter-arguments. After that the GRASP project is introduced from which this research stems. At the end, the objectives of this PhD research are presented.

1.1 Historical Perspective

Hydrogen peroxide was discovered in 1818 by Louis-Jacques Thenard during his work on the development of batteries. While experimenting with alkali metals he noticed the formation of 'oxygenated water', nowadays known as hydrogen peroxide. He studied the reactivity of hydrogen peroxide with different materials and noticed that some were reactive while others were not. With this result he was one of the first observers of catalysis; a type of reaction not known at the time. Thenard then developed a production method for hydrogen peroxide with which he could achieve concentrations up to about 33%. By placing the peroxide in a vacuum for an extended period of time he was able to increase the concentration close to 100% [1].

Hellmuth Walter was the first to exploit the potential of peroxide as propellant on a large scale. He

founded a company, Walterwerke, for the manufacturing of engines which used hydrogen peroxide with a concentration of 80 to 82%. The first applications were assisted take-off (ATO) units in aircrafts and systems to drive turbines in submarines. In both cases, permanganate salts were used as a catalyst. To boost the performance of the ATO units and similar engines further, Walter developed a fuel called C-Stoff. This was a mixture of methanol and hydrazine hydrate and is hypergolic with hydrogen peroxide. It was amongst others applied in engines powering the Messerschmidt Me 163B Komet. Walterwerke manufactured many different hydrogen peroxide fuelled devices such as engines for torpedoes, submarines and catapult launching ramps for weapons [1].

The substantial experience gained from the use of hydrogen peroxide in engines for aircraft and submarines resulted in the application of peroxide in rockets. A well-known example is the peroxide driven turbo-pump gas generator in the German V-2 rocket. It used 80% hydrogen peroxide catalysed with a potassium permanganate solution. After World War II, hydrogen peroxide technology for rockets was developed further. However, the disadvantages of a liquid catalyst are the necessity of a bipropellant system for a monopropellant application and the catalyst being ejected through the nozzle without contributing to the specific impulse. This resulted in the development of catalyst beds consisting of pellets [2].

The first application of pellet based catalyst beds was found in Germany during WWII where it was developed for submarines and torpedoes, which burned a mixture of hydrogen peroxide and kerosene [2]. After the war, pellet based beds were developed further mainly in the UK and the US, where it was used in gas generators to drive the turbo pumps on the Redstone and Jupiter rockets. However, typical problems encountered with pellet based catalysts were that they fractured due to thermal loading and that small particles came off from the pellets [3]. This was resolved by the invention of silver screen catalyst beds. They consist of thin silver wires that are woven like a fine lattice. Further advantages of screens were that the catalyst bed could be made smaller and that they lasted longer than pellets based beds. It has been used in many different rockets, including the Centaur, Viking, X-1, X-15, Mercury, Black Night and Black Arrow. The Black Arrow was a British 3-stage rocket which used a combination of hydrogen peroxide and kerosine as propellants. It is the only launch system to date that used hydrogen peroxide in all three stages to send satellites into a (low) Earth orbit [3].

The Cold War gave a new impulse to the design and manufacturing of rocket propellants and propulsion systems. The most important requirement was high performance measured in terms of specific impulse. Propellants and propulsion systems with low operating costs, low toxicity and manageable physical properties, such as high density and low freezing point, were regarded as second most important requirements. This resulted in the development of propulsion systems using hydrazine, for monopropellant systems, and hydrazine derivatives such as MMH[*] and UDMH[†], for bipropellant systems. For the bipropellant applications NTO[‡] or MON[§] in various concentrations are used as an

[*] monomethylhydrazine, CH_6N_2
[†] unsymmetrical dimethylhydrazine, $C_2H_8N_2$
[‡] nitrogen tetroxide, N_2O_4
[§] mixed oxides of nitrogen

oxidizer.

The superior performance of hydrazine based thrusters is clearly shown in table 1.1, which shows the calculated vacuum specific impulse for: the hydrazine family, hydrogen peroxide, when used as monopropellant, and hydrogen peroxide with three different fuels, for bipropellant applications [4]. For bipropellant applications peroxide serves as the oxidizer. Calculations are based on a chamber pressure of 10 bar, a nozzle expansion ratio of 40 and a chemical equilibrium frozen in the throat [4]. The calculations have been performed with the CEA[¶] code by Gordon and McBride [5]. It is clear that for both monopropellants and bipropellants hydrazine and its derivatives have the better performance, although with 90% peroxide and the right choice of fuel the performance can match the performance of UDMH with NTO. Due to its high performance and the long experience in handling the fuels and designing the propulsion systems, hydrazine, MMH and UDMH are still the dominating non-cryogenic propellants used for space propulsion [6].

Monopropellant application	
fuel	$\mathbf{I_{sp}}$[s]
hydrazine	185
90% H_2O_2	145
100% H_2O_2	161

Bipropellant application		
fuel	**oxidizer**	$\mathbf{I_{sp}}$[s]
MMH	NTO	323
UDMH	NTO	320
turpentine	90% H_2O_2	306
methane	90% H_2O_2	312
cyclopropane	90% H_2O_2	320

Table 1.1: *Vacuum specific impulse for several propellants [4]*

1.2 Demand for Alternative Rocket Propellants

Despite the widespread use of hydrazine and hydrazine derivatives for space propulsion, it has some major disadvantages, of which its toxicity and the associated costs for handling, storing and transportation is one of the biggest problems. As part of the GRASP project, which is further described in section 1.4, a toxicity assessment was performed where hydrazine, MMH and UDMH were compared with hydrogen peroxide and various other propellants. One of the conclusions of this assessment was that there is no universally accepted assessment method and important toxicity data is sometimes not available [4]. However, all the reviewed toxicity studies mentioned in this assessment more or less agree on the qualitative ranking of propellants according their toxicity.

The assessment combines toxicity data for normal working conditions and toxicity data in case of crises such as spillage or unintended contact with the propellant. The former is referred to as *working toxicity data* and the latter as *acute toxicity data*. The assessment of the working toxicity data

[¶]Chemical Equilibrium with Applications

is based on R-phrases (Risk phrases), which is defined in Annex III of European Union Directive 67/548/EEC [7]. The following categories with corresponding R-phrases were used in the assessment:

- indicative of acute lethality (R23 through to R28)
- irreversible, non-lethal effects (R39)
- serious chronic effects (R48, R68)
- carcinogen categories 1 and 2 (R45, R49)
- mutagenic (R46)
- reproduction (R60, R61)
- environmental persistence (R50 through to R53)
- non aquatic toxicity (R54 through to R59)

Table 1.2 gives a summary of the results for R-phrases for hydrogen peroxide, hydrazine and hydrazine derivatives. If one of the chemicals has an R-phrase in one of the categories it receives the value 1. If no R-phrases for that category are specified it receives a zero.
Table 1.2 clearly shows that hydrogen peroxide is less harmful to humans and the environment than

	hydrogen peroxide	**hydrazine**	**MMH**	**UDMH**
R23 - R28	0	1	1	1
R39	0	0	0	0
R48, R68	0	0	0	0
R45, R49	0	1	1	1
R46	0	0	0	0
R60, R61	0	1	0	1
R50 - R53	0	0	0	0
R54 - R59	0	0	0	0
total	**0**	**3**	**2**	**3**

Table 1.2: *Summary of R-phrases for hydrogen peroxide, hydrazine and its derivatives [4]*

hydrazine and hydrazine-like propellants. This means that when working with hydrogen peroxide less stringent precautions for handling and storage are needed compared to the other propellants. It should be noted that the table suggests that peroxide is not toxic at all. However, as was mentioned in the toxicity assessment [4], this is not the case. Swallowing peroxide at high concentrations is fatal.
The EU Hazard Statement is used to categorise the acute toxicity data, which is based on values for oral LD50, dermal LD50 and LC50. LD stands for *lethal dose* and LC for *lethal concentration*. The

LD50 and LC50 values give the dose concentration by which at least 50% of a population, normally a group of rats, mice or rabbits, dies. The categories are shown below in table 1.3.

The higher the category, the less it is considered to be toxic. Data for acute toxicity for the same

	unit	cat. 1	cat. 2	cat. 3	cat. 4	cat. 5
Oral LD50	mg/kg/4h	< 5	< 50	< 300	< 2000	> 2000
Dermal LD50	mg/kg	< 50	< 200	< 1000	< 2000	> 2000
LC50	mg/m^3	< 500	< 2000	< 10000	< 20000	> 20000

Table 1.3: *EU Hazard Statement*

propellants as in table 1.2 is shown in table 1.4 [4]. It shows data for oral LD50, dermal LD50 and LC50 and in brackets the corresponding category.

As was mentioned in the toxicity assessment [4] the LD50 and LC50 data should be used with

	hydrogen peroxide	hydrazine	MMH	UDMH
Oral LD50	805 (4)	60 (3)	32 (2)	122 (3)
Dermal LD50	2000 (5)	91 (2)	95 (2)	1060 (4)
LC50	2876 (3)	330 (1)	34 (1)	252 (1)
lowest cat.	3	1	1	1

Table 1.4: *Summary of acute toxicity data for hydrogen peroxide, hydrazine and its derivatives [4]*

care. Oral LD50 relates to the case that someone inadvertently drinks the propellant; something that is unlikely to happen under normal handling circumstances. LC50 data should be interpreted together with vapour pressure. The lethal concentration might be very low, but if the vapour pressure is extremely low as well, the hazard is minimal. The vapour pressure for different propellants is shown in table 1.5.

Tables 1.4 and 1.5 combined clearly show that the acute toxicity for hydrogen peroxide is lower

	vapour pressure [Pa]
hydrazine	1895
MMH	6526
UDMH	20631
hydrogen peroxide	670

Table 1.5: *Vapour pressure at standard conditions for hydrogen peroxide, hydrazine and its derivatives [4]*

than for hydrazine, MMH and UDMH. The conclusion given in the toxicity assessment [4] is that, although toxicity data is not absolute and can be reported in several ways, hydrogen peroxide has a *"significantly reduced toxicity and carcinogenity risk compared to the hydrazine family."* Besides the significant lower toxicity, Wernimont et al. [3] pointed out hydrogen peroxide offers a number of other

advantages over other propellants. Some of them have not been exploited or fully investigated yet. They are:

- high density specific impulse
  This is favourable for spacecrafts that are severely volume constrained and/or suffer from aerodynamic drag. In the latter case a high density specific impulse results in smaller surface areas and thus reduced drag.

- storable propellant
  Hydrogen peroxide can be stored for long periods of time at room temperature provided that the tanks are well designed.

- non-reactive with the atmosphere
  Hydrogen peroxide is not reactive with elements or compounds from the atmosphere as opposed to hydrazine that reacts with carbon dioxide resulting in material degradation.

- high oxidizer to fuel ratio
  Optimum oxidizer to fuel ratios for hydrogen peroxide and a fuel are typically in the range of 1:7 to 1:10 as opposed to 1:2 for the combination of MMH and NTO. As the density of peroxide is high, a large part of the propellant mass is dense, thus requiring less storage volume and consequently storage mass.

- low vapour pressure
  Due to its low vapour pressure (see table 1.5) turbopumps could operate at lower inlet pressure, resulting in a lower oxidizer tank mass.

- high specific heat
  The specific heat is comparable to that of water and, in combination with the high oxidizer to fuel ratio, very attractive for (regenerative) cooling.

- water can be used as referee liquid
  As water has very similar properties to peroxide, it can be used as referee liquid for system development, acceptance and qualification. Water is much easier to use compared to isopropyl alcohol and freon which is used as referee liquid for MMH/NTO propulsion systems.

- integrated design possibilities
  Hydrogen peroxide could be used for more than one application at the same time such as oxidizer for the main propulsion system, monopropellant for attitude control systems, gas generators or even tank pressurisation.

The implication of the advantages of hydrogen peroxide over other propellants is that costs can be reduced when building and operating a spacecraft [8]. In a study performed by EADS and funded by

ESA, a monopropellant spacecraft based on hydrogen peroxide was designed. The conclusion was that the cost reduction is so large that the development of alternative propellants, often referred to as *green propellants* is beneficial. This explains the increase in interest in those alternative less toxic systems, which is, for instance, clearly visible in the growing number of published papers dealing with green propellants. Kappenstein [9] has shown this graphically for the period 1994 to 2007, see figure 1.1.

Recently, major space agencies such as NASA and the Russian space agency have announced plans

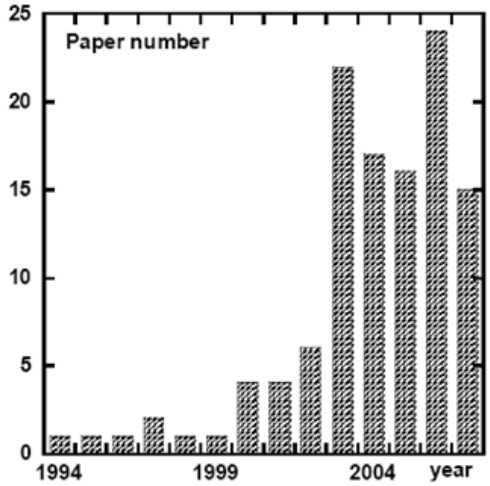

Figure 1.1: *Number of papers dealing with 'green propellants' [9]*

to develop new launchers and space vehicles in an effort to get back to the moon and beyond. Much focus is on reducing cost and the use of green propellants [10].

Despite the significant amount of work done in the past on hydrogen peroxide based engines, as explained in section 1.1, a lot of knowledge has been lost. This is partly due to retirement/passing away of the people that were involved in experimenting, designing and building of hydrogen peroxide thrusters and partly due to the restricted access on research and measurement data. Moreover, the majority of the work on peroxide engines was performed in an era where computers had just been invented and were not capable of performing simulations yet; especially not with the complexity of chemically reacting flows in packed beds. In some cases information is scarce due to language barriers. It is for instance well-known that a lot of development on hydrogen peroxide engines took place in Russia. However, as far as information is disclosed, it is in Russian and consequently difficult to find and read. Only in very recent years has some knowledge been published in English. For these reasons, much research has to be done again.

1.3 Perception of Hydrogen Peroxide in the Space Community

Despite attractive features such as low toxicity and environmental harmless reaction products and the resulting lower costs the space industry in general is very reluctant to switch over to other fuels. This has partly to do with the fact that technology for alternative fuels, such as hydrogen peroxide, have not yet reached the same maturity level as hydrazine. Because developing and building spacecraft is very expensive, space companies are not prepared to take the risk to employ new technology unless absolute reliability has been proven. As far as hydrogen peroxide is concerned there is a general persistent perception that it is unsafe and has a lot of other disadvantages. The major points of concern are:

- detonability
- stability and storability
- catalyst bed lifetime
- high freezing point
- lack of hypergolicity

In the works of Davis et al. [11], Musker et al. [12] and Ventura et al. [13] it is pointed out that most if not all concerns are based on historical anecdotes or on views expressed in reference textbooks written by highly esteemed authors such as Clark [14] and Sutton [15]. An extensive overview of accidents with hydrogen peroxide is given in Davis et al. [11].

1.3.1 Detonability

As far as the detonability is concerned a distinction has to be made between liquid and gas detonations/deflagration. For liquid detonations Davis et al. [11] distinguish three types of tests: impact sensitivity, shock sensitivity and thermal sensitivity. They found that hydrogen peroxide in the liquid phase is not impact sensitive and normally not shock sensitive. Only at very high concentrations, typically 95% or more, and when highly confined and with a strong initiator explosions can occur. A similar conclusion was drawn by Ventura et al. [13]. Peroxide is, however, thermodynamically unstable, meaning that excessively heating results in decomposition of the peroxide leading to further heating of the liquid. Especially at higher concentrations this can lead to runaway reactions. But even in this case, explosions do not occur in the liquid phase.
However, explosions can occur in the vapour phase. A comprehensive study was performed by Satterfield et al. [16, 17]. They concluded that at atmospheric pressure hydrogen peroxide vapour can

explode if the concentration of the vapour is higher than 26 mol%. Explosions were initiated either by a hot wire or a spark gap. Explosions could even occur when a suitable catalyst at room temperature was available. For lower pressures it was determined that the limiting vapour concentration increases while at higher pressure a decrease in ignition limit was observed. The results are summarised in figures 1.2 and 1.3. Note that because of the low quality of the graphs in the original paper it was sometimes hard to determine which symbol was used. The current figures show the best guess.

For higher than atmospheric pressures the ignition limit showed initially a decrease but remained

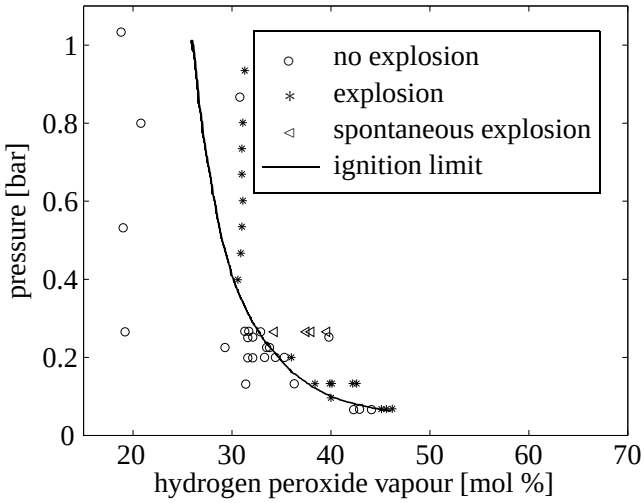

Figure 1.2: *Ignition limit for hot wire initiation [16]*

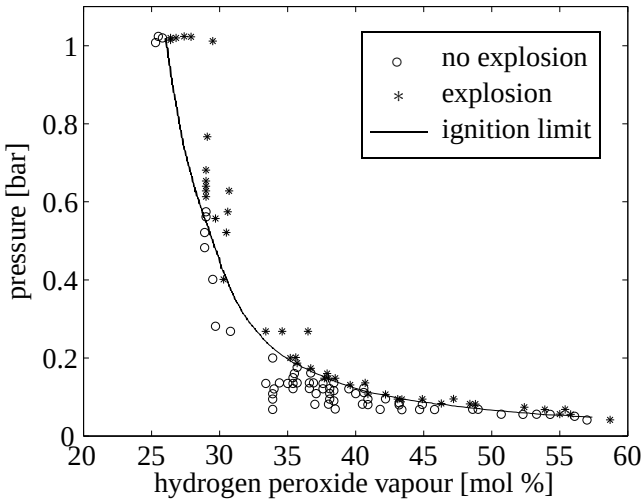

Figure 1.3: *Ignition limit for spark gap initiation [16]*

constant between 2 and 6 atmospheres as is shown in figure 1.4. Also shown in this figure is the ignition limit for pressures lower than atmospheric. The authors note that there is a small offset between the results for higher and lower than atmospheric pressures. However, there is a gap of 8 years in

between the two publications and the authors point out that the criterion for whether an explosion has occurred is slightly different.

The units of pressure in the original papers, mmHg for figures 1.2 and 1.3 and psia for figure 1.4, have been converted to bars. Conversions have been performed with the conversion factors as mentioned in appendix A.

From the work of Satterfield et al. [16] it can be inferred that if in liquid-gas equilibrium situations the

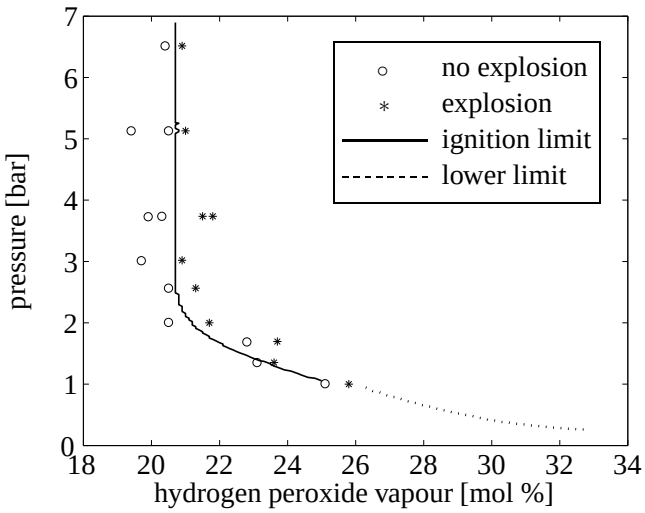

Figure 1.4: *Ignition limit for higher than ambient pressure [17]*

peroxide vapour concentration is higher than 26 mol% an explosion could occur. For certain concentrations at certain temperatures an explosive mixture is indeed present. This is graphically shown in figure 1.5 for atmospheric pressure conditions where the boiling temperature as a function of peroxide concentration is shown. Also shown is the line indicating at which temperature and concentration the equilibrium vapour concentration of hydrogen peroxide is exactly 26 mol%. The area above this line and below the boiling line is the explosive region; this is the shaded part in the graph. Note that to construct the lines, equations for vapour pressure and activity coefficients of both peroxide and water were used as reported by Manatt and Manatt [18]. A more detailed discussion on the construction of these plots is given in section 3.2. Note that figure 1.5 is slightly different from the plot presented by Davis et al. [11]. The reason will be clarified in section 3.2. In appendix B vapour concentrations for pressures other than atmospheric for liquid-gas mixtures are shown.

From the plot it is clear that whenever hydrogen peroxide liquid-gas mixtures are present, either the temperature should be low enough to prevent the formation of any explosive gas mixtures or hydrogen peroxide vapour should be actively removed to ensure it is below explosive concentrations. In the latter case the formation of an equilibrium between the two phases is prevented. As will be shown in chapter 6, for a good working catalyst bed in operation, the vapour concentration will stay below the ignition limit.

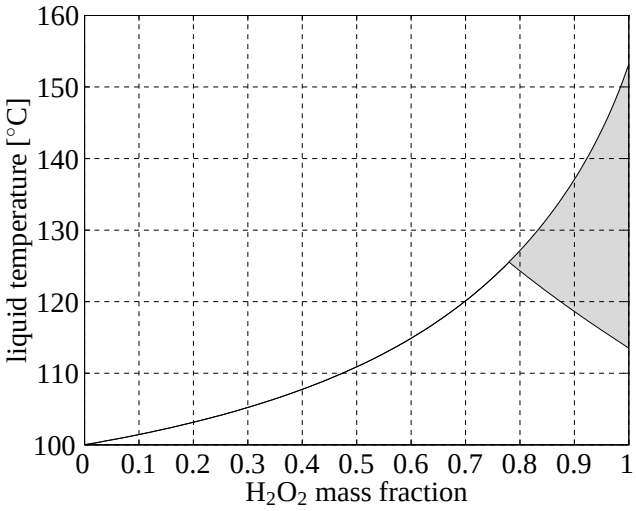

Figure 1.5: *Explosive region for equilibrium liquid-gas mixtures at atmospheric conditions*

1.3.2 Stability and storability

A strong argument against the use of hydrogen peroxide is the persistent belief that peroxide at high concentrations cannot be stored in a reasonable way because even the smallest amount of contamination would result in gradual, unstoppable decomposition of the peroxide. This would result in a decreasing hydrogen peroxide concentration over time rendering it to be unsuitable for long space missions.

Musker et al. [12] state that with the right choice and amounts of stabiliser the rate of decomposition can be drastically reduced, something that was already known since the early days of space flight. They also argue that in the case of a decrease in concentration from 98% to 96% this results in a decrease of specific impulse of just 0.5%. Ventura [19] points out that in the early sixties the Syncom II, Syncom III and Early Bird spacecrafts all used hydrogen peroxide monopropellant rocket motors for orbit and attitude control. The Syncom III and Early Bird spacecraft have both operated for 5 years and with that proving that long term storage of peroxide in sealed containers was not a problem.

Ventura [19] mentions further that long term storage in vented containers is proven as well by giving two examples. In the first example is the storage of a drum of peroxide for over 17 years in the ambient conditions of Texas. The peroxide has initially a concentration of 90% which after 17 years had decreased to 84%. The second example mentions a drum of 90% hydrogen peroxide stored at 5°C for 17 years. The concentration after 17 years had even slightly increased to 90.5%.

Ventura et al. [13] presented the results of a long term storage test in which 90% hydrogen peroxide was stored in a zirconium, aluminium and tantalum beaker respectively for over 10 months at ambient conditions. Based on the results they conclude that no dangerous or unpredictable rapid decomposition takes place. They do note that there is a considerable difference in how much decomposition takes place over the 10 month period between the different beakers, with aluminium showing the most decomposition and zirconium the least. They point out that the concentration of peroxide has not been

taken into consideration. It is mentioned that there is tentative proof that the stability increases with increasing peroxide concentration. Ventura [19] reports the same point and suggests that water acts as a destabilising component in the liquid due to the formation of weak bonds between the different molecules. This would cause a slight deformation in the molecular structure of hydrogen peroxide making it more susceptible for decomposition.
The most important point in the research presented by Ventura [19], Musker et al. [12] and Ventura et al. [13] is that currently available data on storage and stability of hydrogen peroxide is dated. It is expected that current technology is developed enough to tackle most if not all of the problems concerning stability and storability.

1.3.3 Remaining concerns

Next to storability and stability the lifetime of a hydrogen peroxide based thruster is determined by the catalyst bed lifetime. Degradation of the catalyst is determined by propellant contamination, deactivation of the catalyst by stabilisers and resistence against mechanical failure due to pressure and thermal loads [13]. Ventura et al. [13] present a list with proven lifetime of 16 catalyst beds. They note that the indicated lifetime is the time that the catalyst bed has been operated and that in all cases none of the catalyst beds show end of life behaviour. All but one have been operated for more than 1,000 seconds while one catalyst bed has been operated for more than 58,000 seconds.
Another point of concern is the relatively high freezing point for hydrogen peroxide. For anhydrous peroxide it is -0.43°C and decreases to about -10.5°C for 90% hydrogen peroxide [12]. The freezing point for other concentrations is graphically shown in figure B.1 in appendix B. That means that for high concentrations of peroxide the fuel tanks have to be kept at a relatively high temperature. Initially hydrazine faced the same problem; its freezing point is with about 1.57°C even slightly higher. This led to the development of MMH and UDMH. The freezing points for these fuels together with some oxidisers are shown in table 1.6.
Musker et al. [12] pointed out that although peroxide might freeze during long space missions where

chemical	**freezing point [°C]**
hydrazine	1.57
MMH	-52
UDMH	-58
NTO	-11
MON-3	-15

Table 1.6: *Freezing point for several fuels and oxidisers [4]*

little energy from the sun is available, peroxide has very favourable super-cooling properties. They mentioned that it has been shown that 90% hydrogen peroxide can be cooled down to -40°C with-

out freezing even when agitated and independent of cooling rate and amount of oxygen dissolved in the liquid. They gave as a possible explanation the absence of foreign nucleates and thus the lack of initiators for crystallisation. If a method would be developed to further purify hydrogen peroxide, such as is developed for hydrazine [19], the super-cooling properties could be further exploited. If the spacecraft would experience a temporary drop in temperature, the super-cooling properties might prevent it from freezing. Musker et al. [12] further noted that simple and well-established techniques, such as the application of Peltier elements, could prevent the temperature from dropping too much.
One last major concern that is addressed by Musker et al. [12] is the presumed lack of hypergolicity of peroxide with other fuels. For a long time only hydrazine was known to react hypergolically with peroxide. But at the beginning of 2000 it was reported that also pyrrole and ethanolamine are hypergolic with peroxide. Moreover Purcell et al. [20], Sadov [21] and Dobbins [22] have reported several fuels that are hypergolic with hydrogen peroxide when adding certain catalysing chemicals to it. Besides that it is well-known that the decomposition products of fully decomposed hydrogen peroxide are hot enough, see appendix B, to cause auto-ignition with selected hydrocarbon fuels. In a couple of test reports written under the GRASP project, see next section, a number of possible hydrocarbon fuels are mentioned that auto-ignite after contact with the hot decomposition products [23; 24].

1.3.4 The discussion continues?

In the works of Davis et al. [11], Musker et al. [12] and Ventura et al. [13] attempts have been made to refute the criticism towards hydrogen peroxide in the space community. One of the difficulties is that the concerns towards hydrogen peroxide is not debated in an organised way, but seems to be part of a collective prejudices. As pointed out by Ventura et al. [13] hydrogen peroxide was used at the beginning of space flight at a time that little was known about the chemicals used for space flight and space flight itself. The knowledge gained in that time has proved to be invaluable for the development of other propellants such as hydrazine: mistakes that were made with hydrogen peroxide resulting in accidents prevented similar mistakes with hydrazine. This has contributed to the belief that hydrazine and its derivatives are safe while hydrogen peroxide is not.
In 2011 hydrazine was put on the Candidate List of Substances of Very High Concern (SVHC) by the European Chemicals Agency (ECHA) [25] under the REACH Regulation (Regulation, Evaluation, Authorization and Restriction of Chemicals). The aim of REACH is to streamline and improve the legislation of chemicals within the EU. Hydrazine is classified as a CMR, which is an abbreviation of Carcinogenic, Mutagenic and toxic for Reproduction, and therefore also put on the SIN List (Substitute It Now) by the Internal Chemical Secretariat [26] (ChemSec). ChemSec is a non-profit organisation founded in 2002 by a couple of environmental organisations. The list was constructed in collaboration with a number of NGO's aiming to speed up legislation on dangerous chemicals and to help industry with identifying chemicals to avoid and possible alternatives [27].

The addition of hydrazine to the SVHC candidate list has forced the space industry to reconsider their attitude towards green propellants and hydrogen peroxide in particular. It has also resulted in an increase in number of research groups investigating green propellants.

1.4 The GRASP Project

Research in Europe into green propellants is rather scattered, preventing a systematic approach to the development of alternative propellants and propulsion systems. For this reason the GRASP project was initiated which was running from December 2008 until November 2011. GRASP stands for GReen Advanced Space Propulsion [28] and it was aiming at providing the European (space) industry with possible alternatives for hydrazine-like propellants. The project team was a consortium of 11 entities, including universities, companies and other research institutions spread over 7 countries. The University of Southampton was one of the partners in the project. Each partner had a specific expertise, making it possible to consider the whole propulsion system rather than a small subsystem of it. The research is driven by [29]:

- Reduction of cost.
- Reduction in exposure to carcinogens.
- Performance improvement.
- Ensuring the competitiveness of the European industry in a challenging and continuously changing environment.

The goal was to downselect a number of promising propellants for which the propulsion system would be further developed. The development was expressed in terms of TRL's (Technology Readiness Levels) [8; 30]. Not all propellants and corresponding propulsion systems had the same TRL. The goal of the GRASP project was to increase the TRL of each candidate propellant by at least two levels [29] and demonstrate the capabilities in an appropriate demonstrator system. This could be done by showing certain characteristics, such as hypergolicity and material compatibility, for propellants that were at the lowest TRL, or by testing propulsion systems for bipropellant applications, for propellants at a higher TRL. Such demonstrator systems should show that the propellant has:

- Similar or better performance than those propellants currently used.
- System advantages.
- Favourable storage and handling properties.

- Compatibility with existing hardware.
- The potential to reduce operating costs in the long-term.

The research focussed on three major fields:

- propellants
- catalysis
- propulsion systems

The desired outcome would be that the most promising propellants would be recognised as such by industry and/or space organisations. Ideally, this would increase the interest to further develop the technology to a level that it is a reliable and an attractive alternative for hydrazine-based propulsion systems.

1.5 Research Objectives

The University of Southampton will investigate the use of hydrogen peroxide for liquid propulsion systems as part of the GRASP project. Important aspects of the research include the selection and manufacturing of a suitable catalyst material, numerical modelling of the processes taking place in the catalyst bed and the design of the catalyst bed as part a propulsion system. Research student Matthew Palmer will focus on the selection and manufacturing of a suitable catalyst material and will be heavily involved in the design of the catalyst bed and propulsion system. The research undertaken by the author of this thesis will focus on the modelling of the flow of hydrogen peroxide from the tank through the catalyst bed down to the nozzle exit and support the design of the propulsion system by means of simulations. Special attention will be paid to the flow through the catalyst bed.
The goal of this research is to understand the basic mechanism of the processes taking place in the catalyst bed and use this to optimise the catalyst bed design. The main objectives are as follows:

1 To understand how the physical and chemical properties of catalyst pellets influence the bed performance and, based on this, predict the performance of a catalyst bed for a given configuration.

2 To investigate how the fluids and fluid properties vary along the catalyst bed for given input conditions.

3 To reliably predict steady state performance parameters such as temperature and pressure drop over the catalyst bed and vanishing point of the liquid.

For this purpose, a number of numerical tools will be developed that will each focus on one or more particular aspects of the flow in the catalyst bed. In contrast with what has been done in the past in this field, the flow models developed in this thesis will consider each flow separately. Although the concept of separately describing each phase is not new, it is rarely applied to chemically reacting multicomponent flows through packed beds at high mass fluxes, mainly due to the complexity of the system. It requires a description of all possible decomposition mechanisms and a comprehensive description of the interfacial area, something that has not been done before for this type of thrusters. For this reason special attention has to be paid during the development of these models. They are either based on existing in-house codes or developed from scratch.

1.6 Wider Applications

Although this thesis will focus on the the decomposing flow of hydrogen peroxide in a pellet based catalyst bed, the tools developed in this thesis could also be applied to a decomposing flow of hydrazine through a catalyst bed. Besides that, the tools are equally applicable to a number of other fields such as

- biological systems
- environmental systems
- process industry
- nuclear industry

An example of use in biological systems is the modelling tissue growth by means of a multiphase porous flow model [31]. The authors also mention the application of these types of models for modelling cartilage mechanics, cell motion and tumour growth.
Multiphase flows in porous media have also been applied to model the flow of groundwater contaminated with non-soluble or partially soluble substances [32]. The purpose of these models is to study possible scenarios of how groundwater is contaminated and how the contamination is spreading over time. Another example of the application of multiphase flows in porous media in environmental systems is the dense non-aqueous phase liquid (DNAPL) pool dissolution for the storage of carbon dioxide[‖] in geological formations [33].
Duduković et al. [34] presented an overview of multiphase catalytic reactors used for chemical engineering in the process industry and gave numerous examples of applications in which fixed catalytic beds are used such as hydrogenation and oxidation of various compounds. Multiphase flow models become more and more important in this industry given the extensive review on these models by

[‖] CO_2

Duduković et al. [34] and Kuipers and Van Swaaij [35]. A clear example of the use of computational tools in the chemical reactor engineering industry is a recent study by Kuzeljevic and Dudukovic [36]. They performed simulations of a multiphase trickle bed reactor with a commercial CFD** package.
In the nuclear industry multiphase flow models are used as design tool and for safety analysis of nuclear reactors [37]. For example, the heat generated by decay of radioactive material is transferred to surrounding water. The result is that the radioactive material is cooled down and that steam is generated which is further used to generate electricity. However, at boiling the heat transfer to the water becomes less effective due to the formation of gas bubbles [38]. The amount and size of the bubbles determines how effective the cooling is and thus needs to be known during the design of the reactor.
Therefore, apart from people interested in the development and use of hydrogen peroxide based rocket motors, this thesis is potentially also relevant to researchers and designers in the fields mentioned above.

1.7 Thesis Structure

This thesis comprises seven main chapters and can be divided into two parts. The first part comprises Chapters 2 to 4 and deal with the mathematical description of the processes in the catalyst bed and the corresponding discretisation. The second part is formed by Chapters 5 and 6 and discuss the validation of and results obtained with the models developed in the first part. This first chapter explained the motivation of this research by providing the historical background and discussing the origin of the current demand of alternatives for rocket propellants.
Chapter 2 discusses qualitatively the processes taking place in the catalyst bed and the implications this has on modelling of the flow. This is used as a starting point for the development of the model. The two-fluid equations will be introduced as well as a model to describe the presence of catalyst pellets in the catalyst bed. The models will be presented in their most generic form.
Chapter 3 provides a detailed discussion on the source terms that have been introduced in chapter 2. These include mass and heat transfer by evaporation and decomposition and the momentum transfer between the fluids and the fluid and the catalyst pellets. For each mechanism an overview is given of different approaches in the literature and followed by the selection and further detailed discussion of the model employed in this thesis.
Chapter 4 describes the translation of the model into a computer code. As the two-fluid model presented in chapter 2 is too generic and complicated, first a number of simplifications and corresponding justification will be discussed. This is followed by the presentation of the discretisation method with special attention to those aspects that are particular for two-fluid models.
Chapter 5 presents the validation and results of a simple flow model whereby the catalyst bed is modelled as a single control volume. Focus will be on the influence of the shape and size of the catalyst

**Computational Fluid Dynamics

pellets on the pressure drop over the bed.

Chapter 6 presents the validation and results of a one-dimensional unsteady model. Particular attention will be paid to what can be learned from two-fluid models that is not possible with mixture models. Furthermore a number of parametric studies will be presented. A few words will also be spend on higher dimensional models and the use of (commercial) CFD packages.

Finally, in chapter 7 a summary will be given of the whole research presented in the previous chapters, followed by recommendations for further research.

Chapter 2

Mathematical Problem Description

This chapter introduces the two-fluid equations in the most general form. However, for the system under consideration only a limited number of two-phase flow types will be encountered. To get a better idea of what can be expected inside the catalyst bed, the first section starts with a detailed description of how a hydrogen peroxide catalyst works. This is followed by a general discussion of the different aspects of multiphase flow modelling. Also a short overview is given of how several researchers have approached the modelling of the catalyst bed in the past. Section 2.2 will then present the general two-fluid flow conservation equations. As the catalyst bed is filled with catalyst pellets a description is required of the volume these catalyst pellets take up. This is provided in the last section. A detailed description of the source terms appearing in these equations will be given in the next chapter.
In this and subsequent chapters a number of non-dimensional numbers will be used. As a reminder, appendix F gives an overview how they are defined.

2.1 Problem Description

2.1.1 Hydrogen peroxide thruster operation

A hydrogen peroxide based rocket motor uses a catalyst to decompose the hydrogen peroxide into oxygen and steam. The overall reaction equation is written as

$$H_2O_2 \longrightarrow H_2O + \frac{1}{2}O_2 \tag{2.1}$$

Normally, the propellant consists of a mixture of water and hydrogen peroxide. The amount of peroxide in the propellant is usually indicated as the mass percentage of hydrogen peroxide. In this thesis the strength will be indicated by means of the mass fraction of peroxide which is equal to the mass

percentage divided by 100. Typical mass fractions for rocket grade peroxide range from 0.7 to 1.0. It should be noted that in reality impurities are present that can significantly influence the performance in terms of stability and catalyst poisoning, see also section 1.3 in the previous chapter. However, the impurities do not take part in the decomposition reaction itself.

The reaction given in equation 2.1 is exothermic. The resulting temperature is dependent on the strength of peroxide used. In figure A.6 in appendix A the adiabatic decomposition temperature is plotted as a function of the mass fraction of peroxide for several initial temperatures. It shows that the relationship is approximately linear and that, for an increase in mass fraction of 0.01, the adiabatic decomposition temperature increases by roughly 22 to 24 degrees. The reason for the sensitivity is the high specific heat of water, see appendix B. For rocket applications the hot decomposition products are either exhausted through a nozzle, in which case the motor is a 'cool', monopropellant gas thruster, or they are injected and mixed in a combustor with a fuel. In this case the oxygen acts as the oxidiser for combustion in a bipropellant system. As the oxygen is relatively hot the fuel oxidiser mixture could spontaneously ignite provided that the fuel has a sufficient low auto-ignition temperature.

From a performance point of view a high temperature is favourable as, for a given flow rate of propellant(s), this results in a higher thrust. This means that the higher the mass fraction of peroxide the better the performance. On top of that, figure A.4 shows that the higher the mass fraction of peroxide the higher the mass fraction of oxygen in the decomposition products. If a certain amount of oxygen is needed, then for stronger peroxide solutions less propellant is required. In this thesis 87.5%wt hydrogen peroxide will be used as this is the highest concentration that is commercially available in Europe.

Decomposition can be achieved by homogeneous or heterogeneous catalysis or a mix between the two. In the homogeneous case the catalyst is in the same phase as the propellant, i.e. liquid. Such systems have been investigated by amongst others Musker et al. [39]; Musker and Roberts [40]; Musker et al. [41]. Two main disadvantages of homogeneous decomposition is that for a monopropellant thruster a bi-propellant motor layout is required and that the catalyst together with the decomposition products is exhausted through the nozzle without contributing to the specific impulse. In the heterogeneous case the catalyst is in the solid state contained in a shell through which hydrogen peroxide is flowing. Typical forms in which the catalyst appears are (silver) screens [42; 43], pellets [44–46], foams [47] and monoliths [48; 49]. Throughout this research the focus will be on pellet based catalyst beds, although with some minor modifications the models can also be applied to the other types of heterogenous decomposition.

Decomposition starts as soon as the hydrogen peroxide comes into contact with the catalyst. In normal cases the initial temperature is well below the boiling point. In this case the formed water is in the liquid phase. The oxygen is in the gas phase and occur as bubbles in the liquid. The generated heat causes a rise in temperature until the boiling point of the liquid mixture is reached. The increase in temperature also leads to an increase in the reaction rate leading to more gas bubbles in the liquid. Some bubbles will coalesce with other bubbles forming larger bubbles or slugs. Together with the

liquid water part of peroxide evaporates before it can decompose in the liquid phase leading to even more gas. At this point rather than speaking about a liquid phase with gas bubbles dispersed in it, it makes more sense to speak about a gas phase with liquid droplets dispersed in it. Eventually, all of the liquid has vanished either by decomposition or evaporation. Gaseous peroxide will decompose as resulting in a further increase in gas temperature. What remains is a gas mixture of steam and oxygen.

2.1.2 Multiphase flow description aspects

Ishii and Hibiki [50] distinguish three classes of two-phase flows: separated flows, mixed or transitional flows and dispersed flows. The classification is based on the geometry of the interfaces between the fluid phases. Table 2.1 shows the classifications and their subdivision. Based on the description given above, in the catalyst bed the following regimes starting from the injector will be present: single phase liquid flow, bubbly flow, slug flow, droplet flow and single phase gas flow. It should be kept in mind that in reality the geometry of the fluid interface will be distorted due to the presence of catalyst pellets and that next to an interface between gas and liquid phase there also exists an interface between the pellets and the liquid phase and between the pellets and the gas phase. From a model point of view during the development of the equations, no assumptions should be made on the particular type of flow, i.e. both phases should be treated symmetrically.

To model two-phase flows two different approaches are possible. In the first approach the two-phase system is considered as a single fluid whose properties are an average of the properties of each phase. These models are so-called mixture models. They solve mixture conservation equation for mass, momentum and energy, and one additional continuity equation for one of the phases to keep track of changes in concentration of the phases [50]. Mixture models assume mechanical and thermal equilibrium between the phases and can be used when the phases are strongly coupled. An example of a mixture model is the drift-flux model which includes a slip flow model to describe the velocity differences between the two phases. It comes down to solving conservation equations for a single phase flow with an added transport equation to describe the change in relative occupancy of each phase and a special constitutive relation to describe the difference in velocity between the two phases. After having solved the model it is possible to obtain information about the individual phases by correlating the calculated properties with equilibrium data of properties as function of mixture composition [51].

The other approach is to solve the conservation equations for each phase separately. Each conservation equation includes source terms that describe the interaction between the phases. In cases where only two fluids are considered such models are called two-fluid models. These types of models can handle non-equilibrium between the phases as well as dynamic interactions and are therefore particularly suited for investigating transient behaviour and changes in the flow regime. A disadvantage is that for each phase a set of conservation equations has to be solved which leads to higher computational costs compared to mixture models. An additional complication is that a complete mathematical description

Class	Typical regimes	Geometry	Configuration	Examples
Separated flows	Film flow	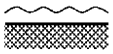	Liquid film in gas; Gas film in liquid	Film condensation Film boiling
	Annular flow	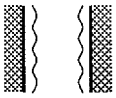	Liquid core and gas film; Gas core and liquid film	Film boiling Boilers
	Jet flow	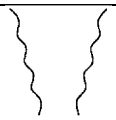	Liquid jet in gas; Gas jet in liquid	Atomization Jet condenser
Mixed or Transitional flows	Cap, Slug or Churn turbulent flow	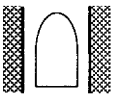	Gas pocket in liquid	Sodium boiling in forced convection
	Bubbly annular flow	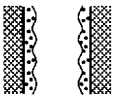	Gas bubbles in liquid film with gas core	Evaporators with wall nucleation
	Droplet annular flow	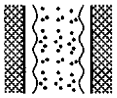	Gas core with droplets and liquid film	Steam generator
	Bubbly droplet annular flow	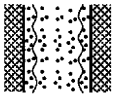	Gas core with droplets and liquid film with gas bubbles	Boiling nuclear reactor channel
Dispersed flows	Bubbly flow	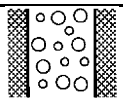	Gas bubbles in liquid	Chemical reactors
	Droplet flow	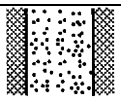	Liquid droplets in gas	Spray cooling
	Particulate flow	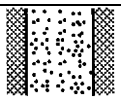	Solid particles in gas or liquid	Transportation of powder

Table 2.1: *Classification of two-phase flows according Ishii and Hibiki [50]*

of the interaction between the phases is not yet available [50].

As can be deduced from section 2.1.1 the liquid and the gas phase inside the catalyst bed will in general not be in equilibrium. Firstly, there is a significant temperature difference between both phases for high mass fractions of peroxide. For 87.5%wt hydrogen peroxide the expected gas temperature is just below 700°C while the liquid temperature is typically a couple of hundred degrees lower, depending on the pressure in the catalyst bed. Secondly, the difference in density is 2 to 3 orders of magnitude. Combined with the large temperature difference it may be assumed that there is no mechanical equilibrium either. For this reason to effectively model the processes inside the catalyst bed a two-fluid

model has to be employed.

A two-fluid model can be formulated in multiple ways. Ishii and Hibiki [50] distinguish three types: Lagrangian description, Boltzmann description and Eulerian description. A Lagrangian description is particularly suited to describe the behaviour of a single particle or a number of particles. It defines the path of each particle through a medium, for instance the path of a bubble or a group of droplets through a liquid or a gas. The medium through which the particles travel is often called the primary or continuous phase and the particles the dispersed phase. When the volume fraction of the droplets/bubbles is close to unity it can no longer be assumed to be a dispersed phase. Neither can a phase with a volume fraction close to zero be considered as a continuous phase. Consequently, for the system described in the previous section a Lagrangian description is not suited.

A different approach is the Boltzmann description in which instead of describing single particles, a group of particles is considered. In this way the behaviour of many particles clustered together can be modelled, which collectively can have dynamical features that are absent when individual particles are considered [50]. The group of particles is described by means of a particle density function known as the Boltzmann transport equation. The interaction between the particles has to be accounted for by a collision model. The continuity, momentum and energy equation can be derived from the lattice Boltzmann equation [52]. However, as the main interest is in averaged quantities and not in the behaviour of individual particles the Bolzmann description is not suited.

The third type is an Eulerian description. For each fluid mass and momentum equation are solved, and dependent on the application, an energy equation and other scalar equations. For this purpose a control volume is defined through which the fluids travel. The amount of each phase inside this control volume is indicated by the fraction of that volume it occupies, also known as the volume fraction. The interaction between the phases is dealt with by means of source and sink terms in the conservation equations. However, to solve these equations the smallest time and length scales need to be resolved and this is numerically so expensive, that this is limited to small domains and low Reynolds numbers only [53]. For this reason the flow is averaged over space and time in such a way that the macroscopic behaviour is preserved and the small scale fluctuations are filtered out. Rigorous derivations of the averaged multifluid conservation equations are provided by for instance Drew [54] and Ishii and Hibiki [50]. The influence of the small scale fluctuations is accounted for by establishing proper constitutive relations, see for instance Drew and Lahey [55]. At the same time constitutive relations account of the discontinuity in properties over a phase boundary [56].

A particular difficulty with averaging is to determine the size of the control volume and the amount of time over which is averaged. If the length and time scales over which is averaged are too small, the solution contains phenomena that are not representative for the average flow properties. On the other hand, if the length and time scales over which is averaged are too large, any change in average flow properties is averaged out [54]. For the system described above, the problem of separation of scales [57] is especially relevant close to the injector, where there is only a tiny amount of gas present, and the part of the catalyst bed where the liquid disappears. Despite these problems the Eulerian

description is still more suited to describe the flow in the catalyst bed than the Lagrangian and Boltzmann description. For this reason the Eulerian formulation is the approach adopted in this research work.

To complete the mathematical description of the system, two additional aspects have to be taken into consideration. Firstly, both the liquid and the gas phase consist of more than one component. This requires the solution of an additional set of species equations to describe the (change in) species concentration. Secondly, the catalyst bed is filled with pellets, which forms a restriction of the fluid flow. For this the same problem of separation of scales is relevant: the control volume should be chosen to be large enough that the pellets can be considered to be homogeneously distributed over the control volume [58; 59]. This means that the geometry of the pellets will not be resolved, but be accounted for by means of a solid volume fraction reducing the volume and cross-sectional area available to fluid flow. This will be further discussed at the end of this chapter.

2.1.3 Previous modelling efforts

Despite the renewed interest in hydrogen peroxide the number of flow models available in the literature describing the processes in the decomposition chamber for porous solid catalysts is limited, probably due to the severe complexity of the system. A simple model was presented by Johnson et al. [60], where the decomposition chamber was modelled by two control volumes: the control volume adjacent to the injector containing all the liquid and a control volume downstream containing the gas portion. The purpose was to investigate pressure oscillations experienced during testing. Liquid to gas mass transfer was assumed to have taken place after the liquid was in the decomposition chamber for a fixed amount of time. No distinction was made between decomposition and evaporation.

A one-dimensional model was developed by Zhou and Hitt [61]. In this model the gas and liquid phase were modelled as a mixture. Contrary to Johnson et al. [60] they considered decomposition and evaporation separately which were driven by the mixture temperature instead of a fixed residence time of the liquid. They only considered catalytic decomposition, which was modelled with Arrhenius kinetics. For the evaporation of the liquid they used a staged approach in which water and peroxide evaporated at their respective normal boiling points. Their results showed that this unphysical assumption only affected a very small fraction of the catalyst bed at the inlet. Validation against experimental data was not given. Their model focussed on a micropropulsion system with a catalyst bed length in the order of hundreds of micrometers. The catalyst bed itself had the form of a monolith. They performed parametric studies in which they varied the Arrhenius parameters and heat loss to the environment to investigate the influence on the required bed length to ensure complete decomposition.

Bonifacio and Russo Sorge [62] investigated the transient behaviour of a monolithic catalyst bed and the thermal response of the walls in particular. For this purpose they developed a lumped-parameter model in which catalytic decomposition took place at the wall. Heat loss to the environment was not

taken into account. To simplify the analysis they only modelled the gas phase and ignored the liquid phase. They found out that during the transient startup the wall could reach higher temperatures than the adiabatic decomposition temperature before a steady state temperature was reached equal to the adiabatic decomposition temperature. This effect was dependent on the relative importance of mass and heat transfer by diffusion.

The heat transfer between reacting hydrogen peroxide and monolithic catalyst bed walls was also studied by Krejci et al. [49]. They also took into account the heat transfer between the monolith and the outer casing of the catalyst bed and the heat transfer to the ambient surrounding. Their one-dimensional mixture model took only catalytic decomposition into consideration. For evaporation they assumed a staged approach in which water and peroxide evaporated at their respective normal boiling points, similar to the approach taken by Zhou and Hitt [61]. They found out that due to heat transfer a radial temperature profile exists in the catalyst bed leading to lower decomposition efficiencies close to the wall.

In a model developed by Corpening et al. [63] special attention was paid to thermal decomposition in the gas phase and evaporation of highly concentrated peroxide droplets. Droplets were assumed to be surrounded by a hot gas with a temperature of $950K$ and higher. The evaporation of these droplets was modelled with the D^2 law under the assumption that the vapour coming from the droplet surface had the same composition as the liquid. They argued that this assumption was allowed as the droplets were small, the surrounding gas temperature high and therefore the evaporation process was very fast.

Pasini et al. [64] developed a one-dimensional mixture model for a pellet based catalyst bed. Contrary to the work by previous researchers they split the decomposition process into adsorption onto and desorption from the catalyst pellets. They also took into account the difference in peroxide concentration between the bulk flow and the fluid near the pellet surface by means of the Reynolds analogy. Similar to Corpening et al. [63] they assumed for evaporation that the vapour coming from the droplet surface had the same composition as the liquid. They also explicitly modelled the viscous interaction between the fluid and the catalyst pellets by means of the Ergun equation.

Two-dimensional models were mentioned by Zhou and Hitt [65] and Bonifacio and Russo Sorge [62]. Zhou and Hitt compared their earlier developed one-dimensional model [61] with a two-dimensional CFD model. They reported a large difference in required bed length to ensure complete decomposition between their one-dimensional model and the CFD model. Bonifacio and Russo Sorge compared the results from their lumped-parameter model with a two-dimensional CFD simulation performed in Fluent. They found a good agreement between the two models. They also mentioned that they had problems in reaching convergence with the CFD model. Unfortunately, in both cases no further details were provided about the CFD model.

The difficulties involved in dealing with multiphase flows in the above discussed works have been dealt with by either focussing on the gas phase and ignoring the liquid phase or by modelling the phases as a fluid mixture. Those researchers that have taken into account the phase change from liquid to gas, simplified the problem by either assuming that the vapour components coming from the

liquid has the same composition as the liquid phase or by evaporating each liquid component separately at their respective normal boiling point.
Employing simple mixture models, where *simple* refers to the fact that no closure models are employed for the slip velocity and slip temperature, to describe the processes inside the catalyst bed implicitly assumes equilibrium between the phases [50]. However, there is reason to believe that such equilibrium does not exist. For example, the adiabatic decomposition temperature of 0.80 hydrogen peroxide initially at room temperature is about 780K, while the critical temperature for peroxide and water is 739.5K and 647.3K respectively [18]. Besides that, the mixture model approach results in a quantitative loss of physics, for instance in the way boiling is modelled and how the pressure drop over the catalyst bed is determined. On top of that, because the mixture is an average between two (very different) phases, the results are an average over the fluid phases as well which gives a reduced accuracy. For this reason a two-fluid model has been developed, which will be further discussed in the next section.

2.2 Multicomponent Two-Fluid Model Equations

The equations presented in this section are the most general ones and are presented as volume averaged instantaneous equations. A detailed derivation of these equations was provided by Ishii and Hibiki [50]. The following convention will be used: subscripts α and A refers to phase α and species component A, respectively, where α can refer to the gas, liquid of solid phase indicated by g, l, and s respectively. Subscript i refers to an interface quantity and subscript m to the mixture quantity and vector quantities are written in bold.
The continuity equation for phase α, indicated with the subscript, is given by

$$\frac{\partial \varepsilon_\alpha \rho_\alpha}{\partial t} + \nabla \cdot (\varepsilon_\alpha \rho_\alpha \mathbf{u}_\alpha) = \Gamma_\alpha, \tag{2.2}$$

where ρ is the density and $\mathbf{u}$ the velocity vector. Γ_α is the mass source term describing the mass transfer between the phases. As there is overall mass conservation, the following interfacial mass transfer condition holds:

$$\sum_\alpha \Gamma_\alpha = 0. \tag{2.3}$$

This implicitly assumes that the interface has no mass capacity. For the fluid volume fractions the following constraint equation holds

$$\varepsilon_g + \varepsilon_l = 1. \tag{2.4}$$

Momentum conservation equation is given by

$$\frac{\partial \varepsilon_\alpha \rho_\alpha \mathbf{u}_\alpha}{\partial t} + \nabla \cdot (\varepsilon_\alpha \rho_\alpha \mathbf{u}_\alpha \mathbf{u}_\alpha) = -\nabla (\varepsilon_\alpha p_\alpha) + \nabla \cdot (\varepsilon_\alpha \boldsymbol{\tau}_\alpha) + \varepsilon_\alpha \rho_\alpha \mathbf{g} + \mathbf{M}_\alpha, \tag{2.5}$$

where p is the pressure, $\mathbf{g}$ the gravitational acceleration and τ the viscous tress tensor. $\mathbf{M}_\alpha$ is the momentum source due to interfacial interaction and can be written as

$$\mathbf{M}_\alpha = \mathbf{u}_{i,\alpha}\Gamma_\alpha + p_{i,\alpha}\nabla\varepsilon_\alpha - \nabla\varepsilon_\alpha \cdot \tau_{i,\alpha} + \mathbf{M}_{i,\alpha}. \tag{2.6}$$

The first term on the righthand side is the momentum of the mass transferred across the interface. The second and third term describe the change in momentum flux due to a change in volume fraction. $\mathbf{M}_{i,\alpha}$ account for any other sources of momentum exchange between the phases, such as frictional forces between the fluids and the packed bed. It is assumed that there are no molecular diffusion fluxes from the interface and no other body forces. The sum of the momentum sources due to interfacial interaction is given by

$$\sum_\alpha \mathbf{M}_\alpha = \mathbf{M}_m. \tag{2.7}$$

$\mathbf{M}_m$ is the mixture momentum source arising from the surface tension effect. This effect consist of two component as is shown in equation 2.8: the first term on the righthand side describes the influence of the mean curvature H_{21} and the mean surface tension σ and the second term takes into account the change in the mean curvature. ε_2 stands for the volume fraction of the other phase.

$$\mathbf{M}_m = 2H_{21}\,\sigma\nabla\varepsilon_2 + \mathbf{M}_m^H. \tag{2.8}$$

Substituting equation 2.6 into equation 2.5 gives after rewriting

$$\begin{aligned}\frac{\partial\varepsilon_\alpha\rho_\alpha\mathbf{u}_\alpha}{\partial t} + \nabla\cdot(\varepsilon_\alpha\rho_\alpha\mathbf{u}_\alpha\mathbf{u}_\alpha) = {} & -\varepsilon_\alpha\nabla p_\alpha + \varepsilon_\alpha\nabla\cdot\tau_\alpha + \varepsilon_\alpha\rho_\alpha\mathbf{g}_\alpha + \mathbf{u}_{i,\alpha}\Gamma_\alpha \\ & + \nabla\varepsilon_\alpha(p_{i,\alpha} - p_\alpha) + \nabla\varepsilon_\alpha(\tau_\alpha - \tau_{i,\alpha}) + \mathbf{M}_{i,\alpha}\end{aligned} \tag{2.9}$$

Conservation of static enthalpy is given by

$$\begin{aligned}\frac{\partial\varepsilon_\alpha\rho_\alpha h_\alpha}{\partial t} + \nabla\cdot(\varepsilon_\alpha\rho_\alpha h_\alpha\mathbf{u}_\alpha) = {} & -\nabla\cdot(\varepsilon_\alpha k_\alpha\nabla T_\alpha) + \frac{D_\alpha}{Dt}(\varepsilon_\alpha p_\alpha) \\ & + \varepsilon_\alpha\tau_\alpha : \nabla\mathbf{u} + Q_\alpha,\end{aligned} \tag{2.10}$$

where T is the temperature and k the thermal conductivity. Q_α is the energy source term due to interfacial interaction and can be written as

$$Q_\alpha = \Gamma_\alpha h_{i,\alpha} - p_{i,\alpha}\frac{D_\alpha\varepsilon_\alpha}{Dt} - \nabla\varepsilon_\alpha\cdot\tau_{i,\alpha}\cdot(\mathbf{u}_{i,\alpha} - \mathbf{u}_\alpha) + \mathbf{M}_{i,\alpha}\cdot(\mathbf{u}_{i,\alpha} - \mathbf{u}_\alpha) + Q_{i,\alpha}. \tag{2.11}$$

The first term on the righthand side describes the enthalpy of the mass transferred across the interface. The second and third term describe, respectively, the work done by the interfacial pressure and the work done by interfacial shear stresses. The work done by other interfacial forces is accounted for by the fourth term and the last term includes all energy sources not accounted for in the other terms such

as due to chemical reactions. The sum of the interfacial energy source terms is given by

$$\sum_{\alpha} Q_{\alpha} = Q_m, \tag{2.12}$$

where Q_m is the mixture energy source term and is analogous to the mixture momentum source $\mathbf{M}_m$ in equation 2.7. It is defined as

$$Q_m = T_i \frac{D_i}{Dt}(a_i) + 2H_{21}\sigma\frac{\partial \varepsilon_1}{\partial t} + E_m^H. \tag{2.13}$$

The first term describes the change in surface energy due to changes in interfacial area. The last two terms define, respectively, the work done by surface tension forces and the effect of changes in the mean curvature.
Substituting equation 2.11 into equation 2.10 results after rewriting in

$$\begin{aligned}\frac{\partial \varepsilon_\alpha \rho_\alpha h_\alpha}{\partial t} + \nabla\cdot(\varepsilon_\alpha \rho_\alpha h_\alpha \mathbf{u}_\alpha) = &-\nabla\cdot(\varepsilon_\alpha k_\alpha \nabla T_\alpha) + \varepsilon_\alpha \frac{D_\alpha}{Dt}(p_\alpha) + \varepsilon_\alpha \boldsymbol{\tau}_\alpha : \nabla \mathbf{u} \\ &+ \Gamma_\alpha h_{i,\alpha} + (p_\alpha - p_{i,\alpha})\frac{D_\alpha \varepsilon_\alpha}{Dt} + Q_{i,\alpha} \\ &+ \mathbf{M}_{i,\alpha}\cdot(\mathbf{u}_{i,\alpha} - \mathbf{u}_\alpha) - \nabla\varepsilon_\alpha \cdot \boldsymbol{\tau}_{i,\alpha}\cdot(\mathbf{u}_{i,\alpha} - \mathbf{u}_\alpha).\end{aligned} \tag{2.14}$$

As both phases consist of multiple components a set of species transport equations have to be solved as well. They are given by

$$\frac{\partial \varepsilon_\alpha \rho_\alpha Y_{A\alpha}}{\partial t} + \nabla\cdot(\varepsilon_\alpha \rho_\alpha \mathbf{u}_\alpha Y_{A\alpha}) = \nabla\cdot(\varepsilon_\alpha j_A) + S_{A\alpha}. \tag{2.15}$$

Here, $Y_{A\alpha}$ is the mass fraction of component A in phase α, j_A the mass flux of component A and S_A the mass source term of component A. Note that the first term on the righthand side describes diffusion of mass. For the binary liquid this can be modelled as Fickian diffusion, however for the multicomponent gas phase the diffusive flux has to be modelled with the generalised Maxwell-Stefan equations [66].

2.3 Catalyst Bed Packing

The presence of the pellets in the catalyst bed manifests itself via the momentum source term $\mathbf{M}_{i,\alpha}$ in equation 2.6, which will be further discussed in section 3.3 in the next chapter, and via the reduced amount of volume available for fluid flow. The relative occupancy of the fluid per unit of catalyst bed volume is called void fraction and is subject to the following constraint

$$\varepsilon_f + \varepsilon_s = 1 \tag{2.16}$$

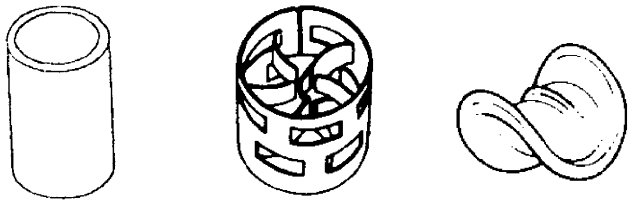

(a) *Raschig ring* ***(b)*** *Pall ring* ***(c)*** *Berl saddle*

Figure 2.1: *Examples of pellet shapes, taken from [67]*

where ε_f is the void fraction and ε_s the relative volume of the catalyst pellets. ε_f and ε_s are related to ε_g and ε_l by

$$(\varepsilon_g + \varepsilon_l)\,\varepsilon_f = 1 - \varepsilon_s \tag{2.17}$$

Note that in the current definition $\varepsilon_f \neq \varepsilon_g + \varepsilon_l$, however the total interstitial volume is equal to $V_g + V_l$. This has to do with the fact that ε_g and ε_l are the volume fractions with respect to the interstitial volume and not with respect to the total volume.

The void fraction depends amongst others on catalyst shape and dimensions and the size of the catalyst bed. Pellets come in many different shapes such as [67] spheres, cylinders, Raschig rings, pall rings and Berl saddles. The last three shapes are shown in figure 2.1.

Afandizadeh and Foumeny [67] showed that the void fraction can also vary for beds containing the pellets with the same shape and dimensions due to difference in loading strategy. Benyahia and O'Neill [68] mentioned that the bed to particle diameter ratio, D_b/D_{ps}, is an important parameter in determining the void fraction. In case of non-spherical particles the diameter of the pellet D_{ps} is defined as the diameter of a sphere with an equivalent volume of the pellet under consideration. They further mentioned that the void fraction is influenced by the vicinity of the catalyst bed wall. This influence can affect the average void fraction for bed to pellet diameter ratios up to $D_b/D_{ps} \approx 12$. The void fraction is further affected by end-of-bed effects.

Several relations exist in literature that describe the average void fraction in the bed and the local void fraction as a function of the bed radius. Martin [69] showed that packed beds can be subdivided into a core region, where the local void fraction fluctuates around a mean, and a region close to the wall where the average void fraction is higher than the average void fraction of the core. Based on this Bey and Eigenberger [70] developed relations for the bed mean void fraction and the local void fraction as a function of the bed radius for spherical and cylindrical pellets and pellets in the form of rings. Other relations for the bed mean void fraction for spherical and cylindrical pellets were presented by Foumeny and Pahlevanzadeh [71] and Benyahia and O'Neill [68]. In both cases the subdivision of the bed in two parts, as was proposed by Martin [69], was ignored and the relations were based on a least-square fit.

Because the rationale behind the relations provided by Bey and Eigenberger [70] is physically more sound, these will be used. The relations for spheres and cylinders are listed in full in appendix C.

Chapter 3

Source Terms

This chapter discusses models for the mass and momentum and heat transfer terms which were introduced in the previous chapter. All terms originate from three sources: decomposition, evaporation and momentum transfer. The first two involve heat and mass transfer and thus feature in the continuity, species and enthalpy equations. The last one describes the drag forces between the fluid phases and the fluid phase and the catalyst bed and thus forms the input for the source term in the momentum equation. Each source will be discussed separately and starts with a discussion on the, sometimes different, approaches taken in the literature and finishes with a justification of the approach taken in this thesis.

3.1 Decomposition of Hydrogen Peroxide

The use of hydrogen peroxide as fuel for rocket motors relies on the decomposition of peroxide into steam and oxygen. The overall reaction equation is written as

$$\mathrm{H_2O_2} \xrightarrow{k_1} \mathrm{H_2O} + \frac{1}{2}\mathrm{O_2}, \tag{3.1}$$

where k_1 is the global reaction rate constant. Reaction 3.1 applies to catalytic as well as thermal decomposition.
The rate with which H_2O_2 is decomposed is expressed by means of a reaction equation

$$\frac{d[\mathrm{H_2O_2}]}{dt} = k_1[\mathrm{H_2O_2}] \tag{3.2}$$

which is a first order reaction. The reaction rate constant k_1 is temperature dependent and is generally

given by the Arrhenius expression [72]

$$k_1 = A_0 e^{\frac{-E_A}{R_c T}}, \tag{3.3}$$

where R_c is the universal gas constant and T the temperature of the phase in which the decomposition is taking place. A_0 and E_A are the Arrhenius parameters. E_A is the activation energy which is the minimum required energy that is necessary for the decomposition to take place. $e^{\frac{-E_A}{R_c T}}$ can then be interpreted as the fraction of collisions for which the relative kinetic energy is larger than the activation energy E_A [73]. The total number of collisions is indicated with A_0 which is called the pre-exponential factor or frequency factor. This factor is in itself a function of temperature [72] which introduces more parameters that need to be determined experimentally. In general, this dependency is not known for highly concentrated hydrogen peroxide decomposition and, therefore, not taken into account by any of the researches summarised in section 2.1.3. Also in this thesis the temperature dependency of the pre-exponential factor will not be taken into account and instead equation 3.3 will be used. Although it gives a very crude approximation of the actual reaction in all its complexity, it is a convenient tool to describe the overall behaviour of the decomposition process.

3.1.1 Thermal decomposition

Thermal decomposition is a unimolecular reaction of which the mechanism can be explained with the Lindemann-Hinshelwood theory [73]. The reaction consists of two steps. The first one is the activation step where a molecule A collides with another molecule M and is consequently brought into an activated state. This is written as

$$\mathrm{A} + \mathrm{M} \underset{}{\overset{k_2}{\rightleftharpoons}} \mathrm{A}^* + \mathrm{M}. \tag{3.4}$$

A^* means that the molecule is in the activated state and k_2 is the reaction constant for the first step. In the second step the activated molecule is decomposed into its products P

$$\mathrm{A}^* \xrightarrow{k_3} \mathrm{P}, \tag{3.5}$$

where k_3 is the reaction constant for the second step.
The rate of production of the activated molecule A^* can be written as $d[\mathrm{A}^*]/dt = k_2[\mathrm{A}][\mathrm{M}]$. Destruction of A^* is due to the reverse reaction and due to the decomposition of the activated molecule into its products. The rate of consumption of A^* due to the reverse reaction can be written as $-d[\mathrm{A}^*]/dt = k_2[\mathrm{A}^*][\mathrm{M}]$ and the rate of consumption due to decomposition as $-d[\mathrm{A}^*]/dt = k_3[\mathrm{A}^*]$. In steady state $[\mathrm{A}^*]$ can now be written as

$$[\mathrm{A}^*] = \frac{k_2[\mathrm{A}][\mathrm{M}]}{k_2[\mathrm{M}] + k_3}. \tag{3.6}$$

The rate of change of the products can now be written as

$$\frac{d[\mathrm{P}]}{dt} = k_3[\mathrm{A}^*] = \frac{k_2 k_3[\mathrm{A}][\mathrm{M}]}{k_2[\mathrm{M}] + k_3}. \tag{3.7}$$

This can also be written as $d[\mathrm{P}]/dt = k_{uni}[\mathrm{A}]$ where k_{uni} is the unimolecular reaction constant given by

$$k_{uni} = \frac{k_2 k_3[\mathrm{M}]}{k_2[\mathrm{M}] + k_3}. \tag{3.8}$$

For situations where the pressure is sufficiently low it can be assumed that $k_3 \gg k_2$. This makes the activation step, equation 3.4, the rate determining step. The rate of formation of the product $[\mathrm{P}]$ can then be simplified to

$$\frac{d[\mathrm{P}]}{dt} = \frac{k_2 k_3[\mathrm{A}][\mathrm{M}]}{k_3} = k_2[\mathrm{A}][\mathrm{M}], \tag{3.9}$$

which is a second-order reaction. On the other hand, if the pressure is sufficiently high it can be assumed that $k_2 \gg k_3$ in which case equation 3.7 reduces to

$$\frac{d[\mathrm{P}]}{dt} = \frac{k_2 k_3[\mathrm{A}][\mathrm{M}]}{k_2[\mathrm{M}]} = k_3[\mathrm{A}], \tag{3.10}$$

which is a first order reaction.

Pearson et al. [74] mentioned that there is general agreement that the order of reaction is one, meaning that the decomposition step, reaction 3.5, is the rate determining one and that it can be described by equation 3.10. Satterfield and Stein [75] were the only researchers who found a reaction order of 1.5 but as was pointed out by Hoare et al. [76] they did not take into account the influence of the carrier gas, represented by $[M]$ in reaction 3.4, on the reaction rate. Hoare et al. [76] also showed that some carrier gases are more effective during the activation step than others.

The above described Lindemann-Hinshelwood theory gives qualitative insight in the reaction mechanism, but when compared with experimental data large discrepancies, in some cases several orders of magnitude, are found in reaction rates. The differences are larger for more complex molecules. The main reason for this is that the Lindemann-Hinshelwood theory does not take into account the structure of and the energy distribution within the molecule [73]. The theory has been extended by considering the quantum mechanical aspects of the reaction mechanism and are known as the Rice-Ramsperger-Kassel (RRK) theory and the Rice-Ramsperger-Kassel-Marcus (RRKM) theory or the transition state theory. The resulting reaction rates from these theories are in much closer agreement with experimental data [73]. Ideally, reaction mechanism and rates are determined from first principles, i.e. quantum mechanical calculations. However, Bell and Head-Gordon [77] mentioned that despite the enormous increase in computing power over the last couple of decades, simulations can only be done for idealised situations for a total of 20 to 200 atoms.

Another problem with the Lindemann-Hinshelwood theory for decomposition of hydrogen peroxide is that the decomposition is assumed to take place in one step, whereas in reality several intermediate

products are formed and consumed. Giguère and Liu [78] proposed the following reaction mechanism

$$H_2O_2 \xrightarrow{k_4} OH + OH \tag{3.11}$$

$$OH + H_2O_2 \xrightarrow{k_5} H_2O + HO_2 \tag{3.12}$$

$$OH + HO_2 \xrightarrow{k_6} H_2O + O_2 \tag{3.13}$$

$$HO_2 + HO_2 \xrightarrow{k_7} H_2O_2 + O_2. \tag{3.14}$$

Based on their found reaction order of 1.5 Satterfield and Stein [75] proposed a reaction mechanism, where the first two steps are the same as equations 3.11 and 3.12 followed by

$$HO_2 + H_2O_2 \rightarrow H_2O + O_2 + OH, \tag{3.15}$$

which would result in a chain reaction. However, Hoare et al. [76] pointed out that in their derivation of the reaction order they had not taken into account the effect of the carrier gas and that if a first order reaction is assumed a chain reaction cannot take place. They proposed the same reaction mechanism as Giguère and Liu [78] but without the last step, equation 3.14.
Hippler et al. [79] performed experiments to determine the reaction rate constants for reactions 3.12 and 3.13. In a more recent study by Hong et al. [80] the rate constants for reactions 3.11 and 3.14 were experimentally determined together with the rate constant for an additional reaction given by

$$OH + OH \xrightarrow{k_8} H_2O + O. \tag{3.16}$$

Both Hippler et al. [79] and Hong et al. [80] performed the measurements at very low hydrogen peroxide partial pressures such that for the overall reaction $k_3 \gg k_2$. Consequently, the rate of formation of the products was a second order reaction given by reaction 3.9. The order of magnitude of the different rate constants are summarised in table 3.1 where the unit of the rate constant is $cm^3\,mol^{-1}\,s^{-1}$. From this table it is clear that reaction 3.11 is the rate limiting step. It should be noted that Hippler et al. [79] and Hong et al. [80] focused on hydrogen peroxide vapours at a temperature of 930K and above. However, in a study performed by Croiset et al. [81] it was stated that reaction 3.11 is generally the rate limiting step in both the gas and liquid phase.
As the rate constant for reaction 3.11 is at least four orders of magnitude lower than the rate constants for all other intermediate reactions it is possible to determine a global reaction rate constant with reasonable accuracy. Such an approach was used by all the researchers mentioned in section 2.1.3. The reaction rate constant is determined by the Arrhenius equation given by equation 3.3.
Giguère and Liu [78] and Hoare et al. [76] both reported an activation energy of $48 kcal\,mol^{-1}$ (equal to $200.8 kJ\,mol^{-1}$) for the thermal decomposition of hydrogen peroxide vapour. There was some disagreement on the value for the pre-exponential factor: Giguère and Liu [78] found a value of $A_0 = 1 \cdot 10^{13} s^{-1}$ and Hoare et al. [76] a value of $A_0 = 1 \cdot 10^{15.4} s^{-1}$. Pearson et al. [74] conducted a literature review on the research into thermal decomposition of peroxide vapour and found that pub-

rate constant	order of magnitude	reference
k_4	7	Hong et al. [80]
k_5	12	Hong et al. [80]
k_6	13	Hippler et al. [79]
k_7	11	Hippler et al. [79]
k_8	12	Hong et al. [80]

Table 3.1: *Order of magnitude for reaction rate constants*

lished values for the activation energy are between 45 and $55 kcal\,mol^{-1}$ (188.3 and $230.1 kJ\,mol^{-1}$). Very little research has been done on determining the Arrhenius parameters for thermal decomposition in the liquid phase. The only known values for the Ahrrenius parameters are by Takagi and Ishigure [82] and Croiset et al. [81]. The latter researchers determined the Arrhenius parameters for pressures from $5-34 MPa$ and found values of $A_0 = 1 \cdot 10^{3.6} s^{-1}$ and $E_A = 49 kJ\,mol^{-1}$. Takagi and Ishigure [82] measured in the pressure range up to $4 MPa$ and reported values of $A_0 = 1 \cdot 10^{5.8} s^{-1}$ and $E_A = 71 kJ\,mol^{-1}$. The values used in this thesis are summarised in table 3.2. For decomposition in the gas phase the values reported by Hoare et al. [76] will be used as these are about the average of the values found by other researchers [74]. For liquid decomposition the values found by Takagi and Ishigure [82] will be used as they measured in the pressure range that is closest to the expected operating pressure of the catalyst bed.

With the Arrhenius parameters known the overall reaction rate $\dot{r}$ for the thermal decomposition of hydrogen peroxide in $kg\,m^{-3}\,s^{-1}$ can be determined by

$$\dot{r}_{H_2O_2} = -A_0 e^{\frac{-E_A}{R_c T}} [\mathrm{H_2O_2}] M_{\mathrm{H_2O_2}}, \tag{3.17}$$

where M is the molar mass.

decomposition type	$\mathbf{A_0}\,[s^{-1}]$	$\mathbf{E_A}\,[kJ\,mol^{-1}]$
liquid	$1 \cdot 10^{5.8}$	71
gas	$1 \cdot 10^{15}$	200

Table 3.2: *Arrhenius parameters for thermal decomposition*

3.1.2 Catalytic decomposition

Catalytic decomposition is a decomposition reaction taking place at the surface of a catalyst and can generally be subdivided into 7 steps:

1 external diffusion; diffusion of the reactant from the bulk liquid of gas phase through the boundary layer to the outside of the catalyst material

2 internal diffusion; diffusion of the reactant from the outside material into the catalyst material

3 adsorption;

4 actual decomposition;

5 desorption;

6 internal diffusion; diffusion of the products from the catalyst material to the outside

7 external diffusion; diffusion of the products through the boundary layer to the bulk liquid or gas phase

Point 1 and 7 describe the transport of species through the diffusional boundary layer which is formed between the bulk phase and the catalyst material. As hydrogen peroxide is consumed during decomposition at the catalyst surface this causes the concentration at the catalyst surface to be lower than the bulk concentration. The decomposition of peroxide at the catalyst surface is dependent on the concentration and the rate constant as is shown in equation 3.2. The overall decomposition velocity is determined by the slowest process being either the diffusion through the boundary layer or the decomposition at the catalyst surface.
As was pointed out by Holub et al. [83] due to the tortuosity of the catalyst bed the full development of a velocity boundary layer is prevented. It is reasonable to assume that the same argument also holds for the diffusional boundary layer. Oehmichen et al. [84] performed experiments where they put a piece of copper in a liquid hydrogen peroxide solution while continuously stirring the copper piece. They varied the peroxide concentration and the stirring speed and showed that for low concentrations the rate of decomposition is dependent on the stirring speed. For concentration of 30% and more the rate of decomposition was independent from the stirring speed. They argued that stirring enhances the mass and heat transfer and thus the concentration at the copper surface. They concluded that for low concentrations the reaction is diffusion limited and for concentrations of 30% and more reaction limited. The independence of stirring speed at high concentrations can be explained as follows. A liquid decomposing on the catalyst surface results in a large increase in volume due to the formation of gas. At a pressure of $10 bar$ and a temperature of $100°C$ the volume of the reaction products is more than 62 times the volume of peroxide that is decomposing (based on the molar masses and liquid densities as listed in appendix B). Almost 99% of that volume increase can be attributed to the formation of oxygen resulting in gas bubbles emerging from the catalyst surface. Due to these bubbles the boundary layer is disturbed. Once the bubble has detached from the surface the gap is filled with liquid once again. This process greatly enhances mixing resulting in a reduced difference in peroxide concentration between the catalyst surface and the bulk fluid.
Very little research has been done on catalytic decomposition of hydrogen peroxide vapour. In cases where catalytic vapour decomposition is mentioned it is done to distinguish it from thermal decomposition when experimentally determining the Arrhenius parameters for thermal decomposition. The

above described mechanism is not present in the gas phase, although the argument of an underdeveloped boundary layer due to the tortuosity still holds. For this reason it will be assumed that also in the gas phase the external diffusion can be neglected.

Point 2 and 6 describe the transport of species through the pores of the catalyst by means of diffusion. For this a model developed by Thiele [85] (see appendix D for a description of the model) is often used [86]. This model implicitly assumes that the diffusion rate is much higher than the rate of reaction at the catalyst surface and chemical reactions that involve phase changes are not accounted for. Datsevich [86] developed a model that explicitly takes phase changes into account. He showed that this can result in oscillatory behaviour of the interaction between the gas and liquid and the catalyst where liquid is being pushed out of the catalyst pores due to the gas formation. After detachment of the bubble from the catalyst surface, the pores fill up with liquid once again. Oehmichen et al. [84] showed that the combination of formation of bubbles and high reaction rates prevent the core of the catalyst from taking part in the decomposition. In the case of 30%wt hydrogen peroxide they showed numerically as well as experimentally that only 2% of the surface area of the pores takes part in the decomposition process. For higher peroxide concentrations the effectiveness factor will decrease further and therefore internal diffusion for the liquid phase can be neglected.

For the gas phase internal diffusion could potentially be an important factor. For now it is assumed that it can be neglected as well. In the next chapter it will be shown that this is an acceptable assumption.

At the surface adsorption and desorption takes place and adsorbed molecules decompose to form reaction products. For an arbitrary molecule of particles A this process can be described by

$$\mathrm{A} + \mathrm{site} \underset{k_{de}}{\overset{k_{ad}}{\rightleftharpoons}} \mathrm{A} - \mathrm{site} \xrightarrow{k_{reac}} \mathrm{products}, \tag{3.18}$$

where k_{ad} and k_{de} are the adsorption and desorption rate constant respectively and k_{reac} the reaction rate constant for decomposition.

Adsorption is the process where a molecule forms a bond with an active site on the catalyst surface. It can do this in two ways: it can form a Van der Waals bond which is referred to as physisorption or it can make a strong chemical bond which is referred to a chemisorption [73]. Chemisorption is required for catalysis, but can be preceded by physisorption [87]. In some cases dissociation takes place at the moment a strong chemical bond is formed. This is often referred to as dissociative adsorption.

The rate of adsorption is a function of the concentration of adsorbate and the availability of active sites on the catalyst surface. The opposite of adsorption is desorption of which the rate is dependent on the fraction of total active sites to which a molecule is chemisorbed. The availability is expressed by the variable θ which represents the fraction of the active sites on the surface that have formed a strong chemical bond with a molecule already. At equilibrium the rate of adsorption is equal to the rate of desorption which can be written as

$$k_{ad}[\mathrm{A}](1-\theta)N = k_{de}\theta N, \tag{3.19}$$

where k_{ad} and k_{de} are the adsorption and desorption rate constant, respectively, and N the number of active sites on the catalyst surface. Solving this equation for the fractional coverage θ results in

$$\theta = \frac{K_r[\mathrm{A}]}{1+K_r[\mathrm{A}]}. \tag{3.20}$$

Here K_r is the equilibrium constant defined as k_{ad}/k_{de}. Equation 3.20 is known as the Langmuir adsorption isotherm [73]. For this isotherm it is assumed that the catalyst surface is homogeneous, that adsorbed molecules do not interact and that only a monolayer of chemisorbed molecules can be formed at the catalyst surface.

If it is now assumed that $k_{reac} \ll k_{de}$, as according Pasini et al. [64] is allowed, then the reaction rate can be expressed as

$$\dot{r}^S = k_{reac} N \frac{K_r[\mathrm{A}]}{1+K_r[\mathrm{A}]} M_A. \tag{3.21}$$

The superscript S refers to the conditions at the catalyst surface. If it is further assumed that decomposition rate constant, k_{reac}, can be written as an Arrhenius equation [64] and that the equilibrium constant, K_r, is very small, then the reaction rate can be written as

$$\dot{r}^S = A_0 e^{\frac{-E_A}{R_c T}} N K_r[\mathrm{A}] M_A. \tag{3.22}$$

Note that equation 3.22 is a surface reaction rate and that the unit of the pre-exponential factor is in $m\,s^{-1}$. Furthermore, it should be noted that the Langmuir adsorption isotherm is only valid for gases. Sohn and Kim [88] proposed a modification of the Langmuir isotherm to describe the adsorption process for liquids. For this purpose they wrote equation 3.20 as $\theta = K_r[\mathrm{A}]^z/(1+K_r[\mathrm{A}]^z)$ where z is a parameter that has to be determined experimentally. They showed that with a proper choice of z a much improved description of the adsorption isotherm can be achieved.

A more general problem with the model developed above is that values for the pre-exponential factor A_0, number of available active sites N and the equilibrium constant K_r are dependent on the catalyst material and, for catalysis of hydrogen peroxide in particular, are generally not known. Zhou and Hitt [61] mentioned this explicitly when choosing their value for A_0. Besides that, Bliznakov and Lazarov [89] stated that the activation energy E_A of catalysts is dependent on the type of crystal and showed this in particular for copper based catalysts. From this it can be concluded that the assumption made above about surface homogeneity is generally not valid. Finally, when the above model is applied directly to the decomposition of hydrogen peroxide into water and oxygen, the formation of intermediate products is neglected.

Haber and Weiss [90] were one of the first who proposed a decomposition mechanism for decompo-

sition of peroxide on metallic surfaces

$$H_2O_2 + \text{site} \longrightarrow \text{site}^+ + OH^- + {}^\bullet OH \tag{3.23}$$

$${}^\bullet OH + H_2O_2 \longrightarrow H_2O + HO_2{}^\bullet \tag{3.24}$$

$$\text{site}^+ + O_2^{\bullet -} \longrightarrow \text{site} + O_2 \tag{3.25}$$

$$\text{site} + HO_2{}^\bullet \longrightarrow \text{site}^+ + HO_2{}^- \tag{3.26}$$

$$\text{site}^+ + HO_2{}^- \longrightarrow \text{site} + HO_2{}^\bullet, \tag{3.27}$$

where the superscript minus and plus sign refer to the charge and the dot indicates a radical. However, McKee [91] stated at the end of the sixties that at that time *"almost every conceivable mechanism for the catalytic decomposition of hydrogen peroxide has been proposed."* Giamello et al. [92] mentioned in the publication about their research in the early nineties that a thorough description of the decomposition mechanism at a catalytic surface is far from being accomplished.

For the modelling of catalytic decomposition in this thesis it will be assumed that the decomposition mechanism can be described accurately enough by a single step where hydrogen peroxide is directly converted into its products, see equation 2.1. This approach is often taken by researchers in the field of hydrogen peroxide based rocket motors, see Zhou and Hitt [61], Corpening et al. [63], Bonifacio and Russo Sorge [62], Pasini et al. [64] and Krejci et al. [49]. To determine the volumetric rate of decomposition a slightly modified version of equation 3.22 will be used

$$\dot{r}^S_{H_2O_2} = -A_0 e^{\frac{-E_A}{R_c T}} K_r [H_2O_2] a_{sp} M_{H_2O_2}, \tag{3.28}$$

where a_{sp} is the surface area per unit volume of catalyst bed. To obtain a volumetric reaction rate from a surface process the pre-exponential factor is multiplied by the surface area per unit volume of catalyst bed. This leads to a reaction rate in $kg\,m^{-3}\,s^{-1}$. In practice when the pre-exponential factor A_0 is determined the influence of the number of active sites N is included and not distinguished separately. The same approach will be followed in this thesis. The equilibrium constant K_r is not known and will have to be determined by correlating the model with experimental data.

Values for the Arrhenius parameters are different for each catalyst material and for each material different researchers have found different values. Instead of choosing a specific catalyst material with corresponding Arrhenius parameters, a set of Arrhenius parameters will be chosen that are representative for typical catalyst for hydrogen peroxide.

Bliznakov and Lazarov [89] reported the activation energy for silver and liquid peroxide to vary between 25.1 and $62.8 kJ\,mol^{-1}$ where the variation was caused by changes in oxygen content. Albers et al. [93] determined for a manganese oxide catalyst an activation energy of $50.7 kJ\,mol^{-1}$ and mentioned that this was close to a previously reported value by another research group of $54.5 kJ\,mol^{-1}$. Lin et al. [94] mentioned that literature values for activation energy are typically ranging from 20.9 to $96.2 kJ\,mol^{-1}$ while Bonifacio and Russo Sorge [62] mentioned a narrower range of 40 to $50 kJ\,mol^{-1}$.

Zhou and Hitt [61] used in their simulations a value of $54.8 kJ\,mol^{-1}$. In this work a value of $52.5 kJ\,mol^{-1}$ will be adopted as a baseline value.

For the pre-exponential factor the variation in values is much larger; spanning several orders of magnitude. One of the possible reasons for this is that during calculation of the pre-exponential factor the influence of the surface area on the results is not always taken into account judged by the stated units: s^{-1} instead of ms^{-1}. For this reason only values will be considered for which the units are stated explicitly. Shteinberg [95] determined the Arrhenius parameters for a number of construction materials and found pre-exponential factor in the range from $1 \cdot 10^3$ to $9 \cdot 10^6 ms^{-1}$. These construction materials, such as stainless steel and aluminium, are typically used to build storage tanks and heat sinks. Albers et al. [93] calculated a pre-exponential factor of $2.6 \cdot 10^4 ms^{-1}$ for a manganese oxide catalyst. This value will be used in this work.

Much less literature is available on the Arrhenius parameter for decomposition of hydrogen peroxide vapour. Most notable is the work of Giguère and Liu [78] who found the activation energy to vary from 41.8 to $50.2 kJ\,mol^{-1}$ and Hoare et al. [76] who mentioned a value of $41.8 kJ\,mol^{-1}$. The latter value will be assumed in the current model. It should be noted that in both cases the catalyst was the wall of the reactor which was used for experiments aimed to determine the rate constant for thermal decomposition. The material of these reactor walls were pyrex treated in such a way to minimise decomposition at the wall. For a good working catalyst the actual activation energy is likely to be lower.

Unfortunately, no data is available in literature on the pre-exponential factor for catalytic decomposition of the peroxide vapour. However, Hoare et al. [76] mentioned that their experiments on homogeneous decomposition a change in reaction rate constant was observed that took place at about 420°C. They also mentioned that several other researchers had noticed this change in the range of 390 to 420°C. They explained this as the transition from catalytic dominated decomposition at low temperatures to thermal dominated decomposition at high temperatures. To determine the value of the pre-exponential factor from the experimental data the reaction rate constant is split into a part caused by thermal and catalytic decomposition and can be written as [81]

$$k_1 = k_{1therm} + k_{1cat} \left(\frac{\text{reactor surface}}{\text{reactor volume}} \right), \tag{3.29}$$

where k_{1therm} and k_{1cat} are the reaction constant due to thermal and catalytic decomposition, respectively. Hoare et al. [76] stated the dimensions of the reactor they used as having an internal diameter of 3.8cm and a length of 20cm. Using equation 3.3 and the appropriate values for the Arrhenius parameters as stated in tables 3.2 and 3.3 the value for the pre-exponential factor for catalytic decomposition can be chosen such that there is a transition from catalytic to thermal decomposition at 420°C. The result for $A_0 = 1 \cdot 10^1$ is shown in figure 3.1, which shows that the decomposition mode change takes place at 420°C.

A summary of the Arrhenius parameters for catalytic decomposition is given in table 3.3.

As is shown above, there is a significant spread in reported values for the Arrhenius parameters for

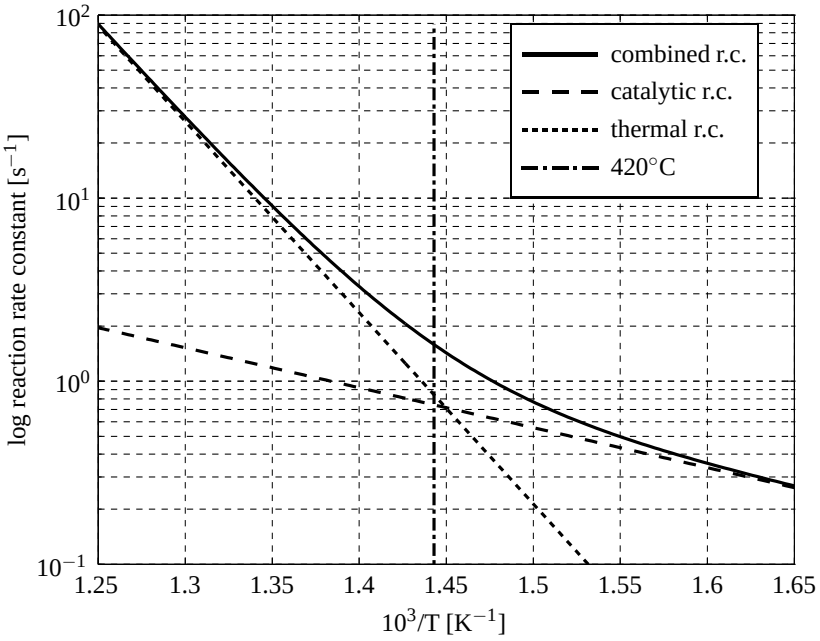

Figure 3.1: *Arrhenius plot of* $\log k_1$ *vs. the reciprocal temperature. r.c. is short for reaction rate constant.*

decomposition type	$\mathbf{A_0}\,[m\,s^{-1}]$	$\mathbf{E_A}\,[kJ\,mol^{-1}]$
liquid	$2.6 \cdot 10^4$	52.5
gas	$1 \cdot 10^1$	41.8

Table 3.3: *Arrhenius parameters for catalytic decomposition*

both catalytic and thermal decomposition. The values adopted in this work are based on best guesses from published values. In chapter 6 parametric studies will be performed which will investigate the sensitivity of the Arrhenius parameters on the catalyst bed performance.

Note that the overall reaction rate for thermal decomposition, see equation 3.17, and catalytic decomposition, see equation 3.28, give the rate at which hydrogen peroxide is consumed. The rate at which water and oxygen is formed can be found by taking into account the stoichiometric reaction ratio ν, see equation 2.1, and the molar mass of the component relative to the molar mass of hydrogen peroxide. The component source term $S_{A\alpha}$, which was introduced in equation 2.15, can now be written as

$$S_{A\alpha}^{dec} = \left(\dot{r}_{H_2O_2,\alpha} + \dot{r}^S_{H_2O_2,\alpha}\right) \nu \frac{M_A}{M_{H_2O_2}} \tag{3.30}$$

The corresponding mass source term $\Gamma_{\alpha dec}$ can then be written as the sum of the component source terms

$$\Gamma_\alpha^{dec} = \sum_A S_{A\alpha}^{dec}. \tag{3.31}$$

3.2 Evaporation of a Binary Liquid

The second mechanism of mass transfer comes from evaporation of the liquid. As the gas and liquid phase are not necessarily in equilibrium with each other, evaporation or condensation will take place. The rate of evaporation increases with temperature and reaches its maximum when the boiling point is reached. Pure hydrogen peroxide and water have different boiling points. The boiling point of a mixture of hydrogen peroxide and water is dependent on the concentration of peroxide and the pressure. The difference in volatility between both components determines the relative amount of evaporation, which affects the concentration of the liquid.
The formulation of the source term should be such that the above described behaviour is captured in such a way that it can be implemented in a CFD code. To do this a number of simplifications and assumptions will be made of which the most significant one is that the evaporation process can be described by droplet evaporation laws for droplets with a spherical shape. As was discussed in the previous chapter a mix of flow regimes will be present with different boiling modes associated with it. The consequence of these assumptions on the actual evaporation rate of each component will be further assessed in chapter 6.
Subsection 3.2.1 discusses how the boiling point for hydrogen peroxide mixtures is constructed and how the equilibrium concentrations in the gas and liquid phase can be calculated. Subsection 3.2.2 will discuss various droplet evaporation models starting with single component liquids. These models form the basis for most of the multicomponent evaporation models, which will be discussed subsequently. The last subsection will present the evaporation model that will be used for simulations. It should be kept in mind that the literature review on evaporation models is not meant to give a complete overview of all the evaporation models, but to give a description of the most important basic models.

3.2.1 Boiling diagrams

Corpening et al. [63] pointed out that water evaporates preferentially from a hydrogen peroxide-water mixture resulting in an increase of peroxide concentration in the liquid phase. This is due to the non-ideal behaviour of the peroxide-water mixture: upon mixing pure hydrogen peroxide with water, the intermolecular forces change slightly due to the difference in molecular structure of both components. This results in a change in vapour pressure or a deviation from Raoult's law.
The vapour pressure of component i in a non-ideal liquid mixture, $p_{i,vap}$, is generally given by [96]

$$p_{i,vap} = \gamma_i x_i p_i^{\circ}, \tag{3.32}$$

where γ_i is the activity coefficient of component i, x_i the mol fraction of component i in the liquid phase and p_i° the vapour pressure of the pure component i. Relations for the activity coefficient and vapour pressure of the pure components water and hydrogen peroxide were presented by Manatt and

Manatt [18] and are listed in appendix B. They critically reviewed pressure measurements reported by Scatchard et al. [97] and in a PhD thesis by Kavanagh [98]. New vapour pressure-temperature relations were derived based on modern well-tested techniques resulting in better fits with experimental data. To improve the results further they also reviewed the measurement techniques and procedures the original authors had used. Manatt and Manatt concluded that the used methods could result in local temperature variations inside the equipment. Taking into account these variations they managed to significantly improve the fits to the experimental data. The relations for vapour pressure and activity coefficients can be found in appendix B.6.

For a given pressure and known vapour pressure of a component the corresponding mol fraction of component *i* in the gas phase, under assumption of equilibrium between the phases, can be found with Dalton's law

$$y_i = \frac{p_{i,vap}}{p}. \tag{3.33}$$

Based on the above equations a boiling diagram can be constructed: a diagram showing the boiling temperature and the corresponding equilibrium gas composition as a function of the liquid composition. The boiling temperature is determined by setting the temperature to a value such that the sum of the vapour pressures of each component is equal to atmospheric pressure. The corresponding mole fraction of each component in the gas phase can then be determined with equation 3.33. The boiling diagram for a mixture of hydrogen peroxide and water at standard atmospheric pressure is shown in figure 3.2. It shows that for pure water the boiling point is 100°C and for pure hydrogen peroxide 153°C. For a peroxide mole fraction of 0.787, equivalent to a peroxide mass fraction of 0.785, the boiling point is 134.4°C. At that temperature the mole fraction of peroxide in the gas phase is 0.432, equivalent to a mass fraction of 0.589. Boiling diagrams for other pressures are presented in appendix B.8.

3.2.2 Heating and evaporation rate of droplets

In equations 3.32 and 3.33 no assumptions are made on the temperature. As a result, if a liquid at an arbitrary temperature is in thermodynamic equilibrium with a gas above it, the combination of equations 3.32 and 3.33 shows that the gas contains all the components that are present in the liquid phase that have a non-zero vapour pressure. The value of the vapour pressure determines the relative amount of the liquid components that is present in the gas phase. If suddenly one of the vapour components is removed, equilibrium will be restored by means of evaporation. The rate of this process is temperature dependent. In reality evaporation is continuously taking place. However, at equilibrium it is balanced by the rate of condensation resulting in no net mass transfer.

In a lot of practical engineering problems the mass transfer between the phases is of importance and requires modelling. The process of evaporation consists of two phases [99]:

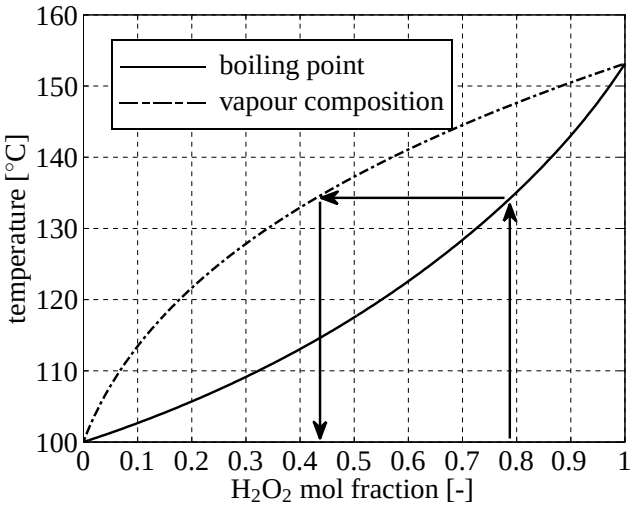

Figure 3.2: *Boiling diagram for standard atmospheric pressure*

1 Detachment of the molecule from the surface of the liquid into the gas in the vicinity of the liquid.

2 Diffusion of the vapour into the ambient gas.

A number of evaporation models only consider the second process and assume that the vapour around the droplet is saturated. These models are called hydrodynamic models. Models taking into account the first process as well can be further divided into kinetic models, based on the Boltzmann kinetic equation, and molecular dynamics models, which model the dynamics of individual molecules [99]. However, this last group of models is not suited for implementation in CFD codes and will not be discussed further.

Single component droplet evaporation

A very basic and widely used hydrodynamic evaporation model was derived in the early fifties [100] and is part of the well-known D^2-law. The main assumptions in this model are constant gas phase properties, constant and uniform droplet temperature, quasi-steady evaporation process, liquid-vapour equilibrium at the droplet surface and no relative velocity between the droplet and the ambient gas [101]. At the droplet surface any vapour formed by evaporation is transported away from the surface into the ambient gas by diffusion and Stefan flow, which is the movement of molecules due to being pushed away by molecule coming from the droplet. The model requires that this is in equilibrium with the mass lost by the droplet due to evaporation. The change in mass of the droplet, $\frac{dm_d}{dt}$, can be expressed as

$$\frac{dm_d}{dt} = -\pi D_d^2 \rho_g \mathcal{D}_g \frac{dY_v}{dr} - \pi D_d^2 \rho_g u_r Y_v, \tag{3.34}$$

where ρ is the density, D_d the droplet diameter, $\mathcal{D}$ the binary diffusion coefficient of the gas, Y_v the mass fraction of the vapour and u_r the radial velocity. Subscripts g and v refer to gas and vapour respectively and subscript r refers to the radial position where the droplet centre is the origin. Because there is no convection the boundary layer stretches from the droplet surface to $r \longrightarrow \infty$.
By solving equation 3.34 it can be shown that the evaporation is driven by $\ln(1+B_M)$ where B_M is the Spalding mass transfer number defined as

$$B_M = \frac{Y_{v,s} - Y_{v,\infty}}{1 - Y_{v,s}}. \tag{3.35}$$

Here $Y_{v,s}$ is the vapour mass fraction at the droplet surface and $Y_{v,\infty}$ the vapour mass fraction in the ambient gas far away from the droplet surface.
In general the droplet temperature will be different from the ambient gas temperature which gives rise to transport of heat. In this model the time rate of change of the enthalpy of the droplet, dh/dt is given by [102]

$$\frac{dh_l}{dt} = \frac{1}{m_d}\left(h_T \pi D_d^2 (T_g - T_l) + \frac{dm_d}{dt}\Delta H_{fg}\right), \tag{3.36}$$

where h_T is the heat transfer coefficient and ΔH_{fg} the liquid latent heat. As mentioned before, it is assumed that the droplet temperature is uniform or that mixing is infinitely fast. For this reason this model is also often referred to as the rapid mixing model [102]. The last term on the right hand side accounts for the energy consumed by evaporation. In this case dm_d/dt is negative and thus cools the droplet. The first term on the right hand side is Newton law of cooling. It should be noted that the effect of Stefan flow is not accounted for in the energy balance as was done for the mass balance. Equations 3.34 and 3.36 are therefore not consistent.
Equation 3.33 shows that the closer the liquid temperature gets to the boiling point, the higher the mol fraction of the vapour at the liquid surface is and thus the higher the vapour mass fraction at the liquid surface, see appendix A. From equation 3.35 it can be seen that in that case the Spalding mass transfer number, and as a result the evaporation rate, tends to infinity. As the first term on the right hand side of equation 3.36 can be assumed to stay finite, it will be dominated by the last term on the right hand side when the liquid temperature approaches the boiling point. As a result in the D^2-law the liquid can never reach a supercritical state.
Law [100] pointed out that the model assumes constant fluid properties which in reality is violated due to the sometimes considerable temperature differences between the liquid and the surrounding fluid. For this reason the fluid properties are often determined at a reference temperature, where the reference temperature is often determined by the so-called 1/3-law [103].
Abramzon and Sirignano [104] extended and improved the above described model on several points. Firstly, their model takes heat and mass transfer by convection into account. For this purpose they define modified Nusselt and Sherwood numbers. Based on these numbers correction factors are formulated for the thermal and diffusion boundary layer thickness. Their model allows for non unitary Lewis numbers, which influences the droplet evaporation rate and thus lifetime. The correction fac-

tors are formulated in such a way that for droplets in a quiescent environment the previously described model is obtained.

Abramzon and Sirignano mentioned that the total droplet evaporation time is for a large part influenced by transient droplet heating. To accurately determine the evaporation time and rate an accurate prediction of the droplet surface temperature with time is required. For this purpose they studied the internal velocity and heat distribution of a droplet during transient heating. They showed that during the the first 30 to 40% of the transient time, when the Peclet number is above 100, the droplet heating is controlled by convection and that during the last third of the transient time, when the Peclet number is below 10, the heating is controlled by conduction [104]. A gradual transition from convection dominated to conduction dominated heating was seen for the period in between. As the employed model would be computationally far too expensive when a spray of droplets is considered, Abramzon and Sirignano introduced the effective conductivity model. This model accounts for the apparent change in liquid conductivity as a function of the liquid Peclet number and provides a smooth transition between the two modes of heat transfer. They mentioned that it does not give any details about the physical features inside the droplet, but that a realistic droplet surface temperature is obtained.

Shrimpton and Laoonual [105] employed an evaporation model to predict the time dependent evaporation of electrically charged sprays in direct-injection spark-ignition engines. The total time of evaporation in these engines is in the order of milliseconds. Their evaporation model follows the same principles as the model by Abramzon and Sirignano. In contrast, however, they determined the values of the Nusselt and Sherwood number by established relations for convective flow. Furthermore, the evaporation rate is proportional to B_M instead of the natural logarithm of the Spalding mass transfer number. Their heat transfer relation incorporates a correction factor to account for the effect of evaporation on the heat transfer.

The actual form of the correction factor for heat transfer is one of the subjects of discussion in a research published by Miller et al. [102], from where the model of Shrimpton and Laoonual was taken. They evaluated the three models described above plus five others with each other and compared them with experimental data. Two of these models were non-equilibrium models. They observed that at temperatures well below the boiling point all eight models performed equally well but that close to the boiling point the non-equilibrium models performed much better than the other models. A closer investigation revealed that for droplets with an initial diameter of $> 50\mu$m the better performance was not a consequence of non-equilibrium effects, but due to a better description of the heat transfer between the droplet and surrounding gas. The six equilibrium models used correction factors for the heat transfer while the non-equilibrium models used a model based on molecular dynamics to describe the process of heat transfer. Miller et al. showed that none of these correction factors were actually able to give a good approximation to the heat transfer as modelled by the non-equilibrium models. By replacing the correction factors with the heat transfer model as provided by the non-equilibrium models, they showed that these models could perform equally well. However, they stated that as the non-equilibrium models they employed were not more complicated than the equilibrium models, the

former should preferably be used as its description is closer to the physical reality.
Dushin et al. [106] developed a non-equilibrium model as well and compared that to an equilibrium version of their model. They came to the same conclusions as Miller et al. that close to the boiling point and for small droplets, better results are obtained with non-equilibrium models. They also pointed out that the main difference between equilibrium and non-equilibrium models become apparent at the final stages of the droplet lifetime. Contrary to equilibrium models in non-equilibrium models the evaporation remains finite and the gas velocity at the interface does not exceed the velocity of sound at the end of the droplet lifetime.
The non-equilibrium model by Miller et al. and Dushin et al. are in fact hydrodynamic models with a jump condition for the mole fraction at the surface of the droplet. This additional boundary condition takes into account the influence of the Knudsen layer surrounding the droplet. The liquid phase of the droplet and the gas phase of the ambient gas is on either side of this very thin layer. In the layer itself it is not possible to distinguish between the gas phase and liquid phase [99]. Strictly speaking, there is also a jump condition for the temperature and velocity, but they are not taken into in the two non-equilibrium models.
Models that take into account all the jump conditions are kinetic models. As mentioned at the beginning of this subsection, kinetic models model the detachment of liquid molecules from the liquid phase into the gas phase in the vicinity of the liquid phase. These models analyse the velocity distribution of gas molecules in the Knudsen layer by considering the multi-particle distribution function [99]. When it is assumed that interaction between the molecules only occur during collisions, the result is a single Boltzmann transport equation. When it is furthermore assumed that external forces on the particles are small enough to be neglected and there is free molecular flow, the Boltzmann transport equation can be solved analytically. The result is the so called Hertz-Knudsen-Langmuir formula describing the mass flux of vapour from the droplet surface [99] and is given by

$$j = \frac{\beta}{\sqrt{2\pi R}} \left(\frac{p_{vs}}{\sqrt{T_s}} - \frac{p_\infty}{\sqrt{T_g}} \right), \tag{3.37}$$

where R is the gas constant and β the evaporation coefficient. The evaporation coefficient is between 0 and 1 shows the relative amount of vapour molecules that are absorbed by the droplet surface once they collide with it. This coefficient can be determined by experiment. It could also be derived theoretically by means of molecular dynamic models.
Kryukov et al. [107] performed comparison between hydrodynamic and kinetic models for the evaporation of Diesel droplets of 5 and 20μm. They simplified the analysis by approximating the Diesel as a fuel consisting of just one component. As the evaporation coefficient for Diesel is not known they took two values ($\beta = 0.5$ and $\beta = 0.04$) to investigate the influence of this coefficient on the results. They showed that for both droplet sizes there is always a difference between kinetic and hydrodynamic models. For kinetic models the evaporations times are larger; for droplets of 5μm evaporation can take 5 to 10% longer depending on ambient temperature. The differences become larger for smaller

droplets, higher ambient temperatures and smaller evaporation constants.
The Hertz-Knudsen-Langmuir formula was successfully applied in a study performed by De Schepper et al. [108]. They modelled the evaporation of a hydrocarbon in a steam cracker. The vapour pressure was determined by means of linearising the Clausius-Clapeyron equations and so their model was only valid for temperatures close to the boiling point. Unfortunately, the results of their numerical model were not compared with experimental data.

Multicomponent droplet evaporation

All the evaporation models discussed up until now assume a single component liquid. However, as has become clear from previous discussions, in the current application the liquid consists of two components. As explained in section 3.2.1 due to a difference in vapour pressure the rate of evaporation of each component is different. Several different approaches exists to capture this behaviour.
Burger et al. [109] developed a model to simulate the evaporation of kerosene, a fuel that consists of several hundreds of different components. The basis of their model is the previously discussed Abramzon and Sirignano model. Within this model it is assumed that there is no spatial variation in temperature and concentration in the liquid phase. The properties of the liquid mixture is based on the distillation curve data of a mixture of n-alkanes and given as a function of the molar mass. In this way the problem of a multicomponent liquid is reduced to one of a single component of which the properties not only change as a function of temperature and pressure, but also as a function of the molar mass. As the model is used for simulations at high pressures, real gas effects are taken into account. The authors show that using this approach gives improved results with respect to experimental data compared to single component models.
The Abramzon and Sirignano model also was the basis for an evaporation model developed by Brenn et al. [110]. In their model the evaporation rate of every single component is computed and added up to obtain the total evaporation rate. To account for the presence of the other components the evaporation rate is multiplied by a radius of which the volume is equivalent to the volume fraction of the component in the liquid mixture. Experiments on several different individual hydrocarbon fuel droplets are performed by levitating the droplets in an acoustic field. The droplet evolution in time was recorded with a CCD camera from which the droplet diameter, shape and location of the center of gravity was determined. Experiments were carried out with ambient temperatures up to 31°C and liquid mixture with up to 5 components. The simulation results showed a very good agreement with experimental data.
A simplified multicomponent droplet evaporation model was presented by Sazhin et al. [111, 112]. The Abramzon and Sirignano model was slightly adjusted by taking into account the dependency of the Reynolds number on the evaporation rate. Relations were provided for the internal droplet temperature and species distribution and the swelling of droplets due to temperature fluctuations. Equations

were derived to describe the coupling between the droplet and the ambient gas. They compared their numerical results with experimentally obtained data and concluded that especially the coupling between the droplet and the ambient gas resulted in much better predictions. The authors also showed that the computational cost of their model is low enough to be implemented in CFD codes. It is, however, not clear if this is also the case for simulations involving many droplets.

3.2.3 Evaporation model in this work

The evaporation model employed in this work is a modification of the model presented by Brenn et al. [110]. Their model is simple to implement, allows for the calculation of evaporation rates for individual species and is based on the well established model for single component evaporation by Abramzon and Sirignano [104]. At the same time the computational costs are low while the results are in good agreement with experimental data. The model by Brenn et al. [110] is listed in full in appendix E. In this section only the modifications will be discussed.

Brenn et al. [110] determine the evaporation rate for each component as if the liquid consists of just a single component. The rates are then multiplied by a volume equivalent partial radius, $r_{V,A}$, which corresponds to the volume fraction of the component for which the evaporation rate is calculated. They found a relation of $r_{V,A} = 0.5 D_l \psi_A^{1/3}$ to give a good agreement with experimental data, where D_l is the droplet diameter and ψ_A the volume fraction of component A in the liquid mixture. It is a scaling factor for the surface area of the droplet that can be interpreted as the reduction in surface area coverage by component A due to the presence of other components at the surface of the droplet. For the current application mass transfer from the liquid to the gas phase is provided by both evaporation and decomposition. Consequently, the relation found by Brenn et al. [110] probably does not hold. In fact it can be expected that a single relation for $r_{V,A}$ for both components is not possible since decomposition consumes peroxide and produces water. For this reason a relation for each component separately will be determined based on experimental results.

The multicomponent Spalding mass transfer number is defined by Brenn et al. [110] by

$$\mathsf{B}_{\mathsf{M}A} = \frac{Y_{A,s} - Y_{A,\infty}}{1 - Y_{A,s}}. \tag{3.38}$$

For a liquid temperature equal to the boiling point $\mathsf{B}_{\mathsf{M}A}$ stays finite as $0 < Y_{A,s} < 1$. In the single component droplet evaporation model of Abramzon and Sirignano [104] on which the model by Brenn et al. [110] was based, the B_{M} tends to infinity when the temperature reaches the boiling point. In this way enough liquid is evaporated to ensure that the temperature never exceeds the boiling point. With the Spalding mass transfer number defined as in equation 3.38 evaporation will not be enough to consume all the energy and the liquid temperature will increase to unphysically high temperatures. Because Brenn et al. [110] validated their model only for temperatures well below the boiling point,

this problem was not apparent. In this work B_{MA} is redefined as

$$\mathsf{B}_{MA} = \frac{Y_{A,s} - Y_{A,\infty}}{1 - \sum_A Y_{A,s}}. \tag{3.39}$$

When the liquid mixture approaches the boiling point $\sum_\alpha Y_{\alpha,s} \to 1$ and consequently $\mathsf{B}_{M,\alpha} \to \infty$. This ensures correct behaviour at and close to the boiling point.
The heat transfer model between the gas and liquid phase as presented by Brenn et al. [110] is replaced by a model proposed by Miller et al. [102], who based their model on the Langmuir-Knudsen non-equilibrium evaporation law. It is defined as

$$\dot{h}_l = G\pi D_d k_g \mathsf{Nu}^*(T_g - T_l) + \sum_A \Delta H_{fg,A} \dot{m}_A^{evap}, \tag{3.40}$$

where k_g is the thermal conductivity of the gas and m_l the mass of the droplet. Note that k_g is calculated as $k_g = \sum_A Y_A k_{A,g}$ and the modified Nusselt number Nu^* as $\mathsf{Nu}^* = \sum_A Y_A \mathsf{Nu}_A^*$. The droplet diameter is chosen such that the surface area equals the gas-liquid interfacial area as calculated by the interfacial area model; see next chapter. The modified Nusselt number for each component is calculated in the same way as proposed by Brenn et al. [110], see appendix E. The parameter G accounts for the heat transfer reduction due to evaporation as is given by

$$G = \frac{\beta_r}{e^{\beta_r} - 1}, \tag{3.41}$$

where β_r is defined as

$$\beta_r = \frac{-c_p}{2\pi D_d} \cdot \sum_A \left| \dot{m}_A^{evap} \right|. \tag{3.42}$$

It is the analytical solution to the Langmuir-Knudsen evaporation law and was derived by Bellan and Summerfield [113].
The model describes the evaporation of a single droplet. As the droplet diameter D_l is based on the gas-liquid interfacial area in a control volume, the unit for $\dot{m}^{evap}$ is in $kg\,s^{-1}$ per unit control volume. Multiplying this by the number of control volumes per m^3, $\overline{n}$, gives the correct unit for the evaporative component mass source term

$$S_{A\alpha}^{evap} = \dot{m}_{A,\alpha}^{evap} \overline{n}. \tag{3.43}$$

The phasic mass source term for evaporation is then calculated by

$$\Gamma_\alpha^{evap} = \sum_A S_{A\alpha}^{evap}. \tag{3.44}$$

Note that the driving force of first term on the RHS of equation 3.40 is the temperature difference between the fluid phases, while the driving force of the last term of equation 3.40 is the evaporation

rate. For the source terms defined in the previous section (see equation 2.14) this means that

$$h_{i,\alpha} = \sum_A \Delta H_{lg,A}, \tag{3.45}$$

$$Q_{i,\alpha} = G\pi D_d k_g \mathrm{Nu}^*(T_g - T_l)\overline{n},. \tag{3.46}$$

3.3 Fluid Interaction with the Catalyst Bed

The interfacial friction is normally determined as a function of the relative velocity between the phases, the interfacial area and the drag coefficient [50]. The interfacial area and the drag coefficient are dependent on the volume fraction and the type of flow. In the system under consideration the gas volume fraction changes from zero to one and consequently the flow type and drag coefficient changes. The situation is further complicated by the presence of catalyst pellets in the catalyst bed. For this reason, rather than developing a model from first principles, an empirical model will be employed.

Phenomenological and empirical pressure drop models for two-phase flows in packed beds have successfully been applied in the past in the chemical reactor engineering and nuclear safety analyses. An overview of pressure drop models used in the chemical reactor engineering together with the flow conditions and pressure range for which these models have been developed is given by Al-Dahhan et al. [114]. Typical examples of pressure drop models used in nuclear safety analyses are those developed by Tung and Dhir [115] and Schmidt [38]. All these models have in common that they have been developed for mass fluxes ranging from $O(-3)\,kg\,m^{-2}\,s^{-1}$ up to about $O(1)\,kg\,m^{-2}\,s^{-1}$ while the mass flux range of interest is from about 50 to $300 kg\,m^{-2}\,s^{-1}$ and higher [116]. As will be shown below, this difference in mass flux is important, because the mass flux determines the Reynolds number and the pressure drop over the catalyst bed is directly dependent on the Reynolds number.

Zeigarnik and Kalmykov [117] developed a pressure drop model for two-phase boiling flow in packed beds for mass fluxes up to $27 kg\,m^{-2}\,s^{-1}$. The model is based on a correlation for pressure drop for two-phase flows in pipes developed by Lockhart and Martinelli [118]. They introduced a dimensionless number, now known as the Lockart-Martinelli parameter χ, defined as

$$\chi = \sqrt{\left(\frac{\Delta p}{L}\right)_l \Big/ \left(\frac{\Delta p}{L}\right)_g}, \tag{3.47}$$

where L is the length of the catalyst bed. Lockhart and Martinelli [118] further postulated that, for a two-phase flow in a pipe, the pressure drop of the two-phase mixture is a function of the pressure drop experienced if only one phase was present in the pipe. They expressed it as

$$\left(\frac{\Delta p}{L}\right)_m = \left(\frac{\Delta p}{L}\right)_\alpha \Psi_\alpha^2. \tag{3.48}$$

Ψ is a so-called two-phase multiplier. Lockhart and Martinelli showed that the parameters χ and Ψ_α are correlated, but could not establish what this correlation was. Chisholm [119] derived this correlation semi-theoretically, but stated it was far too complicated from an engineering point of view and therefore proposed a much simpler one defined as

$$\Psi_l^2 = 1 + \frac{C}{\chi} + \frac{1}{\chi^2}, \tag{3.49}$$

$$\Psi_g^2 = 1 + C \cdot \chi + \chi^2. \tag{3.50}$$

C is the Chisholm constant for which the value is dependent on whether the phases are laminar or turbulent. The values are listed in table 3.4.

Zeigarnik and Kalmykov [117] used this model for boiling two-phase flows in packed beds. The

liquid/gas regime	**Chisholm constant**
turbulent/turbulent flow	20
viscous/turbulent flow	12
turbulent/viscous flow	10
viscous/viscous flow	5

Table 3.4: *Chisholm constants for different liquid/gas flow states*

pressure drop of each phase was modelled with the Ergun equation, normally employed for single phase flows in packed beds [66] and given by

$$\left(\frac{\Delta p}{L}\right)_\alpha = K\mu_\alpha u_{0,\alpha} + \eta\rho_\alpha u_{0,\alpha}^2. \tag{3.51}$$

In this equation μ is the dynamic viscosity and u_0 the superficial velocity related to the true velocity by $u_0 = \varepsilon_f u$ [66]. K and η are sometimes called the permeability and passability respectively [120] and are defined as

$$K = \frac{150}{D_p^2}\frac{\varepsilon_s^2}{(1-\varepsilon_s)^3}, \tag{3.52}$$

$$\eta = \frac{7}{4D_p}\frac{\varepsilon_s}{(1-\varepsilon_s)^3}, . \tag{3.53}$$

A relation for the Chisholm constant was developed by Zeigarnik and Kalmykov [117] and given by

$$C = 4\left(\frac{\eta\rho_l}{Kj\mu_l}\right)^{0.4}, \tag{3.54}$$

where j is the mass flux.

Unfortunately, they did not give any rationale behind this relation other than that it fitted well with experimental data. Sorokin [121] generalised the pressure drop model to one suitable for general

two-phase flows in pebble beds. For this purpose the Chisholm constant was redefined as

$$C = \left(\frac{\eta \rho_l \sigma}{K j \mu_l D_p} \right)^{0.3}, \tag{3.55}$$

and compared with experimental data for mass fluxes up to 27 $kg\,m^{-2}\,s^{-1}$. This showed a good agreement between experimental data and numerical results for mass fluxes up to 17 $kg\,m^{-2}\,s^{-1}$ and a slight overestimation for higher mass fluxes.

In this thesis the pressure drop model as formulated by Sorokin [121] will be used with one modification. The pressure drop for the single phase was modelled with the Ergun equation. But as was pointed out by Tallmadge [122] the Ergun equation is only valid for $10^{-1} < \mathrm{Re}_p < 10^3$ where Re_p is defined as $\mathrm{Re}_p = \rho u_0 d_p/(\mu \varepsilon_s)$. A typical pellet size is in the order of mm and together with the expected mass flux range this gives a Reynolds number for the liquid phase of order 2 and for the gas phase of order 4. Thus for the gas phase the Ergun equation is used outside its valid range. Tallmadge [122] proposed a modification to the Ergun equation to extend the range to $\mathrm{Re}_p < 10^5$ based on reviewing experimental data and given by

$$\left(\frac{\Delta p}{L} \right)_l = K \mu_l u_{0,l} + \eta \rho_l^{5/6} u_{0,l}^{11/6} \mu_l^{1/6}, \tag{3.56}$$

with η redefined as

$$\eta = \frac{4.2}{D_p^{7/6}} \frac{\varepsilon_s^{7/6}}{(1-\varepsilon_s)^3} \tag{3.57}$$

The source term $\mathbf{M}_{i,\alpha}$ as defined in equation 2.6 can now be written as

$$\mathbf{M}_{i,\alpha} = \left(\frac{\Delta p}{L} \right)_\alpha \tag{3.58}$$

The difference between the Ergun and Tallmadge pressure drop relation is best shown when both are written in non-dimensional form. This results in

$$\text{Ergun:} \qquad \frac{\Delta p}{\rho u_0^2} \frac{D_p}{L} \frac{(1-\varepsilon_s)^3}{\varepsilon_s} = \frac{150}{\mathrm{Re}_p} + \frac{7}{4} \tag{3.59}$$

$$\text{Tallmadge:} \qquad \frac{\Delta p}{\rho u_0^2} \frac{D_p}{L} \frac{(1-\varepsilon_s)^3}{\varepsilon_s} = \frac{150}{\mathrm{Re}_p} + \frac{4.2}{\mathrm{Re}_p^{1/6}}. \tag{3.60}$$

Both equations are plotted in figure 3.3 for the range in which they are valid. Also shown is the result for the Ergun equation when it is used outside its range. Up to a Reynolds number of about 10^3 both relations show more or less the same result. But for larger Reynolds numbers the Tallmadge equation predicts a lower pressure drop than the Ergun equation. Comparison with experimental data will have to show whether the Tallmadge equation gives indeed a better estimate of the pressure drop.

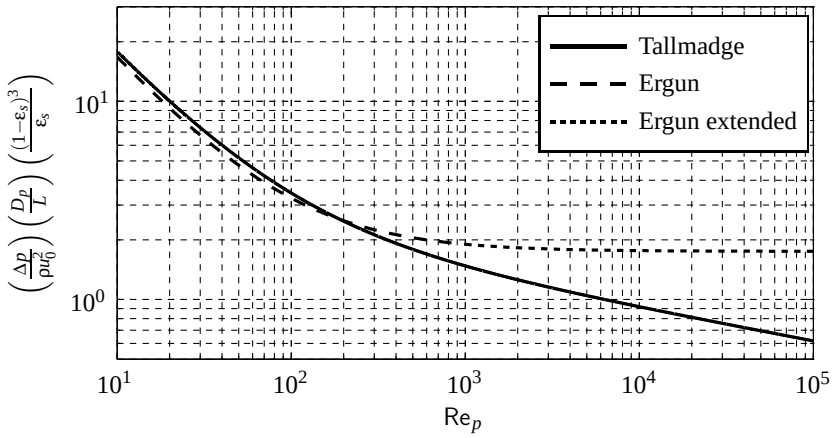

Figure 3.3: *Non-dimensional Ergun and Tallmadge equation*

Chapter 4

Simplifications and Numerical Implementation

The focus of this chapter is on the implementation of the model, as described in the previous two chapters, in order to solve it numerically. For this purpose first a number of simplifications to the model are described. It starts with a simplified description of the interfacial area in section 4.1 and continues in section 4.2 with an order of magnitude analysis to distill the most important terms in the equations as described in chapter 2. In this section also special implementation considerations are discussed. Section 4.4 presents the numerical scheme of the model. Many excellent textbooks have been published on the finite volume methods for CFD problems for example by Patankar [123], Versteeg and Malalasekera [124] and Ferziger and Perić [125] and therefore section 4.4 will only discuss those aspects which, in the present model, deviate from the standard textbooks. Finally, section 4.5 gives an overview of the sequence in which the equations are being solved.

4.1 Interfacial Area

To determine the total amount of catalytic decomposition and evaporation inside the catalyst bed, knowledge is required about the interfacial area between both fluids as well as between each fluid and the catalyst bed. Kocamustafaogullari and Ishii [126] derived a transport equation for the interfacial area concentration based on a fluid particle number density transport equation in which they assumed a dispersed flow of particles. They included descriptions of coalescence and break-up mechanisms applicable to laminar as well as turbulent flow. Hibiki and Ishii [127] developed later from this, what they called, two-group transport equations. The idea behind this model was that the particles can be categorised according their coalescence and break-up mechanism. These mechanisms are different between the two groups caused by the difference in size of the particles.

Morel et al. [128] derived their own interfacial area density model without any assumption on the size or form of the dispersed phase. They showed that, for spherical particles, the model is the same as the one by Kocamustafaogullari and Ishii [126]. Although the model developed by Morel et al. [128] is very rigourous, it is very difficult to implement in any CFD code for practical purposes [129].
Another approach was taken by Graf and Papadimitriou [130] who developed an interfacial area concentration transport equation from a momentum equation at the interphase and the differential of the particle radius. Contrary to the models discussed above, coalescence and break-up is not explicitly modelled, but a result from force interactions at the phase boundaries.
The models above are suited for two-phase flows in hollow pipes, but do not apply to two-phase flows in packed beds. Whitaker [131] derived the governing equations for immiscible two-phase flows in porous media. However, his model is based on Darcy's law and more suited for applications such as groundwater flows. No mass transport across phase boundaries is considered so there was no need to derive models for interfacial area transport.
No other models have been found in literature that give a description of the interfacial area for two-fluid flow in packed beds. For this reason a very simple interfacial area model has been derived based on the dimensions of the pellets and catalyst bed and the volume fractions of the phases. In this model the total surface area of the catalyst material is obtained by modelling the catalyst material as a long slender rod with a diameter equivalent to the diameter of the catalyst particle, D_p. The length of this rod, L_{rod}, is equal to the total volume of the catalyst material divided by the cross sectional area of the pellet

$$L_{rod} = \frac{\varepsilon_s V_{bed}}{\pi(0.5D_p)^2}. \tag{4.1}$$

The part of the rod that is covered with liquid, L_{wet}, is proportional to the ratio of the liquid volume fraction to the total void space in the catalyst bed. This can be expressed as

$$L_{wet} = \frac{\varepsilon_l}{\varepsilon_l + \varepsilon_g} L_{rod}. \tag{4.2}$$

The interfacial area of the liquid and the solid, A_{sl}, is now equal to the surface area of a cylinder with a diameter of D_p and a length of L_{wet}:

$$A_{sl} = \frac{4\varepsilon_l}{\varepsilon_l + \varepsilon_g} \frac{\varepsilon_s V_{bed}}{4} D_p. \tag{4.3}$$

The remainder of the rod is in contact with the gas phase of which the interfacial area, A_{sg}, can be obtained in a similar way:

$$A_{sg} = \frac{4\varepsilon_g}{\varepsilon_l + \varepsilon_g} \frac{\varepsilon_s V_{bed}}{D_p} \tag{4.4}$$

Evaporation is assumed to take place at the gas-liquid surface only, as indicated in figure 4.1. To determine the surface area it is assumed that the liquid around the wetted part of the rod is distributed homogeneously. The thickness, t_r, of the liquid layer is such that the volume of the liquid layer is

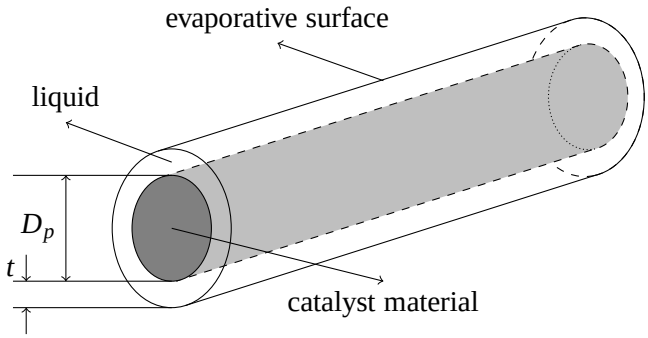

Figure 4.1: *Schematic representation of the liquid distribution around the rod*

equal to the total volume of liquid in the catalyst bed. After some rearrangement this can be written as

$$t_r = 0.5 D_p \left(\sqrt{\frac{1}{\varepsilon_s} - 1} \right). \tag{4.5}$$

The surface area, A_{lg}, can now be worked out and in combination with equation 4.3 it can be written as

$$A_{lg} = A_{sl} \sqrt{\frac{1}{\varepsilon_s}}. \tag{4.6}$$

In this model the end of each pellet is neglected in determining the total surface area of the catalyst material. This can partly be justified by the reduced amount of surface area that is available to both fluid phases at the point where two catalyst pellets touch each other. To assess the impact of errors in the estimate of the actual surface area that is available, a parametric study will be performed in chapter 6.

4.2 Problem Reduction

The system of equations presented in chapter 2 in combination with the source terms presented in the previous chapter is very complex to solve. For this reason the set of equations is simplified by considering only the most important terms. The first simplification that is made is that both phases share the same pressure field, $p_\alpha - p_{i,\alpha} = 0$ [130], and that the phase stresses and interfacial stresses are the same, $\boldsymbol{\tau}_\alpha - \boldsymbol{\tau}_{i,\alpha} = 0$ [132]. Further simplifications are obtained by non-dimensionalising the equations and subsequently performing an order of magnitude analysis.

4.2.1 Non-dimensional analysis

Different geometrical scales can be identified for the system under consideration. A catalyst bed is envisaged with typical dimensions similar to the catalyst beds presented by Palmer et al. [133] and

Pasini et al. [64]. Palmer et al. [133] developed an instrumented catalyst bed with a length of 104*mm* and a diameter of 16*mm*. This bed is slightly longer than the one presented by Pasini et al. [64] whose catalyst bed has a length of 60*mm*. The diameter is with 18*mm* almost similar. Both research groups use pellets as the supporting structure for the catalyst. Pasini et al. [64] use spherical catalyst pellets with a diameter of 0.6*mm* while Palmer et al. [133] use cylindrical pellets with a diameter of about 3*mm* and a length of about 4*mm*.

Changing the length of the catalyst bed will have an effect on the total pressure drop over the bed, see section 3.3. The corresponding change in pressure will result in slightly different boiling points. However, in the decomposition model there is no explicit dependency on pressure except for the change in concentration in the gas phase. A much larger influence can be expected from changing the equivalent pellet diameter D_{ps}, see appendix C, or the catalyst bed diameter. Changing either or both of these dimensions results in a different void fraction and total catalyst area per unit volume, which directly affects the amount of decomposition by catalysis, see equation 3.28, and evaporation, see equation 3.40, and the drag experienced by fluids, see equations 3.51 – 3.53. An appropriate length scale used for non-dimensionalising is therefore $D_{ps}/(1-\varepsilon_f)$ or, by using equation 2.15, D_{ps}/ε_s. For all other parameters the same approach for non-dimensionalising is followed as described in Bird et al. [66]. Table 4.1 shows how the parameters are non-dimensionalised, where the subscript 0 refers to reference conditions and the superscript $*$ to the non-dimensional form of the parameter. Note that the volume fraction ε and mass fractions Y are already non-dimensional and therefore do not require further treatment.

The non-dimensional continuity equation can now be written as

$$\frac{\partial \varepsilon_\alpha \rho_\alpha^*}{\partial t^*} + \nabla \cdot (\varepsilon_\alpha \rho_\alpha^* \mathbf{u}_\alpha^*) = \mathsf{Da}_{\mathsf{I}\alpha} \Gamma_\alpha^*, \tag{4.7}$$

Da_I is the first Damköhler number and is the ratio of the mass transfer rate due to decomposition and evaporation and the mass transfer rate by advection. Strictly speaking decomposition is occurring catalytically as well as thermally. The first type is a surface reaction while the second one is a volumetric reaction. In the case of surface reactions it is more appropriate to use the second Damköhler number defined as the ratio of the mass transfer rate due to decomposition and evaporation and the mass transfer rate by diffusion. However, as the dimension of the source term is in $kg\,m^{-3}\,s^{-1}$, any surface reaction has to be converted into a volumetric reaction and therefore the first Damköhler number is used. An overview of all the non-dimensional numbers used in this work and their definition is given in appendix F.

The non-dimensional form of the momentum equation is given by

$$\begin{aligned}\frac{\partial \varepsilon_\alpha \rho_\alpha^* \mathbf{u}_\alpha^*}{\partial t^*} + \nabla \cdot (\varepsilon_\alpha \rho_\alpha^* \mathbf{u}_\alpha^* \mathbf{u}_\alpha^*) = -A \cdot \varepsilon_\alpha \nabla p^* + \frac{1}{\mathsf{Re}_\alpha} \varepsilon_\alpha \nabla \cdot \boldsymbol{\tau}_\alpha^* + \frac{1}{\mathsf{Fr}_\alpha^2} \varepsilon_\alpha \rho_\alpha^* \mathbf{g}_\alpha^* \\ + \mathsf{Da}_{\mathsf{I}\alpha} \mathbf{u}_{i,\alpha}^* \Gamma_{i,\alpha}^* + \mathbf{M}_{i,\alpha}^*.\end{aligned} \tag{4.8}$$

parameter	unit	normalised
ρ	$kg\,m^{-3}$	$\rho^* = \frac{\rho}{\rho_0}$
$\mathbf{u}$	$m\,s^{-1}$	$\mathbf{u}^* = \frac{\mathbf{u}}{\mathbf{u}_0}$
D_p	m	$D_p^* = \frac{D_{ps}(1-\varepsilon_f)}{D_{ps,0}}$
t	s	$t^* = \frac{tu_0(1-\varepsilon_f)}{D_{ps,0}}$
$\mathbf{g}$	$m\,s^{-2}$	$\mathbf{g}^* = \frac{\mathbf{g}}{\mathbf{g}_0}$
p (incompressible)	$N\,m^{-2}$	$p^* = \frac{p}{\rho_0 u_0^2}$
p (compressible)	$N\,m^{-2}$	$p^* = \frac{p}{p_0}$
h	$J\,kg^{-1}$	$h^* = \frac{h}{h_0}$
k	$W\,m^{-1}\,K^{-1}$	$k^* = \frac{k}{k_0}$
c_p	$J\,kg^{-1}\,K^{-1}$	$c_p^* = \frac{c_p}{c_{p,0}}$
μ	$N\,s\,m^{-2}$	$\mu^* = \frac{\mu}{\mu_0}$
$\boldsymbol{\tau}$	$N\,m^{-2}$	$\boldsymbol{\tau}^* = \frac{\boldsymbol{\tau}}{\boldsymbol{\tau}_0}$
j	$kg\,m^{-2}\,s^{-1}$	$j^* = \frac{j}{j_0}$

Table 4.1: *Parameter normalisation*

The factor A is either 1, when the incompressible phase is considered, or Eu, when the compressible phase is considered, where Eu is the Euler number, which is the ratio of the static pressure to the dynamic pressure, $p/(\rho\mathbf{u}\mathbf{u})$. The reason for this difference is the way in which the pressure is non-dimensionalised as is shown in table 4.1. Re is the Reynolds number, defined as $\mathsf{Re} = \rho\mathbf{u}D_p/(\mu(1-\varepsilon_f))$.
The non-dimensional enthalpy equation can be written as

$$\begin{aligned}\frac{\partial \varepsilon_\alpha \rho_\alpha^* h_\alpha^*}{\partial t^*} + \nabla\cdot(\varepsilon_\alpha \rho_\alpha^* \mathbf{u}_\alpha^* h_\alpha^*) = \frac{1}{\mathsf{Re}_\alpha \mathsf{Pr}_\alpha}\nabla\cdot(\varepsilon_\alpha k_\alpha^* \nabla T_\alpha^*) + B\cdot\varepsilon_\alpha\frac{Dp^*}{Dt^*} + \frac{\mathsf{Ec}_\alpha}{\mathsf{Re}_\alpha}\varepsilon_\alpha \boldsymbol{\tau}_\alpha^* : \nabla\mathbf{u}_\alpha^* \\ + \mathsf{Da}_{\mathrm{I}\alpha}\, h_{i,\alpha}^*\Gamma_\alpha^* + \mathsf{Da}_{\mathrm{III}\alpha}\, Q_{i,\alpha}^* + \mathsf{Ec}_\alpha M_{i,\alpha}^*\cdot\left(\mathbf{u}_{i,\alpha}^* - \mathbf{u}_\alpha^*\right) \\ - \frac{\mathsf{Ec}_\alpha}{\mathsf{Re}_\alpha}\nabla\varepsilon_\alpha\cdot\boldsymbol{\tau}_{i,\alpha}^*\cdot\left(\mathbf{u}_{i,\alpha}^* - \mathbf{u}_\alpha^*\right).\end{aligned} \tag{4.9}$$

Here Pr is the Prandtl number, given by $c_p\mu/k$, and Ec the Eckert number, which is a ratio of the kinetic energy to the thermal energy $u^2/(c_pT)$. $\mathsf{Da}_{\mathrm{III}}$ is the third Damköhler number and is equivalent to Da_{I} except that energy is considered instead of mass: the ratio of the rate of heat generation due to decomposition and evaporation and the heat transfer rate by advection. The factor B is either Ec in case of incompressible flow or $(\gamma-1)\mathsf{Ma}^2$ in case of compressible flow. The reason is the same as

explained above for the momentum equation.
The non-dimensional version of the species equation is given by

$$\frac{\partial \varepsilon_\alpha \rho_\alpha^* Y_{A\alpha}}{\partial t^*} + \nabla \cdot (\varepsilon_\alpha \rho_\alpha^* \mathbf{u}_\alpha^* Y_{A\alpha}) = \frac{1}{\mathsf{Re}_\alpha \mathsf{Sc}_{A,\alpha}} \nabla \cdot (\varepsilon_\alpha j^*) + \mathsf{Da}_\mathsf{I} S_{A\alpha}^*, \tag{4.10}$$

where Sc is the Schmidt number, defined as $\mu/(\rho j)$. For simplicity it will be assumed that the order of magnitude of the Schmidt number for the multicomponent gas phase can be approximated by assuming that the gas phase consists of just two component. In that gas the Fickian diffusion coefficient can be used and the Schmidt number is then defined as $\mu/(\rho \mathcal{D})$.
Table 4.2 shows the order of magnitude of the variables as well as the resulting magnitude of the non-dimensional numbers. The first column gives an overview of the orders of magnitude for each variable. For some variables a range is given as the order changes with position in the catalyst bed. The order of magnitude of the pressure is based on an expected pressure of about 10bar, similar to Pasini et al. [64], and the temperature on standard atmospheric conditions and the maximum adiabatic decomposition temperature for 87.5% hydrogen peroxide of 965K as determined based on the data provided in appendix B. The velocities are based on a minimum inlet mass flux of $50 kg\, m^{-2}\, s^{-1}$. The second column shows the maximum order of magnitude for each non-dimensional number.
Applying the order of magnitude numbers to the non-dimensional conservation equations shows that for the momentum equation the stress term can be neglected as this is at least 4 order of magnitude smaller. It also shows that for the gas phase the first term on the RHS is the dominating term. Finally, body forces due to gravity, the third term in equation 4.8 will be ignored as the order of magnitude is -2 at most. As far as the enthalpy equation is concerned, all the terms containing viscous stresses can be safely ignored as the order of magnitude of Ec/Re is lower than -8. For the same reason the heat conduction term will be ignored as $1/\mathsf{RePr}$ is of order -4. Also the work due to interfacial drag term, $M_{i,\alpha}^* \cdot \left(\mathbf{u}_{i,\alpha}^* - \mathbf{u}_\alpha^*\right)$, will be ignored as its overall impact is small. According to the same reasoning also the third term on the RHS could be neglected as $\mathsf{Ma}^2 = O(-4)$ and $\mathsf{Ec}_l = O(-6)$. However, the term Dp^*/Dt^* can become very large during the first part of the transient simulation and for small time steps. This term will therefore be included in the simulations. Finally, the diffusion term in the species equation can be neglected as well as the second term on the RHS is much larger.
Due to the reduced number of terms the momentum, enthalpy and species conservation equations become much simpler. They can be written as respectively

$$\frac{\partial \varepsilon_\alpha \rho_\alpha \mathbf{u}_\alpha}{\partial t} + \nabla \cdot (\varepsilon_\alpha \rho_\alpha \mathbf{u}_\alpha \mathbf{u}_\alpha) = -\varepsilon_\alpha \nabla p_\alpha + \mathbf{u}_{i,\alpha} \Gamma_\alpha + \mathbf{M}_{i,\alpha}, \tag{4.11}$$

$$\frac{\partial \varepsilon_\alpha \rho_\alpha h_\alpha}{\partial t} + \nabla \cdot (\varepsilon_\alpha \rho_\alpha h_\alpha \mathbf{u}_\alpha) = \varepsilon_\alpha \frac{Dp}{Dt} + \Gamma_\alpha h_{i,\alpha} + Q_{i,\alpha}, \tag{4.12}$$

$$\frac{\partial \varepsilon_\alpha \rho_\alpha Y_{A\alpha}}{\partial t} + \nabla \cdot (\varepsilon_\alpha \rho_\alpha \mathbf{u}_\alpha Y_{A\alpha}) = S_{A\alpha}. \tag{4.13}$$

variable	max. magnitude
$c_p = O(3)$	$\mathsf{Da_I} = O(2)$
$d_p = O(-3)$	$\mathsf{Da_{III}} = O(2)$
$\mathcal{D}_{\alpha,g} = O(-5)$	$\mathsf{Ec}_g = O(-4)$
$\mathcal{D}_{\alpha,l} = O(-9)$	$\mathsf{Ec}_l = O(-6)$
$k_g = O(-2)$	$\mathsf{Eu}_g = O(4)$
$k_l = O(0)$	$\mathsf{Fr}_g = O(2)$
$\dot{r}_g = O(-22) - O(5)$	$\mathsf{Fr}_l = O(1)$
$\dot{r}_l = O(-2) - O(1)$	$\mathsf{Ma} = O(-2)$
$p = O(6)$	$\mathsf{Re}_g = O(4)$
$R = O(2)$	$\mathsf{Re}_l = O(4)$
$T_g = O(2) - O(3)$	$\mathsf{Pr}_g = O(0)$
$T_l = O(2)$	$\mathsf{Pr}_l = O(0)$
$\mathbf{u}_g = O(-1) - O(1)$	$\mathsf{Sc}_g = O(-1)$
$\mathbf{u}_l = O(-1) - O(0)$	$\mathsf{Sc}_l = O(-3)$
$\gamma = O(1)$	
$\mu_g = O(-5)$	
$\mu_l = O(-3)$	
$\rho_g = O(0) - O(1)$	
$\rho_l = O(3)$	

Table 4.2: *Order of magnitude of non-dimensional numbers*

The source terms Γ_α, $\mathbf{M}_{i,\alpha}$, $h_{i,\alpha}$, $Q_{i,alpha}$ and $S_{A\alpha}$ have been defined in the previous chapter, see equations 3.30, 3.31, 3.43, 3.44, 3.45, 3.46 and 3.58. Note that the phasic and component mass source terms Γ_α and $S_{A\alpha}$ consists of contributions from decomposition and evaporation and can be written as, respectively,

$$\Gamma_\alpha = \Gamma_\alpha^{dec} + \Gamma_\alpha^{evap} \tag{4.14}$$

$$S_{A\alpha} = S_{A\alpha}^{dec} + S_{A\alpha}^{evap}. \tag{4.15}$$

4.2.2 Special model considerations

To ensure that the problem is well-posed two situations require special attention: the behaviour of the equations when one of the volume fractions tends to zero and the bounding of the mass and volume fractions prior to achieving steady state. Both issues are discussed below.

Avoiding singularities

Oliveira and Issa [132] pointed out that, if the volume fractions of one of the phases tends to zero, the equations become singular. This is especially a problem for the momentum, enthalpy and species equations. They discarded the enthalpy equation and considered a single component flow only and mentioned that prior to reaching this limit the resulting velocities might show large fluctuations. It is inferred that the same sort of fluctuations can be expected for the temperature and mass fractions.
Oliveira and Issa [132] also devised a way to get around this problem. They start by rewriting the equation in non-conservative form. If an arbitrary equation for a variable ϕ is considered, the rewritten equation takes the form

$$\phi_\alpha \left(\frac{\partial \varepsilon_\alpha \rho_\alpha}{\partial t} + \nabla \cdot (\varepsilon_\alpha \rho_\alpha \mathbf{u}_\alpha) \right) + \varepsilon_\alpha \rho_\alpha \frac{D\phi_\alpha}{Dt} = S_{\phi_\alpha}. \tag{4.16}$$

The part between brackets is the same as the continuity equation. Oliveira and Issa [132] considered a two-phase flow without interfacial mass transfer and consequently this term is zero. In the current case the part between brackets should be replaced by the mass source term Γ_α. Now both sides can be divided by the volume fraction ε_α which after rewriting results in

$$\rho_\alpha \frac{D\phi_\alpha}{Dt} = \frac{S_{\phi_\alpha}}{\varepsilon_\alpha} - \frac{\phi_\alpha}{\varepsilon_\alpha} \Gamma_\alpha. \tag{4.17}$$

Note that both source terms are a function of the volume fraction and would tend to zero when the volume fraction goes to zero. Consequently, both terms tend to zero for $\varepsilon_\alpha \to 0$. In that case the equation is no longer singular and the variable ϕ reaches it termination value. This approach works only for a fluid that is vanishing and cannot be used for a fluid to be created. In that case ϕ and ε_α are initially zero, which results in a singular equation. Because the liquid volume fraction for the current application is expected to tend to zero, this approach will be applied to all equations except the continuity equation.

Bounding of mass and volume fractions

The mass and volume fractions are bounded; $0 \leq \varepsilon_\alpha \leq 1$ and $0 \leq Y_A \leq 1$. Furthermore, they are both subject to a constraint equation given by

$$\sum_n \phi_n = 1 \tag{4.18}$$

where n represents the number of components. For the volume fractions and liquid mass fractions $n = 2$ and for the gas mass fractions $n = 4$.
Patankar [123] showed that as long as the coefficients in the in the linearised algebraic equations are positive, the variable that is solved for is always positive. To ensure that ϕ_n is bounded by one, Carver

[134] devised an underrelaxation method where the underrelaxation factor becomes smaller when ϕ approaches one. The variable ϕ is solved for only one of the components, while the other one is found by applying the constraint equation, equation 4.18. However, in the method by Carver [134] the underrelaxation factor is always larger than zero and consequently does not necessarily guarantee an upper bound of one. Furthermore, although this approach might work for situations where $n = 2$, boundedness is not guaranteed for $n > 2$, as is the case for the gas phase.
A solution to this was presented by Oliveira and Issa [132]. In their method ϕ is solved for every component. To guarantee an upper bound they normalise ϕ as

$$\phi_n = \frac{\phi'_n}{\sum_n \phi'_n} \tag{4.19}$$

where $'$ indicates the initial solution of ϕ. When overall convergence is reached $\phi_n = \phi'_n$ and thus $\sum_n \phi'_n = 1$.

4.3 Final Set of Equations

Taking into account the points that were discussed in the previous section, a set of conservation equations can be written that is much simpler to solve and is more stable. The momentum conservation equation for phase α is given by

$$\rho_\alpha \frac{D\mathbf{u}_\alpha}{Dt} = -\nabla p + \frac{(\mathbf{u}_{i,\alpha} - \mathbf{u}_\alpha)\Gamma_\alpha + \mathbf{M}_{i,\alpha}}{\varepsilon_\alpha}, \tag{4.20}$$

and the enthalpy conservation equation by

$$\rho_\alpha \frac{Dh_\alpha}{Dt} = \frac{Dp}{Dt} + \frac{(h_{i,\alpha} - h_\alpha)\Gamma_\alpha + Q_{i,\alpha}}{\varepsilon_\alpha}. \tag{4.21}$$

The main difference with equations 2.9 and 2.14 is caused by ignoring the stress terms. The species conservation is given by

$$\rho_\alpha \frac{DY_A}{Dt} = \frac{S_A}{\varepsilon_\alpha} - \frac{Y_A}{\varepsilon_\alpha}\Gamma_\alpha. \tag{4.22}$$

which is solved for all species and then normalised according to equation 4.19. The continuity equation has not been simplified any further and remains the same as equation 2.2. The original set of conservation equations as presented in chapter 2 is now reduced to a simpler set of convection equations with a source term.

4.4 Discretisation Scheme

To solve the set of equations the finite volume method is employed [125]. For this purpose the domain is subdivided into small cells and for each of these cells the system of equations will be solved. Many different discretisation schemes have been developed in the past and some of the most used ones are presented and discussed by Ferziger and Perić [125]. In this thesis the upwind formulation will be used. In section 4.2 the simplifications led to a set of equations where mass, momentum and heat diffusion was neglected and only advection and source terms remained. This approach is further supported by considering the Péclet numbers for mass and heat diffusion which are defined as $\mathsf{Pe} = \mathsf{Re}\,\mathsf{Sc}$ and $\mathsf{Pe} = \mathsf{Re}\,\mathsf{Pr}$ respectively. The resulting order of magnitudes are shown in table 4.3.

This table shows that the flow under consideration is dominated by convection terms. For these types

Péclet number	**order**
Pe gas mass diffusion	$O(3)$
Pe liquid mass diffusion	$O(1)$
Pe gas heat diffusion	$O(4)$
Pe liquid heat diffusion	$O(4)$

Table 4.3: *Péclet numbers for mass and heat diffusion*

of flow the upwind discretisation scheme is most appropriate. In chapter 6 the validity of this approach will be further discussed. The details of the upwind formulation will be given in section 4.4.1.

As can be seen from equation 2.2 and equations 4.20 through 4.22 the set of conservation equations are coupled and cannot be solved independently from each other. Traditionally, coupled solvers, or density based methods, are used for high speed flows for shock capturing [135] and steep pressure gradients [136] and segregated solvers, or pressure based methods, are used for low speed flows [136]. Since for the envisaged inlet mass fluxes it is not expected that sonic or supersonic conditions will be reached, a segregated approach will be followed. The coupling between the conservation equations will be further discussed in section 4.4.2.

4.4.1 Upwind formulation and time integration

As stated in section 4.3 the equations that have to be solved are time dependent convection equations with a source term. For an arbitrary variable ϕ the generalised form of the equations that have to be solved can be expressed as

$$\rho_\alpha \frac{\partial \phi_\alpha}{\partial t} + \rho_\alpha \left(\mathbf{u}_\alpha \cdot \nabla \phi_\alpha\right) = B_\alpha, \tag{4.23}$$

where B is a general source terms representing the righthand side of any of equations 4.20 to 4.22. The implementation of the source term will be discussed in more detail in section 4.4.3. Equation 4.23

is in differential form. Because the finite volume method is employed, it should be written in integral form. For clarity, the flow in one direction only will be considered but it is applicable to any direction.

$$\int_t^{t+\Delta t}\int_V \rho_\alpha \frac{\partial \phi_\alpha}{\partial t}\,dV\,dt + \int_t^{t+\Delta t}\int_V \rho_\alpha u_\alpha \frac{\partial \phi_\alpha}{\partial x}\,dV\,dt \approx \int_t^{t+\Delta t}\int_V B_\alpha\,dV\,dt \tag{4.24}$$

As was explained above, a segregated approach will be used to solve the system of equations. That means that when equation 4.24 is solved for ϕ the other variables, ρ_α and u_α, remain constant during the evaluation. Taking into account the divergence theorem [137] equation 4.24 can now be rewritten as

$$\int_t^{t+\Delta t}\int_V \rho_\alpha \frac{\partial \phi_\alpha}{\partial t}\,dV\,dt + \int_t^{t+\Delta t}\left[\rho_\alpha u_\alpha \int_A \phi_\alpha\,dA\right] dt \approx \int_t^{t+\Delta t}\int_V B_\alpha\,dV\,dt. \tag{4.25}$$

If it is now assumed that the value of ϕ at the cell centre is a good measure for the average value of ϕ in the control volume then the first term on the lefthand side of equation 4.25 can be written as [124]

$$\int_t^{t+\Delta t}\int_V \rho_\alpha \frac{\partial \phi_\alpha}{\partial t}\,dV\,dt = \int_V \left[\int_t^{t+\Delta t} \rho_\alpha \frac{\partial \phi_\alpha}{\partial t}\,dt\right] dV \approx \rho_\alpha \left(\phi_{\alpha P} - {\phi_\alpha^{n-1}}_P\right)\Delta V\,\Delta t. \tag{4.26}$$

For the other terms integration over the control volume only results in

$$\int_t^{t+\Delta t}\left[\rho_\alpha u_\alpha \int_A \phi_\alpha\,dA\right] dt = \int_t^{t+\Delta t}\left[\rho_\alpha u_\alpha \left(\phi_{\alpha_e} A_e - \phi_{\alpha_w} A_w\right)\right] dt \tag{4.27}$$

$$\int_t^{t+\Delta t}\int_V B_\alpha\,dV\,dt = \int_t^{t+\Delta t} B_\alpha \Delta V\,dt. \tag{4.28}$$

The superscript $n-1$ in equation 4.26 refers to the value of ϕ from the previous outer loop iteration. The subscripts P, e and w in the above equations are defined as indicated in figure 4.2. It shows a one-dimensional grid with three nodes. A control volume is drawn around the centre node, node P, in such a way that P is in the centre of the control volume. The node left of P is indicated with W and right of P with E. All scalar variable are stored at these nodes. The face of the control volume between nodes P and W is indicated with a small w and the face between nodes P and E with a small e. The total width of the control volume is Δx. As an equisized grid is used all control volumes have the same width.

For the time integration on the right hand side of equations 4.27 and 4.28 a time integration scheme has to be chosen. Many different schemes have been developed, see for instance the scheme explained by Ferziger and Perić [125] and Versteeg and Malalasekera [124]. In this work a first order fully implicit time integration scheme is used as this scheme is unconditionally stable [124] as opposed to explicit or semi-implicit schemes. That means that the value for ϕ_{α_e} and ϕ_{α_w} is evaluated at time

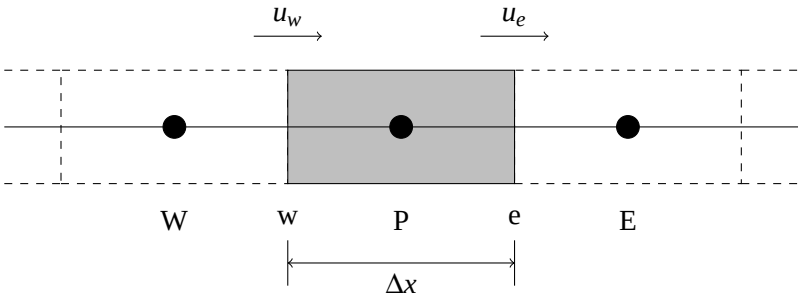

Figure 4.2: *Nodal point and face definition in a grid*

$t+\Delta t$. Equation 4.25 together with equations 4.26 through 4.28 can be written in discretised form as

$$\rho_\alpha \left(\phi_{\alpha P} - \phi_\alpha^{n-1}{}_P\right) \Delta V + \rho_\alpha u_\alpha \left(\phi_{\alpha_e} A_e - \phi_{\alpha_w} A_w\right) \Delta t \approx B_\alpha \Delta V \, \Delta t. \tag{4.29}$$

As the values of ϕ_α are stored at the nodes, values at the cell faces require interpolation. In the upwind scheme the interpolation is carried out by considering upstream nodes only. In this thesis only a simple upwind scheme is employed in which the face value is set equal to the value at the node upstream of the face. If a positive flow direction is defined as from left to right in figure 4.2, so $u_w > 0$ and $u_e > 0$, and a negative flow direction as a flow from right to left, $u_w < 0$ and $u_e < 0$, then the following holds

$$positive: \quad \phi_{\alpha_w} = \phi_{\alpha W} \qquad \phi_{\alpha_e} = \phi_{\alpha P} \tag{4.30}$$

$$negative: \quad \phi_{\alpha_w} = \phi_{\alpha P} \qquad \phi_{\alpha_e} = \phi_{\alpha E}. \tag{4.31}$$

For a flow in positive direction equation 4.29 can, after rearranging, be written as

$$\left(\rho_\alpha \frac{\Delta V}{\Delta t} + \rho_\alpha u_\alpha A_e\right) \phi_{\alpha P} \approx \rho_\alpha u_\alpha A_w \phi_{\alpha W} + \rho_\alpha \phi_\alpha^{n-1}{}_P \frac{\Delta V}{\Delta t} + B_\alpha \Delta V, \tag{4.32}$$

and for a flow in a negative direction as

$$\left(\rho_\alpha \frac{\Delta V}{\Delta t} + \rho_\alpha u_\alpha A_w\right) \phi_{\alpha P} \approx \rho_\alpha u_\alpha A_e \phi_{\alpha E} + \rho_\alpha \phi_\alpha^{n-1}{}_P \frac{\Delta V}{\Delta t} + B_\alpha \Delta V. \tag{4.33}$$

Both equations can be written in a more compact form that is more suited for implementation in a computer code

$$a_{\alpha P} \phi_{\alpha P} \approx a_{\alpha W} \phi_{\alpha W} + a_{\alpha E} \phi_{\alpha E} + \rho_\alpha \phi_\alpha^{n-1}{}_P \frac{\Delta V}{\Delta t} + B_\alpha \Delta V, \tag{4.34}$$

where a are the coefficients defined as

$$a_{\alpha W} = \max\left(0, \rho_\alpha u_\alpha A_w\right) \tag{4.35}$$

$$a_{\alpha E} = \max\left(0, -\rho_\alpha u_\alpha A_e\right) \tag{4.36}$$

$$a_{\alpha P} = a_{\alpha W} + a_{\alpha E} + \rho_\alpha u_\alpha \left(A_e - A_w\right) + \rho_\alpha \frac{\Delta V}{\Delta t}. \tag{4.37}$$

Because a two-fluid model is employed, the upwind formulation as written above should be applied to each fluid separately.

4.4.2 Pressure-velocity-density coupling

To avoid a checker-board pressure field as a solution of the equations [123–125] a back staggered grid configuration is used where all the scalars are stored at the nodes in the centre of the control volume and all velocities at the cell faces. To facilitate the discussion on the pressure-velocity-density coupling the notation as indicated in figure 4.3 will be used. The main grid is indicated with solid lines while the back staggered grid is indicated with dashed lines. For readability the back staggered grid is drawn under the main grid, but they should be thought of as positioned on top of each other. Locations indicated with a capital letter I designate the location of the centre of the control volume of the main grid. Those indicated with a small letter i designate the centre of the control volume of the back staggered grid.

The coupling between the pressure, velocity and density is based on the SIMPLE*-algorithm [123]

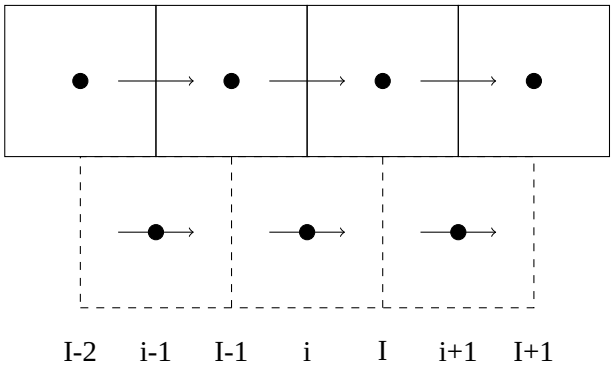

Figure 4.3: *Staggered grid arrangement and notation*

extended to multiphase flows. For incompressible as well as compressible flows a SIMPLE-algorithm was derived by Moukalled et al. [138], who provided a version based on mass conservation and on volume conservation. The first step in the mass conservation based SIMPLE-algorithm is to solve the momentum equation based on a guessed pressure field, p^*, and corresponding density field for the compressible (gas) phase, ρ_g^*. Assuming a flow with a positive velocity, the discretised momentum

*Semi Implicit Method for Pressure-Linked Equations

equations that have to be solved can then be written as [124]

$$a_{\alpha i} u^*_{\alpha i} = \sum_{nb} a_{\alpha nb} u^*_{\alpha nb} + \left(p^*_{I-1} - p^*_I\right) A_i + b_{\alpha,i}, \tag{4.38}$$

where the subscript nb refers to the values at the neighbouring nodes and b_i contain all the other terms. u^*_α is the result from a guessed pressure field and thus indicated with $*$. u^*_α will satisfy the momentum equations for both fluids but in general not the continuity equations.
The difference between the guessed values and the true values can be obtained by subtracting equation 4.38 from the discretised momentum equation with the true values. This results in

$$a_{\alpha i} u'_{\alpha i} = \sum_{nb} a_{\alpha nb} u'_{\alpha nb} + \left(p'_{I-1} - p'_I\right) A_i. \tag{4.39}$$

The primed values are the corrections to the guessed values and defined as

$$p' = p - p^* \qquad u'_\alpha = u_\alpha - u^*_\alpha \qquad \rho'_g = \rho_g - \rho^*_g. \tag{4.40}$$

The term $b_{\alpha,i}$ is the same for a guessed pressure field and the true pressure field and therefore cancels after subtraction. Note that in the momentum equation as presented in equation 4.20 an additional term is present which has the velocity as a variable. In equations 4.38 and 4.39 the velocity correction to this term has been ignored and assumed to stay constant during the time step. As long as the simulations converge this is justified as at convergence the corrections are zero by definition.
The main approximation in the SIMPLE-algorithm is to ignore the velocity correction for the neighbouring nodes to simplify equation 4.39. The velocity correction equation can then be written as

$$u'_{\alpha i} = d_{\alpha,i} \left(p'_{I-1} - p'_I\right), \tag{4.41}$$

where $d_{\alpha,i}$ is defined as

$$d_{\alpha,i} = \frac{A_i}{a_{\alpha i}} \tag{4.42}$$

The SIMPLE-algorithm for multiphase flows as derived by Moukalled et al. [138] considers mass conservation over both phases instead of mass conservation for each individual phase. The discretised form of global mass conservation can be written as

$$\sum_\alpha \left(\varepsilon_{\alpha,I} \rho_{\alpha,I} - \varepsilon^{n-1}_{\alpha,I} \rho^{n-1}_{\alpha,I}\right) \frac{\Delta V}{\Delta t} + \sum_\alpha \left(\varepsilon_{\alpha,i+1} \rho_{\alpha,i+1} u_{\alpha,i+1} A_{i+1} - \varepsilon_{\alpha,i} \rho_{\alpha,i} u_{\alpha,i} A_i\right) = 0. \tag{4.43}$$

Note that the sum over all phases of the source term is 0 according to equation 2.3. Although the liquid phase is considered to be incompressible, the density can still change between time steps as the liquid density is dependent on both the relative amount of each constituent in the liquid and the temperature. Both can/will change during the simulation.
The next step is to replace ρ_α and u_α by $\rho^*_\alpha + \rho'_\alpha$ and $u^*_\alpha + u'_\alpha$ respectively. Note that despite the liquid

density can change between time steps, it is still an incompressible liquid so the correction to the liquid density within the timestep is $\rho'_l = 0$ Equation 4.43 can then be written as

$$\begin{aligned}&\sum_{\alpha}\left(\varepsilon_{\alpha,I}\left(\rho^*_{\alpha,I}+\rho'_{\alpha,I}\right)-\varepsilon^{n-1}_{\alpha,I}\rho^{n-1}_{\alpha,I}\right)\frac{\Delta V}{\Delta t}\\&+\sum_{\alpha}\left(\varepsilon_{\alpha,i+1}\left(\rho^*_{\alpha,i+1}+\rho'_{\alpha,i+1}\right)\left(u^*_{\alpha,i+1}+u'_{\alpha,i+1}\right)A_{i+1}\right.\\&\left.-\varepsilon_{\alpha,i}\left(\rho^*_{\alpha,i}+\rho'_{\alpha,i}\right)\left(u^*_{\alpha,i}+u'_{\alpha,i}\right)A_i\right)=0.\end{aligned} \tag{4.44}$$

This equation can be grouped in a part containing ρ^* and u^* only and in a part containing the other terms. Although not explicitly mentioned in the work of Moukalled et al. [138] it will be further assumed that the product of 2 corrections is so small that it can be neglected, so

$$\left(\rho^*_g+\rho'_g\right)\left(u^*_g+u'_g\right)\approx\rho^*_g u^*_g+\rho'_g u^*_g+\rho^*_g u'_g. \tag{4.45}$$

Equation 4.45 is only applicable to the gas phase as only this phase is compressible. The first part of equation 4.44, designated as B_S, can now be written as

$$B_S=\sum_{\alpha}\left(\varepsilon_{\alpha,I}\rho^*_{\alpha,I}-\varepsilon^{n-1}_{\alpha,I}\rho^{n-1}_{\alpha,I}\right)\frac{\Delta V}{\Delta t}+\sum_{\alpha}\left(\varepsilon_{\alpha,i+1}\rho^*_{\alpha,i+1}u^*_{\alpha,i+1}A_{i+1}-\varepsilon_{\alpha,i}\rho^*_{\alpha,i}u^*_{\alpha,i}A_i\right). \tag{4.46}$$

In this equation ρ^*_α is the result of the guessed pressure field in case of the gas density, or the result of the composition of the liquid and the temperature in case of the liquid density. u^*_α is the result from the solution of equation 4.38 which was based on a guessed pressure field. By writing equation 4.44 explicitly in terms of gas and liquid variables and substituting equations 4.45 and 4.46 into it, the following result is obtained

$$\begin{aligned}&\varepsilon_{g,I}\rho'_{g,I}\frac{\Delta V}{\Delta t}+\left(\varepsilon_{g,i+1}\rho'_{g,i+1}u^*_{g,i+1}+\varepsilon_{g,i+1}\rho^*_{g,i+1}u'_{g,i+1}+\varepsilon_{l,i+1}\rho^*_{l,i+1}u'_{l,i+1}\right)A_{i+1}\\&\qquad-\left(\varepsilon_{g,i}\rho'_{g,i}u^*_{g,i}+\varepsilon_{g,i}\rho^*_{g,i}u'_{g,i}-\varepsilon_{l,i}\rho^*_{l,i}u'_{l,i}\right)A_i=-B_S.\end{aligned} \tag{4.47}$$

Assuming that the gas phase behaves like an ideal gas, ρ'_g can be replaced by p'/RT_g and u'_α by equation 4.42. This gives

$$\begin{aligned}&\varepsilon_{g,I}\frac{p'_I}{RT_I}\frac{\Delta V}{\Delta t}+\left(\varepsilon_{g,i+1}\frac{p'_{i+1}}{RT_{i+1}}u^*_{g,i+1}+\varepsilon_{g,i+1}\rho^*_{g,i+1}d_{g,i+1}\left(p'_I-p'_{I+1}\right)\right.\\&\left.+\varepsilon_{l,i+1}\rho^*_{l,i+1}d_{l,i+1}\left(p'_I-p'_{I+1}\right)\right)A_{i+1}\\&-\left(\varepsilon_{g,i}\frac{p'_i}{RT_i}u^*_{g,i}+\varepsilon_{g,i}\rho^*_{g,i}d_{g,i}\left(p'_{I-1}-p'_I\right)+\varepsilon_{l,i}\rho^*_{l,i}d_{l,i}\left(p'_{I-1}-p'_I\right)\right)A_i=-B_S\end{aligned} \tag{4.48}$$

The only unknowns in this equation are the pressure corrections p'. All other variables are either known or estimated. Values for scalars on the cell faces are obtained by linear interpolation between

the nodes. The upwinding scheme as discussed in section 4.4.1 is used to obtain the value for p'_i. By grouping all the pressure correction terms equation 4.48 can be written as

$$\begin{aligned}
&\left[\frac{1}{RT_I}\frac{\Delta V}{\Delta t} + \max\left(u^*_{g,i+1},0\right)\frac{\varepsilon_{g,i+1}A_{i+1}}{RT_{i+1}} + \max\left(-u^*_{g,i},0\right)\frac{\varepsilon_{g,i}A_i}{RT_i}\right.\\
&\quad + \left(\varepsilon_{g,i+1}\rho^*_{g,i+1}d_{g,i+1} + \varepsilon_{l,i+1}\rho^*_{l,i+1}d_{l,i+1}\right)A_{i+1}\\
&\quad\left. + \left(\varepsilon_{g,i}\rho^*_{g,i}d_{g,i} + \varepsilon_{l,i}\rho^*_{l,i}d_{l,i}\right)A_i\right]p'_I = \left[\max\left(-u^*_{g,i+1},0\right)\frac{\varepsilon_{g,i+1}}{RT_{i+1}} + \varepsilon_{g,i+1}\rho^*_{g,i+1}d_{g,i+1}\right.\\
&\qquad\left. + \varepsilon_{l,i+1}\rho^*_{l,i+1}d_{l,i+1}\right]A_{i+1}p_{I+1} + \left[\max\left(u^*_{g,i},0\right)\frac{\varepsilon_{g,i}}{RT_i} + \varepsilon_{g,i}\rho^*_{g,i}d_{g,i} + \varepsilon_{l,i}\rho^*_{l,i}d_{l,i}\right]A_i p_{I-1} - B_S.
\end{aligned} \tag{4.49}$$

Equation 4.49 is the pressure correction equation for multiphase flows. Solving this equation and substituting the result in equation 4.40 gives an updated value for p, u_α and ρ_g which is closer to the real value. This procedure is repeated a couple of times and once the value do not change anymore, the solution has converged and the updated values are equal to the real values.

4.4.3 Implementation of source terms

The mass source terms which have been described in the previous chapter are given as a function of mass fractions and temperature and therefore are generally nonlinear. To implement them in a finite volume formulation linearisation is required. The simplest way of doing that is to write the source term B, which was introduced in equation 4.23, as

$$B_\alpha = B_{\alpha C} + B_{\alpha P}\phi_{\alpha P}, \tag{4.50}$$

where $B_{\alpha C}$ is the constant part of the source term and $B_{\alpha P}$ the coefficient of the variable $\phi_{\alpha P}$. Substituting this into equation 4.34 and rearranging the terms results in

$$a_{\alpha P}\phi_{\alpha P} = a_{\alpha W}\phi_{\alpha W} + a_{\alpha E}\phi_{\alpha E} + \rho_\alpha {\phi^{n-1}_\alpha}_P\frac{\Delta V}{\Delta t} + B_{\alpha C}\Delta V, \tag{4.51}$$

with $a_{\alpha P}$ redefined as

$$a_{\alpha P} = a_{\alpha W} + a_{\alpha E} + \rho_\alpha u_\alpha\left(A_e - A_w\right) + \rho_\alpha\frac{\Delta V}{\Delta t} - B_{\alpha P}\Delta V. \tag{4.52}$$

Patankar [123] stated that for an algorithm to be stable one of the requirements is that all the coefficients should stay positive throughout the simulation. Consequently, the requirement for the source term is that $B_{\alpha C} > 0$ and $B_{\alpha P} < 0$. For the code developed in this work this is implemented in the

following way

$$B_{\alpha C} = \begin{cases} B_\alpha & \text{for} \quad B_\alpha \geq 0 \\ 0 & \text{for} \quad B_\alpha < 0 \end{cases} \tag{4.53}$$

$$B_{\alpha P} = \begin{cases} 0 & \text{for} \quad B_\alpha \geq 0 \\ \frac{B_\alpha}{\phi_{\alpha P}} & \text{for} \quad B_\alpha < 0 \end{cases} \tag{4.54}$$

The reason for dividing by $\phi_{\alpha P}$ in equation 4.54 is that the source term B_α is dependent in a complicated way on $\phi_{\alpha P}$ which prohibits the possibility to write it as the product of $\phi_{\alpha P}$ and a coefficient not containing $\phi_{\alpha P}$.

4.5 Calculation Sequence

The order in which the equations are solved is schematically shown in figure 4.4. To enhance the stability further underrelaxation is applied to each variable (see appendix G for an explanation of underrelaxation). The temperature for each phase is determined from the enthalpy by means of the secant algorithm [139].

MATLAB is used as platform to solve the equations. Two codes have been used to simulate the decomposing flow of hydrogen peroxide through the catalyst bed and are discussed in Chapter 5 and 6. Chapter 5 discusses a model that does not have any spatial discretisation. It has been derived from an existing in-house code and was used to become familiar with the equations that have to be solved. Further simplifications were made for this model, which will be further explained in the next chapter. Chapter 6 presents the simulations of the equations developed in this chapter when only one dimension is considered. No further simplifications have been made then discussed in this section.

The models are suited for single core computations only. As will become clear in subsequent chapters a large number of parameter sweeps will be performed. To solve this embarrassingly parallel problem Iridis3, the supercomputer of the University of Southampton, will be used [140].

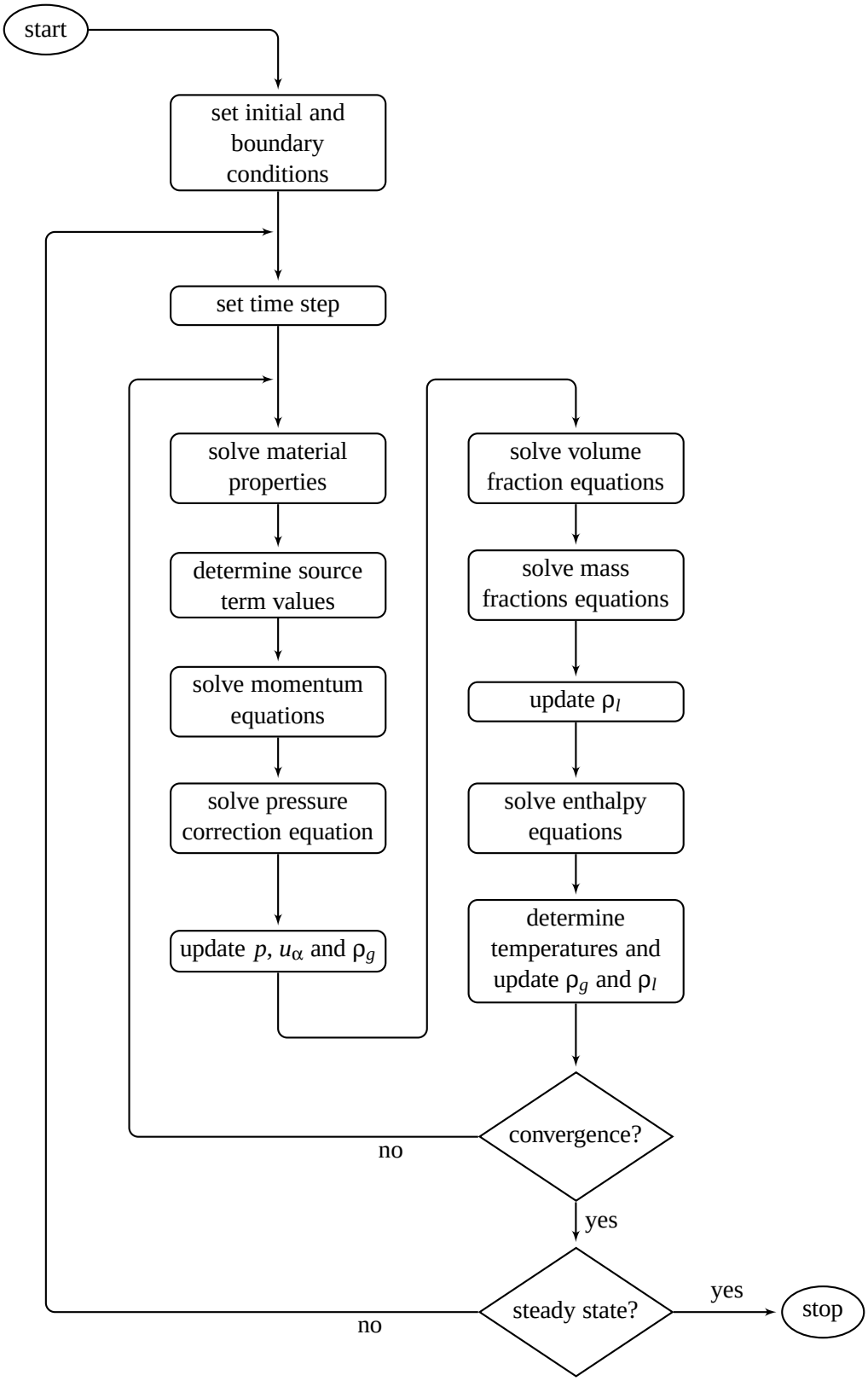

Figure 4.4: *Flow sequence of the solution procedure*

Chapter 5

On the Shape and Size of Catalyst Pellets

The aim of this chapter is to investigate the influence of the pellet shape and size on the catalyst bed performance. The performance will be measured in terms of catalyst bed length and pressure drop over the catalyst bed. To investigate the performance a simple model has been developed. The outline of this model is discussed in the next section. The basic equations for this model have been discussed in the previous three chapters, however, a couple of further simplifications are made which will be discussed in this section as well. In section 5.2 the simple flow model is validated against experimental data. Section 5.3 assesses two basic assumptions and show the influence they have on the overall result. With the validated model the shape and size of catalyst pellets will be investigated in section 5.4. Finally, in section 5.5 possible radial effects will be discussed.

5.1 A Simple Flow Model

5.1.1 General features

The purpose of the current model is to perform parametric studies on pellet shapes and sizes and investigate the influence this has on the pressure drop. Johnson et al. [60] showed that even a model consisting of two control volumes with variable sizes can give a good qualitative insight into the factors that are important for the pressure drop over the bed. A significant advantage of such an approach is that it is computationally far less expensive than employing a one-dimensional model.
The pressure drop over the catalyst bed is dependent on the velocity and density and thus indirectly on the temperature as can be seen from the model used by Pasini et al. [64]. As was pointed out above there is a large difference in density and temperature between the phases. These differences will be averaged out when employing a mixture model and for this reason a two-fluid model will be used in which every phase is described separately.

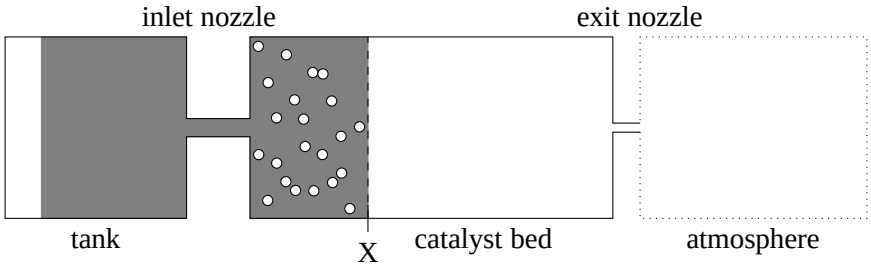

Figure 5.1: *Schematic representation of the flow model*

The current model is derived from a two-fluid model with no spatial discretisation presented by Ju et al. [141], who used it to describe the flow of a multicomponent flashing but non-reacting propellant through a medical metered dose inhaler. This model, of which a schematic is shown in figure 5.1, contains a reservoir (tank), which contains a fixed mass of volatile liquid and vapour, and an expansion chamber (catalyst bed), where the liquid flashes. An inlet nozzle provides the link between the reservoir and the expansion chamber and an exit nozzle consisting of a converging section only provides the link between the expansion chamber and the atmosphere. A common feature of the present model and that of Ju et al. [141] is that mass and energy are conserved within the tank and bed through internal changes within each volume. In contrast to the model of Ju et al. [141] for momentum conservation the catalyst bed is split into a part containing a mix of liquid and gas situated adjacent to the injector and a part further downstream where liquid is no longer present. The pressure drop over each of these parts is determined separately and subsequently combined to give the overall pressure drop. The interface between these two parts is designated as plane X as shown in figure 5.1. The distance from the injector to this plane is assumed to be dependent on the residence time of the liquid and the contact time of the liquid with the catalyst material and thus similar to the approach by Johnson et al. [60]. The reference location of plane X will be determined experimentally, see section 5.2. Further differences from the Ju et al. [141] model are that the fluid phases are multicomponent, a third phase is introduced in the catalyst bed representing the solid catalyst material, there is momentum transfer between the catalyst bed and the fluid phases and mass transfer between the fluid phases is described by chemical reactions and evaporation.

5.1.2 Simplifying assumptions

The equations that are being solved in this model are the same as discussed in chapters 2, 3 and 4, with a couple of exceptions. The first simplification is that the compressibility in the energy equation, Dp/Dt term in equation 4.21, is not taken into account. This is not a problem as this model is only used for steady state calculations. At steady state the contributions from the terms containing time derivatives vanish. All the other time derivatives are calculated for the purpose of underrelaxation

during the calculation procedure. The model itself is first order and explicit in time.

The liquid phase in the tank consists of water and hydrogen peroxide which has a fixed mass percentage of peroxide of 87.5%, a concentration that is available commercially. Due to decomposition the concentration decreases; however, Corpening et al. [142] pointed out that at the same time water preferentially evaporates from the liquid which would increase the concentration. The actual concentration will determine the catalytic decomposition rate and should thus in principle determine the location of plane X. However, due to the simplifying assumption in the model the relative contribution of each of these processes cannot be determined and therefore the location of plane X must be determined experimentally. The concentration of the liquid will be assumed to stay constant throughout the simulation. As the model will be used for parametric studies only, it is believed that this assumption will not influence the results.

The evaporation model that was introduced in section 3.2.3 calculates the evaporation rate for each individual component while taking account for the presence of other components. As the constant concentration assumption forms a constraint for the evaporation of the liquid, this level of detail is not necessary and, therefore, the evaporation model presented in section 3.2.3 will be replaced by a simpler version.

The model that will be used is based on the Hertz-Knudsen-Langmuir equation, shown in equation 3.37. De Schepper et al. [108] applied this equation successfully when studying the evaporation of a hydrocarbon in a steam cracker. Due to decomposition the concentration decreases, however, Corpening et al. [142] pointed out that at the same time water preferentially evaporates from the liquid which would increase the concentration. The actual concentration will determine the catalytic decomposition rate and should thus in principle determine the location of plane X. However, due to the simplifying assumptions in the model the relative contribution of each of these processes cannot be determined and therefore requires to empirically determine the location of plane X. The concentration of the species in the liquid will be assumed to stay constant throughout the simulation. As the model will be used for parametric studies only, it is believed that this assumption will not influence the results.

The current evaporation model further assumes that the vapour pressure is equal to the saturation pressure. This means that the liquid is continuously boiling. The evaporation rate is only calculated for hydrogen peroxide. The evaporation rate of water follows then from the constraint of constant liquid peroxide species concentration. Substituting these assumptions into equation 3.37 and multiplying by the gas-liquid interfacial area A_{gl} results in

$$S_{H_2O_2 l}^{\ evap} = \frac{2p_{sat}}{\sqrt{2\pi R}} \left(\frac{1}{\sqrt{T_l}} - \frac{1}{\sqrt{T_g}} \right) A_{gl}. \tag{5.1}$$

It should be noted that equation 5.1 assumes thermodynamic equilibrium between the phase, while the state inside the catalyst bed is in general in non-equilibrium. Consequently, the rate of evaporation is underestimated. However, as the catalyst bed is modelled as a single control volume, equation (5.1)

is applied to all of the liquid, including the liquid just entering the catalyst bed. In reality only a small portion of the liquid is boiling. The continuously boiling liquid thus results in an overestimation of the evaporated mass and is thus counteracting the underestimation due to the thermodynamic equilibrium assumption. It is therefore thought that equation (5.1) gives a reasonable estimation of the amount of evaporation.

The saturation pressure in equation 5.1 for hydrogen peroxide is calculated with an approximation equation devised by Kuznetsov and Frolov [143]

$$p_{sat} = \left[\left(\frac{T_l}{\zeta_{H_2O_2}} \right)^{1/8} - \kappa_{H_2O_2} \right]^8 \cdot p_{atm}. \tag{5.2}$$

An advantage of this equation is that the inverse is easily obtained and this can be used to calculate the boiling point of a hydrogen peroxide mixture at a given pressure [143].

$$T_b = \zeta_{H_2O_2} \left[Z + \kappa_{H_2O_2} \right]^8 (1 - x_{H_2O_2}) + \zeta_{H_2O} \left[Z + \kappa_{H_2O} \right]^8 x_{H_2O_2}, \tag{5.3}$$

where $Z = (p/p_{atm})^{0.125}$ and ζ and κ are constants with values given in table 5.1.

Finally, the interfacial area model as presented in section 4.1 has been slightly adjusted. In the original model the surface area of the end of each pellet was ignored. The model employed in this chapter takes the surface area of the end of each pellet into account. This is to make comparisons between spherical and cylindrical pellets easier, as will become clear in section 5.4.

parameter	value	unit
$\zeta_{H_2O_2}$	$3.7642 \cdot 10^{-7}$	K
ζ_{H_2O}	$3.4679 \cdot 10^{-7}$	K
$\kappa_{H_2O_2}$	12.5302	–
κ_{H_2O}	12.4575	–

Table 5.1: *Liquid constants for approximation of the boiling point according to Kuznetsov and Frolov [143]*

5.1.3 Calculation procedure

The flow model described above describes in principle the flow through a single control volume. To solve the state of the catalyst bed at a given time first the inlet mass flux is determined. This is dependent on the pressure difference between the tank and the catalyst bed. As only liquid is injected through the injector, the inlet mass flux is calculated as

$$\rho_l u_{l_{inlet}} = c_{d,inj} \sqrt{2\rho_l (p_{tank} - p_{bed})}, \tag{5.4}$$

where c_d is the discharge coefficient, the subscript inj refers to the injector and the subscript $tank$ refers to the tank. The next step is to calculate the mass flux through the nozzle based on the exit pressure and the nozzle plenum pressure. The nozzle is assumed to have a convergent section only. The nozzle plenum pressure is equal to the catalyst bed pressure minus the pressure drop over the bed as calculated in the previous iteration. Because only gas is assumed to be exhausted through the nozzle, it is calculated as

$$\rho_g u_{g_{outlet}} = c_{d,noz}\,(p_{bed} - \Delta p)\,\mathrm{Ma}\sqrt{\frac{\gamma}{RT_g}}\left(1+\frac{\gamma-1}{2}\mathrm{Ma}^2\right)^{-(\gamma+1)/(2(\gamma-1))}, \tag{5.5}$$

where γ is the ratio of specific heats. The Mach number is calculated as

$$\mathrm{Ma} = \max\left(\sqrt{\frac{2}{\gamma-1}\left(\left(\frac{p_{bed}}{p_{atm}}\right)^{\frac{\gamma-1}{\gamma}}-1\right)}, 1\right). \tag{5.6}$$

To calculate the pressure drop over the catalyst bed the mass flux is required as input, see section 3.3. As the model is unsteady the inlet and outlet mass flux are generally not the same except when steady state is reached. For this reason the average of the mass flux through the injector and the nozzle is used to determine the pressure drop over the catalyst bed. The calculated pressure drop will in general be different from the pressure drop that was initially used to calculate the nozzle plenum pressure from the previous step. To correct this the mass flow rate through the nozzle is calculated again, but now based on the updated pressure drop over the catalyst bed. This process continues until the difference between the two is $< 0.01\%$ of the atmospheric pressure after which the tank pressure is updated based on the amount of mass that is injected into the catalyst bed. The value of $< 0.01\%$ is believed to be low enough to not influence the results. This procedure is in essence the pressure-velocity coupling between the mass and momentum conservation equation as discussed in section 4.4.2.
The next step is to determine the mass source terms and the corresponding energy source terms, see section 3.1. It is assumed that the catalyst bed is pre-heated to $100^{\circ}C$ in advance, so initial decomposition takes place at this temperature. Then the mass fractions of all the components in the gas phase are determined. Finally, the energy conservation equation is solved and from that the temperature is determined. All values are then stored and made ready for the next time step. This whole process is graphically shown in figure 5.2 below.

5.2 Model Validation

To validate the model an instrumented catalyst bed has been designed and built. The basic design is similar to the instrumented catalyst bed described in detail by Palmer et al. [133], except that the mass flux is higher and there is a greater density of instrumentation on this new bed. A picture of the

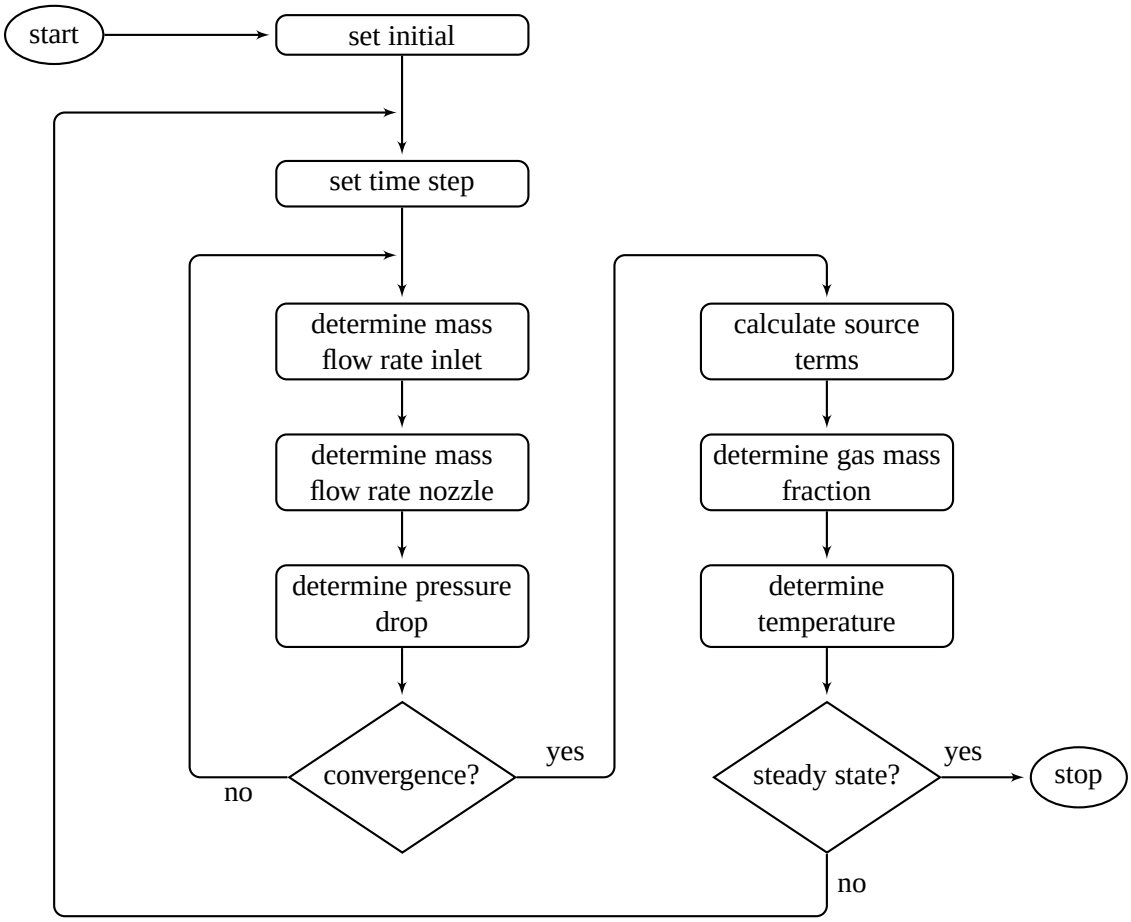

Figure 5.2: *Flow sequence of the solution procedure for the single control volume model*

catalyst bed, including the solenoid valve and standpipes, is shown in figure 5.3. The peroxide flow is from left to right. The catalyst bed has a diameter of 16*mm* and a length of 96*mm* and is made of AISI 316 stainless steel. The inlet is provided by an injector plate with 4 holes with a diameter each of 0.4*mm*. The injector plate is connected to a solenoid valve which controls the opening and closing of hydrogen peroxide supply to the catalyst bed. To protect the solenoid valve against damage from thermal soak-back a mass of stainless steel is placed between the injector plate and the solenoid valve which acts as a thermal sink. Upstream of the solenoid valve a mass flow meter is placed (not shown in the picture) and is connected to a propellant tank which is pressurised with nitrogen. The system is designed for a nitrogen feed pressure up to 20*bar*. A retainer plate is located at the downstream side of the bed to keep the catalyst pellets in the catalyst bed. A nozzle with a convergent part only is used to pressurise the bed exit. The throat diameter of the nozzle is 3.55*mm* with a discharge coefficient assumed to be 1.

Three standpipes are located at every 16*mm* along the catalyst, which provide access for thermocouples and pressure transducers. At every location the pressure, axial and wall temperature is measured; however, in this study only the pressure and axial temperature are of interest. A heating strip was used to heat up the catalyst bed to a predetermined temperature prior to firing. An additional set of two standpipes is located between the solenoid valve and injector plate to measure the inlet pressure and temperature of the liquid peroxide. Two other standpipes are placed between the retainer plate and the nozzle to measure the nozzle plenum pressure and temperature. All the transducers are connected to a data acquisition system which measures and records the pressure, temperature and mass flow rate and controls the operating of the solenoid valve and heating strip.

For validation the catalyst bed was filled with platinum coated α-alumina pellets which had a mean

Figure 5.3: *Instrumented catalyst bed used for validation*

diameter of 3.22mm and a cylindrical length of 3.35mm. During the tests 87.5%wt hydrogen peroxide was used, fed by a propellant tank at a fixed pressure of about 17bar. The catalyst bed was wrapped in an insulation blanket to reduce the heat transfer through the wall as much as possible. Note that in figure 5.3 the catalyst bed is shown without insulation.

The measurement frequency was set to 200Hz and to 1Hz for temperature measurements. The bed was preheated to 150°C to reduce the time required to reach steady state. The tank was filled with enough peroxide to run the catalyst bed for about 30 seconds at which point it was assumed steady state conditions will have been reached.

To match the simulation conditions with experimental conditions the mass flow rate through the injector was fixed at $12.6 \cdot 10^{-3} kg\,s^{-1}$ rather than the result of the pressure difference between the catalyst bed and the tank. This is equivalent to a inlet mass flux of about $62.67 kg\,m^{-2}\,s^{-1}$. In this way the inlet boundary conditions are guaranteed to be the same.

After the experiments had been performed the catalyst bed was carefully emptied and the number of catalyst pellets was counted. In total there were 406 pellets which, for the dimensions of the pellets and catalyst bed given earlier, results in a void fraction of $\varepsilon_f = 0.4262$. Using equation for cylindrical pellets of the given dimensions, see appendix C, a void fraction of $\varepsilon_f = 0.4215$ is predicted, which shows very good agreement with the experimental result.

The measured pressure as a function of the distance from the injector in L/D-ratios, defined as the distance from the injector divided by the diameter of the catalyst bed, is shown in figure 5.4. The rightmost data point is located in the nozzle plenum chamber, located at L/D ≈ 7.7, downstream of the retainer plate, which is located at L/D $= 6$. Experimental data are plotted with a box plot with the mean of the measurements superimposed on that. The mean and the median of the measurements are almost identical. The pressure at L/D $= 1$ shows a peak. However, it is believed that the reason for this is a faulty pressure transducer rather than a physical event taking place at that location and will therefore not be considered during the data analysis. Also shown is the inaccuracy margin of the pressure data, which was generated with a Monte-Carlo simulation of the inaccuracy of the pressure transducer and data acquisition system. The margin is about 0.9 bar wide. All the measurement data fall within this margin. For further explanation of the Monte-Carlo simulations see appendix H.

Catalyst pellets are present between $0 \leq$ L/D ≤ 6. The pressure difference between the nozzle plenum chamber and L/D $= 6$ can be interpreted as the pressure drop over the retainer plate and is found to be 0.36bar. This pressure drop is accounted for during all simulations presented in this section. The pressure drop over the part that contains the pellets is about 1.25bar.

Figure 5.5 shows the measured temperature along the catalyst bed as well as the local boiling temperature as determined by equation 5.3. Initially the measured temperature increases gradually but there is large jump in temperature between L/D $= 2$ and L/D $= 3$. After that the measured temperature stays fairly constant at about 900K with the exception of the temperature at L/D $= 6$, which shows a sudden drop in temperature of about 150K. The temperature further downstream is about 900K again. L/D $= 6$ is also the location that the retainer plate is positioned. A possible explanation for the sudden

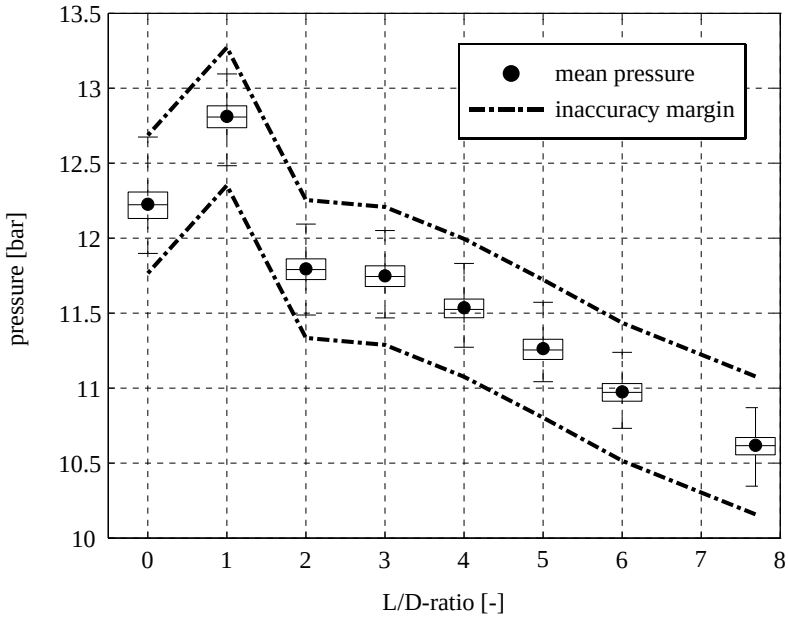

Figure 5.4: *Measured pressure at several locations in the catalyst bed for the 0D-model*

decrease in temperature is that the thermocouple is touching, or very close to, the retainer plate. As this is made of stainless steel, it acts as a heat sink and consequently the temperature is lower than the actual fluid temperature.

The temperature up to just before L/D = 2 is below the boiling point, based on equation 5.3 and

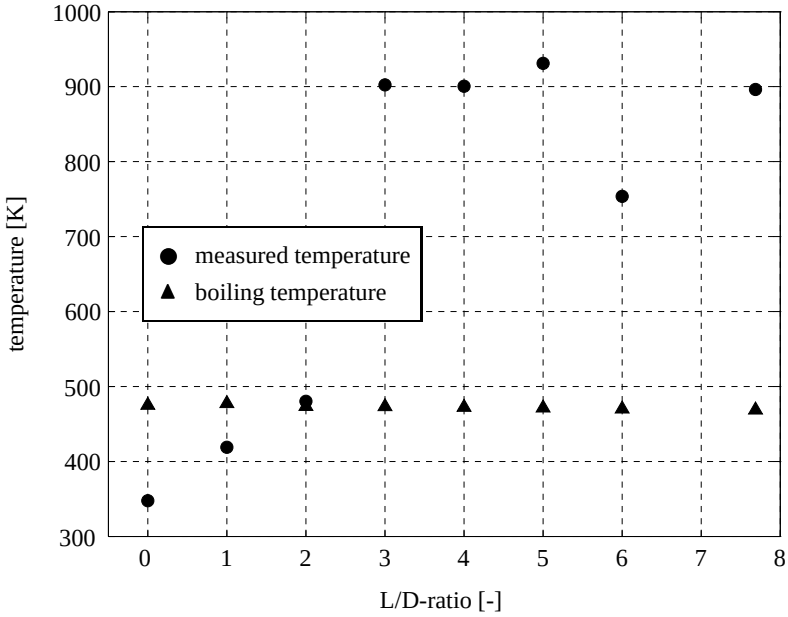

Figure 5.5: *Measured axial temperature at several locations in the catalyst bed for the 0D-model*

figure 5.4. From the fluid properties as provided in appendix B the adiabatic decomposition tempera-

ture is determined to be about $965K$. This means that at L/D $= 3$ most of the hydrogen peroxide has decomposed and complete decomposition is achieved at about L/D $= 5$. The very large increase in temperature between L/D $= 2$ and L/D $= 3$ is probably due to the fact that all liquid disappears between those two locations due to decomposition and evaporation. The measured temperature is in fact an average temperature over the measurement time. The averaging process not only smooths the temperature fluctuations within a phase, but also the temperature differences between the phases. Where the measured temperature is well above the boiling point of the liquid, it may be assumed that only gas is present and thus that the measured temperature is in fact the gas temperature. This assumption is based on two arguments; one which is more mathematical and the other which is more physical in nature. From a mathematical point of view if liquid were present its influence on the average temperature would be so low that it can be regarded as not being present. From a physical point of view if the average temperature is well above the boiling point of the liquid the thermal imbalance between the phases, if a small amount of liquid is present, is large. Consequently the interphase heat transfer will be large which will lead to a rapid increase in liquid temperature, or higher evaporation rates if the liquid is at the boiling point.

In section 5.1.1 the unknown variable X was introduced, signifying the maximum distance in the catalyst bed from the injector where liquid is present and in section 3.1.2 the unknown equilibrium constant K_r was introduced. It was mentioned that both variables required experimental determination. It has already been established above that $2 < X/D < 3$. The sensitivity of the exact location of X on the pressure drop over the bed is shown in figure 5.6, where K_r was arbitrarily set to $K_r = 70$, where the simulated pressure drop is non-dimensionalised by dividing by the measured pressure drop. Note that in general the equilibrium constant for the liquid phase is different from the gas phase. However, tuning of the gas equilibrium constant is not necessary for the purpose of the model and will therefore be left out of the analysis.

Also shown in the same figure is the pressure drop over the part downstream of X, which accounts for about 99% of the pressure drop over the whole bed. This indicates that the gas phase is predicted to be the major contributor to the overall pressure drop. The pressure drop varies linearly with the location of X. The simulated pressure drop is equal to the measured pressure drop for X/D ≈ 2.5. However, when considering the pressure drop upstream and downstream of X separately, large deviations with the measured pressure drop are found. The measured pressure drop between $0 \leq$ L/D ≤ 2 accounts for about 35% of the total pressure drop and the measured pressure drop between $3 \leq$ L/D ≤ 6 for about 62%. This suggests that the Tallmadge equation, which was used as the basis for the pressure drop model, results in a overestimation of the pressure drop for a single phase flow in a packed bed. It also means that the model as proposed by Sorokin [121] underestimates the pressure drop for a two-phase flow in a packed bed. But, as will be shown in the next section, the current formulation is a large improvement on the more traditionally employed Ergun equation.

The pressure drop as a function of the equilibrium constant is shown in figure 5.7 where the location of X was fixed at L/D $= 2.5$. Here the simulated pressure drop is divided by the measured pressure

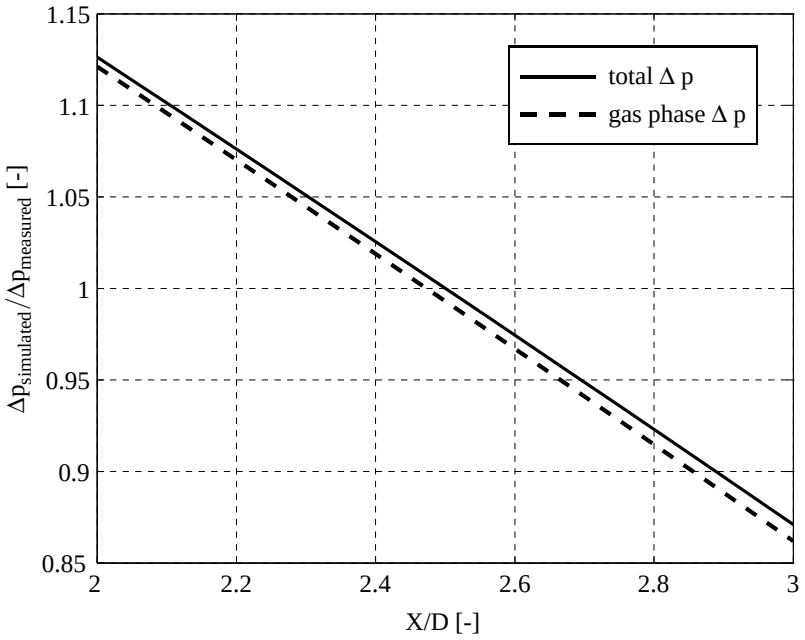

Figure 5.6: *Total and gas phase relative pressure drop as a function of X/D relative to the measured pressure drop*

drop. Also shown in the same plot is the liquid volume fraction upstream of X. For increasing K_r, the reaction rate for catalytic decomposition increases as well, see equation 3.28. As a result the mass transfer from liquid to gas is higher. Because the majority of the pressure drop is caused by the gas phase, this results also in a higher pressure drop over the catalyst bed.

The increase in pressure drop seems to accelerate for increasing K_r and not to obtain a constant value for even smaller liquid volume fractions. However, K_r is plotted on a logarithmic scale and would show a constant increase in pressure drop if it was plotted on a linear scale. Two reasons can be identified for the ever increasing pressure drop. The first one is shown in figure 5.8 which shows that the gas temperature increases as K_r increases. This is to be expected because the catalyst bed is getting closer to a state of complete decomposition. For higher values of K_r the temperature tends to a constant value of about $965K$, which was earlier identified as the adiabatic decomposition temperature for 0.875 hydrogen peroxide. A higher temperature results in a higher pressure and gas density. From the pressure drop model it can be seen that a higher (gas) density results in a higher pressure drop.
The second reason is that due to the large density difference between the gas and the liquid phase, the mass transfer from liquid to gas results in an increase in pressure; even if the increase in gas temperature is not taken into consideration. As explained above, an increase in pressure results in a higher gas density and consequently a higher pressure drop over the bed. Although not shown in this plot, for much higher values of K_r ($K_r > 10^6$) the pressure drop eventually reaches a constant value of just below $2bar$ over the whole bed. At this point the liquid volume fraction is very close to zero.

Based on the plots that are presented, it is not possible to select a value for X and K_r that would give

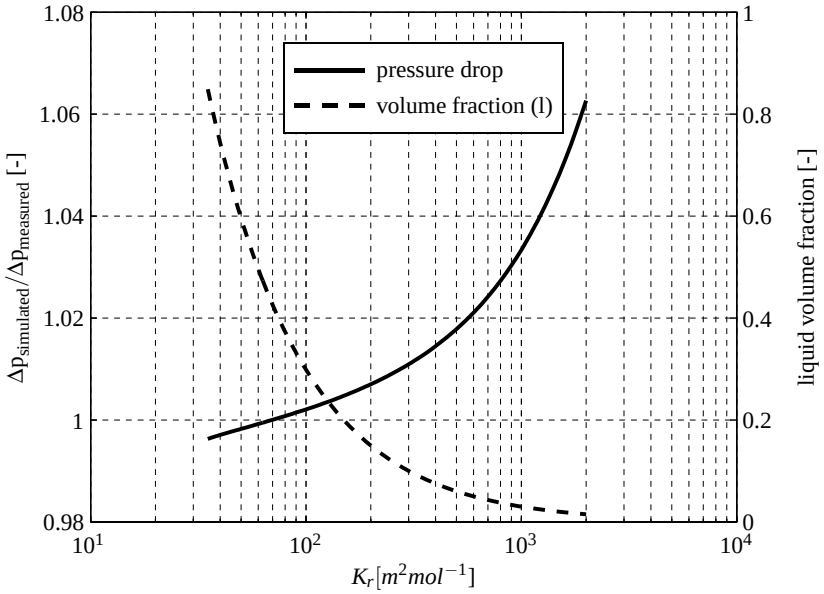

Figure 5.7: *Pressure drop relative to the measured pressure drop and liquid volume fraction as a function of K_r for the 0D-model*

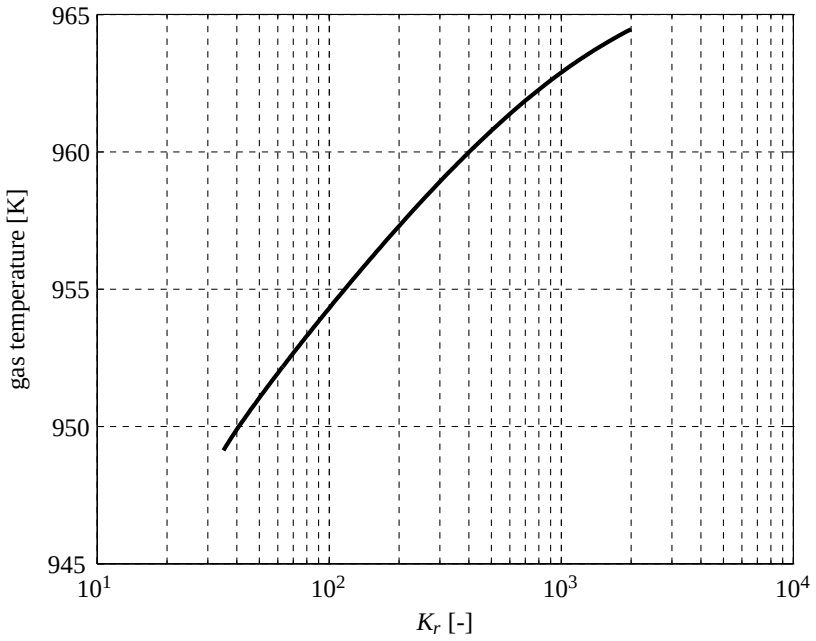

Figure 5.8: *Gas temperature as a function of K_r for the 0D-model*

the best prediction of the actual state in the catalyst. However, figures 5.6 and 5.7 also show that the sensitivity of X and K_r on the pressure drop is small, where the sensitivity of K_r is considerably smaller than that of X. Besides that, the purpose of the current model is two compare different scenarios with each other and not to accurately predict the state of the catalyst bed for a given input condition. Based on these considerations in the following simulations the location of X is set to L/D $= 2.5$ and the value

for K_r is fixed at 70 as for these values the simulated pressure drop is the same as that obtained experimentally. The corresponding pressure drop is close to the measured pressure drop in the validation case and the resulting liquid volume fraction is about 0.5, which is thought to be a reasonable estimate.

5.3 Some Basic Assumptions Reconsidered

Because there is no spatial discretisation it is implicitly assumed that the liquid between the injector and plane X is equally distributed. To investigate the influence of the distribution of liquid in this part of the bed on the pressure drop, two simulations were performed with different liquid distribution assumptions for the pressure drop model under the same conditions as the validation runs. One simulation assumed a linear decrease to zero in liquid volume fraction from the injector to point X and the other one an exponential distribution. In all cases the pressure drop was considered for X at a distance of X/D = 2.5 from the injector. The results were then compared with a simulation assuming an equal distribution of liquid.

The results are shown in table 5.2. The second column shows the resulting pressure drop in the first part of the catalyst bed, where both liquid and gas are present, in bar. For the linear and exponential liquid distribution the percentage difference from the result with the constant distribution is shown in brackets. The third column shows the same but for the pressure drop downstream of plane X and the last column shows the effect on the pressure drop over the whole catalyst bed. From the second column it appears that the actual distribution strongly influences the local pressure gradient in the region where gas and liquid coexist. However, as the pressure drop in this region is significantly lower than in the part where gas only is present, the effect on the total pressure drop over the bed is limited, as is shown in the last column.

With the current model and the way in which the validation has been performed it is not possible to

distribution	**two-phase Δp** [bar]	**downstream Δp** [bar]	**total Δp** [bar]
constant	$8.91 \cdot 10^{-3}$	1.26	1.27
linear	$13.97 \cdot 10^{-3}$ (57%)	1.29 (2.4%)	1.31 (3.1%)
exponential	$71.52 \cdot 10^{-3}$ (703%)	1.29 (2.4%)	1.36 (7.1%)

Table 5.2: *Effect of liquid distribution on the pressure drop*

determine which liquid distribution gives a better description of reality. It can be stated with certainty that the liquid distribution will not be constant. However, given the purpose of the current model as discussed in section 5.1.1 the assumption of a constant liquid distribution is viable.

The basis for the pressure drop model is formed by the Tallmadge equation, which is an extension of the Ergun equation to higher Reynolds numbers. It was argued that the expected value for Re_p is outside the range for which the Ergun equation originally was established and would consequently

give a too high estimate of the pressure drop. To verify this figure 5.6 was reconstructed with the Ergun pressure drop equation as the basis for the pressure drop model instead of the Tallmadge equation. The comparison of the total pressure drop over the bed between these two equations is shown in figure 5.9.

It is clear that the Ergun equation gives an pressure drop estimation about twice as high as the Tall-

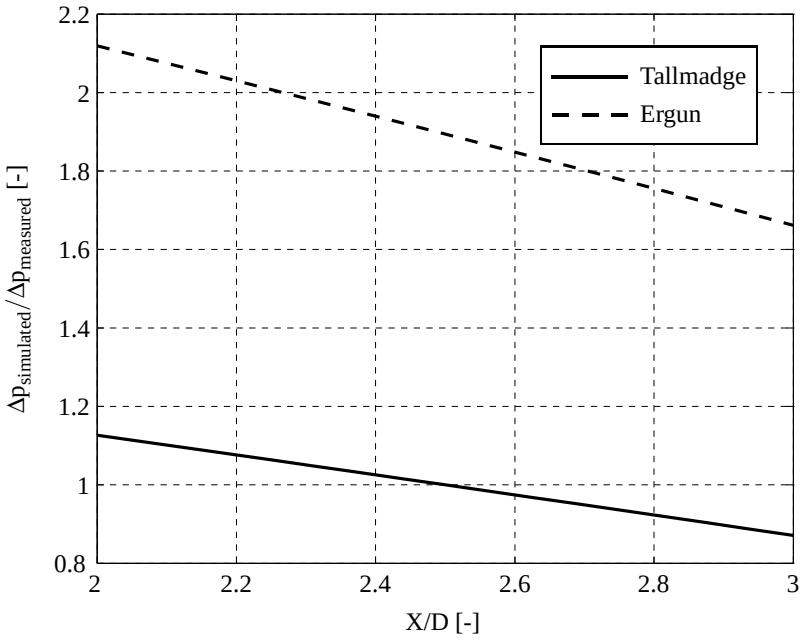

Figure 5.9: *Pressure drop comparison between the Tallmadge and the Ergun equation as a function of X/D*

madge equation. As is shown in the figure, the Ergun equation severely overestimates the pressure drop under the present conditions. As was pointed out in section 3.3 the expected value for Re_p is higher than the range for which the Ergun equation is valid and figure 5.9 shows the consequence of that.

5.4 Spheres vs. Cylinders

Pasini et al. [64] used spherical catalyst pellets in the catalyst bed while for validation of the current model cylindrical pellets were used. The geometry of the pellets influences the void fraction, see appendix C, and the interfacial area, see section 4.1. Consequently, the pressure drop over the catalyst bed as well as the required length of the catalyst bed are influenced by the shape of the pellets as well. This is graphically shown in figures 5.10 and 5.11.

Figure 5.10 shows the void fraction and the total catalyst pellet surface area as a function of the bed to pellet diameter ratio for spherical pellets. To make the results independent of the size of the bed,

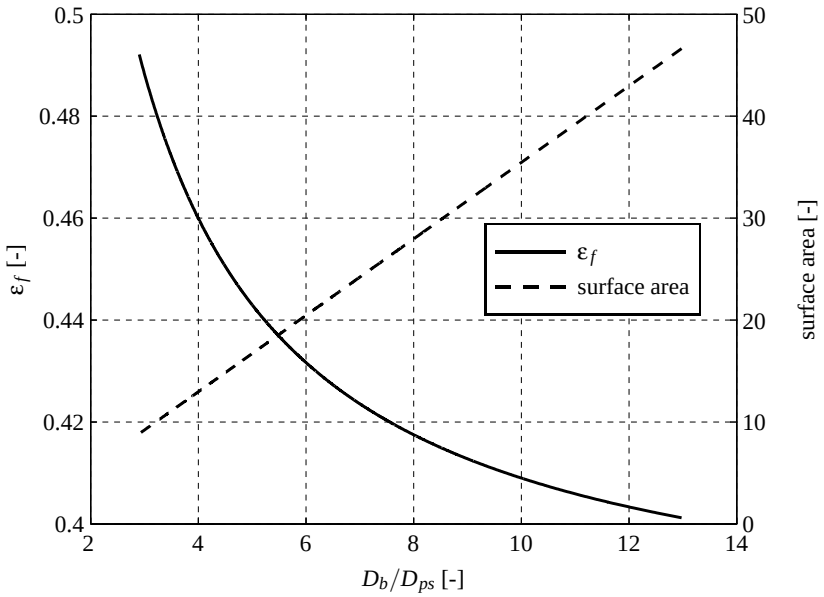

Figure 5.10: *Void fraction and non-dimensional catalytic surface area as a function of the bed to pellet diameter ratio*

the horizontal axis is non-dimensionalised by dividing the bed diameter by the pellet diameter. The catalytic surface area in the bed is relative to the total surface area had the catalyst bed been filled with pellets with a diameter equal to diameter of the catalyst bed and is thus also independent of the catalyst bed dimensions. As is shown the catalytic surface area scales linearly with the bed to pellet diameter ratio with more surface area for higher ratios, whilst the void fraction is inversely proportional to the bed to pellet diameter ratio. It can thus be expected that for higher diameter ratios, the plane X will be located closer to the injector as more hydrogen peroxide can be decomposed over a smaller distance. Based on the pressure model as presented in section 3.3, a higher pressure gradient is therefore expected for higher diameter ratios.

To investigate the influence on the pressure drop simulations were performed for different pellet di-

parameter	**value**	**unit**
ambient pressure	101325	*Pa*
ambient temperature	293	*K*
inlet temperature	293	*K*
bed diameter	16	*mm*
nozzle throat diameter	3.55	*mm*
peroxide mass fraction	0.875	–

Table 5.3: *Initial and boundary conditions for the 0D-model*

ameters. The inlet mass flux was set to $60 kg\,m^{-2}\,s^{-1}$ (slightly lower than the validation case) and for the Arrhenius parameters the values as mentioned in tables 3.2 and 3.3 were used. All other relevant

initial and boundary conditions are shown in table 5.3. As X/D was determined above based on an certain inlet mass flux and particular pellet dimensions, its location will change as soon as one of these parameters change. For this reason the same approach as Johnson et al. [60] will be followed who kept the residence time for fluid particles constant and determined based on that how far plane X would be from the injector. This is applied to the liquid phase as well as to the gas phase to ensure that the total residence time is kept constant. The initial values for X/D and the catalyst bed length are X/D $= 2.5$ and $L = 96mm$. The response of changing the spherical pellet diameter on the distance from the injector to location X and the pressure drop over the bed together with the total bed length is shown in figure 5.11. The distance from the injector to location X and the total bed length is made non-dimensional by dividing by the bed diameter.

As expected the total bed length as well as the distance from the injector to X decrease with increas-

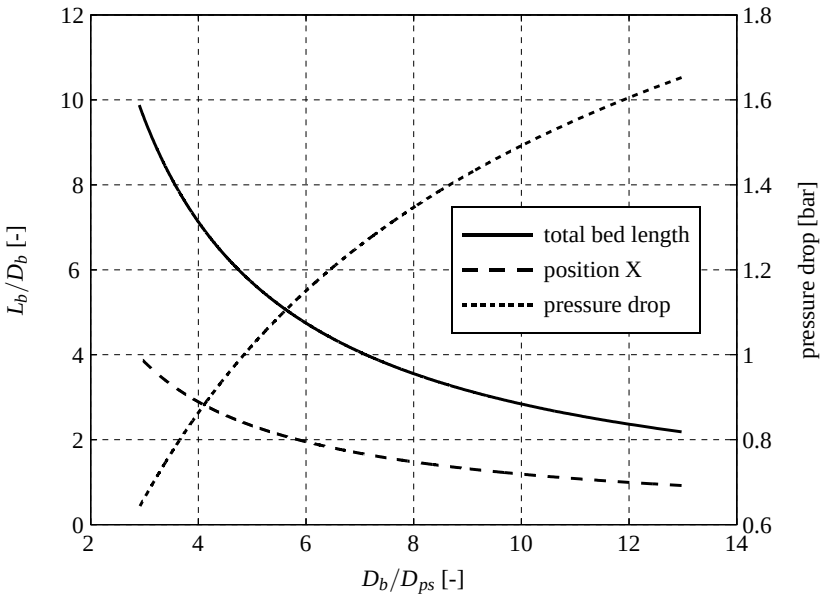

Figure 5.11: *Simulated bed length to diameter ratio and pressure drop as a function of the bed to pellet diameter ratio*

ing bed to pellet diameter ratio due to an increased total catalytic surface area. However, in both cases the length tends to an asymptotic value different from 0 and is caused by a decrease in void fraction resulting in higher fluid velocities and thus a reduced contact time with the surface. The corresponding pressure drop shows an increase with an increasing diameter ratio, but the increase diminishes for higher diameter ratios. This is partly due to smaller variations in void fraction for higher bed to pellet diameter ratios, as shown in figure 5.10, and partly due to the smaller change in required bed length.

The results described above are for spherical pellets. When using cylindrical pellets different void fractions and a different catalytic surface area would be obtained and consequently different results for pressure drop and bed length should be expected. In general, the resulting void fraction is lower for cylindrical pellets. The difference increases for increasing bed to pellet diameter ratio. Subtracting

the equation for the void fraction of cylindrical pellets from that of spherical pellets and subsequently differentiating and solving the equation shows that the maximum difference between the two void fractions is about 0.035 for a bed to pellet diameter ratio of about 5.83. With the same equations it can also be shown that for a diameter ratio of about 2.52 the void fraction for both geometries is the same. Based on this it is expected that the pressure gradient in the catalyst bed is generally higher for cylindrical pellets. Although the differences in void fraction seem to be small, the effect on pressure drop, bed length and distance from the injector to X is large, as will be shown below.

The catalytic surface area in the bed for cylindrical particles is compared with the surface area for spherical pellets in figure 5.12. The surface area is non-dimensionalised in the same way as in figure 5.10. For cylindrical pellets the catalytic surface area as a function of the diameter ratio cannot be represented by a single curve. Instead, results are shown for two different pellet lengths: $L_p = 1.5mm$ and $L_p = 4.5mm$. Although not shown, for all other pellet lengths the catalytic surface area for cylindrical pellets is higher than for spherical pellets for a given diameter ratio. From this result it is expected that the required bed length and the distance from the injector to X is smaller for cylindrical pellets.

This trend is confirmed by figure 5.13. It shows the required bed length divided by the bed diameter as a function of the pellet to bed diameter ratio for spheres and cylinders with a pellet length of $L_p = 1.5mm$ and $L_p = 4.5mm$. For a given diameter ratio the length for cylindrical pellets is less than for spherical pellets.

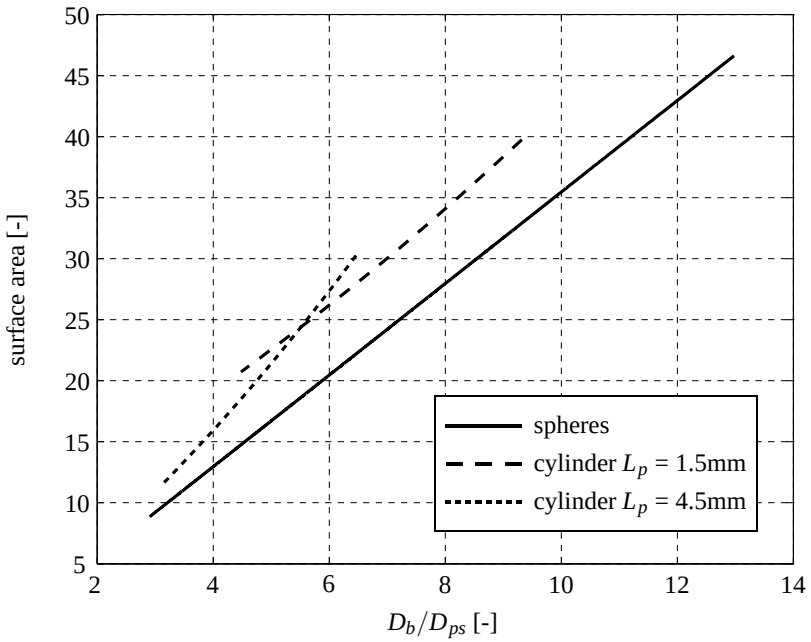

Figure 5.12: *Non-dimensional catalytic surface area for spherical and cylindrical pellets*

Lower void fractions would be expected to result in a higher pressure drop over the catalyst bed, see section 3.3. On the other hand, the results presented in figures 5.12 and 5.13 showed that the surface

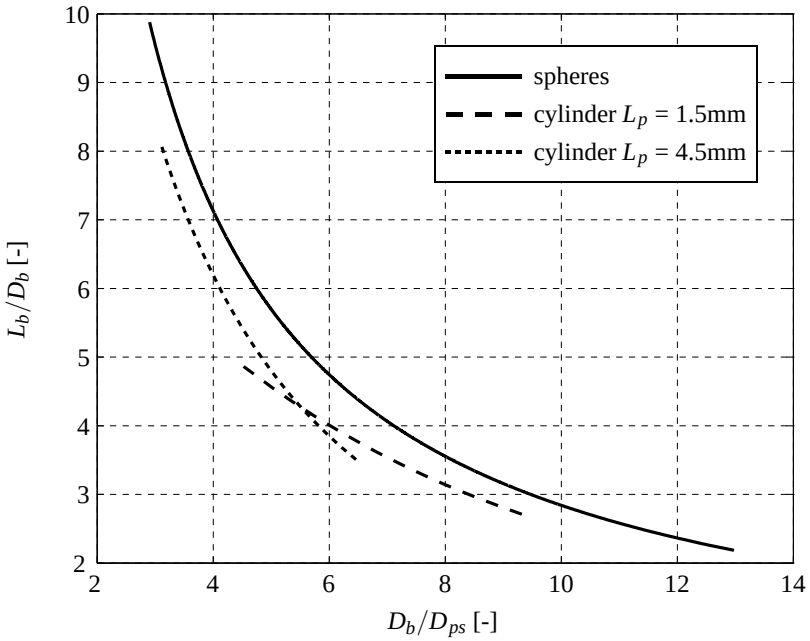

Figure 5.13: *Required bed length to diameter ratio for spherical and cylindrical pellets*

area for cylindrical pellets is higher than for spherical pellets resulting in a smaller required bed length and smaller distance of X from the injector. This would lead to a lower pressure drop over the catalyst bed for cylindrical particles. The combined effect is shown in figure 5.14, which shows the pressure drop over the bed as a function of the diameter ratio. The results for cylindrical pellets are only shown for pellets with $L_p = 1.5mm$ and $L_p = 4.5mm$. In all cases, including those not shown in the figure, the total pressure drop is higher for cylindrical pellets. However, the difference in pressure drop between the two shapes is very small, especially for low diameter ratios for a given pellet length. Also note that for a given pellet length the difference in pressure drop for increasing diameter ratio seems to increase to a maximum after which the difference in pressure drop is decreasing again.

An optimal catalyst bed design requires the optimisation of the pressure drop over the bed and the total bed length. Combining figures 5.13 and 5.14 gives the pressure drop as a function of the bed length and is shown in figure 5.15; this indicates that there is a higher pressure drop for short catalyst beds which may at first seem counter-intuitive. However, for the residence time to stay constant a higher surface area per unit volume is required which can only be achieved by using pellets with smaller dimensions. Larger bed to pellet diameter ratios result in lower void fraction and this leads to a higher pressure gradient. Figure 5.15 shows that the effect of the increase in pressure gradient is stronger than the decrease in required bed length and therefore for shorter bed lengths the pressure drop over the bed will be higher.

Figure 5.15 shows the result for both spherical and cylindrical pellets. For cylindrical pellets only two sample results are shown: for $L_p = 1.5mm$ and $L_p = 4.5mm$. For a given pellet length the pellet diameter increases from left to right and ranges from 0.5 to $4.5mm$. It shows that for certain dimensions

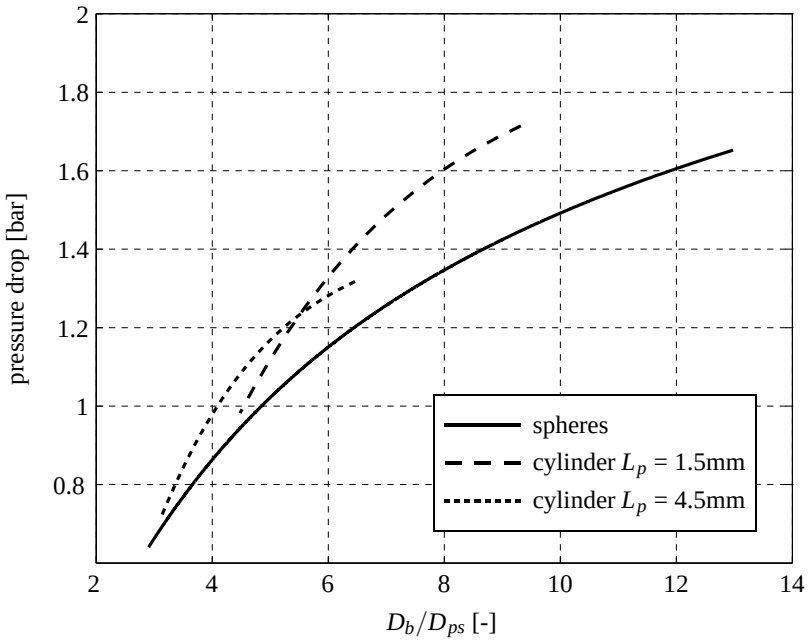

Figure 5.14: *Pressure drop as a function of bed to pellet diameter ratio for spherical and cylindrical pellets*

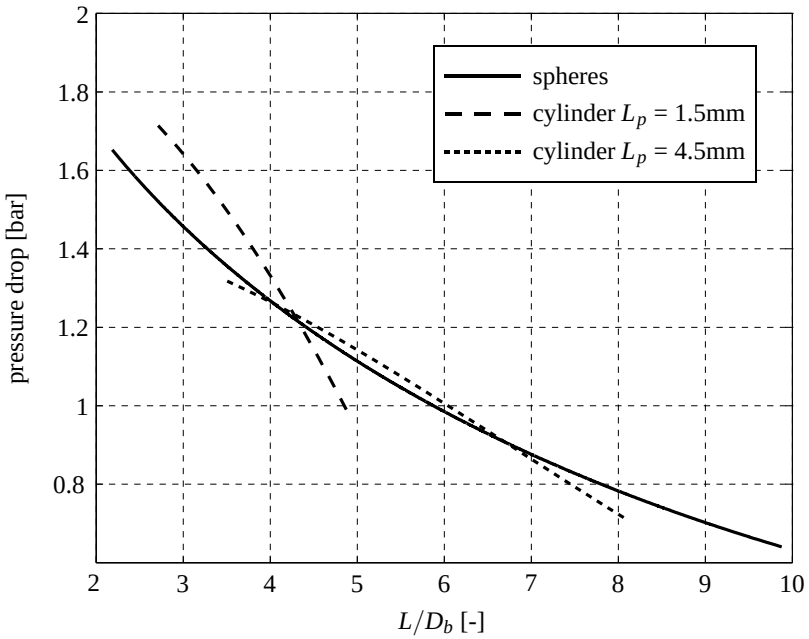

Figure 5.15: *Pressure drop over the bed as a function of required bed length to diameter ratio for spheres and cylinders*

of cylindrical pellets and given bed length a lower pressure drop is achieved. For a cylindrical pellet with a length of 1.5*mm* this is only the case for large enough pellet diameters, but for pellet lengths of 4.5*mm* this is the case for small enough and large enough diameters. For diameters in between,

spherical pellets give a lower pressure drop.

From figure 5.15 it can be concluded that the dimensions of the pellets determine whether either spherical or cylindrical pellets result in a lower pressure drop for a given bed length. The limits for these are shown in figure 5.16, which shows a map for cylindrical pellets indicating the range for which spherical pellets give better results (dark grey) and for which cylindrical pellets perform better (light grey). The horizontal axis shows the bed to pellet diameter ratio and the vertical axis the pellet aspect ratio, which is defined as the pellet diameter over the pellet length. Note that for spherical pellets the aspect ratio is always unity. The box bounded by the dash-dotted line indicates the range of cylindrical pellets that have been used for the simulations. Also shown are the contour lines for which the pressure drop for cylindrical pellets is 90, 75, 50 and 30% of the pressure drop for spherical pellets. The step pattern of these contour lines is due to the limited resolution. Finally, the black diamond around diameter ratio 4 and aspect ratio 1 indicates the position of the catalyst bed and pellets used for validation.

To construct the map 3900 simulations were performed on the Iridis3 [140], the supercomputer of the University of Southampton. Each simulation required about 250 seconds of CPU time on a 2.4GHz Intel Westmere processor. A one-dimensional model would have required substantially more CPU time per simulation. Given the amount of simulations omitting any spatial discretisation clearly shows the advantages of such an approach.

Figure 5.16 shows that in general that for aspect ratios of 2 and more, so for disk-like pellets, the

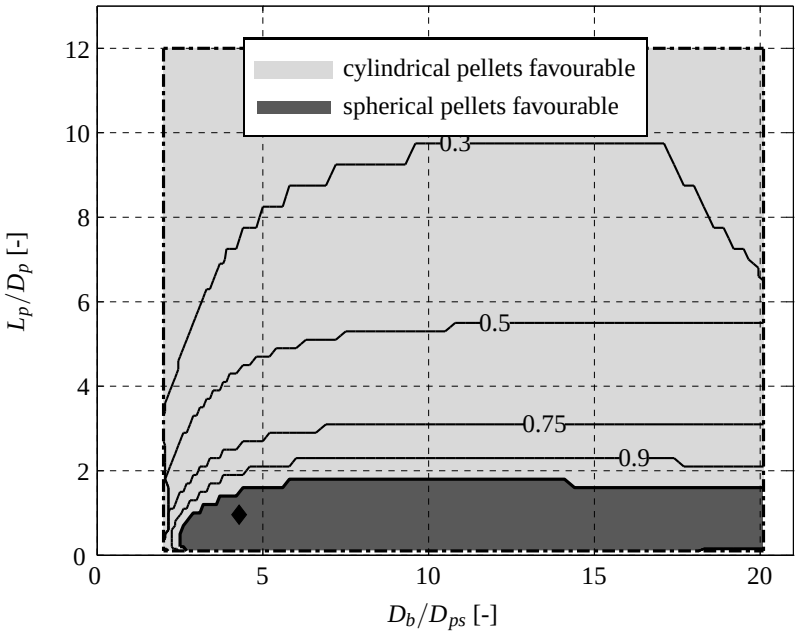

Figure 5.16: *Pressure drop as a function of the pellet aspect ratio and bed to pellet diameter ratio for an inlet mass flux of* $60 kg\,m^{-2}\,s^{-1}$*. Contours show the fraction of the pressure drop in comparison with spherical pellets.*

pressure drop for cylindrical pellets are lower for a given catalyst bed length. For diameter ratios of 2.5 and lower, cylindrical pellets always give a lower pressure drop, regardless the aspect ratio. The figure further shows that large changes in pressure drop difference occur for small changes in aspect ratio around the line where spherical and cylindrical pellets give an equal pressure drop. Figure 5.16 also shows that each size of spherical pellet can be replaced by a range of cylindrical pellets that gives a lower pressure drop for a given catalyst bed length. Obviously, other requirements such as mechanical strength and thermodynamic properties of the pellets might put further requirements on the dimensions of the pellets.

Figure 5.16 was the result for an inlet mass flux of $60 kg\,m^{-2}\,s^{-1}$. To see the influence of the inlet mass flux, the same simulations have been performed with an inlet mass flux of $80 kg\,m^{-2}\,s^{-1}$. It was found that the plots are practically identical which shows that the result is independent for a limited increase of the inlet mass flux.

In section 5.3 it was argued that the liquid volume fraction distribution in the first part of the catalyst bed would not affect the results despite resulting in a different estimation of the pressure drop over the bed. To verify this assumption the calculations for a mass flux of $60 kg\,m^{-2}\,s^{-1}$ have been repeated, but now under the assumption of a exponential liquid void fraction distribution. Again this result is almost identical to the one shown in figure 5.16. This proves the assumption that was made is justified.

5.5 Radial Effects

The results obtained above assume a constant void fraction in the catalyst bed and do not take into account any variation in radial or longitudinal void fraction distribution. The work of Bey and Eigenberger [70] provides also approximate relations for the variation of void fraction in the radial direction. The radial distribution for spheres and cylinders with a bed to pellet diameter ratio of 4.3 and an aspect ratio of 0.96 for the cylindrical pellets is shown in figure 5.17. The chosen diameter ratio is equal to that of the experiments which have been used for validating the current model, see section 5.2. The plot shows the void fraction on the vertical axis and the non-dimensional radius on the horizontal axis, where 0 indicates the centre of the catalyst bed and 1 the wall.

It is clear that, for both spherical and cylindrical pellets, there is a considerable change of void fraction with the radius and a constant void fraction, as was assumed above, is not achieved in practice. The variability for cylindrical pellets is considerably less than for spherical pellets. Another difference between the two shapes is the location of local maximum and minimum void fractions: the peak-to-peak distance for spheres is slightly larger than for cylinders. This is important to take into consideration if it is decided to narrow the catalyst bed locally to redirect the liquid flow from the wall to the centre of the bed in order to obstruct the channeling.

The variation in void fraction changes for different bed to pellet diameter ratios. For spherical pellets this is shown in figure 5.18 and for cylindrical pellets in figure 5.19, in both cases for bed to pellet

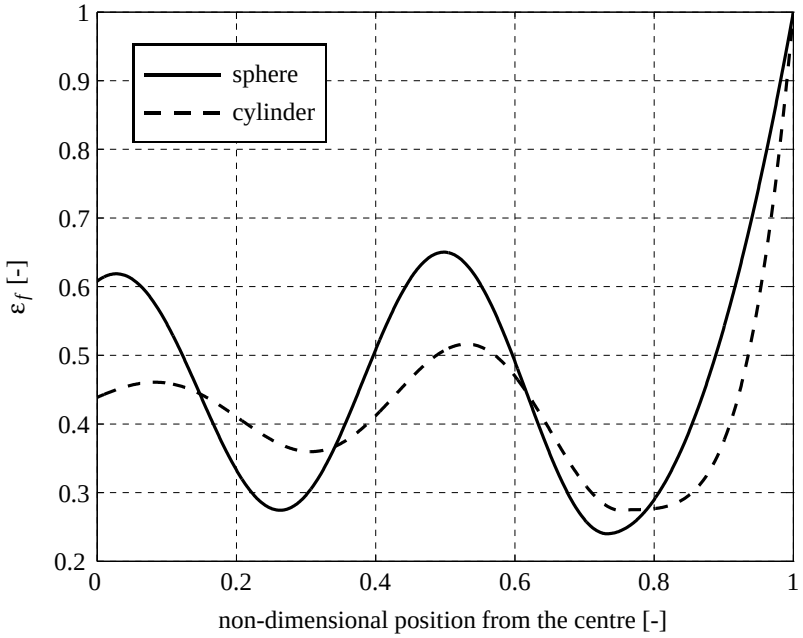

Figure 5.17: *Radial void fraction distribution for spherical and cylindrical pellets with a bed to pellet diameter ratio of 4.3*

diameter ratios of 5, 10 and 20. In the case of spherical pellets it is shown that even for larger diameter ratios there is still a relatively large variation in void fraction in the centre of the catalyst bed. For cylindrical pellets a constant void fraction is reached for higher diameter ratios. In the case of a diameter ratio of 20 the variation in void fraction is only a near wall effect; for about 90% of the diameter the void fraction is constant. For diameter ratios of 10 for up to 65% of the diameter the variation in void fraction is within 0.01 from the mean.

Based on the discussion above, the results obtained in the previous section (which assumed a constant void fraction) should be viewed with some caution. For high bed to pellet diameter ratios the map presented in figure 5.16 can considered to be reliable. Figure 5.18 shows for diameter ratios from 10 and higher so many local minima and maxima in void fraction that the average void fraction can considered to be a reasonable estimate. For diameter ratios of 5 and smaller this is not the case and figure 5.16 cannot be used as an absolute reference. Besides that, all the results so far assume an optimum packing density. For low diameter ratios even a small deviation from an optimum packing could result in considerable changes in local as well as average void fractions. For this reason it is recommended that low bed to pellet diameter ratios are avoided in practical applications.

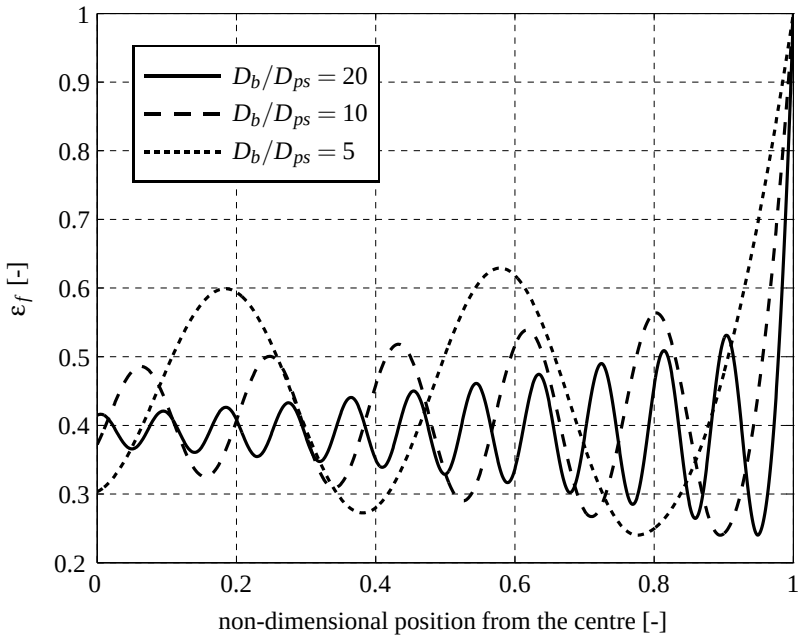

Figure 5.18: *Radial void fraction distribution for spherical pellets as a function of bed to pellet diameter ratios*

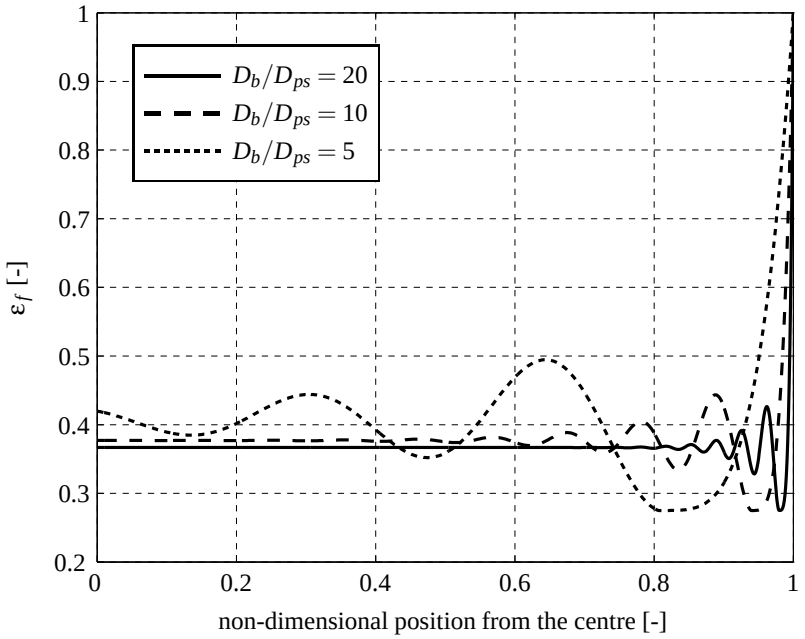

Figure 5.19: *Radial void fraction distribution for cylindrical pellets as a function of bed to pellet diameter ratios*

Chapter 6

One-Dimensional Two-Fluid Solution

In this chapter equations 2.2, 4.20, 4.21 and 4.22 are solved in the axial direction. The solution method was discussed in sections 4.4 and 4.5. However, before the model can be used, it first needs to be validated. This is done in section 6.1. In section 6.2 a typical steady state result is presented. The choices made for the pressure drop model as discussed in section 3.3 will be revisited again. A sensitivity analysis to the Arrhenius parameters and interfacial area is presented in section 6.3. An attempt has also been made to solve the equations in a commercial CFD package. More information on that is given in appendix I.

6.1 Experimental Validation of the One-Dimensional CFD Model

To validate the model the same instrumented catalyst bed is used as described in section 5.2. The model described simulates only the processes in the catalyst bed, i.e. between the injector and retainer plate. The measured values just downstream of the injector and just upstream of the retainer plate are therefore used as boundary conditions for the numerical model. The outlet pressure boundary condition was set equal to the measured pressure just before the retainer plate, equal to $10.8 \cdot 10^5 Pa$. At the inlet the gas volume fraction was set to 0.05 and the gas mass fractions to 0.001 for hydrogen peroxide, steam and oxygen and 0.997 for air. The inlet temperature was set equal to the measured peroxide temperature just before filling the propellant tank. The inlet gas velocity was set to $0.07 ms^{-1}$ and the liquid velocity was derived from the measured mass flow rate at steady state of $12.6 \cdot 10^{-3} kgs^{-1}$, which is equivalent to a mass flux of about $62.5 kgm^{-2}s^{-1}$ or a liquid velocity of $4.6 \cdot 10^{-2} ms^{-1}$. By setting these inlet conditions for the gas phase it is assured that a two-fluid flow condition exists at the inlet, but with negligible contribution to the overall inlet mass, momentum and heat flux, while assuring stable simulations. The values for the Arrhenius parameters are taken from tables 3.2 and 3.3.
The effect of the mesh density is shown in figure 6.1, where the pressure as function of distance from

the injector is plotted for different grid sizes. A non-dimensional pressure is obtained by dividing by the outlet pressure. Grid independence is shown for grids of 1600 cells and more for the current length of the catalyst bed. All the results hereafter were obtained with this number of cells.
The figures shown are the result of steady state simulations. However, when steady state is reached the values are actually undulating around a mean value and is particularly noticeable in the gas temperature. This is caused by small liquid temperature fluctuations near the boiling point. Close to the boiling point, the Spalding mass transfer B_M, which drives the evaporation rate, is very sensitive to temperature changes. This results in fluctuating evaporation rates and thus in fluctuating amounts of energy that is consumed during evaporation. For this reason an average was taken over 300 iterations to smooth the fluctuations as much a possible. In that case the standard deviation for the liquid temperature is less than 1.5%.
The measured temperature as a function of the distance from the injector together with the simulated

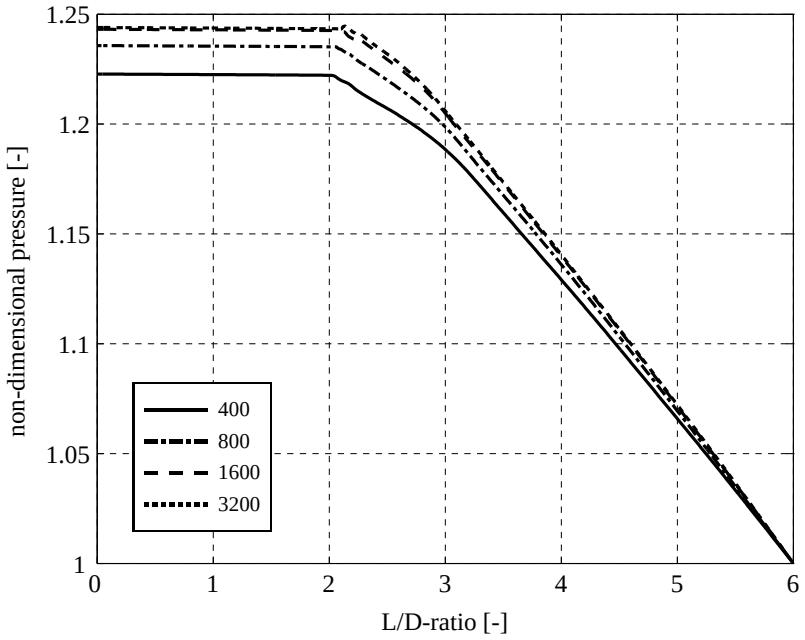

Figure 6.1: *Grid independence study result for the 1D-model*

gas and liquid temperature is shown in figure 6.2. The distance is again shown in L/D-ratios and the temperature is non-dimensionalised by dividing it by the local boiling temperature, which is a function of the local pressure and composition of the liquid. The measured temperature is below the boiling point up to and including L/D = 2 and gradually rising from the injector. At L/D = 3 a large increase in temperature is shown to a boiling ratio of about 1.8 after which it gradually increases to about 2 at L/D = 5. The temperature then decreases to a ratio of about 1.6 at the end of the catalyst bed.
As was argued in the previous chapter it can be assumed that liquid is present up to a distance of at least L/D = 2 from the injector and no liquid is present beyond L/D = 3. The decrease in temperature towards the end of the catalyst bed is most likely due to non-adiabatic effects. The simulated liquid

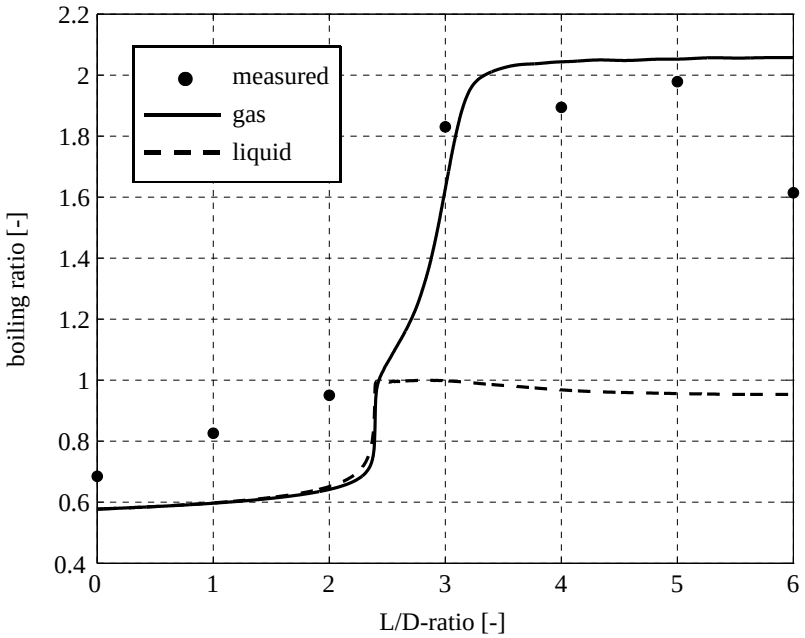

Figure 6.2: *Temperature ratio of experimental data at the centre of the bed and numerical results for the 1D-model*

and gas temperature are almost the same for temperature ratios below one. In this part of the catalyst bed the gas temperature is mainly the result of decomposition in the liquid phase as can be deduced from the Arrhenius parameters given in tables 3.2 and 3.3. The simulated liquid temperature does not exceed a boiling ratio of one, whereas the gas temperature rises to about 2 and stays almost constant in the remainder of the catalyst bed.

The figure also shows a large difference between measured and simulated temperature for L/D < 3.

parameter	**value**	**unit**
density	3984	kg m^{-3}
heat capacity	755	J kg^{-1} K^{-1}
thermal conductivity	33	W m^{-1} K^{-1}

Table 6.1: *Properties for α-alumina pellets [144]*

This is most likely caused by neglecting the thermal mass and heat transport in the catalyst pellets. This is supported by data shown in figure 6.3, which shows the cell Péclet number for thermal diffusion as a function of the L/D-ratio as well as the thermal diffusivity defined as $k/\rho c_p$ for both fluids. Here the Péclet number is defined as $\mathrm{Pe} = u\Delta L/\beta_T$ where ΔL is the length of the control volume and β_T the thermal diffusivity. First of all figure 6.3 shows that thermal diffusion in both fluids can safely be neglected as Pe_g and Pe_l, the Péclet number of the gas and liquid respectively, is well above 10 except Pe_g for L/D < 0.5. But as will be shown later, for this part of the catalyst bed the gas volume fraction is low and consequently the effect of thermal diffusion in the gas phase very small. $\beta_{T,g}$ and

$\beta_{T,l}$ are the thermal diffusivities for the gas and liquid, respectively. This is compared to a thermal diffusivity of $1.1 \cdot 10^{-5}$ for the pellets based on values for ρ, c_p and k for the pellets as given by table 6.1. For L/D < 3 this is almost one order of magnitude higher than the thermal diffusivity for the gas phase and two orders of magnitude higher than the thermal diffusivity of the liquid phase. It shows that for L/D < 3 the thermal diffusion inside the pellets is significant and cannot be neglected. The difference between measured and simulated temperature could thus be explained by the thermal soak back in the pellets from the hot part of the catalyst bed to the cooler part close to the injector. For L/D $>= 3$, which coincides with the part of the catalyst bed where the boiling ratio is larger than unity, transport by convection is far more important and thermal diffusion can be ignored.

The measured and simulated pressure as a function of the distance from the injector in L/D-ratios is

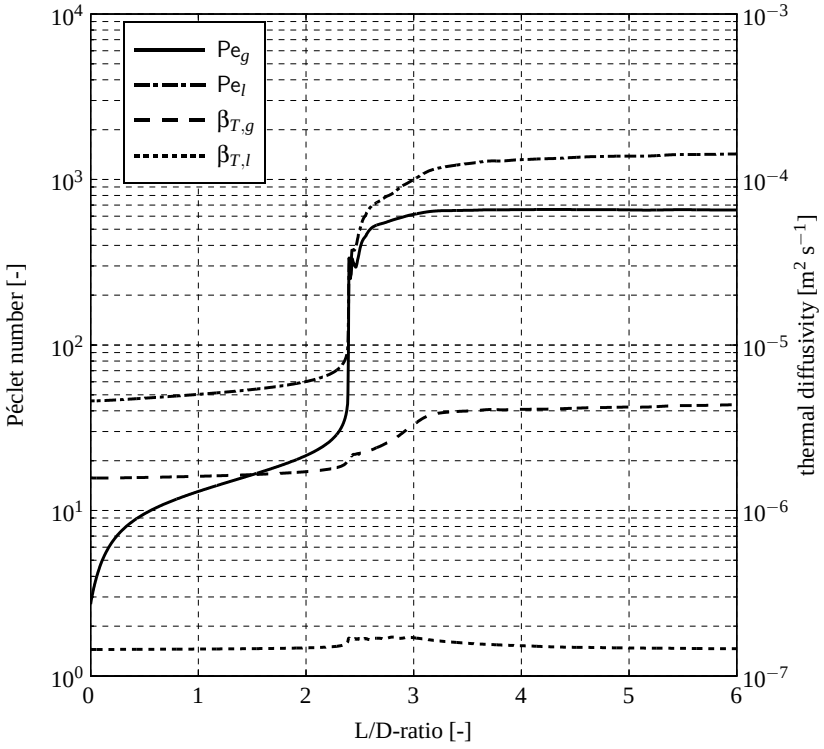

Figure 6.3: *Cell Péclet numbers*

shown in figure 6.4 where the pressure is divided by the outlet pressure to make it non-dimensional. Experimental data are plotted in the same way as in the previous chapter, see figure 5.4. The solid line represents the simulation result.

For the latter, two regions can be distinguished: a region where the pressure hardly changes and a region where the pressure decreases more rapidly with distance. The pressure hardly changes close to the injector and coincides with the part of the catalyst bed where liquid is present as discussed above. The part of the catalyst bed where the pressure does change coincides with the part that was identified above as the part where only gas is present. A small transition region between the two regions exists. In section 3.1.2 the equilibrium constant K_r was introduced for catalytic decomposition. It was men-

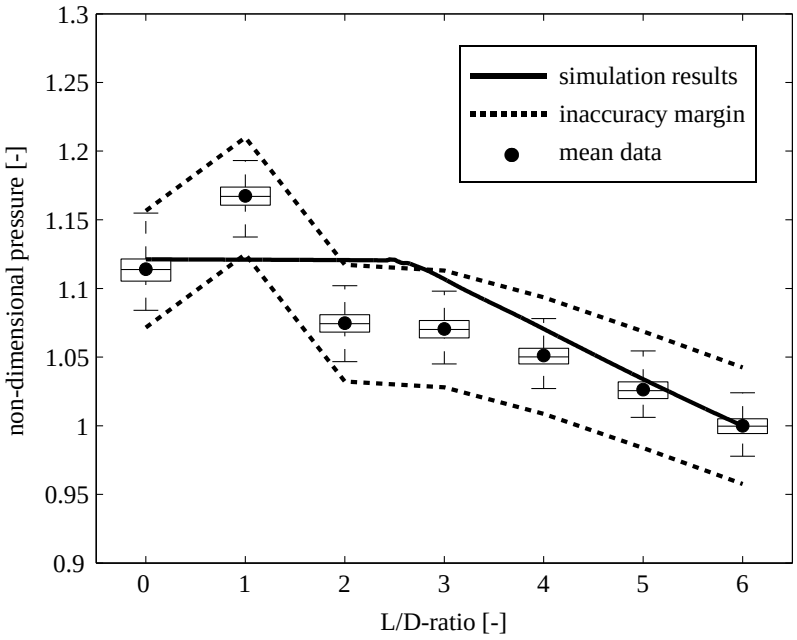

Figure 6.4: *Measured and simulated pressure data for the 1D-model*

tioned that a value has to be found experimentally. The value influences the location at which the liquid temperature reaches a boiling ratio of one and the gas temperature its maximum temperature of about $965K$. The higher the value of K_r, the higher the reaction rates will be, see equation 3.17 and 3.28, the closer to the injector this location will be. And the closer this location is to the injector, the larger the pressure drop over the catalyst bed will be as a larger portion of the bed contains gas, which is responsible for most of the pressure drop. The simulations shown in figures 6.2 and 6.4 were obtained with values of $K_r = 3$ for the liquid and $K_r = 400$ for the gas.

Figure 6.5 shows the location at which the boiling ratio is unity for the first time as a function of the equilibrium constant for the liquid phase. Also shown on the vertical axis is the percent deviation from the measured pressure drop over the catalyst bed for a given equilibrium constant. A similar plot for the gas equilibrium constant is shown in figure 6.6. The vertical axis on the left side shows the distance between the point where the boiling ratio is unity for the first time and the point where the gas temperature reaches 95% of the maximum gas temperature for the first time. The vertical axis on the right side shows the percent deviation from the measured pressure drop over the catalyst bed. Note that the results for the gas phase are not as smooth as for the liquid phase. This has to do with the small fluctuations in temperature at the boiling point as explained above.

The value for $K_{r,l}$ should be chosen such that the L/D-ratio where the boiling ratio reaches unity for the first time is close to but larger than 2 for a minimum percentage deviation in pressure. A value of $K_{r,l} = 3.3$ is chosen for the liquid equilibrium constant, which gives a distance of L/D ≈ 2.5 and a pressure overestimation of just under 1%. Based on the measured temperature in figure 6.2, the distance between the point where the boiling ratio is unity for the first time and the point where the

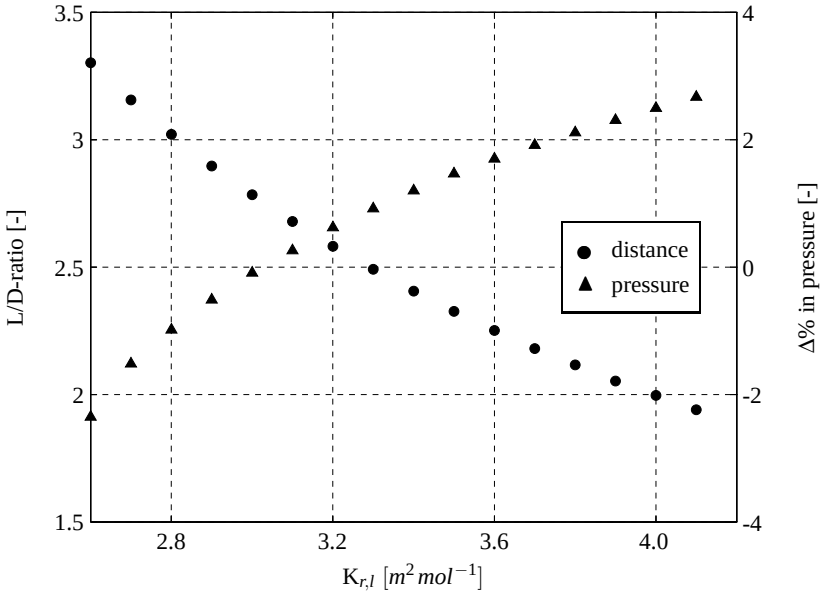

Figure 6.5: *Influence of liquid equilibrium constant on pressure and 'reaction' distance for the 1D-model*

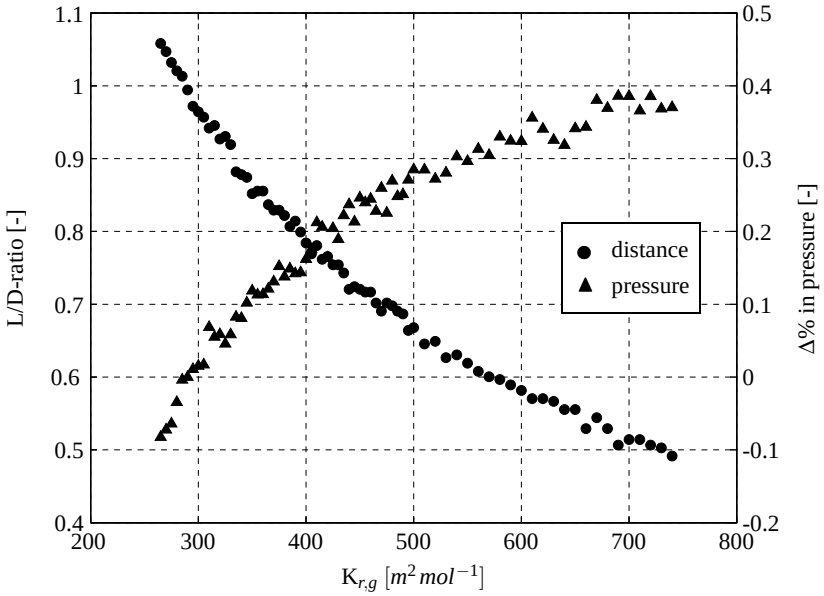

Figure 6.6: *Influence of gas equilibrium constant on pressure and 'reaction' distance for the 1D-model*

gas temperature reaches 95% of the maximum gas temperature for the first time is L/D $\approx$ 0.8. An equilibrium constant for the gas phase of $K_{r,g} = 400$ gives a distance of slightly less than 0.8 and an overestimation of the pressure of about 0.2%. As can been seen from figure 6.6 the model is not very sensitive to the value of the gas equilibrium constant, but much more sensitive to the liquid equilibrium constant, see figure 6.5.

In section 3.2.3 the multicomponent evaporation model was presented. The volume equivalent radius $r_{V,A}$ was introduced as a scaling factor to account for the presence of other components at the droplet surface. It was argued that due to the different modes of evaporation in the catalyst bed and due to the consumption of peroxide by decomposition that this factor should be determined experimentally. $r_{V,A}$ has an influence on the maximum gas temperature and the pressure as is shown in figures 6.7 and 6.8. In both plots the vertical axis on the left side shows the percentage deviation of maximum achieved gas temperature of 965K for 0.875 hydrogen peroxide as determined with the properties from appendix B. Here the percentage deviation is calculated as

$$T\Delta\% = \frac{T_{ad} - T_{max,sim}}{T_{ad} - T_{inlet}}, \tag{6.1}$$

where T_{ad} is the adiabatic decomposition temperature, $T_{max,sim}$ the maximum simulated temperature and T_{inlet} the inlet temperature. The axis on the right side shows the percentage deviation from the measured pressure drop over the catalyst bed. The simulations shown in figures 6.2 and 6.4 were obtained with values of $r_{V,H_2O_2} = 0.5$ for the liquid and $r_{V,H_2O} = 3$ for the gas.
The values for $r_{V,A}$ should be set such that the maximum simulated temperature is as close as possible to the adiabatic temperature, while keeping the deviation in simulated pressure from measured pressure as small as possible. Based on these restrictions for hydrogen peroxide a value of $r_{V,H_2O_2} = 0.5$ was set and for water a value of $r_{V,H_2O} = 2.5$.

Substituting the experimentally determined value for the equilibrium constants, K_r, and volume

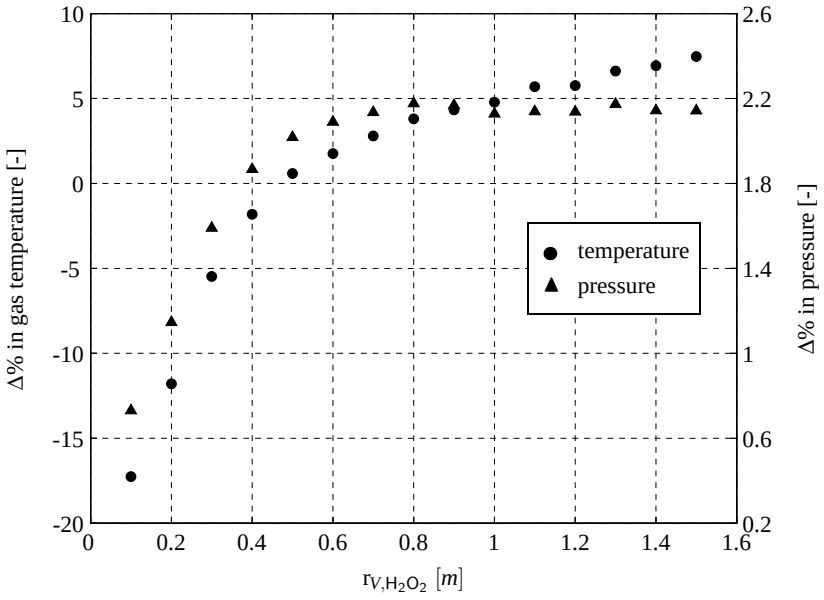

Figure 6.7: *Influence of r_{V,H_2O_2} on pressure and gas temperature*

equivalent radius, r_V, into the model results in a pressure and temperature profile as shown in figures 6.9 and 6.10. Figure 6.9 shows the temperature normalised to the local boiling temperature

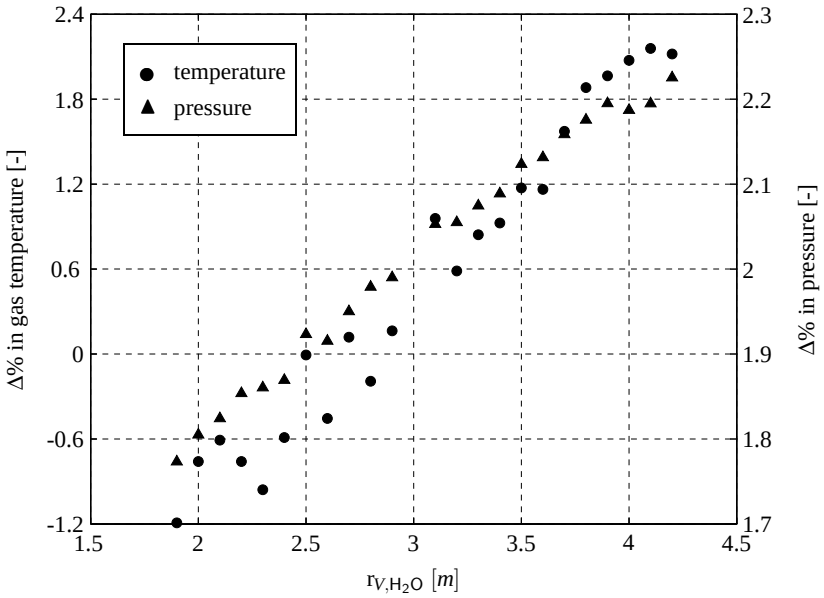

Figure 6.8: *Influence of r_{V,H_2O} on pressure and gas temperature*

together with the experimental data as a function of the distance from the injector. Figure 6.10 shows the same for pressure data normalised to the bed exit pressure. Note that the sudden change in pressure drop gradient is at the same location as the sudden increase in gas and liquid temperature.

The temperature below a boiling ratio of 1 currently cannot be predicted accurately as was explained above, but the sudden increase in temperature and the distance over which this increase takes place shows reasonable agreement with experimental data. Despite the fact that the model assumes adiabatic conditions, the location of the maximum temperature is predicted reasonably well.

The overall deviation between measured and simulated pressure drop over the catalyst bed is less than 2.5%, where the measured pressure drop was 1.27bar absolute. The pressure drop gradient is slightly underestimated for the part of the catalyst bed where the boiling ratio is less than unity and slightly overestimated for the rest of the catalyst bed. However, the simulated pressure drop is for most part within the accuracy uncertainty of the measurements.

6.2 Typical Steady State Results

With the validated 1D-model, a steady state simulation was performed with the same geometry as the instrumented catalyst bed and initial and boundary conditions as shown in table 6.2. The initial concentration of hydrogen peroxide was 0.875 and the initial mass fraction for gaseous hydrogen peroxide, water vapour and oxygen were all set to 0.001 with the rest of the gas being air.

Figure 6.11 shows the results for the gas and liquid temperature and gas volume fraction. The vertical axis on the left side shows the temperature as a fraction of the maximum temperature which can be

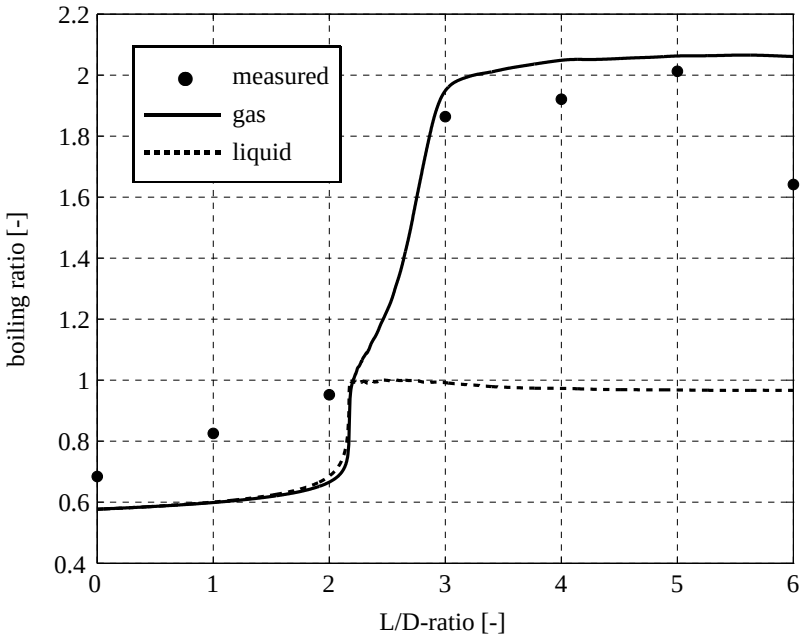

Figure 6.9: *Temperature ratio after tuning the 1D-model*

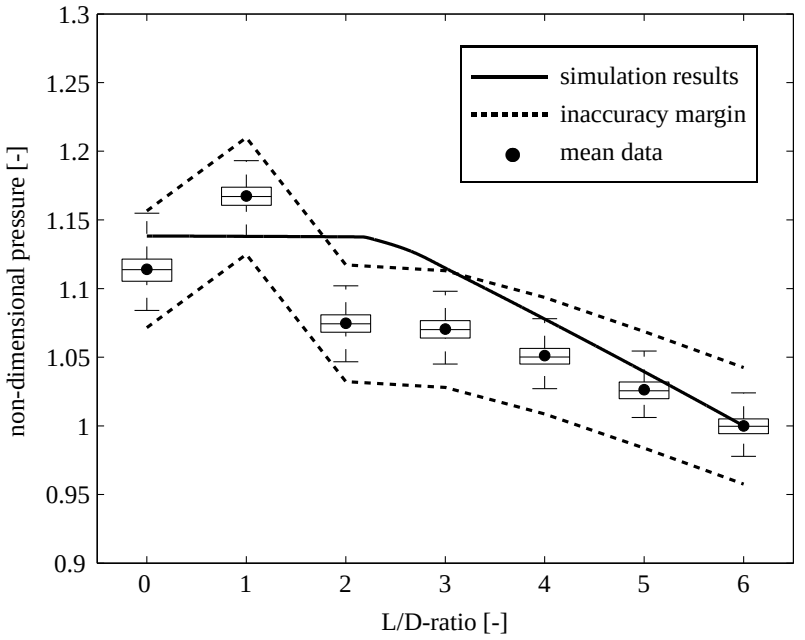

Figure 6.10: *Pressure data after tuning the 1D-model*

expressed in a similar way as equation 6.1

$$T_{k,rel} = \frac{T_{k,sim} - T_{k,inlet}}{T_{k,max} - T_{k,inlet}}, \tag{6.2}$$

parameter	value	unit
catalyst bed length	96	mm
catalyst bed diameter	16	mm
pellet shape	cylindrical	-
pellet length	3.35	mm
pellet diameter	3.22	mm
inlet liquid mass flux	50	kg m^{-2} s^{-1}
inlet gas velocity	0.07	m s^{-1}
inlet temperature	293	K
gas inlet volume fraction	0.05	-
bed exit pressure	10	bar

Table 6.2: *Geometry, initial and boundary conditions for the 1D-model*

where $T_{k,sim}$ is the simulation result of the temperature, $T_{k,inlet}$ the inlet temperature and $T_{k,max}$ the local boiling temperature when the liquid phase is considered and the adiabatic decomposition temperature when the gas phase is considered. The vertical axis on the right side shows the gas volume fraction. Both temperatures and gas volume fraction are plotted against the distance from the injector expressed in L/D-ratios. Note that due to a different normalisation of the gas temperature, the result presented in figures 6.2 and 6.9 differs from the result shown in figure 6.11.

The liquid temperature gradually increases from zero until 0.2 from the injector up to L/D = 1.5 after

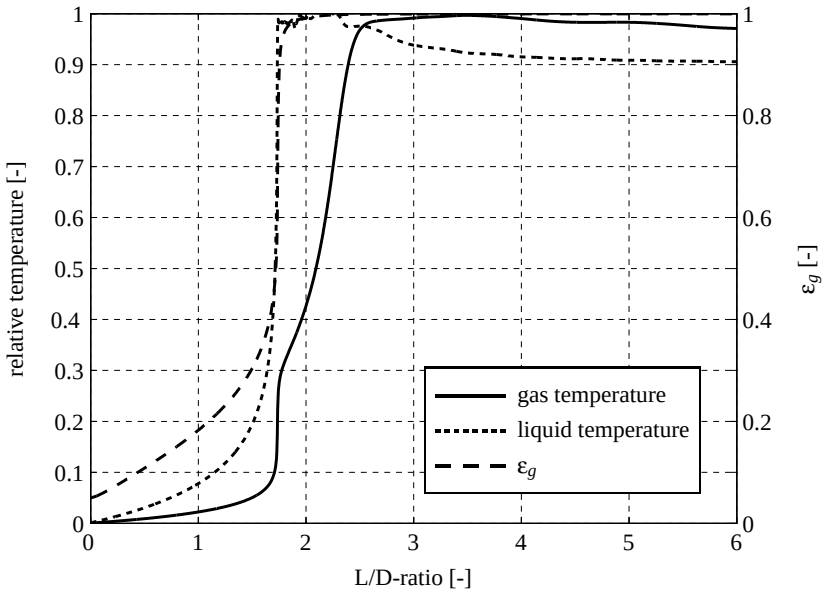

Figure 6.11: *Temperature and gas volume fraction for the 1D-model*

which a sharp increase to about 1 is observed over a distance of just L/D = 0.25. It stays at its boiling point for a distance of about L/D = 0.5 and then gradually decreases to a value of about 0.9. The gas

volume fraction shows the same initial behaviour as the liquid temperature. It increases gradually to about 0.3 at L/D = 1.5 from the injector and then a very rapid increase to nearly 1 over a distance of just L/D = 0.25. The gas temperature shows an initial gradual increase to about 0.05 at L/D = 1.5. Then a sharp increase to about 0.3 is observed over a distance of about L/D = 0.25 and then a less sharp, but still significant, increase to 0.95 over a distance of L/D = 0.75. From L/D = 2.5 the increase in gas temperature is gradual until it reaches its maximum temperature at about L/D = 3.5. After that the temperature slowly decreases, despite the fact that the system is assumed to be adiabatic. The reason for this is the heat transfer between the gas and the liquid, which causes the gas temperature to slowly decrease while the liquid temperature reaches a constant temperature for L/D > 4. Note that the gas volume fraction is not exactly one and consequently there is still a small amount of liquid left. This is also shown in figure 6.12 in which the liquid volume fraction is plotted on a log scale as a function of the distance from the injector. The decrease in liquid volume fraction is slowed down from about L/D = 2.5 onwards. As there is still evaporation taking place in the liquid phase, which consumes heat, the liquid is not heated up and an equilibrium is reached between the energy transferred from the gas to the liquid and the energy consumed by evaporation.

Figures 6.11 and 6.12 also provide a solid indication that the method to stabilise the scalar equations,

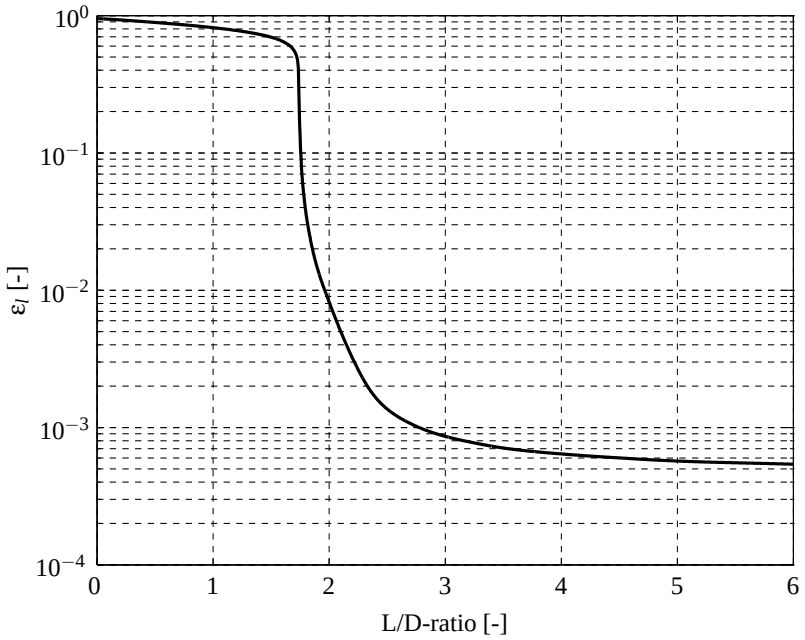

Figure 6.12: *Liquid volume fraction as a function of the distance from the injector for the 1D-model*

as proposed by Oliveira and Issa [132] and further developed in section 4.2.2, works, of which the lack of oscillations for a liquid volume fraction approaching zero is proof. It furthermore shows that even in an adiabatic catalyst bed a maximum gas temperature exists, which is very close but not equal to the adiabatic decomposition temperature, in cases where there is a small amount of liquid left. This result cannot be reproduced in a mixture model as the energy of the mixture is considered and not of

each fluid separately. Heat transfer between the fluids is only possible in a two-fluid model.
The increase in gas temperature beyond L/D-ratio = 1.75 until the maximum as temperature is reached, is caused by decomposition in the gas phase. Proof of this is shown in figure 6.13, which shows the gas mass fractions as a function of the L/D-ratio. Note that the mass fraction of air is not shown. At L/D = 1.75 the peroxide vapour mass fraction suddenly increases to about 21% as soon as the liquid temperature is at the boiling point. The corresponding mole fraction of peroxide vapour at this point is about 0.15. In section 1.3.1 it was mentioned that in the neighbourhood of a suitable catalyst hydrogen peroxide can explode spontaneously if the mole fraction is higher than a certain threshold value [17]. This value depends on the pressure, see also appendix B.9. It was found that between 3 and 7*bar* the threshold value was constant at a mole fraction of 0.207. The peroxide vapour mole fraction of 0.15 from the simulation stays well below this ignition limit and explains why a catalyst bed decomposing 0.875 peroxide does not explode. It should be noted that Satterfield et al. [17] did not conduct any experiments at a pressure over 7*bar*, but that the experiments at 3*bar* and higher suggested that the critical mole fraction would stay constant. As soon as the gas volume fraction is nearly 1, the peroxide vapour mass fraction reaches its maximum and subsequently decreases until it is almost zero at L/D-ratio = 2.5. At this point the peroxide is practically fully decomposed.
In section 3.2.1 the boiling diagram was introduced showing the equilibrium hydrogen peroxide gas concentration for a given liquid peroxide concentration. Figure 3.2 shows the boiling diagram at atmospheric pressure and in appendix B the boiling diagrams for other pressures is shown. Comparing these figures with figure 6.13 reveals that in reality there is no equilibrium. This supports the choice to employ two-fluid models rather than mixture models to describe what is happening inside the catalyst bed.

When the gas volume fraction is nearly one, a negligible amount of liquid hydrogen peroxide will evaporate. As decomposition in the gas phase continues, peroxide is consumed and energy is released, which causes the peak in peroxide vapour mass fraction. Also shown in figure 6.13 is that initially the gas phase composition is mainly oxygen indicating that the majority of the mass transfer is caused by decomposition. At the boiling point a lot of steam and peroxide vapour is generated due to evaporation causing a sharp decrease in the oxygen mass fraction and a sharp increase in the hydrogen peroxide vapour and steam mass fraction.
In section 3.3 a model was introduced to describe the pressure drop resulting from the interaction between the fluids and the fluids with the catalyst bed. In section 5.3 it was shown that there was a large difference of the predictive capabilities depending on whether the Ergun equation or the Tallmadge equation was used as the basis for the pressure drop model. However, the model from the previous chapter was a single control volume model and consequently cannot take into account any changes in fluid properties. Besides that, in the past several researchers have proposed different constants for the Euler equation, which they claimed to give better results. For these reasons, the difference between

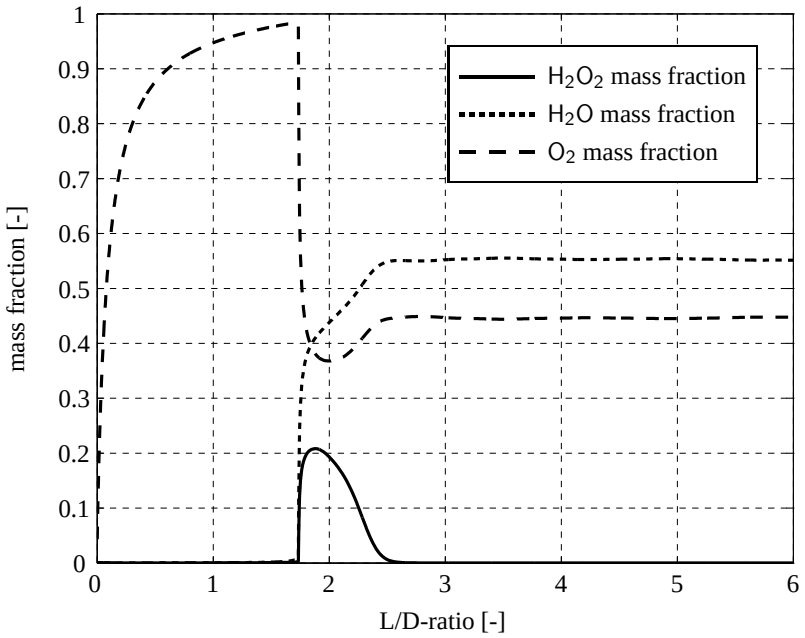

Figure 6.13: *Gas mass fractions results*

the Ergun and Tallmadge equation is revisited. For this purpose the Ergun equation is written as

$$\frac{\Delta p}{L} = \left(\frac{A}{\mathrm{Re}} + B\right) \frac{1-\varepsilon_f}{\varepsilon_f^3} \frac{\rho u^2}{D_p}, \tag{6.3}$$

where in the original Ergun equation $A = 150$ and $B = 1.75$. Macdonald et al. [145] tested this equation against several sets of experimental data and modified the constants A and B to $A = 180$ and $B = 1.8$–4 where the exact value of B is dependent on how smooth the particles are. To investigate the influence of the different pressure models on the overall pressure drop as well as to investigate the difference between mixture and two-fluid models, the mixture pressure gradient has been computed based on the results for the two-fluid model. For this purpose first the mixture density, ρ_m, and mixture velocity, u_m, were determined by

$$\rho_m = \varepsilon_g u_g + \varepsilon_l u_l \tag{6.4}$$

$$u_m = \frac{\varepsilon_g \rho_g u_g + \varepsilon_l \rho_l u_l}{\rho_m}. \tag{6.5}$$

ρ_m and u_m were then substituted into equation 6.3. The result of this was then divided by the pressure gradient as was computed by the two-fluid model. The resulting pressure gradient for mixture models for the original Ergun equation, the Ergun equation with the modification proposed by Macdonald et al. [145] and the modification proposed by Tallmadge [122] is shown in figure 6.14. For the parameter B for the Macdonald modification the value $B = 1.8$ was used, corresponding to smooth pellets. In this figure the gradients are divided by the gradient as computed by the two-fluid model, a pressure

gradient ratio higher than 1 means that a higher pressure drop is achieved.

First of all it is evident that original Ergun equation as well as the modification proposed by Macdon-

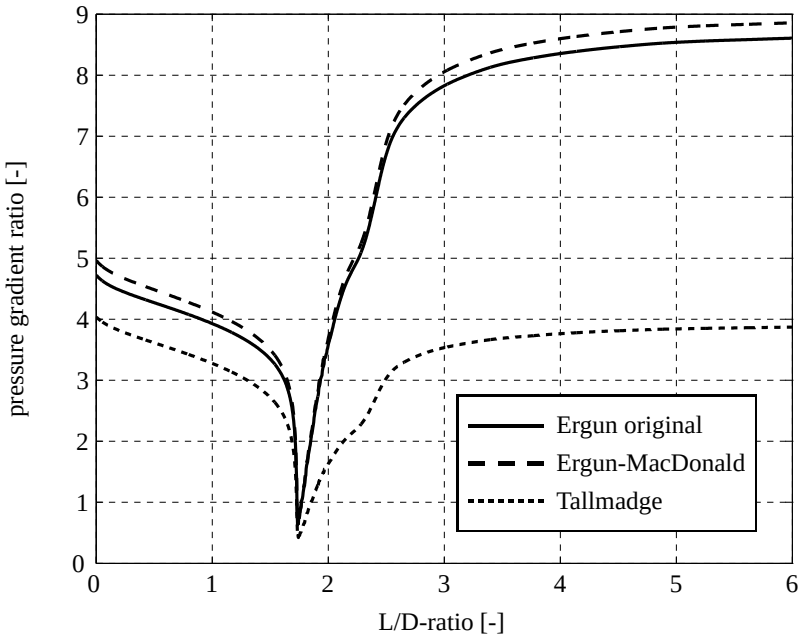

Figure 6.14: *Pressure gradient ratio for several mixture pressure drop models*

ald et al. [145] result in very much higher pressure gradients than the extension proposed by Tallmadge [122]. Especially when the gas temperature approaches its maximum, the Tallmadge equation gives a pressure gradient which is at least a factor 2 lower. Also shown is that the Macdonald modification results in higher pressure gradients than the original Ergun equation. Note that in this plot smooth pellets were assumed. For less smooth pellets the value for B would increase resulting in even higher gradients.

The second point that becomes clear from this plot is that all mixture models give a higher pressure gradient than the two-fluid model except for a small region around L/D $= 1.75$. Only in the region where the temperature reaches the boiling point for the first time is the ratio lower than unity.

The reason for this difference can be explained with figures 6.12 and 6.15. The latter shows the gas and liquid phase velocity as computed by the two-fluid model divided by the mixture velocity u_m determined by equation 6.5. From the result 1 is subtracted to enhance the readability: values below zero indicate a velocity less than the mixture velocity and values above zero indicate values higher than the mixture velocity.

The relative gas velocity in figure 6.15 is about 0.17 beyond $L/D = 3$, which means that it is about 17% higher than the mixture velocity. As can be seen, in the part of the catalyst bed where liquid is present the difference between the gas velocity and the mixture velocity is very large. The relative liquid velocity is about -0.92 or 92% lower than u_m. As is shown in figure 6.12, there is still a small amount of liquid left in the catalyst bed. Consequently, part of the pressure gradient is due to the

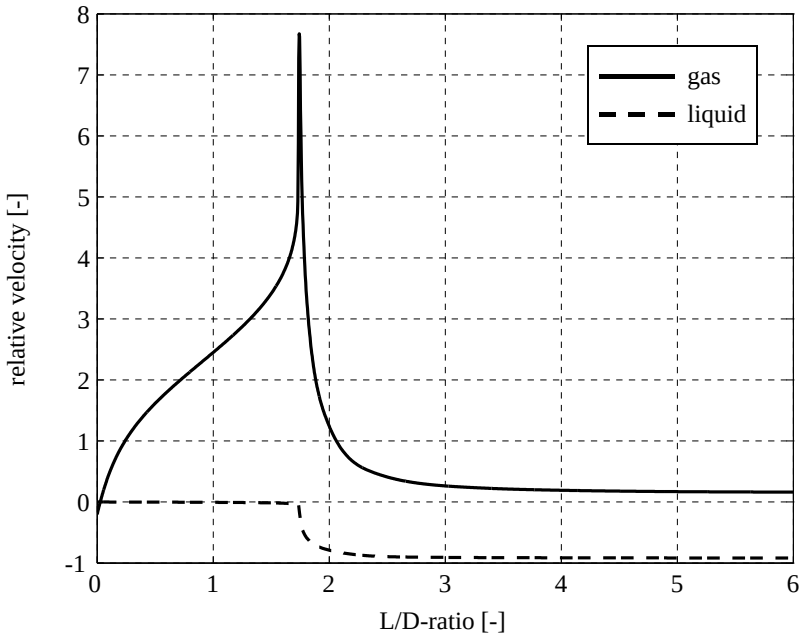

Figure 6.15: *Gas and liquid velocity relative to the mixture velocity*

(higher than u_m) gas velocity and part due to the (lower than u_m) liquid velocity.
About 90% of the total mass transfer between the gas and liquid phase takes place in a very narrow section of the catalyst bed: for the current simulation it is $1.75 < \text{L/D} < 2$ as is shown in figure 6.16. The solid line in this figure indicates the cumulative mass transfer as a function of the distance to the injector. Only a small amount, less than 5%, takes place between the inlet and $\text{L/D} = 1.75$. Also shown is the relative contribution of decomposition, mass transfer due to formation of oxygen during decomposition of the liquid phase, and evaporation. Evaporation accounts for the majority of the mass transfer: about 90%. It should be noted that despite it being the major mode of mass transfer, it becomes important only after the liquid approaches the boiling point. This is shown in figure 6.17, in which the ratio is shown of the cumulative decomposition to the total mass transfer and the cumulative total mass transfer. This plot supports the argument given earlier that decomposition is responsible for the mass transfer close to the inlet.
Based on these plots three regions can be distinguished inside the catalyst bed. These are:

- pre-boiling region: from the injector to the point where the liquid reaches the boiling point for the first time,
- rapid conversion region: from the point where the liquid reaches the boiling point for the first time to the point where the gas volume fraction is more than 0.99,
- dry-out region: from the point where the gas volume fraction is more than 0.99 to the outlet.

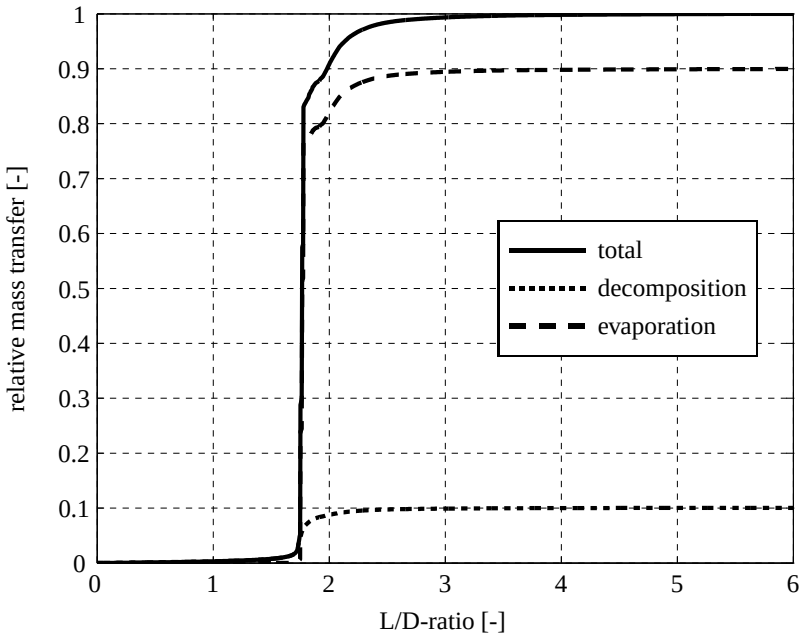

Figure 6.16: *Cumulative relative mass transfer*

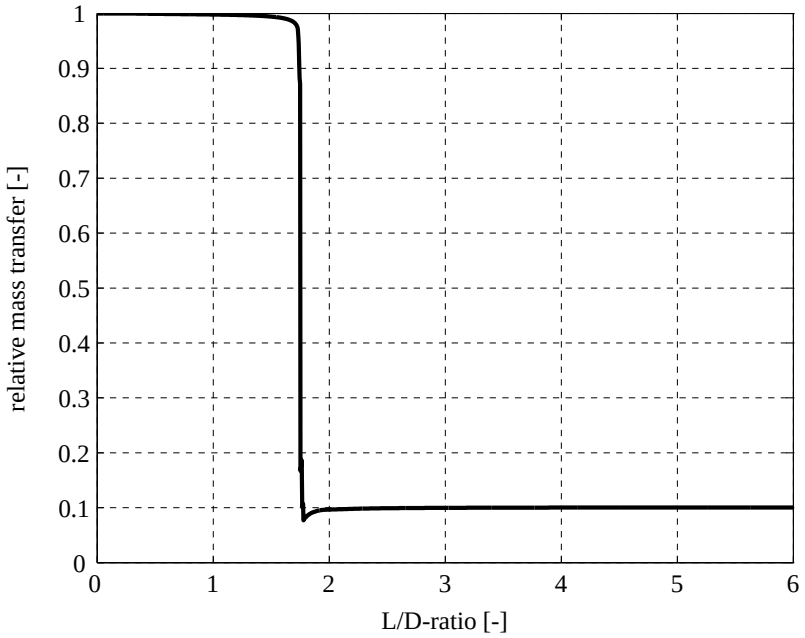

Figure 6.17: *Relative contribution of decomposition to mass transfer*

In the pre-boiling region decomposition accounts for most of the mass transfer between the gas and liquid, but accounts for only a small fraction of the total mass transfer in the catalyst bed. Despite that, the gas volume fraction increases significantly. In the rapid conversion region about 90% of the total mass transfer takes place mainly by means of evaporation. This is also the region where there is

the largest liquid temperature increase and where the gas volume fraction becomes nearly unity. The dry-out region is characterised by a significant increase in gas temperature and only a small amount of mass transfer.
The three regions identified above can also be identified in the works by Zhou and Hitt [61] and Pasini et al. [64]. The results presented by Zhou and Hitt [61] also show a very rapid increase in temperature from well below the boiling point to a temperature far above it. However, any information on the gas and liquid volume fractions cannot be obtained from their model. Also the relative contribution of each transfer mode cannot be obtained. The results presented by Pasini et al. [64] show a gradual increase in temperature and an almost linear variation in pressure drop. Similar to the work of Zhou and Hitt, no information is available on volume fractions. This shows once more the advantages of the two-fluid model.

6.3 Sensitivity Analysis of Arrhenius Parameters and Interfacial Area

In section 3.1 values have been selected that are believed to be most suitable as Arrhenius parameters for the different modes of decomposition. An interfacial area model has been introduced in section 4.1 to estimated the surface area between the different phases. Both have in common that the actual values are highly uncertain. In both cases it was therefore mentioned that a sensitivity analysis would be performed to assess the impact of variations in these values on the catalyst bed performance.

6.3.1 Variations in Arrhenius parameters

In section 3.1 the Arrhenius parameters have been introduced. It was shown that the values used for these parameters by different researchers vary many orders of magnitude. In this work a set of values has been chosen which are believed to give a representative description of the catalyst activity. To investigate how sensitive the choice of these values are on the overall catalyst bed performance, each Arrhenius parameter is varied parametrically.
From section 6.2 it has become clear that most of the liquid to gas conversion takes place in a very small region of the catalyst bed. The change of this location for varying Arrhenius parameters for liquid decomposition is shown in figure 6.18. The difference in Arrhenius parameter and corresponding change in location is expressed in fractions of the normal value, where the normal value is obtained for Arrhenius parameters as listed in tables 3.2 and 3.3. Note that a negative value for the conversion location means that this location moves upstream towards the injector. The plot is the result of several simulations where for each simulation just one of the parameters is varied while keeping the other parameters at their initial value.

From the plot it becomes immediately clear that the location of rapid conversion is very sensitive

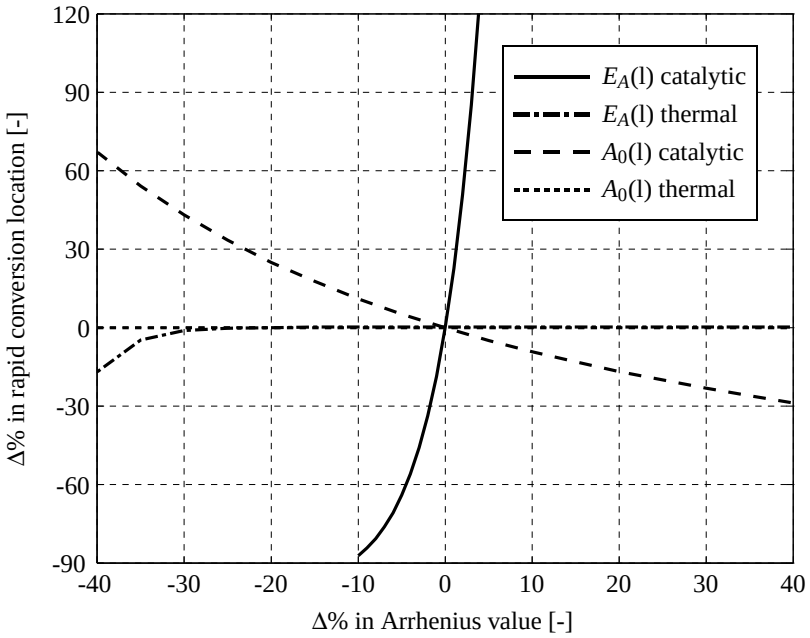

Figure 6.18: *Change in rapid conversion location for changing Arrhenius parameters for the liquid phase*

to the activation energy for liquid catalytic decomposition. It is also sensitive to the pre-exponential factor for liquid catalytic decomposition, but not to the same extent. This is to be expected as the reaction rate is exponentially dependent on the activation energy, see equations 3.17 and 3.28. The location of rapid conversion is also sensitive to the activation energy for liquid thermal decomposition, but only if its value is low enough. No dependency for A_0 for liquid thermal decomposition is shown for the range of values that have been investigated. This means that the location of rapid conversion is determined by liquid catalytic decomposition and that, as a simplifying assumption, thermal decomposition of the liquid phase can be neglected without influencing the results.

Figure 6.13 shows the mass fractions in the gas phase. To study the effect of changing Arrhenius parameters the change in location of the maximum mass fraction for gaseous peroxide is used as well as the point where the peroxide mass fraction drops below 0.02 after the peak. These two points are related to the temperature profile of the gas phase, plotted in figure 6.11. The location of the maximum gaseous peroxide mass fraction is the same as the location where the rapid conversion from liquid to gas takes place. At this location the gas temperature rapidly changes to a value equal to the boiling temperature of the liquid. Note that at this point the simulated gas is very close to the simulated liquid temperature. After this point the simulated liquid temperature stays practically constant while the simulated gas temperature sharply increases to about 98% of its maximum value at L/D = 2.5. At this point most of the gaseous peroxide is consumed by decomposition and the gas mass fraction for hydrogen peroxide has dropped to about 0.02. Further downstream the gas temperature increases gradually until it has reached its maximum adiabatic decomposition temperature.

For changing Arrhenius parameters for the liquid phase the change in location of the maximum mass

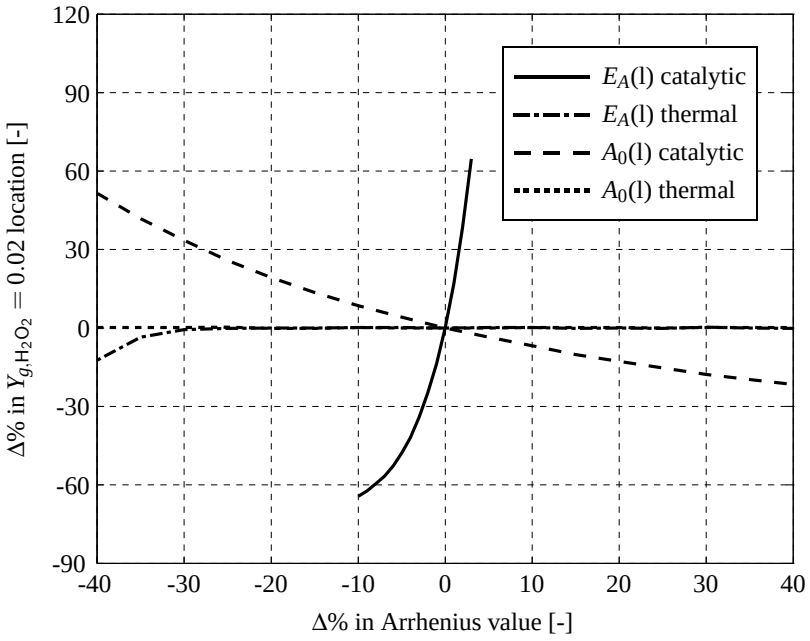

Figure 6.19: *Change in location of $Y_{g,H_2O_2} = 0.02$ for changing Arrhenius parameters for the liquid phase*

fraction for peroxide was found to be exactly the same as the for the location of rapid conversion, shown in figure 6.18 and therefore not plotted separately. The effect on the location of the point for $Y_{g,H_2O_2} = 0.02$ is shown in figure 6.19. Although the figure shows a similar pattern to figure 6.18 the change in location of $Y_{g,H_2O_2} = 0.02$ is slightly less sensitive to changing Arrhenius parameters; for higher reaction rates the distance between the maximum peroxide mass fraction and $Y_{g,H_2O_2} = 0.02$ becomes larger. The reason for this is that at higher reaction rates a smaller amount of peroxide evaporates. This results in a decrease in concentration for gaseous hydrogen peroxide, which reduces the reaction rates of gaseous decomposition: both for catalytic and thermal decomposition. The fact that there is a difference between the plots of $Y_{g,H_2O_2} = 0.02$ and the rapid conversion location indicates that the length over which gaseous hydrogen peroxide is present changes for different liquid Arrhenius parameters. In other words, the liquid Arrhenius parameters also affect the decomposition process in the gas phase. This is due to the amount of liquid peroxide that is evaporating. For lower activation energies and higher pre-exponential factors, more peroxide is decomposed instead of evaporated. The peak mass fraction of gaseous peroxide is thus lower and consequently requires less time to decompose.

The location of $Y_{g,H_2O_2} = 0.02$ is also dependent on the Arrhenius parameters of the gas phase. This is shown in figure 6.20. As for the liquid phase, catalytic decomposition is responsible for the largest changes in location, however, thermal decomposition plays a more important role than in the liquid phase and catalytic decomposition is slightly less sensitive to changes in Arrhenius parameters. It is

to be expected that thermal decomposition becomes more prominent for higher peroxide inlet concentration as the resulting gas temperature will be higher; see also figure A.6 in appendix A.

Finally, the influence of changing Arrhenius parameters for catalytic decomposition on the pressure

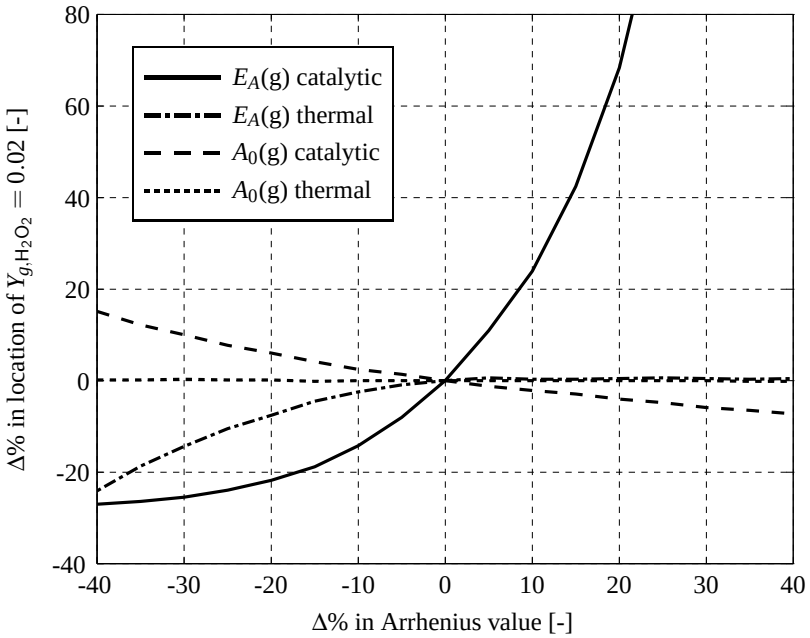

Figure 6.20: *Change in location of $Y_{g,H_2O_2} = 0.02$ for changing Arrhenius parameters for the gas phase*

drop in the bed is shown in figure 6.21. For liquid catalytic decomposition the shape is similar to the inverted shape shown in figure 6.18. As the gas phase is dominating in contributing to the pressure drop over the bed, a change in location of rapid conversion immediately results in a similar change in pressure drop. The sensitivity of catalytic decomposition in the gas phase is much less, but still present. The reason for this is that for higher reaction rates the gas temperature is higher closer to the injector. Consequently, a larger part of the catalyst bed experiences a high gas temperature and thus high gas velocity, which results in a higher pressure gradients.

This sensitivity analysis shows that the state inside the catalyst bed is highly sensitive to the choice of Arrhenius parameters, primarily those for catalytic decomposition but for liquid catalytic decomposition in particular. However, as has been pointed out in section 3.1 several researchers have used Arrhenius parameters with units that are not consistent. Those values that have been reported do not mention the number of active sites present on the catalyst under consideration. A difference in manufacturing conditions can lead to a difference in number of active sites, which then results in different values for Arrhenius parameters. The universality of published values of Arrhenius parameters is thus questionable.

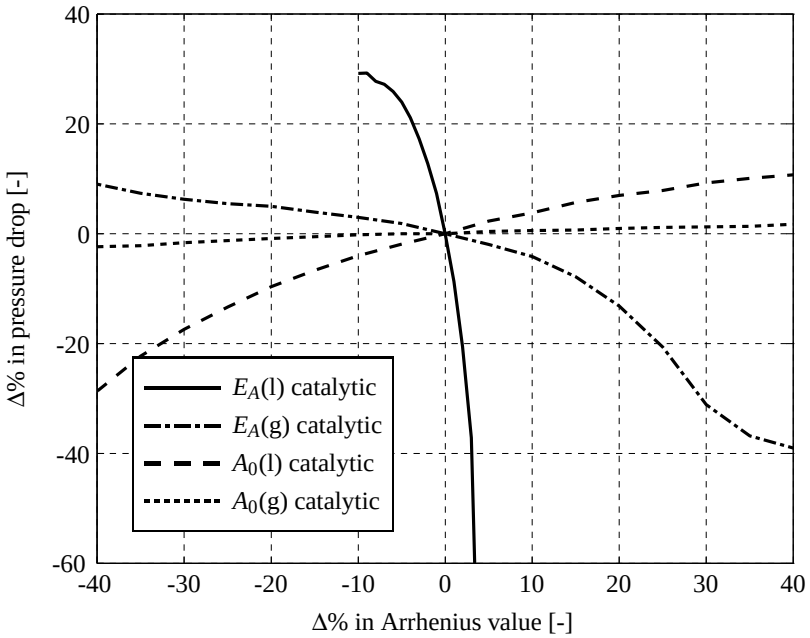

Figure 6.21: *Change in pressure drop for changing Arrhenius parameters for catalytic decomposition*

6.3.2 Variations in interfacial area

In section 4.1 an interfacial area model was developed. In this model it was assumed that the total catalytic surface area is made up by the surface area of the cylindrical part only, so neglecting the ends of each particle, and that the part of the pellet in contact with each fluid is dependent on the relative amount of each fluid present in the catalyst bed. This subsection investigates the influence of these assumptions on the catalyst bed performance. Note that for the dimensions of the pellets used during experimental validation, i.e. $D_p = 3.22mm$ and $L_p = 3.35mm$, taking into account the ends of the pellets would result in a total catalytic surface area that is about 48% higher than the assumed value.
Figure 6.22 shows the change in rapid conversion location as a function of a change in total catalytic surface area, designated as A_{tot}, A_{gl} and A_{sl}. Note that $A_{sg} = A_{tot} - A_{sl}$, so if A_{sl} decreases with x percent, A_{sg} will increase by the same amount. In the figure the line for A_{sl} is on top of the line for A_{tot}. As was shown in figure 6.17 decomposition accounts for almost all of the mass transfer in the pre-boiling region. From equation 3.28 can be seen that a change in catalytic surface area results in a corresponding change in reaction rate and thus in the location of the rapid conversion area. Note that from a catalytic decomposition point of view a change in A_{tot} has the same effect as a change in A_{sl}. Also shown in the figure is that there is no relation between the location of rapid conversion and A_{gl} as could be expected.

The change in location where the gas temperature reaches 95% of its adiabatic decomposition temperature, denoted as T_{95}, is shown in figure 6.23. It shows largely the same behaviour as in figure 6.22. In contrast with figure 6.22, for increasing A_{gl} the location of T_{95} moves closer towards the injector.

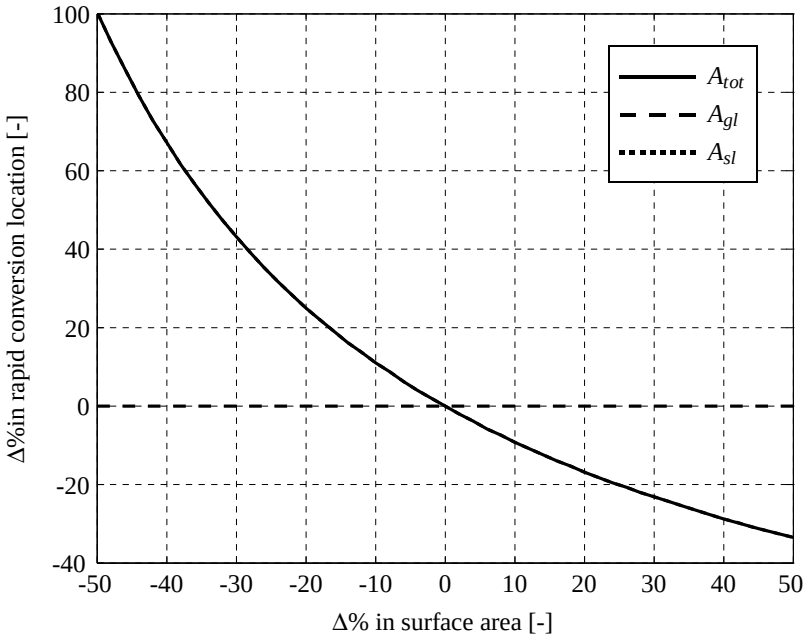

Figure 6.22: *Change in rapid conversion location for changing interfacial areas*

A larger gas-liquid surface area results in higher evaporation rates and thus higher higher gaseous peroxide mass fractions closer to the injector. However, the dependency is very weak and this suggests that the imbalance between the phases rather than the interfacial area is driving the evaporation. Comparing figures 6.22 and 6.23 reveals that most of the change in location of T_{95} is caused by the change in rapid conversion location. The additional change is directly related to the change in A_{gl}.

In the previous section it was explained that the locations where $Y_{g,\mathrm{H_2O_2}}$ reaches its maximum value and a value of 0.02 give a good indication of the state of the catalyst bed in the dry-out region. The change in these locations for varying A_{tot} and A_{gl} shows the same behaviour as shown in figure 6.22. Both locations vary with the same amount and in the same way for a change in surface area of A_{tot} and A_{gl} as shown in the plot. However, a change in A_{sl} results in a different behaviour of the locations for $Y_{g,\mathrm{H_2O_2}} = \max$ and $Y_{g,\mathrm{H_2O_2}} = 0.02$ as is shown in figure 6.24. The location for $Y_{g,\mathrm{H_2O_2}} = \max$ varies in exactly the same way as the rapid conversion location in figure 6.22; however, the location for $Y_{g,\mathrm{H_2O_2}} = 0.02$ does not. For smaller A_{sl} the location of $Y_{g,\mathrm{H_2O_2}} = 0.02$ moves away from the injector, but not as much as the location for $Y_{g,\mathrm{H_2O_2}} = \max$. This means that the part of the catalyst bed where hydrogen peroxide is present in gaseous form decreases for decreasing A_{sl}. For an increase in A_{sl} the part of the catalyst bed where hydrogen peroxide is present in gaseous form increases. The reason for this behaviour is that a decrease in A_{sl} results in an increase in A_{sg}. This means that the total surface area at which gaseous peroxide can catalytically decompose increases. From equation 3.28 it can be seen that this results in an increase in reaction rate and thus hydrogen peroxide is consumed faster. Note that the sensitivity of the location for $Y_{g,\mathrm{H_2O_2}} = 0.02$ for a change in A_{sl} is the same as the sensitivity of T_{95} as shown in figure 6.23.

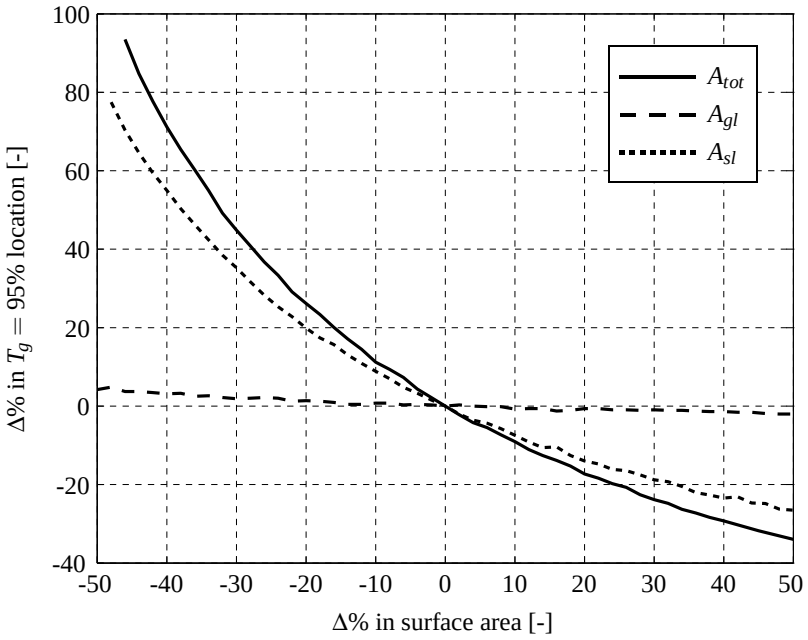

Figure 6.23: *Change in T_{95} location for changing interfacial areas*

In figure 6.16 it was shown how much of the interphase mass transfer was caused by decomposition

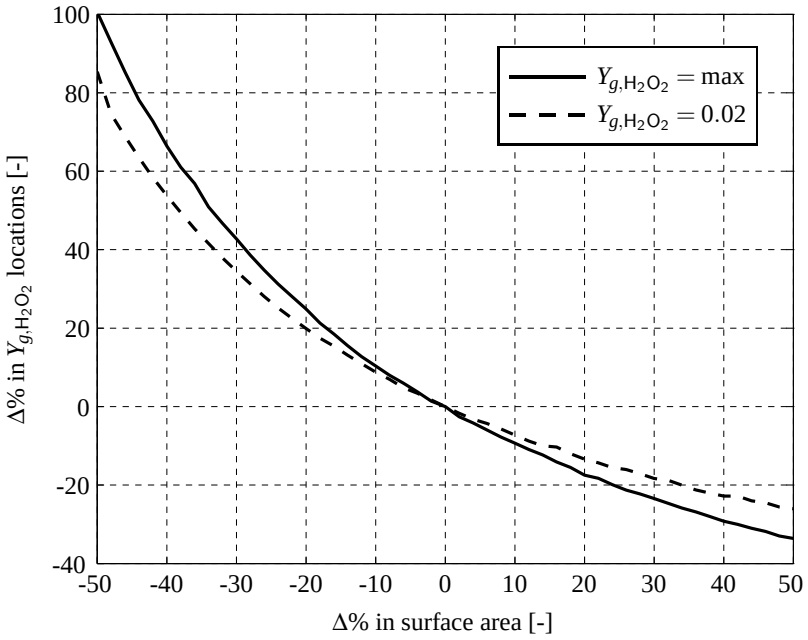

Figure 6.24: *Change in $Y_{g,H_2O_2} = max$ and $Y_{g,H_2O_2} = 0.02$ location for changing A_{sl}*

and evaporation. The change in the contribution from decomposition for changing surface area is shown in figure 6.25. Here the change is taken at the outlet of the catalyst bed. The first observation is that the points are scattered and do not lie on a line. The reason for this can be found in the fluctuating

evaporation rates as was explained at the beginning of section 6.1. A least squares analysis has been performed which is shown in the plot as well. In general, for increasing surface area the contribution from decomposition decreases indicating that the increase in mass transfer due to evaporation is stronger than the mass transfer due to decomposition. However, also note that although the surface area varies from -50% to +50%, the contribution from decomposition changes by about 5% at maximum.

From the sensitivity analysis on the interfacial area it can be concluded that the conditions in the

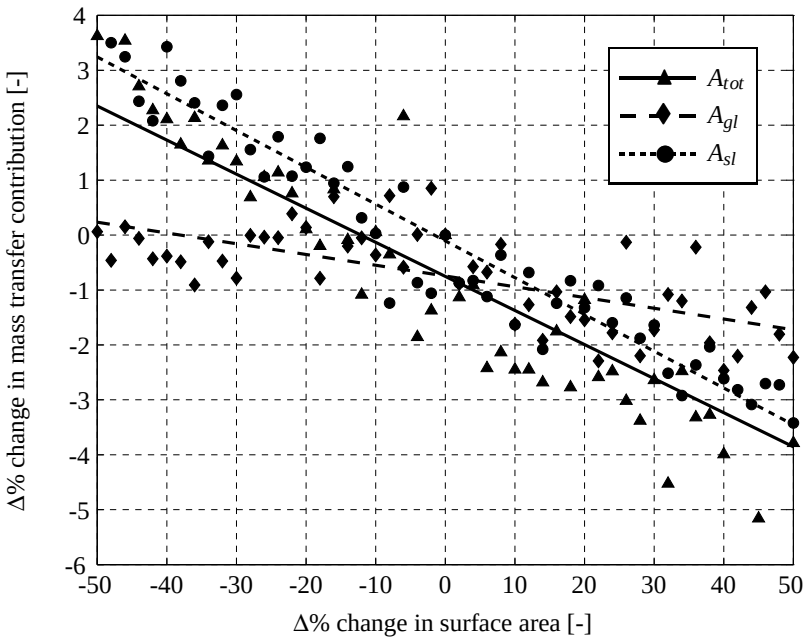

Figure 6.25: *Change in mass transfer contribution for changing interfacial areas*

catalyst bed are particularly sensitive to changes in A_{tot} and A_{sl}. Changes in A_{tot} result in a change the location of rapid conversion. The corresponding change in T_{95} and the locations for $Y_{g,H_2O_2} = \max$ and $Y_{g,H_2O_2} = 0.02$ change with the same amount. In principle the total catalytic surface area inside the catalyst bed should be relatively easy to determine with techniques such as X-ray tomography with the μ-vis facility of the University of Southampton [146]. Information about A_{sl} are harder to obtain, but very important at the same time as has been shown in this analysis. Hardly any sensitivity has been found to changes in A_{gl}. This is due to the fact that evaporation is driven due to non-equilibrium between the phases rather than due to equilibrium conditions at the interface.

Chapter 7

Conclusions and Recommendations

The final chapter of this thesis summarises the main results and achievements, presented in section 7.1 and gives recommendations for future research, see section 7.3.

7.1 A Summary of Results

In the first chapter a short history of the use of highly concentrated hydrogen peroxide has been given. Reasons were given why, after extensive use in the early days of space flight, it was gradually replaced by other propellants. A toxicity analysis showed that hydrogen peroxide is far less toxic than currently used propellants and that this is one of the reasons why there is a renewed interest in alternatives, so called green propellants, of which hydrogen peroxide is an example. The heritage of the use of peroxide has also resulted in a large part of the space community being negatively biased towards it. The main reservations towards peroxide have been discussed. It was argued that most arguments against the use of peroxide stem from accidents from a period in which the knowledge of peroxide was limited and that current advances in technology and knowledge allow safe handling and operation of highly concentrated hydrogen peroxide. It has been further explained that toxicity concerns and the recent change in legislation with respect to currently used propellants have resulted into renewed interest into, amongst others, hydrogen peroxide. The GRASP project was introduced which has been initiated to give an impulse to this research. This work stems from it.

Chapter 2 started with a qualitative description of the processes taking place in the catalyst bed. Based on this description a suitable model description was looked for. It has been argued that the basic assumptions to employ a mixture model (hydrodynamic and thermodynamic equilibrium) are violated and that a lot of quantitative information is lost with such models and that therefore two-fluid models are favourable. The various possibilities for two-fluid models were discussed. The Eulerian description was found to be most suitable despite the problems arising from very small volume fractions in certain parts of the catalyst bed. The available literature on hydrogen peroxide thruster modelling has

been analysed from which it has become clear that mixture models have been used until now. The basic equations of the Eulerian two-fluid model were then presented in the most general form. To model the presence of catalyst material inside the catalyst bed a model has been presented describing the void fraction distribution as a function of the size of the catalyst bed and size and shape of the catalyst pellets.

The source terms, appearing in the equations presented in chapter 2, have been discussed in chapter 3. For each source a literature review has been presented and a suitable model has been selected. Several reaction mechanisms for the decomposition of hydrogen peroxide have been discussed. It has been shown that there is one rate determining step that therefore allows the modelling of decomposition of peroxide with a single reaction equation. It has also been shown that in the literature there is a wide spread of values of the Arrhenius parameters.

For evaporation a number of basic single component and multicomponent droplet evaporation models have been reviewed. A multicomponent evaporation model has been selected that calculates the evaporation rate of individual components and is computationally efficient. Finally, a model has been presented to describe the momentum exchange between the fluids and the catalyst material. It has been argued that the Tallmadge equation rather than the Ergun equations should be used as a basis for the model.

In chapter 4 the complete model as described in chapter 2 has been simplified to make numerical implementation possible with reasonable effort, while keeping the required level of detail. For this purpose first a simple interfacial area model has been developed and presented based on the Eucledian shape of catalyst pellets. A dimensional analysis has been performed to justify the simplifications of the model. The calculation procedure for the mass and volume fractions is such that a lower bound of zero and an upper bound of unity is guaranteed. Then the discretisation scheme has been discussed, where those elements that deviate from standard textbooks on CFD were highlighted.

A model with no spatial discretisation has been presented in chapter 5. The aim of this model is to investigate the pressure drop over the catalyst bed and the factors influencing this. It has been shown that the choice for the Tallmadge equation instead of the Ergun equation as the basis for the pressure drop model results in better predications. It was also shown that the actual distribution of the liquid in the catalyst bed greatly influences the pressure drop experienced in the part of the catalyst bed where both gas and liquid are present. However, as the pressure drop in the latter part of the catalyst bed, where only gas is present, is much larger, the overall effect of the liquid distribution is minimal.

The influence of the pellet shape and size on the pressure drop and bed length have been investigated. It has been shown that for disk-shaped pellets with a diameter to length ratio larger than 2, cylindrical pellets results always in a lower pressure drop for a given bed length. It has been demonstrated that this result is independent of the inlet mass flux and of the liquid volume fraction distribution.

A limitation of the results from the adjusted model is that radial void fraction variations have not been taken into consideration. It has been shown that especially for spherical pellets these radial variations are significant; even for large bed to pellet diameter ratios. For cylindrical pellets the radial variation

in void fraction was found in general to be less and only confined to a narrow region near the wall for large diameter ratios. It has been argued that, for larger diameter ratios, the average void fraction is a representative figure and thus that the map with diameter and aspect ratio is reliable.
A one-dimensional solution to the equations presented in chapters 2, 3 and 4 has been presented in chapter 6. Good agreement as found between the prediction of the sudden increase in temperature and gas volume fraction and experimental data. However, the temperature and pressure profile can be improved. Overall a reasonable agreement between simulations and experimental data was found. It has been shown that the lack of a thermal description of the catalyst material in the current model causes a large difference between the simulated and measured temperature in the upstream region of the catalyst where gas and liquid are both present. However, these differences are not present in the region of the catalyst bed dominated by the gas phase.
It has been shown that a two-fluid model gives a much more reliable estimation of the pressure drop over the catalyst bed than a simple mixture model. It has also been shown that a two-fluid formulation in general reveals features in the catalyst bed that are not reproducible by mixture models due to the lack of a description of interphase energy transport. From a sensitivity analysis on the Arrhenius parameters it has become clear that catalytic decomposition, for the liquid phase in particular, is the most important mode of decomposition. The sensitivity analysis on the interfacial area has shown that changes in gas-liquid surface area have hardly any effect due to the fact that evaporation is driven due to non-equilibrium between the phases rather than due to equilibrium conditions at the interface. The other interfacial areas have a much larger influence on the state inside the catalyst bed. Of particular concern is the determination of the solid-liquid and solid-gas interfacial area as it has a large influence on the performance in the catalyst, but is very difficult to determine with either a model or experimentally.
Finally, it has been shown that the catalyst bed can be subdivided into three regions: pre-boiling region, rapid conversion region and dry-out region. The pre-boiling region is characterised by a relatively large increase in gas volume fraction driven by decomposition in the liquid phase, but hardly any mass transfer. The rapid conversion region is characterised by a large increase in gas volume fraction to almost unity and a high liquid to gas mass conversion rate, primarily caused by evaporation. The dry-out phase is characterised by a small amount of mass transfer at a sharply increasing gas temperature. Most of the conversion is achieved by evaporation. These three regions can also be identified in the works of other researchers, but have never been identified as such.

7.2 Contributions

In this thesis several novel approaches have been used to shed light on unknown aspects. They are summarised in arbitrary order below:

- A multicomponent two-fluid model including mass, momentum and energy transfer in a packed bed has been developed and applied to a hydrogen peroxide based rocket motor. This requires the use of a multicomponent evaporation model and a description of the decomposition process in the liquid as well as in the gas phase. Compared to other models less empirical constants are required while giving a better match with experimental data. The current implementation of the model is in one dimension only, however, it could relatively easily be extended to higher dimensions. Such a tool would not only be valuable for simulation decomposing hydrogen peroxide in a packed bed, but also in many other fields such as chemical reactor engineering in general or nuclear safety analyses.

- A simple interfacial area model has been developed to described the gas-liquid, solid-liquid and solid-gas interfacial area. No such models are available in the literature. The present model could be further extended to give a physically more accurate description.

- A pressure drop model has been introduced suited for the mass fluxes typically encountered in peroxide based rocket engines. Consequently, the estimated pressure drop gives a much better match with experimental data compared to traditionally used methods.

- The influence of the pellet shape and size has been investigated. This has revealed that catalyst beds with cylindrical pellets with a pellet diameter to length is larger than 2 perform better than spherical pellets, where the improved performance is measured in terms of pressure drop and required length to achieve complete decomposition. Only spherical and cylindrical pellets have been investigated, however, the model could be easily adjusted to include different pellet shapes.

- It has been shown that the catalyst bed can be subdivided into three regions, each with distinctive features. The significance of this is that based on these features the catalyst bed could be optimised with different solutions in each region such as for pellet shape and size, catalyst bed diameter of even catalyst material.

7.3 Directions for Future Research

Although the research associated with this PhD has come to an end, the research into modelling of chemically reacting multicomponent multiphase flows in packed beds is far from finished. Many different aspects could be researched, ranging from fundamental reaction modelling to optimisation of pellet size and distribution. Below a couple of possible research directions are given that are felt to be the most important based on experience gained over the last couple of years. It should be kept in mind that, although these recommendations are mentioned in the context of hydrogen peroxide based rocket motors, they could easily be applied to other fields of study such as was mentioned in section 1.6.
A very simple interfacial area model was developed in section 4.1 and employed in chapters 5 and 6.

It has been shown that especially the modelling of the solid-gas and solid-liquid interfacial area is important. It has been mentioned that several descriptions of the interfacial area of two-phase flows are described in the literature, but no models are available that predict the interfacial area of multiphase flows in packed beds. Ishii and Hibiki [50] provide a derivation of their gas-liquid interfacial area model. This could be used as a basis to derive one that takes into account the presence of a solid.
In section 6.1 it has shown that the inclusion of a thermal model of the catalyst material is important for an accurate prediction of the temperature of the fluids in the first part of the catalyst bed. Oehmichen et al. [84] have shown that the formation of bubbles in general affects the overall reaction rate of decomposition and heat transfer and is dependent on which part of the catalyst material that is in contact with highly concentrated peroxide and which part is in contact with the gas. Satterfield and Audibert [147] showed that there is a resemblance between catalytic decomposition in the liquid phase and the heat transfer during nucleate and film boiling. This could be further exploited and could possibly be an alternative for a three-phase interfacial area model as mentioned in the previous paragraph.
In section 5.5 it was shown that the void fraction varies radially with the catalyst bed. It was shown in section 5.4 that different void fractions give rise to different velocities and consequently to different pressure gradients. It can thus be expected that reaction rates vary radially as well. On top of that, non-adiabatic catalyst walls will result in a temperature gradient over the radius of the catalyst bed as well. To understand these phenomena the model as presented in chapter 2 should be solved in at least a two dimensions, with a non-adiabatic wall boundary condition.
It has become clear in section 3.1 that Arrhenius parameters for catalyst material for hydrogen peroxide are not widely available and that the values that are available are not in agreement with each other. However, in section 6.3 it was shown that an accurate and consistent description is necessary to avoid the need of validating and tuning the model for each new catalyst. This is especially the case for the Arrhenius parameters describing liquid catalytic decomposition. One possibility would be to devise a protocol or use an existing one to determine the Arrhenius parameters and build up a database with all possible catalysts for hydrogen peroxide. This would result in a consistent set of values and could also give directions to further improvements in the design and manufacturing of catalyst pellets.
There are many options to improve the current model. However, for anyone wishing to continue with this, it is strongly advised to take the following path in this order:

- Include a description of the thermal mass of the catalyst pellet as well as the heat transfer between the pellets and the fluids. Due to thermal conductivity of the pellets it is expected that heat is transported from the hot gas region to the cool injector region. This will result in a better match between simulated results and experimental data especially in the two-phase flow part of the catalyst bed. It will also stabilise the fluctuations in the liquid temperature at the boiling point and the resulting fluctuations in the gas temperature in the dry-out region.

- Extend the model to at least two dimensions in cylindrical coordinates. As has been shown

in section 5.5 there is a strong variation in void fraction in radial direction. This results in velocity gradients in radial directions and consequently in reaction rates, gas volume fraction distribution, pressure drop, gas and liquid temperatures etc. This will also give the possibility to study channeling; a phenomenon well known in packed beds.

- Include normal stress effect. It is expected that especially in the region with large fluid accelerations this will play a significant effect.

Appendix A

Conversions

A.1 Conversion Constants

1 torr $\approx$ 1 mmHg	=	133.32237 Pa
1 psia	=	6895 Pa
1 atm	=	101325 Pa
1 bar	=	$1 \cdot 10^5$ Pa
1 cal	=	4.184 J

Note that the difference between $1torr$ and $1mmHg$ is less than $1.5 \cdot 10^{-5}$% and therefore for most practical applications considered to be the same.

A.2 Conversion Graphs

Figures A.1, A.2 and A.3 show the relation between mass, mole and volume fractions for liquid hydrogen peroxide. The mass-mole fraction conversion in figure A.1 is also valid for gaseous peroxide. Note that although density is temperature dependent, it has hardly any influence on the conversion.
For a given mass fraction Y_A of component A the corresponding mole fraction, Y_{Amol}, and volume fraction, Y_{Avol}, are calculated as

$$Y_{Amol} = \frac{Y_A/M_A}{\sum_i Y_i/M_i} \tag{A.1}$$

$$Y_{Avol} = \frac{Y_A/\rho_A}{\sum_i Y_i/\rho_i}. \tag{A.2}$$

The conversion from mass to mole fractions and vice versa is routinely done in the models. All other plots in this section are for illustration purposes only.

Figures A.4 and A.5 show the mass and mole fraction relation between H_2O_2 and O_2. This is valid for peroxide in the liquid as well as gas phase. Figure A.6 shows the adiabatic decomposition temperature for four different inlet temperatures.

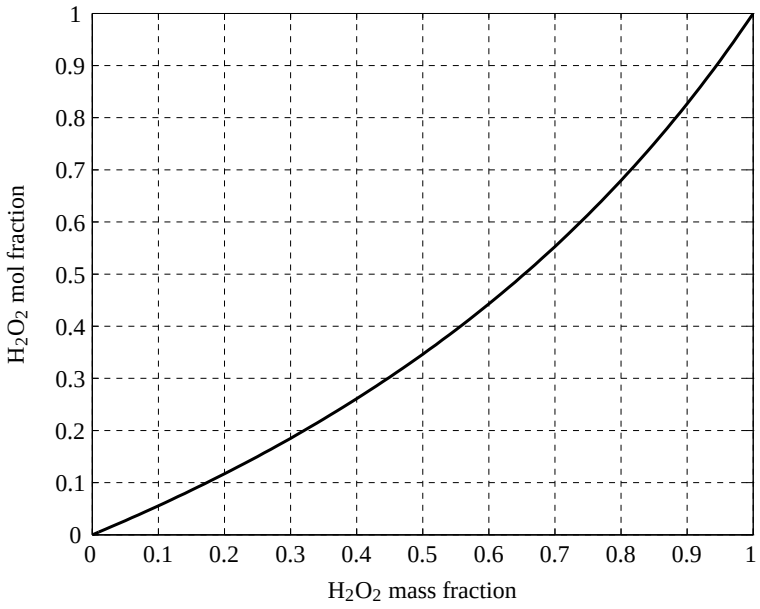

Figure A.1: *Mol-mass fraction conversion*

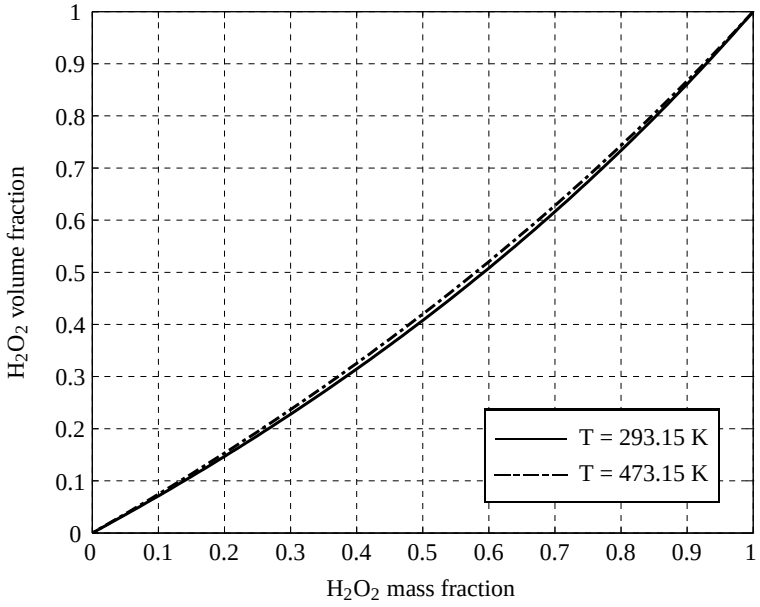

Figure A.2: *Volume-mass fraction conversion*

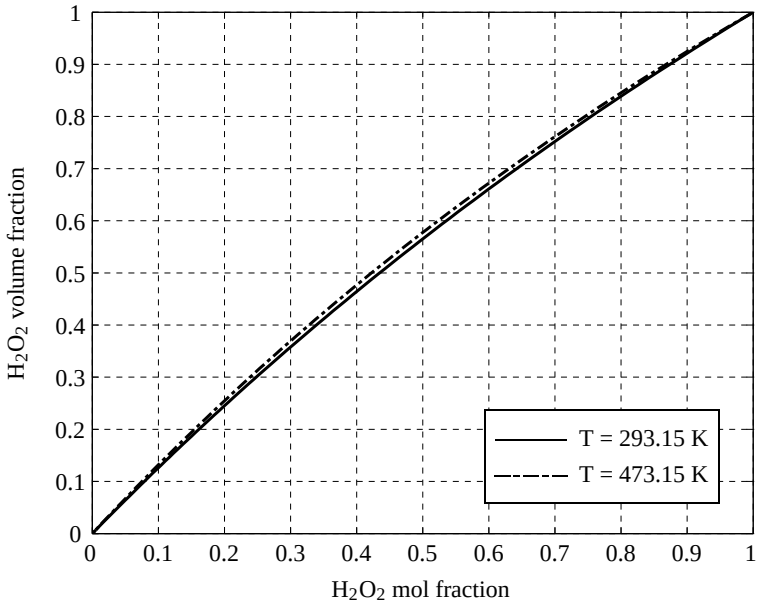

Figure A.3: *Mol-volume fraction conversion*

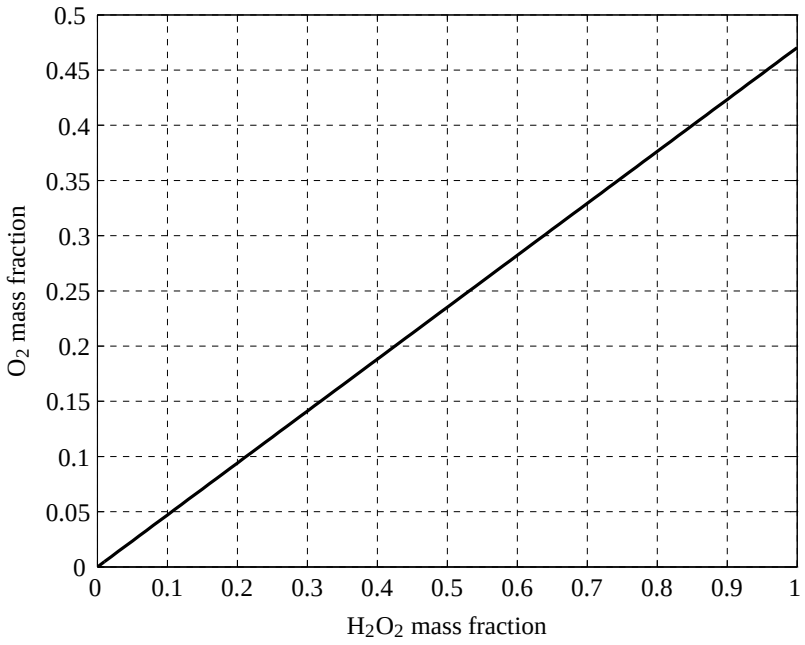

Figure A.4: $H_2O_2 \rightarrow O_2$ *mass conversion*

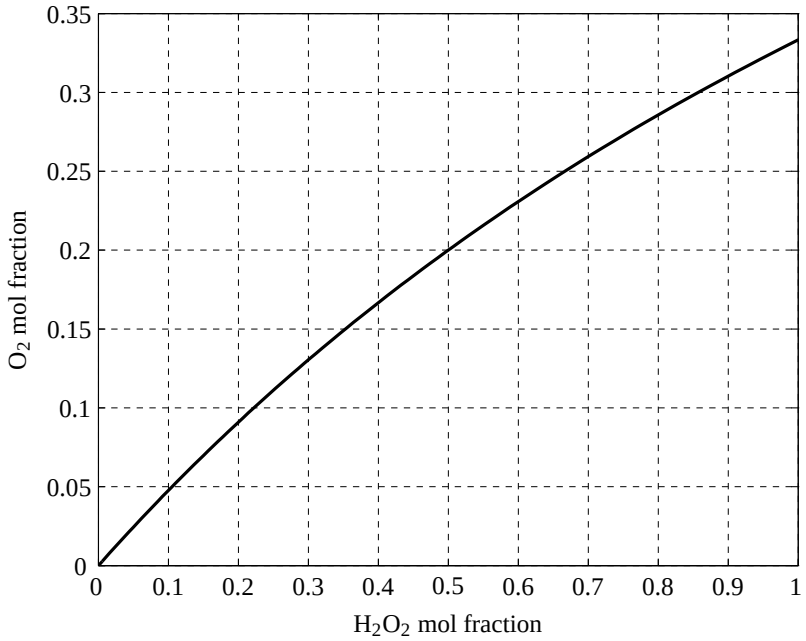

Figure A.5: $H_2O_2 \rightarrow O_2$ *mole conversion*

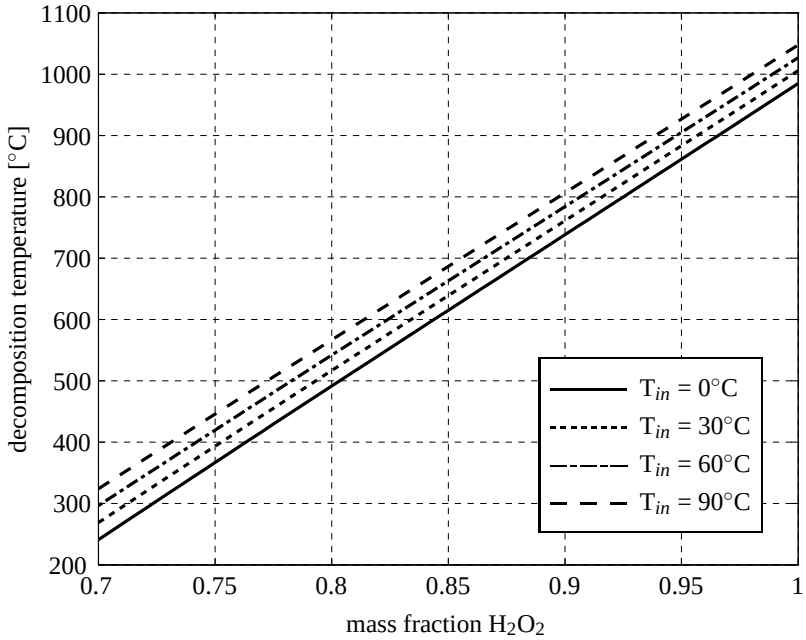

Figure A.6: *Adiabatic decomposition temperature as a function of mass fraction*

Appendix B

Component Properties

B.1 Molar Masses

component	molar mass $[g\,mol^{-1}]$
$\mathbf{H_2O_2}$	34.0147
$\mathbf{H_2O}$	18.0153
$\mathbf{O_2}$	31.9988
air	28.97

Table B.1: *Molar masses [148]*

B.2 Liquid Density

The density of pure liquid hydrogen peroxide and water is temperature dependent. For hydrogen peroxide it is given by [149]

$$\rho_{l,H_2O_2} = 1597 + 0.0784 T_l - 0.00197 T_l^2 \tag{B.1}$$

and for water by [150]

$$\rho_{l,H_2O_2} = (A + B \cdot T_{l,C} + C \cdot T_{l,C}^2 + D \cdot T_{l,C}^3 + E \cdot T_{l,C}^4 + F \cdot T_{l,C}^5)/(1 + G \cdot T_{l,C}) \cdot 1000 \tag{B.2}$$

where $T_{l,C}$ is the liquid temperature in degrees Celsius and the coefficients are given in table B.2.

constant	value
A	0.9998396
B	$18.224944 \cdot 10^{-3}$
C	$-7.92221 \cdot 10^{-6}$
D	$-55.44846 \cdot 10^{-9}$
E	$149.7562 \cdot 10^{-12}$
F	$-393.2952 \cdot 10^{-15}$
G	$18.159725 \cdot 10^{-3}$

Table B.2: *Constants for the density of water [150]*

B.3 Freezing Point

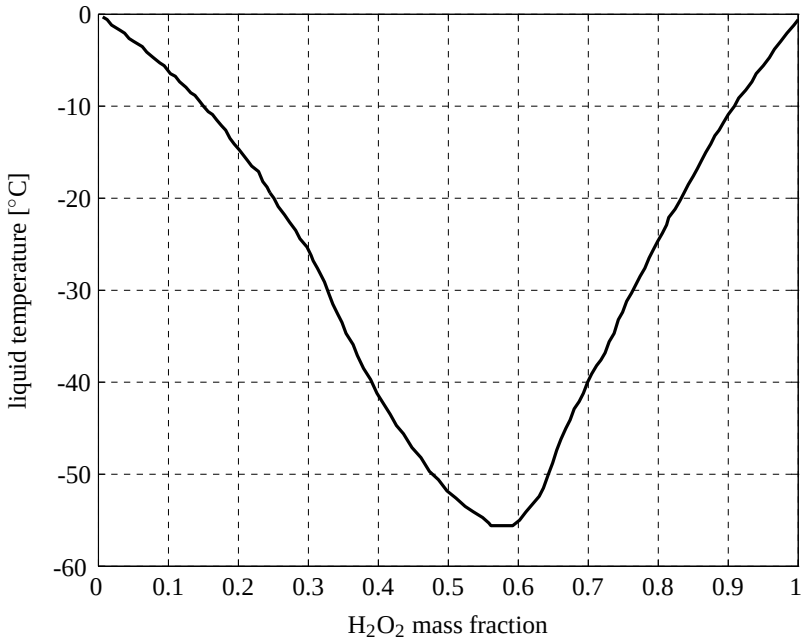

Figure B.1: *Freezing point as a function of peroxide concentration [151]*

B.4 Specific Heat and Enthalpies

The specific heat in $J\,mol^{-1}\,K^{-1}$ for hydrogen peroxide vapour, water, steam and oxygen is given by a polynomial of the form

$$c_p = A + B \cdot t + C \cdot t^2 + D \cdot t^3 + \frac{E}{t^2}, \tag{B.3}$$

where $t = T_\alpha/1000$. The values for the constants are given in table B.4 below. For liquid hydrogen peroxide and air the specific heat is given by a constant, see table B.3.

component	c_p $[J\,mol^{-1}\,K^{-1}]$
$H_2O_2(l)$	89.377 [152]
air	29.086

Table B.3: *Specific heat at constant pressure for liquid hydrogen peroxide [153] and air*

The specific enthalpy can be found by integrating the specific heat over the temperature. Applying this to equation B.3 and using a reference temperature of 298.15K gives

$$h_\alpha = \int_{298.15}^{T_\alpha} c_p\,dT = A\cdot t + \frac{1}{2}B\cdot t^2 + \frac{1}{3}C\cdot t^3 + \frac{1}{4}D\cdot t^4 - \frac{E}{t} + F, \tag{B.4}$$

where H_α is in $kJ\,mol^{-1}$.

constant	$H_2O_2(g)$	$H_2O(l)$	$H_2O(g)$	$O_2(T \leq 700K)$	$O_2(T > 700K)$
A	34.25667	-203.606	30.09200	31.32234	30.03235
B	55.18445	1523.29	6.832514	-20.23531	8.772972
C	-35.15443	-3196.413	6.7934535	57.86644	-3.988133
D	9.087440	2474.455	-2.534480	-36.50624	0.788313
E	-0.422157	3.855326	0.082139	-0.007374	-0.741599
F	-13.8034	29.2826	-9.0546	-8.903471	-11.32468

Table B.4: *Specific heat constants [148]*

B.5 Latent Heat

The latent heat for both hydrogen peroxide and water is a function of temperature and can be approximated by the Watson equation [154]:

$$\Delta H_{fg} = \Delta H_{fg,T_b}\left(\frac{1-T_r}{1-T_{br}}\right)^q. \tag{B.5}$$

In this equation $\Delta H_{fg,T_b}$ is the latent heat at the normal boiling point as given in table B.5, T_r the reduced temperature and T_{br} the reduced normal boiling point. The reduced temperature is defined as:

$$T_r = \frac{T}{T_c}. \tag{B.6}$$

T_c is the critical temperature and together with normal boiling point is given in table B.5 [18].

The parameter q can be calculated according to Fishtine by [154]

$$q = \begin{cases} 0.30 & \text{for} \quad T_{br} < 0.57 \\ 0.740 T_{br} - 0.116 & \text{for} \quad 0.57 \leq T_{br} \leq 0.71 \\ 0.41 & \text{for} \quad T_{br} > 0.71. \end{cases} \tag{B.7}$$

species	ΔH_{fg} $[J\,mol^{-1}]$	T_b $[K]$	T_c $[K]$
H_2O_2	42969.68	426.305	739.5
H_2O	40706.136	373.15	647.3

Table B.5: *Latent heat properties [150]*

B.6 Vapour Pressure

The vapour pressure in mmHg of pure hydrogen peroxide and pure water as a function of the temperature of the liquid is generally given by the following relation

$$\log_{10} p_{vap} = A + \frac{B}{T_l} + C \cdot \log_{10} T_l + D \cdot T_l + E \cdot T_l^2 + F \cdot T_l^3 + G \cdot T_l^4. \tag{B.8}$$

The values for the constants are given in table B.6

constant	H_2O_2 ($T < 363.15\,K$)	H_2O_2 ($T \geq 363.15\,K$)	H_2O
A	24.8436	38.8572	19.389127
B	-3511.54	-3627.72	-2861.9133
C	-4.61453	-11.2133	-3.2418662
D	$-3.60245 \cdot 10^{-3}$	$4.74132 \cdot 10^{-3}$	$-1.0799994 \cdot 10^{-4}$
E	$-7.73423 \cdot 10^{-6}$	0	$-7.9189289 \cdot 10^{-6}$
F	$1.78355 \cdot 10^{-8}$	0	$1.5411774 \cdot 10^{-8}$
G	$-2.27008 \cdot 10^{-13}$	0	$-8.1926991 \cdot 10^{-12}$

Table B.6: *Vapour pressure constants [18]*

B.7 Activity Coefficients

The activity coefficient for both hydrogen peroxide and water is expressed in terms of the liquid mole fraction and Redlich-Kister parameters [155]. For hydrogen peroxide it is

$$\ln\gamma_{H_2O_2} = \frac{x_{H_2O}^2}{RT_l}\cdot\left[B_0(T_l) + B_1(T_l)\cdot(3-4x_{H_2O}) + B_2(T_l)\cdot(1-2x_{H_2O})(5-6x_{H_2O}) + B_3(T_l)\right. \\ \left.\cdot(1-2x_{H_2O})^2(7-8x_{H_2O})\right] \tag{B.9}$$

and for water

$$\ln\gamma_{H_2O} = \frac{1-x_{H_2O}^2}{RT_l}\cdot\left[B_0(T_l) + B_1(T_l)\cdot(1-4x_{H_2O}) + B_2(T_l)\cdot(1-2x_{H_2O})(1-6x_{H_2O})\right. \\ \left. + B_3(T_l)\cdot(1-2x_{H_2O})^2(1-8x_{H_2O})\right]. \tag{B.10}$$

The parameters B_i are temperature dependent. B_1 is given by a Lorentzian function of the form

$$B_1 = C_0 + \frac{C_1C_2}{\pi\left(C_2^2 + (T_l - C_3)^2\right)}. \tag{B.11}$$

The parameters B_2 and B_3 are described by sigmoid function of the form

$$B_i = C_{0i} + \frac{C_{1i}}{1+e^{C_{2i}(T-C_{3i})}}. \tag{B.12}$$

B_0 consists of 4 different regions. For temperatures between 273.150 and 317.636 K the curve is described by a Lorentzian function of the same form as given in equation B.11. For temperatures between 348.222 and 391.463 K the curve takes the form of a second order polynomial:

$$B_0 = P_0 + P_1T_l + P_2T_l^2. \tag{B.13}$$

For temperatures between 317.636 and 348.222 K B_0 is the average of the Lorentzian curve given by equation B.11 and the second order polynomial given by equation B.13. And finally, for temperature above 391.463 up to 433.150 K B_0 is a constant with a value of $B_0 = -612.9613$. All the coefficients mentioned in equations B.11 to B.13 are given in table B.7 below together with the temperature range over which they are applicable.

parameter	temperature range	curve type	constants
B_0	273.150 - 317.636 K	Lorentzian	$C_0 = -999.8830$
			$C_1 = -2499.584$
			$C_2 = 8.261924$
			$C_3 = 327.4487$
	317.636 - 348.222 K	average of above Lorentzian	$P_0 = 17418.34$
		and 2nd order polynomial	$P_1 = -109.9125$
			$P_2 = 0.1663847$
	348.222 - 391.463 K	2nd order polynomial	$P_0 = -6110.401$
			$P_1 = 28.08669$
			$P_2 = -0.03587408$
	391.463 - 433.150 K	constant	$B_0 = -612.9613$
B_1	273.150 - 433.150 K	Lorentzian	$C_0 = 126.7385$
			$C_1 = -2558.776$
			$C_2 = 12.33364$
			$C_3 = 343.1050$
B_2	273.150 - 433.150 K	sigmoid	$C_{02} = 63.18354$
			$C_{12} = -149.9278$
			$C_{22} = 0.4745954$
			$C_{32} = 348.1642$
B_3	273.150 - 433.150 K	sigmoid	$C_{03} = 59.42228$
			$C_{13} = -199.2644$
			$C_{23} = 0.8321514$
			$C_{33} = 346.2121$

Table B.7: *Coefficients for the Redlich-Kister parameters [18]*

B.8 Boiling Diagrams

The boiling diagrams as shown in figures B.2, B.3 and B.4 are constructed based on equations for vapour pressure and activity coefficients as described above. Although the boiling temperature for hydrogen peroxide for any concentration at atmospheric pressure can easily be obtained from the literature, boiling diagrams, particularly at elevated pressures, are not available. Based in the research by Manatt and Manatt [18] several boiling diagrams have been constructed at higher than atmospheric pressures. These plots are for illustration purposes only.

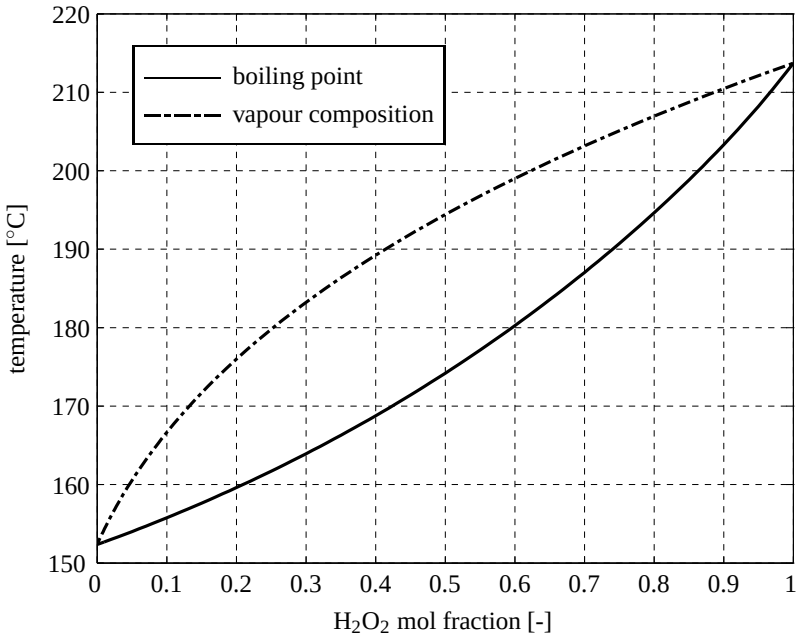

Figure B.2: *Boiling diagram for hydrogen peroxide at 5 bar*

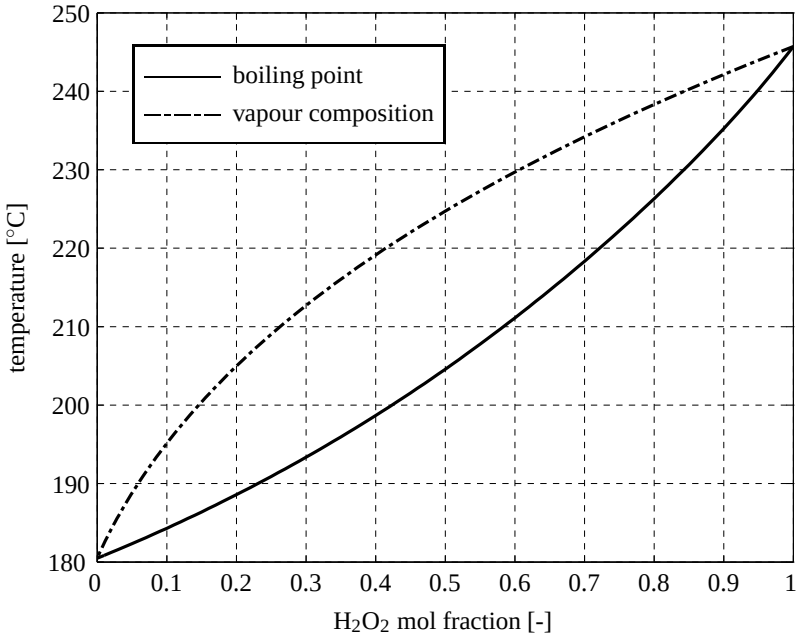

Figure B.3: *Boiling diagram for hydrogen peroxide at 10 bar*

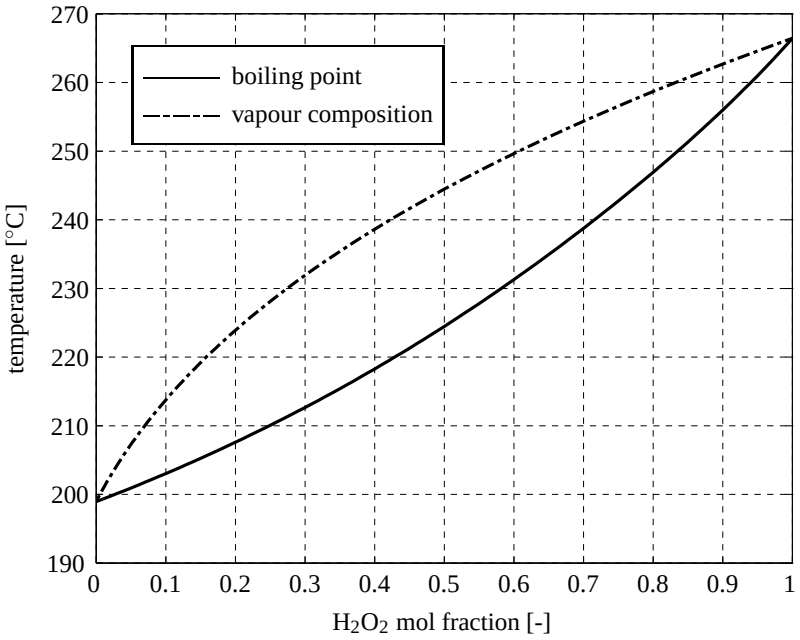

Figure B.4: *Boiling diagram for hydrogen peroxide at 15 bar*

B.9 Explosive Region

The construction of the explosive region is based on the data presented by Satterfield et al. [17]. The limiting vapour concentration is summarised in table B.8. Note that ignition limits are only determined for pressures for which the limit has been determined experimentally and that these are lower than typically lower than experienced in typical thruster catalyst beds. These plots are for illustration purposes only.

pressure [bar]	limit [mol%]
1.5	22.65
2.0	21.20
3.0	20.70
5.0	20.70

Table B.8: *Vapour ignition limits*

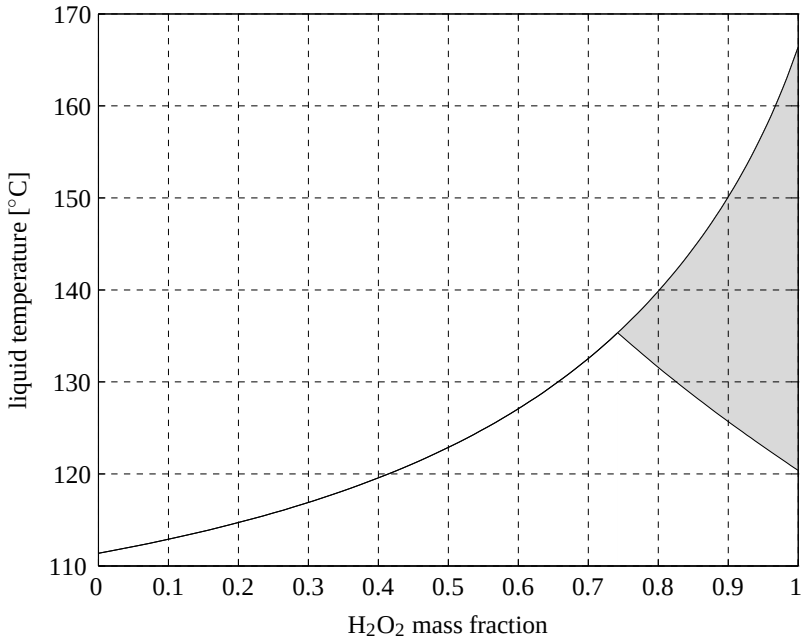

Figure B.5: *Explosive region for hydrogen peroxide at p = 1.5 bar*

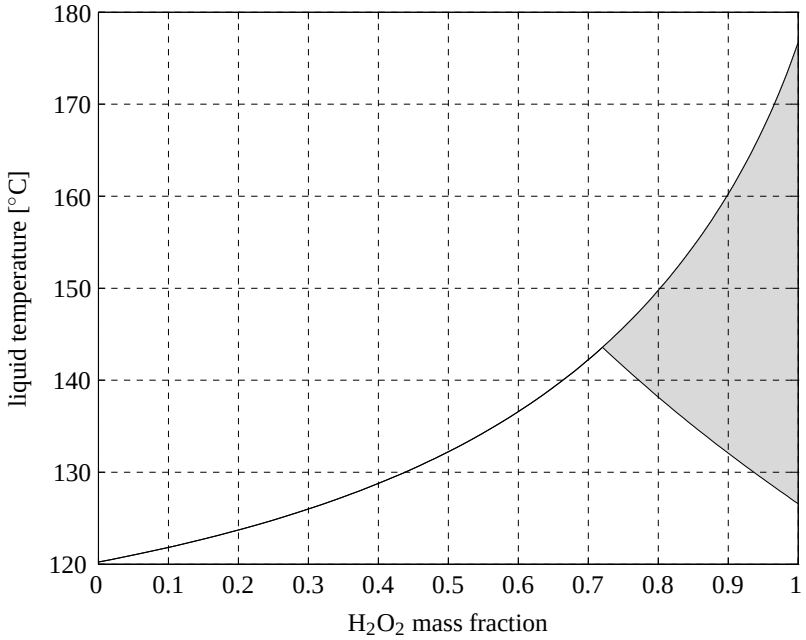

Figure B.6: *Explosive region for hydrogen peroxide at p = 2.0 bar*

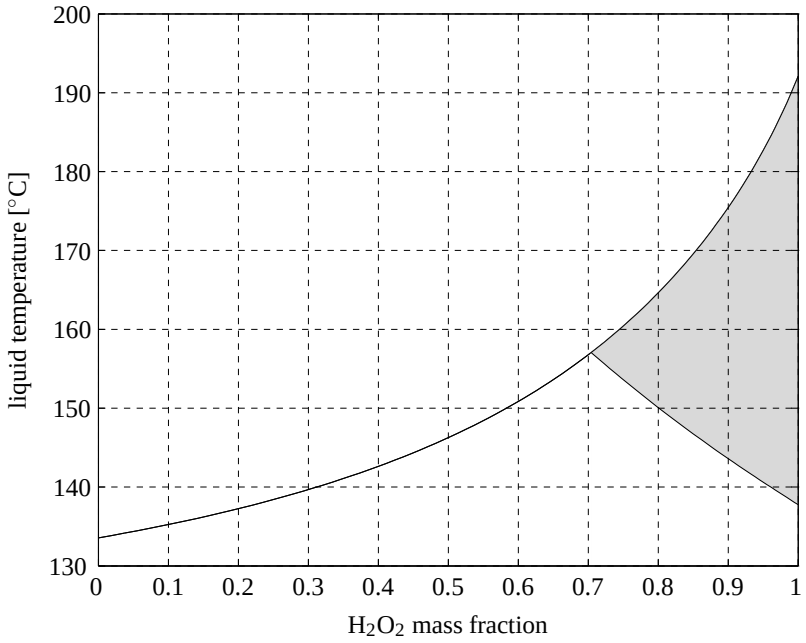

Figure B.7: *Explosive region for hydrogen peroxide at p = 3.0 bar*

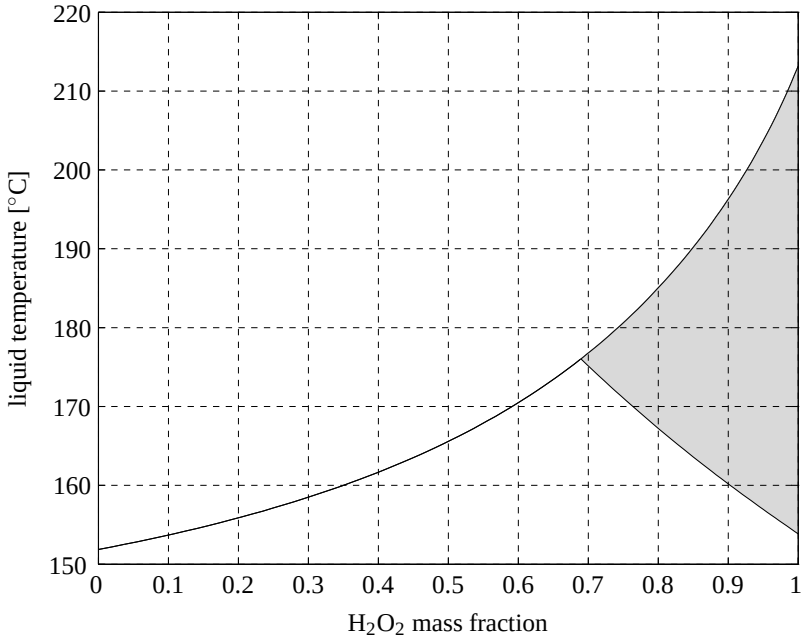

Figure B.8: *Explosive region for hydrogen peroxide at p = 5.0 bar*

Appendix C

Void Fraction Profiles by Bey and Eigenberger

C.1 Spherical Pellets

Describing the void fraction profiles starts with defining a non-dimensional radial coordinate r' by

$$r' = \frac{\frac{D_b}{2} - r}{r_{min}} - 1, \tag{C.1}$$

where D_b is the bed diameter and r_{min} the reference value for the radius and defined as

$$r_{min} = 0.5\left(D_b - \sqrt{(D_b - D_{ps})^2 - D_{ps}^2}\right). \tag{C.2}$$

Here D_p is the diameter of the sphere. The radial coordinate divides the catalyst bed in two parts: the part of the catalyst bed in the vicinity of the wall for $r' < 0$ and the core region for $r' \geq 0$. The corresponding local void fraction distribution for $r' < 0$ is given by

$$\varepsilon_{f,loc} = \varepsilon_{min} + (1 - \varepsilon_{min})\, r'^2, \tag{C.3}$$

and for $r' \geq 0$ by

$$\varepsilon_{f,loc} = \varepsilon_0\,(\varepsilon_{min} - \varepsilon_0)\, exp\left(-\frac{r'}{c}\right)\cos\left(\frac{\pi}{b}r'\right). \tag{C.4}$$

The values for ε_{min} and ε_0 are given in table C.1 below. The constants b and c are $b = 0.876$ and $c = 10$.

The bed mean void fraction is given by

$$\varepsilon_{f,mean} = 0.375 + 0.34\frac{D_{ps}}{D_b}. \tag{C.5}$$

C.2 Cylindrical Pellets

For cylindrical pellets the void fraction profile is defined along similar lines. The non-dimensional radial coordinate is given by

$$r' = a_0 \frac{\frac{D_b}{2} - r}{D_p} - 1, \tag{C.6}$$

where a_0 is an empirical factor defined by

$$a_0 = 1.8 - 2\frac{D_p}{D_b}. \tag{C.7}$$

The relation for the local void fraction in the vicinity of the wall of the catalyst bed is only different in the power of r'

$$\varepsilon_{f,loc} = \varepsilon_{min} + (1 - \varepsilon_{min})\, r'^4. \tag{C.8}$$

The local void fraction of the core is the same as for spherical pellets, see equation C.4, with b the same and $c = 2$. Values for ε_{min} and ε_0 are given in table C.1.
The bed mean void fraction is given by

$$\varepsilon_{f,mean} = 0.36 + 0.1\frac{D_{ps}}{D_b} + 0.7\left(\frac{D_{ps}}{D_b}\right)^2. \tag{C.9}$$

Here D_{ps} is the diameter of a sphere with an equivalent volume as the cylindrical pellet. Equation C.9 is valid for $D_{ps}/D_b \leq 0.6$.

shape	$\mathbf{D_p} \cdot 10^{-3}\ [m]$	$\mathbf{L_p} \cdot 10^{-3}\ [m]$	$\boldsymbol{\epsilon_{min}}$	$\boldsymbol{\epsilon_0}$
sphere	4.5	–	0.27	0.39
	6.3	–	0.24	0.39
	7.5	–	0.24	0.395
	9.8	–	0.24	0.41
	14	–	0.24	0.41
cylinder	4.5	4.5	0.275	0.365
	6	6	0.275	0.375
	12	12	0.3	0.42
	6	5-20	0.275	0.365

Table C.1: *Constants for void fraction profiles*

Appendix D

Diffusion and Chemical Reaction inside a Porous Catalyst by Thiele

The model developed by Thiele [85] considers a chemical reaction taking place on the surface of a porous catalyst pellet. The reaction rate of component A due to decomposition at the surface is generally given by

$$\dot{r}_A = k'' a_{sp} [A] M_A, \tag{D.1}$$

where a_{sp} is the surface area per unit catalyst volume, M_A the molar mass of component A and k'' the surface reaction rate constant determined by the Arrhenius equation $k'' = A_0 e^{E_A/(R_c T)}$. Bird et al. [66] rewrite equation D.1 by assuming the catalyst material is in pellet form with a spherical shape. They express r_A in terms of effective diffusion coefficient and the concentration of peroxide in the catalyst particle as a function of the distance to the center of the particle.

$$\mathcal{D}_{eff} \frac{1}{r^2} \frac{d}{dr} \left(r^2 \frac{dc_A}{dr} \right) = k^* a_{sp} c_A \tag{D.2}$$

This equation can be integrated. The boundary conditions for this are $[A] = [A]_p$ at $r = r_p$, where r_p is the radius of the pellet, and $[A]$ has a finite value at $r = 0$. This results in

$$\frac{[A]}{[A]_p} = \left(\frac{r_p}{r} \right) \frac{\sinh\left(\sqrt{k'' a_{sp}/\mathcal{D}_{eff}}\, r \right)}{\sinh\left(\sqrt{k'' a_{sp}/\mathcal{D}_{eff}}\, r_p \right)}. \tag{D.3}$$

The molar flux across the surface of the catalyst pellet J_p can be expressed as [66]

$$J_p = -4\pi r_p^2 \mathcal{D}_{eff} \left. \frac{d[A]}{dr} \right|_{r=r_p}. \tag{D.4}$$

Substituting equation D.3 into D.4 gives after rewriting

$$J_p = 4\pi r_p \mathcal{D}_{eff}[A]_p \left(1 - \sqrt{\frac{k'' a_{sp}}{\mathcal{D}_{eff}}} r_p \coth \sqrt{\frac{k'' a_{sp}}{\mathcal{D}_{eff}}} r_p\right). \tag{D.5}$$

To express the influence of the diffusivity on the molar flow rate, the molar flow as expressed in equation D.5 is compared with the molar flow when it is assumed that the available catalytic surface is exposed directly to the flow with concentration $[A]_p$. This theoretical molar flow is expressed as:

$$J_{p,0} = a_{sp} \cdot \left(\frac{4}{3}\pi r_p^3\right)(-k''[A]_p). \tag{D.6}$$

Dividing equation D.5 by D.6 gives the effectiveness factor.

$$\eta_{eff} = \frac{J_p}{J_{p,0}} = \frac{3}{\psi^2}(\psi \coth \psi - 1), \tag{D.7}$$

where $\psi = \sqrt{k'' a_{sp}/\mathcal{D}_{eff}} r_p$, which is better known as the *Thiele modulus*.
The above equations are derived under the assumption that the change in molar volume is negligible during the decomposition. However, in case of decomposition of hydrogen peroxide in liquid form into water and oxygen, a liquid is converted into another liquid and a gas. The conversion to a gas will cause a significant rise in volume. Thiele has shown that when the volume increases, the effectiveness factor will decrease for a given Thiele modulus [85].
The Thiele module assumes catalyst pellets with a spherical shape. Aris [156] has shown that when the characteristic dimension is taken to be the volume of the pellet over the surface area of the pellet, $r_p = V_p/S_p$, the effectiveness factor η_{eff} becomes almost independent of the actual pellet shape. For non-spherical particles the radius r_p has to be redefined as $r_{pn} = 3V_p/S_p$ where V_p is the volume of the particle and S_p the external surface area of the particle. Substituting this into equation D.7 the following relation for the effectiveness factor is obtained

$$\eta_{eff} = \frac{1}{3\Phi^2}(3\Phi \coth 3\Phi - 1), \tag{D.8}$$

where $\Phi = \sqrt{k'' a_{sp}/\mathcal{D}_{eff}}(V_p/S_p)$ and also known as the generalised Thiele modulus.

Appendix E

Multicomponent Evaporation Model by Brenn et al.

The total evaporation rate of a multicomponent liquid according Brenn et al. [110] is defined as the sum of the evaporation rate of the individual components and is given by

$$\dot{m}^{evap} = \sum_A \dot{m}_A = -2\pi \sum_A r_{V,A} \rho_g \mathcal{D}_{A,g} \mathsf{Sh}_A^* \ln(1 + \mathsf{B}_{MA}), \tag{E.1}$$

where the subscript g refers to the gas phase and $r_{V,A}$ is the volume equivalent partial radius. It is a scaling factor for the surface area of the droplet that can be interpreted as the reduction in surface area coverage by component A due to the presence of other components at the surface of the droplet. It was experimentally determined that $r_{V,A} = 0.5 D_l \psi_A^{1/3}$, where d_l is the droplet diameter and ψ_A the volume fraction of component A in the liquid mixture. Note that a negative value for the total evaporation rate denotes evaporation. B_{MA} is the Spalding mass transfer number for component A and is defined as

$$\mathsf{B}_{MA} = \frac{Y_{A,s} - Y_{A,\infty}}{1 - Y_{A,s}}. \tag{E.2}$$

Sh^* is the modified Sherwood number. It modifies the Sherwood number to take into account the effect of Stefan flow on the thickness of the boundary layer of the droplet. It is defined as

$$\mathsf{Sh}_A^* = 2 + \frac{\mathsf{Sh}_0 - 2}{F(\mathsf{B}_{MA})}. \tag{E.3}$$

The Sherwood number Sh_0 is calculated with the Frössling correlation

$$\mathsf{Sh}_0 = 2 + 0.552 \mathsf{Re}^{1/2} \mathsf{Sc}^{1/3}. \tag{E.4}$$

The function $F(B)$ in equation E.3 is generally given by

$$F(B) = (1+B)^{0.7}\frac{\ln(1+B)}{B} \tag{E.5}$$

The heat transfer rate of the droplet is given by

$$\dot{h}_l = \sum_{A=1}^{N}\frac{\dot{m}_A}{m_d}\left[\frac{c_{p,A}(T_\infty - T_s)}{\mathsf{B}_{\mathsf{T}A}} - \Delta H_{fg}(T_s)\right], \tag{E.6}$$

where c_p is the specific heat at constant pressure, m_d the mass of the droplet, T_∞ the temperature of the gas far away from the droplet surface and T_s the temperature of the droplet surface. $\mathsf{B}_{\mathsf{T}A}$ is given by

$$\mathsf{B}_{\mathsf{T}A} = (1+\mathsf{B}_{\mathsf{M}A})^{\psi_A} - 1, \tag{E.7}$$

where ψ_A is calculated by

$$\psi_A = \frac{c_{p,A}}{c_{p_g}}\frac{\mathsf{Sh}_A^*}{\mathsf{Nu}_A^*}\frac{1}{\mathsf{Le}}. \tag{E.8}$$

Le is the Lewis number calculated (see appendix F) and Nu_A^* is the modified Nusselt number, which is calculated in a similar way as the modified Sherwood number

$$\mathsf{Nu}_A^* = 2 + \frac{\mathsf{Nu}-2}{F(\mathsf{B}_{\mathsf{T}A})}. \tag{E.9}$$

The Nusselt number Nu is calculated in the same way as the Sherwood number, see equation E.4, with the Schmidt number substituted by the Prandtl number. Note that an iteration loop between equations E.8 and E.9 is required.

Appendix F

Dimensionless Numbers

As a reminder, all the non-dimensional numbers used in this work are summarised here. Note that the non-dimensional numbers are for packed bed, so the characteristic length is $D_p/(1-\varepsilon_f)$. See chapter 4 for further explanation.

Eckert number – Ec

$$\mathrm{Ec} = \frac{\text{kinetic energy}}{\text{heat capacity}} = \frac{u^2}{c_p T} \tag{F.1}$$

Euler number – Eu

$$\mathrm{Eu} = \frac{\text{static pressure}}{\text{dynamic pressure}} = \frac{p}{\rho u^2} \tag{F.2}$$

Damköhler number – Da

There are four Damköhler numbers generally describing the ratio of reaction rate and mass transport. The form of the Damköhler number is dependent on whether mass or heat transfer is considered and whether volumetric or surface reactions is considered. The number are defined as follows:

First Damköhler number – $\mathrm{Da_I}$

$$\mathrm{Da_I} = \frac{\text{volumetric mass transfer rate}}{\text{mass transport by convection}} = \frac{k_A'''[A]M_A D_p}{\rho u(1-\varepsilon_f)} \tag{F.3}$$

Second Damköhler number – $\mathsf{Da_{II}}$

$$\mathsf{Da_{II}} = \frac{\text{surface mass transfer rate}}{\text{mass transport by diffusion}} = \frac{k''_A \delta}{\mathcal{D}} \tag{F.4}$$

Third Damköhler number – $\mathsf{Da_{III}}$

$$\mathsf{Da_{I}} = \frac{\text{volumetric heat transfer rate}}{\text{heat transport by convection}} = \frac{k'''_A [A] M_A \Delta_r H D_p}{\rho u (1-\varepsilon_f) c_p T} \tag{F.5}$$

Fourth Damköhler number – $\mathsf{Da_{IV}}$

$$\mathsf{Da_{IV}} = \frac{\text{surface heat transfer rate}}{\text{heat transport by conduction}} = \frac{k''_A \Delta_r H \rho \delta}{kT} \tag{F.6}$$

Froude number – Fr

$$\mathsf{Fr} = \frac{\text{body forces}}{\text{inertia forces}} = \sqrt{\frac{D_p}{u^2 g (1-\varepsilon_f)}} \tag{F.7}$$

Lewis number – Le

$$\mathsf{Le} = \frac{\text{thermal diffusivity}}{\text{mass diffusivity}} = \frac{k}{\rho c_p \mathcal{D}} \tag{F.8}$$

Mach number – Ma

$$\mathsf{Ma} = \frac{\text{flow velocity}}{\text{wave velocity}} = \frac{u}{\sqrt{\gamma R T}} \tag{F.9}$$

Nusselt number – Nu

$$\mathsf{Nu} = \frac{\text{convective heat transfer}}{\text{conductive heat transfer}} = \frac{h_T D_p}{(1-\varepsilon_f) k} \tag{F.10}$$

Péclet number – Pe

The Péclet number is the ratio of advection and diffusion. Depending on whether mass or heat is considered it is called the mass Péclet number of thermal Péclet number, respectively. They can be calculated as

$$\mathrm{Pe}_{mass} = \frac{\text{mass transport by advection}}{\text{mass transport by diffusion}} = \frac{uD_p}{(1-\varepsilon_f)\mathcal{D}} \tag{F.11}$$

and

$$\mathrm{Pe}_{thermal} = \frac{\text{heat transport by advection}}{\text{heat transport by diffusion}} = \frac{\rho u c_p D_p}{(1-\varepsilon_f)k} \tag{F.12}$$

Prandtl number – Pr

$$\mathrm{Pr} = \frac{\text{momentum transport by diffusion}}{\text{thermal thermal transport diffusion}} = \frac{c_p \mu}{k} \tag{F.13}$$

Reynolds number – Re

$$\mathrm{Re} = \frac{\text{inertia forces}}{\text{viscous forces}} = \frac{\rho u D_p}{(1-\varepsilon_f)\mu} \tag{F.14}$$

Schmidt number – Sc

$$\mathrm{Sc} = \frac{\text{rate of viscous diffusion}}{\text{rate of molecular diffusion}} = \frac{\mu}{\rho \mathcal{D}} \tag{F.15}$$

Sherwood number – Sh

$$\mathrm{Sh} = \frac{\text{mass diffusion}}{\text{molecular diffusion}} = \frac{k_M D_p}{(1-\varepsilon_f)\mathcal{D}} \tag{F.16}$$

Appendix G

Underrelaxation

Although a first-order fully implicit discretisation scheme is employed, to help stabilise the iterative process further underrelaxation is applied to all variables that are being solved. For the pressure correction equation this is simply achieved by

$$p = p^* + \omega_p p', \tag{G.1}$$

where ω is the underrelaxation factor, a value between 0 and 1. For all other variables underrelaxation is applied as follows. The general algebraic discretised equation for an arbitrary variable ϕ can be written as

$$a_P \phi_P + \sum_{nb} a_{nb} \phi_{nb} = B. \tag{G.2}$$

The new value for ϕ_P at the end of the time step n, written as ϕ_P^n, is dependent on the value from the previous time step ϕ_P^{n-1} and the solution of equation G.2, which is not yet underrelaxed and written as ϕ_P^{new}. It can be expressed as

$$\phi_P^n = \phi_P^{n-1} + \omega_\phi \left(\phi_P^{new} - \phi_P^{n-1} \right). \tag{G.3}$$

After rewriting this equations the following is obtained

$$\phi_P^n = \left(1 - \omega_\phi\right) \phi_P^{n-1} + \omega_\phi \phi_P^{new}. \tag{G.4}$$

Substituting equation G.2 for ϕ_P^{new} in equation G.4 gives

$$\phi_P^n = \left(1 - \omega_\phi\right) \phi_P^{n-1} + \omega_\phi \frac{B - \sum_{nb} a_{nb} \phi_{nb}^n}{a_P}. \tag{G.5}$$

This can be rewritten as

$$\frac{a_P}{\omega_\phi} \phi_P + \sum_{nb} a_{nb} \phi_{nb} = B - \frac{1 - \omega_\phi}{\omega_\phi} a_P \phi_P^{n-1}. \tag{G.6}$$

The advantage of this method is that underrelaxation is applied before the equation is actually being solved causing the coefficient matrix to be more diagonally dominant than without underrelaxation. This helps to stabilise the solution procedure.

Appendix H

Monte Carlo Simulation for Accuracy Determination

H.1 Accuracy Analysis Details

To assess the accuracy of the pressure transducer used for validation of the models discussed in chapters 5 and 6 a Monte Carlo simulation has been performed. In this approach the uncertainty of the output of every device involved in acquiring data is added to the signal as well as the error caused by digitising the signal. In each device specification several error sources are identified and quantified, however, the exact error is not known: only the boundaries of the errors are known.
In the current Monte Carlo simulation it is assumed that the actual error can be statistically described with a uniform distribution around the mean. To the original signal a error signal is added of which the value is determined randomly from a set ranging from $[-err : +err]$, where err is the error bound as found in the device specification. Error signals are added to the original signal. The difference between the final and the original signal indicates how accurate the measurement is. This approach is repeated many times. The average of the difference between the final and the original signal is then determined which gives the accuracy of the measurements. The number of loops for which the average is determined should be so high that the average does not vary anymore.
For the pressure measurements four main sources of error have been identified: pressure transducer, power supply, data acquisition system and digitising error. The pressure transducer, power supply and data acquisition system have each multiple sources of error which are specified in tables H.1, H.2 and H.3 respectively.
During measurements an input voltage of $V_{input} = 22V$ was delivered by the power supply to the pressure transducer. The nominal output span of the pressure transducer is $V_{P,out} = 5V$ for a measurement range of $P_{range} = 1-20bar$ resulting in a sensitivity of $P_{sens} = 0.2V\ bar^{-1}$. The pressure was measured with $200Hz$. The accuracy can now be determined as follows:

Power supply

The voltage coming from the power supply is the combination of the set voltage plus the errors as specified in table H.1. The voltage as experienced by the pressure transducer can then be expressed as

$$V_1 = \left(1 + V_{1,\lambda} \sim U(-1,1) + V_{1,abs} \sim U(-1,1) + \frac{V_{1,rms} \sim U(-1,1)}{\sqrt{200}}\right) \cdot V_{input}. \tag{H.1}$$

The notation of $V_{n,x} \sim U(-1,1)$ means that the value of $V_{n,x}$ is multiplied by a random number between $[-1;1]$ with a uniform probability distribution.

	value	**symbol**
device	power supply	–
make	Tenma	–
part	72-7245	–
non-linearity	0.01% FS	$V_{1,\lambda}$
absolute uncertainty	3mV	$V_{1,abs}$
noise	1mV˙rms	$V_{1,rms}$

Table H.1: *Error specification power supply*

Pressure transducer

The errors introduced by the pressure transducer are summarised in table H.2. Together with the uncertainty in the supply voltage this results in a output voltage from the pressure transducer that can be calculated as

$$\begin{aligned} V_2 = P_{range} \cdot P_{sens} + V_{2,\lambda} \sim U(-1,1) + (V_{P,out} + FS_{error}) \cdot V_{2,therm} \sim U(-1,1) \\ + \frac{V_1}{V_{input}} V_{2,sens} \sim U(-1,1), \end{aligned} \tag{H.2}$$

where FS_{error} is the span error calculated by

$$FS_{error} = V_{2,span} \sim U(-1,1) \cdot V_{P,out}. \tag{H.3}$$

Data acquisition system

An extensive accuracy description is available in the documentation of the data acquisition system [157]. All the errors are specified in table H.3. To determine the output signal from the system

	value	symbol
device	pressure transducer	–
make	Gems Sensors & Controls	–
part	2200RGB2501F3FA	–
span tolerance	1% FS	$V_{2,span}$
non-linearity	0.25% FS	$V_{2,\lambda}$
thermal error	1.5% FS	$V_{2,therm}$
input sensitivity error	0.01% FS/V	$V_{2,sens}$

Table H.2: *Error specification pressure transducer*

the errors are grouped as gain error, offset error of noise. For each of these 3 groups the uncertainty is calculated as

$$V_{3,gain} = V_{3,Gres} \sim U(-1,1) + \Delta T_{cal} \cdot (V_{3,GTco} \sim U(-1,1) + V_{3,OTrefco} \sim U(-1,1)) \tag{H.4}$$

$$V_{3,offset} = V_{3,Ores} \sim U(-1,1) + \Delta T_{cal} \cdot V_{3,OTco} \sim U(-1,1) + V_{3,OTref} \sim U(-1,1) \tag{H.5}$$

$$V_{3,noise} = \frac{V_{3,Nrms} \sim U(-1,1)}{\sqrt{200}}. \tag{H.6}$$

ΔT_{cal} is the temperature offset since the last calibration and was set to $10^{\circ}C$. Varying this number showed that it hardly influences the results. The output from the data acquisition system can now be determined by

$$V_3 = (1 + V_{3,gain}) \cdot V_2 + V_{3,offset} \cdot V_{P,out} + V_{3,noise}. \tag{H.7}$$

	value	symbol
device	data acquisition system	–
make	National Instruments	–
part	NI 9205	–
residual gain error	$135 \cdot 10^{-6}$ V	$V_{3,Gres}$
gain temperature coefficient	$11 \cdot 10^{-6}$ V/°C	$V_{3,GTco}$
reference temperature coefficient	$5 \cdot 10^{-6}$ V/°C	$V_{3,OTrefco}$
residual offset error	$20 \cdot 10^{-6}$	$V_{3,Ores}$
offset temperature coefficient	$47 \cdot 10^{-6}$ V/°C	$V_{3,OTco}$
reference temperature offset	$76 \cdot 10^{-6}$	$V_{3,OTref}$
noise	$3 \cdot 116 \cdot 10^{-6}$ V˙rms	$V_{3,Nrms}$

Table H.3: *Error specification data acquisition system. Detailed instructions how to determine accuracies are available from Instruments [157].*

Digitising error

The output from the data acquisition system is finally saved on a computer. This requires digitising of the signal. If it is assumed that a 16-bit A/D-convertor is used then this value is calculated as

$$V_4 = 0.5 \cdot \frac{V_{span}}{2^{16} - 1}. \tag{H.8}$$

Finally, the output signal can be expressed as

$$V_{out} = V_3 + V_4. \tag{H.9}$$

H.2 Monte-Carlo Simulation Results

The procedure described above was implemented in Matlab. In total 10^6 iterations were done to obtain steady results. They are shown in figures H.1 and H.2 and show the relative inaccuracy and maximum deviation from the mean respectively. Each plot contains the result of the whole simulation and of a simulation where the thermal error was excluded.

Figure H.1 shows that for pressure measurements below 5*bar* the relative inaccuracy increases

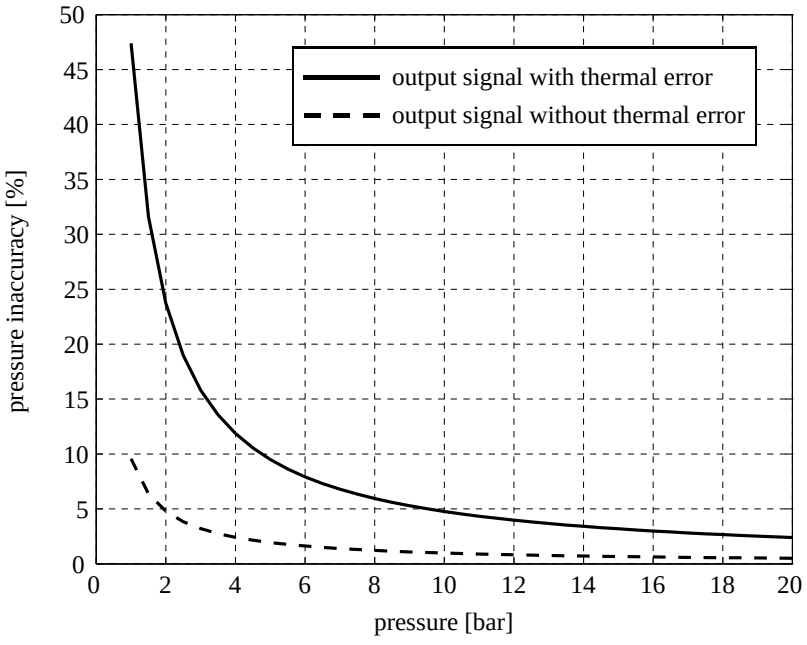

Figure H.1: *Relative inaccuracy of pressure measurements*

rapidly. However, the design of the instrumented catalyst has been such that the pressure in the plenum chamber was always 10*bar* or more and thus that the relative inaccuracy was always lower than 5%. Both figures show that the thermal error is by far the largest contributor in the total inaccu-

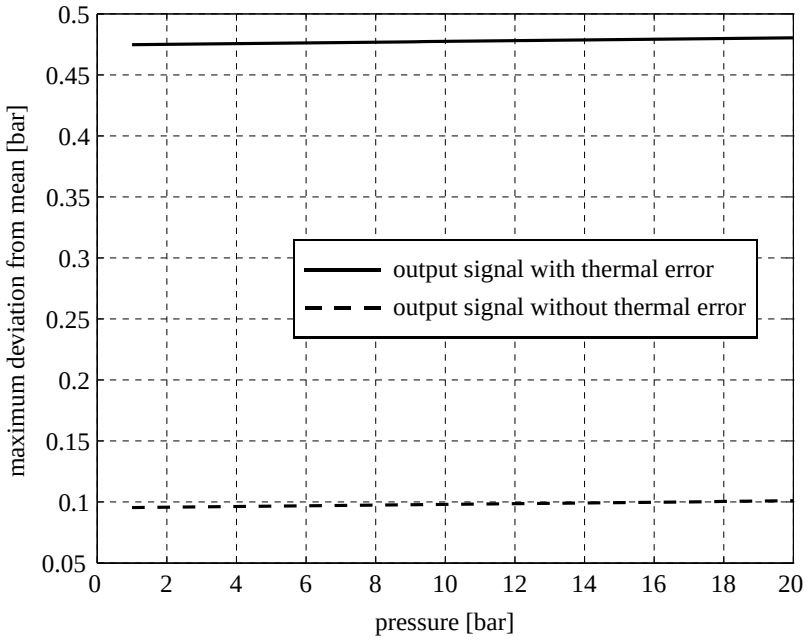

Figure H.2: *Maximum absolute deviation from the mean pressure*

racy. As the catalyst bed experience temperature change from about $15°C$ to a temperature close to the adiabatic decomposition temperature of about $690°C$ the thermal error cannot be ignored.

Appendix I

Simulations with Commercial CFD Packages

At the beginning of 2009 a survey was carried out to assess which CFD package in use within the Aerodynamics and Flight Mechanics group would be most suitable for modelling the decomposing flow of highly concentrated hydrogen peroxide through a packed bed. The packages in use were Fluent, Ansys CFX, StarCD and OpenFoam. For each of these it was investigated whether it could handle the following combined set of requirements:

- capable of handling Eulerian gas-liquid flows
- capable of handling flows through porous media
- capable of handling a mix of compressible and incompressible flows
- capable of handling multicomponent flows
- capable of modelling interphase mass, momentum and energy transfer

The survey revealed that Fluent and StarCD were not capable of meeting the combination of requirements. OpenFoam offered a number of standard solvers, but not a standard solver for a system of compressible and incompressible fluids. However, as it is open source software, the standard solvers could be modified to solve for such a system. Only Ansys CFX was able to meet the full set of requirements. As OpenFoam would require significant modification of the standard solvers and because the author is not familiar with the programming language C++ in which OpenFoam is written, it was decided to use Ansys CFX for the flow modelling.
To reduce the computational cost only the catalyst bed was modelled as a wedge with an angle of $1 rad$. This is schematically shown in figure I.1 where the grey area indicates the part of the catalyst bed that was modelled. The wall of the catalyst bed (the arc in figure I.1) was modelled as a slip-free

wall. Periodic boundary conditions were set for the boundary with the rest of the catalyst bed with rotational symmetry, meaning that the flux across one boundary is mapped onto the other boundary. At the inlet the mass flux was specified and at the outlet the static pressure. The inlet liquid volume fraction was set to $\varepsilon_l = 0.95$ and the inlet mass fractions to $Y_{H_2O_2} = 0.875$ for the liquid phase and $Y_{H_2O_2} = 0.001$, $Y_{H_2O} = 0.001$ and $Y_{O_2} = 0.001$ for the gas phase. The inlet gas volume fraction and the inlet mass fraction for liquid water and air are determined from the constraint that the sum of the volume fractions and the sum of the mass fractions for each phase equal 1. The initial conditions for the fluids were set equal to the inlet boundary conditions. Source terms were implemented by user defined functions written in FORTRAN77.

As it was expected that simply running the simulation would result in divergence, a staged approach

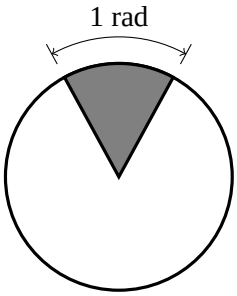

Figure I.1: *Catalyst bed section used for modelling*

was used. In this approach the source terms are reduced in strength to minimise their influence on the results. The simulations was then performed and the converged solution was used as initial condition for the next simulation in which the source terms were made slightly larger. In this way it was hoped that after several runs a converged solution was reached in which the source terms were at full strength.

Unfortunately, this approach has not led to stable solutions. Although initial simulations reached convergence, subsequent simulations showed divergence which eventually led to crashes. Several initial conditions have been varied in an attempt to stabilise the calculations, such as level of turbulence, initial velocities and time steps. This has led to the decision to develop an in-house code to solve the system of equations.

One of the biggest problems with commercial CFD packages is that for the user it is not clear how the equations are solved: it is effectively a black box. As has been discussed and shown in chapter 4 the developed one-dimensional code uses a couple of ”tricks” to stabilise the calculation procedure. For an user of commercial CFD software it is not clear if and how such tricks are implemented. This problem is also reflected in the fact that the majority of computational studies of multiphase flow presented in literature employ in-house developed codes.

Bibliography

[1] M. Ventura and G. Garboden. A brief history of concentrated hydrogen peroxide uses. In *35th AIAA/ASME/SAE/ASEE Joint Propulsion Conference and Exhibit, Los Angeles, California*, number 1999-2739, 1999.

[2] E. Wernimont and P. Mullens. Capabilities of hydrogen peroxide catalyst beds. In *36th AIAA/ASME/SAE/ASEE Joint Propulsion Conference and Exhibit, Huntsville, Alabama*, number 2000-3555, 2000.

[3] E. Wernimont, M. Ventura, G. Garboden, and P. Mullens. Past and present uses of rocket grade hydrogen peroxide. In *International Hydrogen Peroxide Propulsion Conference, West Lafayette, USA*, 1999.

[4] GRASP team. General assessment of green propellants (D2.1). Seventh framework programme (FP7/2007-2013), grant agreement no 218819, 2009.

[5] B.J. McBride and S. Gordon. Computer program for calculation of complex chemical equilibrium compositions and applications. *NASA reference publication*, 1311, 1996.

[6] O. Frota, B. Mellor, and M. Ford. Proposed selection criteria for next generation liquid propellants. In *Proceedings of the 2nd International Conference on Green Propellants for Space Propulsion (ESA SP-557). 7-8 June 2004, Chia Laguna (Cagliari), Sardinia, Italy.*, 2004.

[7] EC. website, August 2008. http://ec.europa.eu/environment/chemicals/dansub/pdfs/annex3_en.pdf.

[8] V. Bombelli, M. Ford, and T. Marée. Road map for the demonstration of the use of reduced-hazard mono-propellants for spacecraft. In *Proceedings of the 2nd International Conference on Green Propellants for Space Propulsion (ESA SP-557). 7-8 June 2004, Chia Laguna (Cagliari), Sardinia, Italy.*, 2004.

[9] C. Kappenstein. Contribution to the green propulsion workshop, 2008. Crete.

[10] BBC. website, March 2009. http://news.bbc.co.uk/1/hi/sci/tech/7946689.stm.

[11] D.D. Davis, L.A. Dee, B. Greene, S.D. Hornung, M.B. McClure, and K.A. Rathgeber. Fire, explosion, compatibility and safety hazards of hydrogen peroxide. Technical report, White Sands Test Facility, Las Cruses, New Mexico, NASA, 2004.

[12] A.J. Musker, J.J. Rusek, C. Kappenstein, and G.T. Roberts. Hydrogen peroxide-from bridesmaid to bride. In *Proceedings of 3rd International Conference on Green Propellant for Space Propulsion and 9th International Hydrogen Peroxide Propulsion Conference*. ESA, 2006.

[13] M.C. Ventura, E. Wernimont, S. Heister, and S. Yuan. Rocket grade hydrogen peroxide (RGHP) for use in propulsion and power devices-historical discussion of hazards. In *43th AIAA Joint Propulsion Conference and Exhibit, Cincinnati, Ohio*, number 2007-5468, 2007.

[14] J.D. Clark. *Ignition! An Informal History of Liquid Rocket Propellants*. Rutgers University Press New Brunswick, NJ, 1972.

[15] G.P. Sutton. *Rocket propulsion elements*. Wiley, 1992.

[16] C.N. Satterfield, G.M. Kavanagh, and H. Resnick. Explosive characteristics of hydrogen peroxide vapor. *Industrial & Engineering Chemistry*, 43(11):2507–2514, 1951.

[17] C.N. Satterfield, F. Feakes, and N. Sekler. Ignition limits of hydrogen peroxide vapor at pressures above atmospheric. *Journal of Chemical and Engineering Data*, 4(2):131–133, 1959.

[18] S.L. Manatt and M.R.R. Manatt. On the analyses of mixture vapor pressure data: The hydrogen peroxide/water system and its excess thermodynamic functions. *Chemistry-A European Journal*, 10(24):6540–6557, 2004.

[19] M.C. Ventura. Long term storability of hydrogen peroxide. In *41st Joint Propulsion Conference and Exhibit, Tucson, Arizona*, number 2005-4551, 2005.

[20] N. Purcell, A. Diede, and M. Minthorn. Test results of new reduced-toxicity hypergols for use with hydrogen peroxide oxidizer. In *5th International Hydrogen Peroxide Propulsion Conference, Purdue University, September*, 2002.

[21] V.N. Sadov. Self-ignition of low-toxicity fuel Diran-A with hydrogen peroxide in combustion chamber. In *5th International Hydrogen Peroxide Propulsion Conference, Purdue University, September*, 2002.

[22] T.A. Dobbins. An improved catalyst system for rendering organic propellants hypergolic with hydrogen peroxide. In *5th International Hydrogen Peroxide Propulsion Conference, Purdue University, September*, 2002.

[23] GRASP team. DC/SOTON test report, issue 1 (D6.1). Seventh framework programme (FP7/2007-2013), grant agreement no 218819, 2010.

[24] GRASP team. DC/SOTON test report, issue 2 (D6.1). Seventh framework programme (FP7/2007-2013), grant agreement no 218819, 2010.

[25] European Chemicals Agency. website, June 2011. http://echa.europa.eu/en/view-article/-/journal_content/56acf53c-dbb4-4537-b119-9579619a3db0.

[26] International Chemical Secretariat. website, May 2011. http://www.chemsec.org/images/stories/2011/chemsec/SIN_List_2.0_all_378.pdf.

[27] International Chemical Secretariat. website, January 2013. http://www.chemsec.org/what-we-do/sin-list/.

[28] FOTEC. website, 2008. https://www.grasp-fp7.eu/grasp/?q=content/welcome-grasp-project-homepage.

[29] GRASP team. Annex 1: Description of work. seventh framework programme (FP7/2007-2013), grant agreement no 218819, 2008.

[30] Ministery of Defence UK. website, September 2008. http://www.aof.mod.uk/aofcontent/tactical/techman/content/trl_whatarethey.htm.

[31] G. Lemon, J.R. King, H.M. Byrne, O.E. Jensen, and K.M. Shakesheff. Mathematical modelling of engineered tissue growth using a multiphase porous flow mixture theory. *Journal of Mathematical Biology*, 52(5):571–594, 2006.

[32] L.M. Abriola. Multiphase flow and transport models for organic chemicals: A review and assessment. *Electric Power Research Institute, Palo Alto, CA. EA-5976*, 1988.

[33] J. Niessner and S.M. Hassanizadeh. Modeling kinetic interphase mass transfer for two-phase flow in porous media including fluid–fluid interfacial area. *Transport in Porous Media*, 80(2): 329–344, 2009.

[34] M.P. Duduković, F. Larachi, and P.L. Mills. Multiphase catalytic reactors: a perspective on current knowledge and future trends. *Catalysis Reviews*, 44(1):123–246, 2002.

[35] J.A.M. Kuipers and W.P.M. Van Swaaij. Computational fluid dynamics applied to chemical reaction engineering. *Advances in Chemical Engineering*, 24:227–328, 1998.

[36] Z.V. Kuzeljevic and M.P. Dudukovic. Computational modeling of trickle bed reactors. *Industrial & Engineering Chemistry Research*, 51(4):1663–1671, 2012.

[37] G. Yadigaroglu. Computational fluid dynamics for nuclear applications: from cfd to multi-scale cmfd. *Nuclear Engineering and Design*, 235(2):153–164, 2005.

[38] W. Schmidt. Interfacial drag of two-phase flow in porous media. *International Journal of Multiphase Flow*, 33(6):638–657, 2007.

[39] A. Musker, G. Roberts, P. Chandler, J. Grayson, and J. Holdsworth. Optimisation study of a homogeneously-catalysed HTP rocket engine. In *ESA Special Publication*, volume 557, page 9, 2004.

[40] A.J. Musker and G.T. Roberts. The effect of stabilizer content on the catalytic decomposition of hydrogen peroxide. In *41st AIAA/ASME/SAE/ASEE Joint Propulsion Conference & Exhibit*, number 2005-3981, 2005.

[41] A. Musker, G. Roberts, R. Horabin, A. Kawar, M. Payne, M. Pollard, and C. Ryan. An assessment of homogeneous catalysts for the rapid decomposition of hydrogen peroxide. In *42th AIAA Joint Propulsion Conference and Exhibit, Sacramento, California*, number 2006-4545, 2006.

[42] W.J. Helms, J.S. Mok, J.C. Sisco, and W.E. Anderson. Decomposition and vaporization studies of hydrogen peroxide. In *38th AIAA/ASME/SAE/ASEE Joint Propulsion Conference and Exhibit, Indianapolis, Indiana*, number 2002-4028, 2002.

[43] K.J. Miller, J.C. Sisco, B.L. Austin, T.N. Martin III, and W.E. Anderson. Design and ground testing of a hydrogen peroxide/kerosene combustor for rbcc application. In *39th AIAA/ASME/SAE/ASEE Joint Propulsion Conference and Exhibit, Huntsville, Alabama*, number 2003-4477, 2003.

[44] A. Cervone, L. Romeo, L. Torre, L. dAgostino, F. Calderazzo, A.J. Musker, G.T. Roberts, and G. Saccoccia. Development of green hydrogen peroxide monopropellant rocket engines and testing of advanced catalytic beds. In *3rd International Conference on Green Propellants for Space Propulsion, Poitiers, France, September*, pages 17–20, 2006.

[45] L. Romeo, L. Torre, A. Pasini, A. Cervone, L. dAgostino, and F. Calderazzo. Performance of different catalysts supported on alumina spheres for hydrogen peroxide decomposition. In *43th AIAA/ASME/SAE/ASEE Joint Propulsion Conference and Exhibit, Cincinnati, Ohio*, number 2007-5466, 2007.

[46] A. Pasini, L. Torre, L. Romeo, A. Cervone, and L. d'Agostino. Testing and characterization of a hydrogen peroxide monopropellant thruster. *Journal of Propulsion and Power*, 24(3):507–515, 2008.

[47] J.T. Richardson, D. Remue, and J.K. Hung. Properties of ceramic foam catalyst supports: mass and heat transfer. *Applied Catalysis A: General*, 250(2):319–329, 2003.

[48] E. Fanelli, M. Turco, A. Russo, G. Bagnasco, S. Marchese, P. Pernice, and A. Aronne. MnO_x/ZrO_2 gel-derived materials for hydrogen peroxide decomposition. *Journal of Sol-Gel Science and Technology*, 60(3):426–436, 2011.

[49] D. Krejci, A. Woschnak, C. Scharlemann, and K. Ponweiser. Structural impact of honeycomb catalysts on hydrogen peroxide decomposition for micro propulsion. *Chemical Engineering Research and Design*, 2012.

[50] M. Ishii and T. Hibiki. *Thermo-fluid dynamics of two-phase flow*. Springer, 2006.

[51] C.Y. Wang and P. Cheng. Multiphase flow and heat transfer in porous media. *Advances in heat transfer*, 30:93–182, 1997.

[52] M. Manninen, V. Taivassalo, and S. Kallio. On the mixture model for multiphase flow. *VTT Publications*, 1996.

[53] D.A. Drew. Mathematical modeling of two-phase flow. *Annual review of fluid mechanics*, 15 (1):261–291, 1983.

[54] D.A. Drew. Averaged field equations for two-phase media. *Studies in Applied Mathematics*, 50(2):133–166, 1971.

[55] D.A. Drew and R.T. Lahey. Application of general constitutive principles to the derivation of multidimensional two-phase flow equations. *International Journal of Multiphase Flow*, 5(4): 243–264, 1979.

[56] J.M. Delhaye. Jump conditions and entropy sources in two-phase systems. local instant formulation. *International Journal of Multiphase Flow*, 1(3):395–409, 1974.

[57] A. Prosperetti and G. Tryggvason. *Computational methods for multiphase flow*. Cambridge University Press, 2007.

[58] J.R. Philip. Flow in porous media. *Annual Review of Fluid Mechanics*, 2(1):177–204, 1970.

[59] S. Whitaker. Flow in porous media I: A theoretical derivation of darcy's law. *Transport in Porous Media*, 1(1):3–25, 1986.

[60] C. Johnson, W. Anderson, R. Ross, and G. Lyles. Catalyst bed instability within the USFE H_2O_2/JP-8 rocket engine. In *36th AIAA/ASME/SAE/ASEE Joint Propulsion Conference and Exhibit, Huntsville, Alabama*, number 2000-3301, 2000.

[61] X. Zhou and D. Hitt. One-dimensional modeling of catalyzed h_2o_2 decomposition in microchannel flows. In *33rd AIAA Fluid Dynamics Conference and Exhibit*, number AIAA/ASME/SAE/ASEE 2003-3584, 2003.

[62] S. Bonifacio and A. Russo Sorge. Modelling hydrogen peroxide decomposition in monolithic beds. In *Proceedings of 3rd International Conference on Green Propellant for Space Propulsion and 9th International Hydrogen Peroxide Propulsion Conference*, SP-635. ESA, 2006.

[63] J.H. Corpening, S.D. Heister, W.E. Anderson, and B.J. Austin. Thermal decomposition of hydrogen peroxide, part 2: Modeling studies. *Journal of Propulsion and Power*, 22(5):996, 2006.

[64] A. Pasini, L. Torre, L. Romeo, A. Cervone, and L. D'Agostino. Reduced-order model for H_2O_2 catalytic reactor performance analysis. *Journal of Propulsion and Power*, 26(3):446–453, 2010.

[65] X. Zhou and D.L. Hitt. Numerical modeling of monopropellant decomposition in a micro-catalyst bed. In *35th AIAA/ASME/SAE/ASEE Fluid Dynamics Conference and Exhibit*, number 2005-5033, 2005.

[66] R.B. Bird, W.E. Stewart, and E.N. Lightfoot. *Transport Phenomena*. John Wiley & Sons, USA, 2nd edition, 2002.

[67] S. Afandizadeh and E.A. Foumeny. Design of packed bed reactors: guides to catalyst shape, size, and loading selection. *Applied thermal engineering*, 21(6):669–682, 2001.

[68] F. Benyahia and K.E. O'Neill. Enhanced voidage correlations for packed beds of various particle shapes and sizes. *Particulate science and technology*, 23(2):169–177, 2005.

[69] H. Martin. Low peclet number particle-to-fluid heat and mass transfer in packed beds. *Chemical Engineering Science*, 33(7):913–919, 1978.

[70] O. Bey and G. Eigenberger. Fluid flow through catalyst filled tubes. *Chemical Engineering Science*, 52(8):1365–1376, 1997.

[71] E.A. Foumeny and H. Pahlevanzadeh. Evaluation of plug flow assumption in packed beds. *Chemical engineering & technology*, 13(1):161–171, 1990.

[72] P. Atkins and J. De Paula. *Atkins Physical Chemistry*. Oxford University Press, uk edition, 2006.

[73] M.J. Pilling, P.W. Seakins, et al. *Reaction kinetics*. Oxford University Press, 1996.

[74] N. Pearson, T. Pourpoint, and W.E. Anderson. Vaporization and decomposition of hydrogen peroxide drops. In *39th AIAA/ASME/SAE/ASEE Joint Propulsion Conference and Exhibit, Huntsville, Alabama*, number 2003-4642, 2003.

[75] C.N. Satterfield and T.W. Stein. Homogeneous decomposition of hydrogen peroxide vapor. *The Journal of Physical Chemistry*, 61(5):537–540, 1957.

[76] D.E. Hoare, J.B. Protheroe, and A.D. Walsh. The thermal decomposition of hydrogen peroxide vapour. *Transactions of the Faraday Society*, 55:548–557, 1959.

[77] A.T. Bell and M. Head-Gordon. Quantum mechanical modeling of catalytic processes. *Annual Review of Chemical and Biomolecular Engineering*, 2:453–477, 2011.

[78] P.A. Giguère and I.D. Liu. Kinetics of the thermal decomposition of hydrogen peroxide vapor. *Canadian Journal of Chemistry*, 35(4):283–293, 1957.

[79] H. Hippler, H. Neunaber, and J. Troe. Shock wave studies of the reactions HO + $H_2O_2 \rightarrow H_2O$ + HO_2 and HO + $HO_2 \rightarrow H_2O$+ O_2 between 930 and 1680k. *The Journal of chemical physics*, 103(9):3510–3516, 1995.

[80] Z. Hong, R.D. Cook, D.F. Davidson, and R.K. Hanson. A shock tube study of OH + $H_2O_2 \rightarrow$ H_2O + HO_2 and H_2O_2 + M $\rightarrow$ 2OH + M using laser absorption of H_2O and OH. *The Journal of Physical Chemistry A*, 114(18):5718–5727, 2010.

[81] E. Croiset, S.F. Rice, and R.G. Hanush. Hydrogen peroxide decomposition in supercritical water. *AIChE Journal*, 43(9), 1997.

[82] J. Takagi and K. Ishigure. Thermal decomposition of hydrogen peroxide and its effect on reactor water monitoring of boiling water reactors. *Nucl. Sci. Eng.;(United States)*, 89(2), 1985.

[83] R.A. Holub, M.P. Dudukovic, and P.A. Ramachandran. Pressure drop, liquid holdup, and flow regime transition in trickle flow. *AIChE Journal*, 39(2), 1993.

[84] T. Oehmichen, L. Datsevich, and A. Jess. Influence of bubble evolution on the effective kinetics of heterogeneously catalyzed gas/liquid reactions. part i: Reactions with gaseous products. *Chemical Engineering & Technology*, 33(6):911–920, 2010.

[85] EW Thiele. Relation between catalytic activity and size of particle. *Industrial & Engineering Chemistry*, 31(7):916–920, 1939.

[86] L.B. Datsevich. Some theoretical aspects of catalyst behaviour in a catalyst particle at liquid (liquid-gas) reactions with gas production: oscillation motion in the catalyst pores. *Applied Catalysis A: General*, 247(1):101–111, 2003. ISSN 0926-860X.

[87] D.A. Frank-Kameneëtìskiæi. *Diffusion and heat transfer in chemical kinetics*. Plenum Press (New York), 1969.

[88] S. Sohn and D. Kim. Modification of langmuir isotherm in solution systems–definition and utilization of concentration dependent factor. *Chemosphere*, 58(1):115–123, 2005.

[89] G. Bliznakov and D. Lazarov. Surface heterogeneity of metals of the copper group in the catalytic decomposition of hydrogen peroxide. *Journal of Catalysis*, 14(2):187–192, 1969.

[90] F. Haber and J. Weiss. The catalytic decomposition of hydrogen peroxide by iron salts. *Proceedings of the Royal Society of London. Series A, Mathematical and Physical Sciences*, 147 (861):332–351, 1934.

[91] D.W. McKee. Catalytic decomposition of hydrogen peroxide by metals and alloys of the platinum group. *Journal of Catalysis*, 14(4):355–364, 1969.

[92] E. Giamello, P. Rumori, F. Geobaldo, B. Fubini, and M.C. Paganini. The interaction between hydrogen peroxide and metal oxides: Epr investigations. *Applied Magnetic Resonance*, 10(1): 173–192, 1996.

[93] R.K.E. Albers, M.J.J. Houterman, T. Vergunst, E. Grolman, and J.A. Moulijn. Novel monolithic stirred reactor. *AIChE journal*, 44(11):2459–2464, 2004.

[94] C.C. Lin, F.R. Smith, N. Ichikawa, T. Baba, and M. Itow. Decomposition of hydrogen peroxide in aqueous solutions at elevated temperatures. *International journal of chemical kinetics*, 23 (11):971–987, 1991.

[95] A.S. Shteinberg. *Fast reactions in energetic materials: high-temperature decomposition of rocket propellants and explosives*. Springer, 2008.

[96] G.N. Hatsopoulos and J.H. Keenan. *Principles of general thermodynamics*. Krieger, 1981.

[97] G. Scatchard, G.M. Kavanagh, and L.B. Ticknor. Vapor-liquid equilibrium. viii. hydrogen peroxide water mixtures. *Journal of the American Chemical Society*, 74(15):3715–3720, 1952.

[98] G.M. Kavanagh. *The vapor-liquid equilibrium and related properties of hydrogen peroxide-water solutions*. PhD thesis, MIT, 1949.

[99] S.S. Sazhin. Advanced models of fuel droplet heating and evaporation. *Progress in Energy and Combustion Science*, 32(2):162–214, 2006.

[100] C.K. Law. Recent advances in droplet vaporization and combustion. *Progress in Energy and Combustion Science*, 8(3):171–201, 1982.

[101] S.R. Turns. *An introduction to combustion: concepts and applications*, volume 10. McGraw-hill New York, 1996.

[102] R.S. Miller, K. Harstad, and J. Bellan. Evaluation of equilibrium and non-equilibrium evaporation models for many-droplet gas-liquid flow simulations. *International Journal of Multiphase Flow*, 24(6):1025–1055, 1998.

[103] G.L. Hubbard, V.E. Denny, and A.F. Mills. Droplet evaporation: effects of transients and variable properties. *International Journal of Heat and Mass Transfer*, 18(9):1003–1008, 1975.

[104] B. Abramzon and W.A. Sirignano. Droplet vaporization model for spray combustion calculations. *International Journal of Heat and Mass Transfer*, 32(9):1605–1618, 1989.

[105] J.S. Shrimpton and Y. Laoonual. Dynamics of electrically charged transient evaporating sprays. *International Journal for Numerical Methods in Engineering*, 67(8):1063–1081, 2006.

[106] V.R. Dushin, A.V. Kulchitskiy, V.A. Nerchenko, V.F. Nikitin, E.S. Osadchaya, Y.G. Phylippov, and N.N. Smirnov. Mathematical simulation for non-equilibrium droplet evaporation. *Acta Astronautica*, 63(11):1360–1371, 2008.

[107] A.P. Kryukov, V.Y. Levashov, and S.S. Sazhin. Evaporation of diesel fuel droplets: kinetic versus hydrodynamic models. *International Journal of Heat and Mass Transfer*, 47(12):2541–2549, 2004.

[108] S.C.K. De Schepper, G.J. Heynderickx, and G.B. Marin. Modeling the evaporation of a hydrocarbon feedstock in the convection section of a steam cracker. *Computers and Chemical Engineering*, 33(1):122–132, 2009.

[109] M. Burger, R. Schmehl, K. Prommersberger, O. Schäfer, R. Koch, and S. Wittig. Droplet evaporation modeling by the distillation curve model: accounting for kerosene fuel and elevated pressures. *International Journal of Heat and Mass Transfer*, 46(23):4403–4412, 2003.

[110] G. Brenn, L.J. Deviprasath, F. Durst, and C. Fink. Evaporation of acoustically levitated multicomponent liquid droplets. *International Journal of Heat and Mass Transfer*, 50(25-26):5073–5086, 2007.

[111] S.S. Sazhin, A. Elwardany, P.A. Krutitskii, G. Castanet, F. Lemoine, E.M. Sazhina, and M.R. Heikal. A simplified model for bi-component droplet heating and evaporation. *International Journal of Heat and Mass Transfer*, 53(21-22):4495–4505, 2010.

[112] S.S. Sazhin, A.E. Elwardany, P.A. Krutitskii, V. Deprédurand, G. Castanet, F. Lemoine, E.M. Sazhina, and M.R. Heikal. Multi-component droplet heating and evaporation: numerical simulation versus experimental data. *International Journal of Thermal Sciences*, 2011.

[113] J. Bellan and M. Summerfield. Theoretical examination of assumptions commonly used for the gas phase surrounding a burning droplet. *Combustion and Flame*, 33:107–122, 1978.

[114] M.H. Al-Dahhan, F. Larachi, M.P. Dudukovic, and A. Laurents. High-pressure trickle-bed reactors: A review. *Ind. Eng. Chem. Res*, 36(8):3292–3314, 1997.

[115] V.X. Tung and V.K. Dhir. A hydrodynamic model for two-phase flow through porous media. *International journal of multiphase flow*, 14(1):47–65, 1988.

[116] M.J. Palmer, A.J. Musker, and G.T. Roberts. Design, build and test of a 20N hydrogen peroxide monopropellant thruster. In *47th AIAA/ASME/SAE/ASEE Joint Propulsion Conference and Exhibit, San Diego, California*, number 2011-5697, 2011.

[117] Y.A. Zeigarnik and I.V. Kalmykov. Experimental study of the flow resistance of porous structures in the adiabatic motion of steam-water mixtures. *High Temp.(Engl. Transl.);(United States)*, 23(5), 1985.

[118] R.W. Lockhart and R.C. Martinelli. Proposed correlation of data for isothermal two-phase, two-component flow in pipes. *Chemical Engineering Progress*, 45(1):39–48, 1949.

[119] D. Chisholm. A theoretical basis for the lockhart-martinelli correlation for two-phase flow. *International Journal of Heat and Mass Transfer*, 10(12):1767–1778, 1967.

[120] S. Crone, C. Bergins, and K. Strauss. Multiphase flow in homogeneous porous media with phase change. Part I: numerical modeling. *Transport in porous media*, 49(3):291–312, 2002.

[121] V.V. Sorokin. Calculation of two-phase adiabatic flow in a pebble bed. *High Temperature*, 46 (3):432–434, 2008.

[122] J.A. Tallmadge. Packed bed pressure drop An extension to higher Reynolds numbers. *AIChE Journal*, 16(6):1092–1093, 1970.

[123] S. Patankar. *Numerical heat transfer and fluid flow*. Taylor & Francis, 1980.

[124] H.K. Versteeg and W. Malalasekera. *An introduction to computational fluid dynamics: the finite volume method, 1995*. Harlow-Longman Scientific & Technical, London, 1996.

[125] J.H. Ferziger and M. Perić. *Computational Methods for Fluid Dynamics*. Springer Verlag, 1999.

[126] G. Kocamustafaogullari and M. Ishii. Foundation of the interfacial area transport equation and its closure relations. *International Journal of Heat and Mass Transfer*, 38(3):481–493, 1995.

[127] T. Hibiki and M. Ishii. Two-group interfacial area transport equations at bubbly-to-slug flow transition. *Nuclear engineering and design*, 202(1):39–76, 2000.

[128] C. Morel, N. Goreaud, and J.M. Delhaye. The local volumetric interfacial area transport equation: derivation and physical significance. *International journal of multiphase flow*, 25(6): 1099–1128, 1999.

[129] I. Kataoka. Development of research on interfacial area transport. *Journal of Nuclear Science and Technology*, 47(1):1–19, 2010.

[130] U. Graf and P. Papadimitriou. Simulation of two-phase flows in vertical tubes with the cfd code *FLU*box. *Nuclear Engineering and Design*, 237(20):2120–2125, 2007.

[131] S. Whitaker. Flow in porous media II: The governing equations for immiscible, two-phase flow. *Transport in Porous Media*, 1(2):105–125, 1986.

[132] P.J. Oliveira and R.I. Issa. Numerical aspects of an algorithm for the eulerian simulation of two-phase flows. *International Journal for Numerical Methods in Fluids*, 43(10-11):1177–1198, 2003.

[133] M.J. Palmer, A.J. Musker, and G.T. Roberts. Experimental assessment of heterogeneous catalysts for the decomposition of hydrogen peroxide. In *47th AIAA/ASME/SAE/ASEE Joint Propulsion Conference and Exhibit, San Diego, California*, number 2011-5695, 2011.

[134] M.B. Carver. A method of limiting intermediate values of volume fraction in iterative two-fluid computations. *Journal of Mechanical Engineering Science*, 24(4):221–224, 1982.

[135] E. Romenski and E.F. Toro. Compressible two-phase flows: two-pressure models and numerical methods. *Computational Fluid Dynamics Journal*, 13:403–416, 2004.

[136] C.M. Xisto, J.C. Páscoa, P.J. Oliveira, and D.A. Nicolini. A hybrid pressure–density-based algorithm for the euler equations at all mach number regimes. *International Journal for Numerical Methods in Fluids*, 2011.

[137] J.D. Anderson Jr. *Fundamentals of Aerodynamics*. McGraw-Hill, 1991.

[138] F. Moukalled, M. Darwish, and B. Sekar. A pressure-based algorithm for multi-phase flow at all speeds. *Journal of Computational Physics*, 190(2):550–571, 2003.

[139] R.L. Burden and J.D. Faires. *Numerical Analysis*. COLE Thomson Learning Inc., 2001.

[140] University of Southampton. website, April 2013. http://www.southampton.ac.uk/isolutions/computing/hpc/iridis/.

[141] D. Ju, J. Shrimpton, and A. Hearn. The effect of reduction of propellant mass fraction on the injection profile of metered dose inhalers. *International Journal of Pharmaceutics*, 391: 221–229, 2010.

[142] J. Corpening, S. Heister, and W. Anderson. A model for thermal decomposition of hydrogen peroxide. In *40th AIAA/ASME/SAE/ASEE Joint Propulsion Conference and Exhibit*, 2004.

[143] N.M. Kuznetsov and S.M. Frolov. The calculation of liquid-vapor phase equilibrium in H_2O-H_2O_2 two-component system. *High Temperature*, 46(6):775–781, 2008.

[144] M. Munro. Evaluated material properties for a sintered α-alumina. *Journal of the American Ceramic Society*, 80(8):1919–1928, 1997.

[145] I.F. Macdonald, M.S. El-Sayed, K. Mow, and F.A.L. Dullien. Flow through porous media - the Ergun equation revisited. *Industrial & Engineering Chemistry Fundamentals*, 18(3):199–208, 1979.

[146] University of Southampton. website, April 2013. http://www.southampton.ac.uk/muvis/.

[147] C.N. Satterfield and F.P. Audibert. Nucleate and film boiling in catalytic decomposition of hydrogen peroxide. *Industrial & Engineering Chemistry Fundamentals*, 2(3):200–202, 1963.

[148] NIST. Nist chemistry webbook. website, June 2005. http://webbook.nist.gov/chemistry/.

[149] A.L. Tsykalo and A.G. Tabachnikov. Density, viscosity, and bond energy of molecules in aqueous hydrogen peroxide solutions. *Theoretical and Experimental Chemistry*, 2(6):604–605, 1966.

[150] J.H. Perry. Chemical engineers' handbook. *Journal of Chemical Education*, 27(9):533, 1950.

[151] US Peroxide. website, 2012. http://www.h2o2.com/technical-library/physical-chemical-properties/physical-properties/default.aspx?pid=22&name=Boiling-Points-and-Freezing-Points.

[152] Becco Chemical Division. Properties of hydrogen peroxide solutions, 1955. personal correspondance.

[153] J.C. McCormick. *Hydrogen Peroxide Rocket Manual*. FMC Corporation, 1965.

[154] P. Li, Y.H. Liang, P.S. Ma, and C. Zhu. Estimations of enthalpies of vaporization of pure compounds at different temperatures by a corresponding-states group-contribution method. *Fluid Phase Equilibria*, 137(1-2):63–74, 1997.

[155] S. Radl, S. Ortner, R. Sungkorn, and J.G. Khinast. The engineering of hydrogen peroxide decontamination systems. *Journal of Pharmaceutical Innovation*, 4(2):51–62, 2009.

[156] R. Aris. On shape factors for irregular particles I. *Chemical Engineering Science*, 50(24): 3897–3898, 1995.

[157] National Instruments. website, January 2012. http://sine.ni.com/ds/app/doc/p/id/ds-190/lang/en.